High repetition rate laser-driven ion acceleration using cryogenic low-Z jets

by

Chandra Breanne Curry

A thesis submitted in partial fulfillment of the requirements for the degree of

Doctor of Philosophy

in

Photonics and Plasmas

Department of Electrical and Computer Engineering
University of Alberta

Abstract

Proton and deuteron beams accelerated through high-intensity laser-plasma interactions have the potential to be used in a wide range of applications in research, medicine, and industry. More specifically, they are expected to revolutionize radiography in civil and aerospace engineering and national security applications. They may also supplant nuclear reactors for the production of medical isotopes.

This thesis, completed in the High Energy Density Sciences (HEDS) Division at SLAC National Accelerator Laboratory, has laid the foundation for the creation of bright multi-MeV high-repetition rate proton and deuteron sources. The experimental findings presented herein utilized continuous, high-speed, low-Z cryogenic jets compatible with up to kHz repetition rate petawatt-class laser-plasma interactions. The tunable dimensions, near-critical density, and single-element composition of the cryogenic low-Z jets enable the exploration of previously inaccessible plasma regimes and acceleration mechanisms in the laboratory. They could ultimately be used to produce pulsed charged particle beams with ultra-low emittance and sub-nanosecond pulse durations, thereby surpassing the current state-of-the-art capabilities of large-scale linear accelerators and cyclotrons.

This thesis investigates laser-accelerated ion beams from Target Normal Sheath Acceleration and advanced acceleration regimes with 100-terawatt (TW) and petawatt (PW) class laser systems. Laser-driven ion beams with improved spatial uniformity and high peak brightness have been demonstrated, and this sets a clear path toward the creation of high repetition rate (HRR) laser-driven ion sources.

Preface

The Introduction and Thesis Content (Chapter 1), Motivation (Chapter 2), Theoretical Background (Chapter 3), High-power Short Pulse Lasers (Chapter 4), Diagnosing Laser-Accelerated Proton and Deuteron Beams Introduction (Section 6.1 and 6.2), and the Conclusion and Outlook (Chapter 9) are original work by the author. Chapter 8 contains material that is in preparation for submission to scientific journals. Section 5.1, Section 6.3, and Section 7.1 are Prefaces that describe context and the contributions made by each co-author to the following published papers:

1. **C. B. Curry**, C. Schoenwaelder, S. Goede, J. B. Kim, M. Rehwald, F. Treffert, K. Zeil, S. H. Glenzer, M. Gauthier, *Cryogenic Liquid Jets for High Repetition Rate Discovery Science*, J. Vis. Exp., **159**, e61130, (2020). doi: 10.3791/61130

2. **C. B. Curry**, C. A. S. Dunning, M. Gauthier, H.-G. J. Chou, F. Fiuza, G. D. Glenn, Y. Y. Tsui, M. Bazalova-Carter, and S. H. Glenzer, *Optimization of radiochromic film stacks to diagnose high-flux laser-accelerated proton beams*, Rev. Sci. Instrum., **91**, 093303 (2020). doi: 10.1063/5.0020568

3. M. Gauthier, **C. B. Curry**, S. Goede, F.-E. Brack, J. B. Kim, M. J. MacDonald, J. Metzkes, L. Obst, M. Rehwald, C. Roedel, H.-P. Schlenvoigt, W. Schumaker, U. Schramm, K. Zeil, and S. H. Glenzer, *High repetition rate, multi-MeV proton source from cryogenic hydrogen jets*. Appl. Phys. Lett. **111**, 114102 (2017). doi: 10.1063/1.4990487

Some of the research conducted for this thesis was part of an international research collaboration led by Prof. Dr. Siegfried H. Glenzer (Stanford University/SLAC National Accelerator Laboratory), Prof. Dr. Ulrich Schramm (Technische Universität/Helmholtz-Zentrum Dresden Rosendorf), and Prof. Dr. Thomas E. Cowan (Technische Universität/Helmholtz-Zentrum Dresden Rosendorf).

This thesis was edited by S. Nevalainen, A. Longman, S. Malko, S. H. Glenzer, and Y. Y. Tsui.

For my father who never saw this adventure.

Acknowledgements

Firstly, I would like to express my gratitude to my grandmother and stepmother, H. Curry and S. McGillicky, for their love and unwavering support.

I would also like to extend my thanks to Team Canada - A. Longman, C. Longman, S. M. Kerr, M. Z. Mo, and Z. Chen - for always being there and reminding me of home. To my dearest neighbors - E. Skrabo, F. Nistal, A. Dragone, and J. McCormack - thank you for the good wine, food, and conversations during the COVID-19 pandemic. Lastly, I want to thank S. Malko, whom I only met this year, but it feels like I've known her forever.

I would like to express my appreciation to the many past and present members of the High Energy Density Sciences Division at SLAC National Accelerator Laboratory. From deep scientific discussions to lighthearted coffee chats about our lives, the world, and what we've been watching on Netflix, it was an unforgettable experience. J. B. Kim, I am a better experimentalist because of your mentorship. I promise to always look for opportunities that let me "do cool sh*t." M. Gauthier, your high standards encouraged me to do careful, meticulous science, and motivated me to get things done, even if it meant working late nights in the lab. To the High Energy Density Short Pulse (HED-SP) Group - M. Gauthier, F. Treffert, C. Schoenwaelder, G. D. Glenn - we lived, worked, meal-prepped, and traveled together, sometimes for months at a time, becoming the researchers that we are today. I will cherish the many inside jokes and memories forever. The work in this thesis would not have been possible without the following songs: "I Want to Break Free" by Queen, "It's a Long Way to the Top (If You Wanna Rock 'N' Roll)" by AC/DC, "Mah-na Mah-na, do doo do do do, Mah-na Mah-na!" by The Muppets, and "Only Time" by Enya.

D. Hernandez, you were the unsung hero of our many experiments. Thank you for coordinating our equipment shipments, ensuring all our purchases went through smoothly and arrived on time, and helping me navigate complex supply chains (*i.e.* global helium shortages).

Lastly, I want to express my gratitude to my many collaborators over the years. I have learned so much from you, from lab skills to an improved theoretical understanding of the experiments we performed together.

Above all, I would like to thank my advisors S. H. Glenzer and Y. Y. Tsui. You pushed me, gave me many opportunities to learn, and always provided sound advice and mentorship at critical points during my PhD.

Contents

List of Tables

List of Figures

List of Abbreviations

ASE	Amplified Spontaneous Emission
AR	Anti-Reflection
BBO	Barium Borate
BOA	Breakout Afterburner
BSPM	Beam Splitting Plasma Mirror
CE	Coulomb Explosion
CCD	Charge-Coupled Device
CPA	Chirped Pulse Amplification
CR-39	Allyl Diglycol Carbonate Nulclear Track Detector
CSWA	Collisionless Shockwave Acceleration
DEMO	DEMOnstration power plant
D-T	Deuterium-Tritium
EMP	Electromagnetic Pulse
ESF	Enhanced Sheath Field
FEL	Free Electron Laser
FI	Fast Ignition
FWHM	Full Width at Half Maximum
HB	Hole Boring
HDPE	High Density Polyethylene
HED	High-Energy-Density
HEDS	High-Energy-Density Sciences
HRR	High repetition rate
HZDR	Helmholtz-Zentrum Dresden-Rossendorf

ICF	Inertial Confinement Fusion
IFE	Inertial Fusion Energy
IP	Imaging Plate
KDP	Potassium Dihydrogen Phosphate
LANL	Los Alamos National Laboratory
LCLS	Linac Coherent Light Source
MCP	Microchannel Plate
MEC	Matter in Extreme Conditions
MEC-U	Matter in Extreme Conditions Upgrade
MVA	Magnetic Vortex Acceleration
Nd:Glass	Neodymium: Glass
Nd:YAG	Neodymium: Yytrium-Alumunium-Garnet
NIST	National Institute of Standards and Technology
OAP	Off-Axis Parabola
Oh	Ohnesorge Number
OPCPA	Optical Parametric Chirped Pulse Amplification
OPA	Optical Parametric Amplifier
PIC	Particle-in-Cell
P&ID	Piping and Instrumentation Diagram
P-I-D	Proportional-Integral-Derivative
PM	Plasma Mirror
PMT	Photomultiplier Tube
PSL	Photostimulated Luminescence
Re	Reynolds number
RF	Radio Frequency
RPA	Radiation Pressure Acceleration

RCF	Radiochromic Film
RTI	Rayleigh Taylor-like Instability
SEM	Standard error of the mean
SF	Spatial Filter
SHG	Second Harmonic Generation
SRIM	Stopping Range of Ions in Matter
SSD	Source-to-Surface Distance
TC	Target Chamber
TCC	Target Chamber Center
Ti:Sa	Titanium-doped Sapphire
TNSA	Target Normal Sheath Acceleration
TP	Thomson Parabola Ion Spectrometer
TPW	Texas Petawatt
WDM	Warm Dense Matter
We	Weber Number
XFEL	X-ray Free Electron Laser
XPW	Cross-Polarized Wave

Funding Acknowledgements

The work of the author was partially support by the Natural Sciences and Engineering Research Council of Canada (NSERC) through the Postgraduate Doctoral Scholarship (PGS-D), the University of Alberta President's Doctoral Prize of Distinction, the Queen Elizabeth II Graduate Scholarship – Doctoral, and the Queen Elizabeth II Graduate Scholarship – Master's.

Work presented in this thesis was supported by the U.S. Department of Energy Office of Science, Fusion Energy Science under FWP No. 100182 with additional support from FWP No. 100331, and Contract No. DE-SC0019167: the LaserNetUS initiative at the Texas Petawatt Laser facility, the National Science Foundation under Grant No. 1632708, EC H2020 LASERLAB-EUROPE/LEP (Contract No. 654148). Experiments at JLF/LLNL received partial support by LLNL under contract DE-AC52-07NA27344 and the U.S. DOE Office of Science, Fusion Energy Science ACE HEDLP Diagnostics. Simulations presented in Chapter 6 and Chapter 8 were performed on Cori (NERSC) through an ALCC award and on Mira (ANL). The OSIRIS Consortium consisting of UCLA and IST (Portugal) is acknowledged for the use of the OSIRIS3.0 framework and the visXD framework.

Chapter 1
Introduction

The development of high-intensity lasers was enabled by the chirped-pulse amplification (CPA) technique developed by Strickland and Mourou [1]. They were awarded the 2018 Nobel Prize in Physics for revolutionizing laser physics and opening a new field of relativistic laser-plasma interactions.

Ion acceleration via these high-intensity laser-plasma interactions was subsequently discovered [2, 3]. The most thoroughly studied and well-understood laser-driven ion acceleration mechanism is Target Normal Sheath Acceleration (TNSA) [4]. The ion beam properties achieved with TNSA, namely energy distribution, laser-to-ion conversion efficiency, and 6-D beam brightness, still fall short of meeting the requirements of many high-repetition rate applications such as direct injection into an RF linear particle accelerator.

Particle-in-cell (PIC) simulations have identified more favorable ion acceleration regimes that use higher peak laser intensities and advanced target designs. Examples include Enhanced Sheath Field Acceleration (ESF) Acceleration [5], Radiation Pressure Acceleration (RPA) [6], Breakout Afterburner Acceleration (BOA) [7] Collisionless Shockwave Acceleration (CSWA) [8–10], and Magnetic Vortex Acceleration (MVA) [11].

Since most laser-driven ion acceleration experiments have been performed at single-shot ($\sim$1 shot/hour) high-power laser facilities, the rate of progress in identifying laser and target parameters for optimized ion acceleration has been slower than initially anticipated. The first laser-plasma experiments investigating these advanced ion acceleration regimes have only recently been performed [12], and they have revealed complex relationships between laser parameters such as energy, pulse duration, contrast, and spectral phase and target parameters including geometry, thickness, density, pre-formed plasma scale length, and species. A full exploration of the high-dimensional parameter space is now conceivable following the paradigm shift to laser-driven ion acceleration up to multi-MeV energies at repetition rates exceeding 0.5 Hz [13–23]. A table summarizing the experiments that have been performed to date can be found in Appendix A. The implementation of active laser-target-diagnostic-simulation feedback loops and the application of machine learning techniques such as Bayesian optimization are also envisioned to accelerate progress in the field [24–26]. Already, first experiments have shown that Bayesian optimization will require robust on-shot laser and target characterization and a series of shots at the same conditions to account for systematic fluctuations.

This thesis lays groundwork for the exploration and optimization of laser-driven ion acceleration via high repetition rate studies. Its three parts are:

i. Development and characterization of cryogenic hydrogen and deuterium jets for use in high-intensity laser-matter interactions to produce MeV-energy proton and deuteron beams;

ii. Development of a high repetition rate experimental platform consisting of absolutely-calibrated charged particle diagnostics to monitor the spatial and energy distributions of the laser-accelerated ion beam; and

iii. Investigation of the microphysical processes occurring during laser-driven ion acceleration from cryogenic low-Z jets, which are a self-replenishing, high-repetition-rate compatible target. The transition from TNSA to ESF has been explored with terawatt (TW) and petawatt (PW) class laser systems including the Draco laser (3 J, 30 fs) and the Texas Petawatt laser (100 J, 100 fs). The experiments were designed with and then interpreted using 2-D/3-D PIC simulations.

The culmination of this work was the demonstration of high brightness, >65 MeV proton and >42 MeV deuteron beams with 500 TW on target in a relativistic transparency enhanced laser ion acceleration regime using a high-repetition-rate compatible experimental platform. Future work will optimize PW-laser-driven proton and deuteron sources at high repetition rates (>1 Hz) enabled by our state-of-the-art high-repetition rate target and future laser technologies.

The thesis chapters are summarized as follows:

Chapter 2: **Motivation for High-Repetition Rate Ion Sources**

This chapter introduces the characteristic trajectory of ballistic MeV-energy ions through matter and introduces Bragg peaks. Four applications of high repetition rate laser-driven ion sources are described, and context is provided by describing the contributions made by this thesis.

Chapter 3: **Theoretical Background**

We review the motion of a charged particle due to a electromagnetic plane wave including the concepts of the ponderomotive force and relativistic effects. This is followed by an overview of hot electron heating mechanisms and the physics of laser-driven ion acceleration.

Chapter 4: **High-power Short Pulse Lasers**

Techniques for generating and characterizing high-power short-pulse lasers are described. This chapter also introduces the concept of laser-pulse contrast and describes existing methods to improve including fast optical gating using a plasma mirror. It concludes with the development of a beam-splitting plasma mirror for high laser-pulse-contrast, multi-beam experiments.

Chapter 5: **Cryogenic Liquid Jets for High Repetition Rate Laser-Driven Ion Acceleration**

The operation and characterization of a high repetition rate compatible cryogenic liquid jet target system is presented.

Chapter 6: **Diagnosing Laser-Accelerated Proton and Deuteron Beams**

This chapter describes experimental methods for diagnosing laser-accelerated ion beams. Thomson Parabola Ion Spectrometers and Radiochromic Film Stacks, which are used to measure the energy and spatial distribution of an ion beam, are discussed. A numerical optimization study is presented that addresses radiochromic film stack designs for high-flux laser-accelerated proton beams from high-energy petawatt lasers.

Chapter 7: **High-Repetition Rate, Multi-MeV Proton Source from Cryogenic Hydrogen Jets** The first demonstration of high repetition rate laser-driven proton acceleration at 1 Hz using cylindrical cryogenic liquid hydrogen jets is presented. Average proton numbers up to $\sim 10^{13}$ protons/MeV/sr/min are obtained using the Draco laser at Helmholtz-Zentrum Dresden-Rosendorf (HZDR).

Chapter 8: **High-Brightness Proton Acceleration from Planar Cryogenic Hydrogen Jets**

This chapter discusses an experiment on laser-driven ion acceleration using the high-energy Texas Petawatt Laser at the University of Texas at Austin. Bright, high-flux proton and deuteron beams are produced from a high-repetition-rate compatible planar cryogenic low-Z liquid jet. The Texas Petawatt laser and experimental setup are described. A review of the diagnostics used to measure the proton energy spectrum, spatial profile, and divergence is given. The results are discussed and compared to numerical simulations.

Chapter 2
Motivation for High-Repetition-Rate Ion Sources

Laser-plasma-based ion accelerators operating at high repetition rates are an attractive alternative to conventional microwave or radiofrequency (RF) accelerators. In laser-plasma interactions, the laser energy is efficiently coupled to the electrons then transferred to the ions mediated by the plasma. The electric field, responsible for electron or ion acceleration in laser-plasma accelerators, is typically on the order of 1 GeV/m. Simulations lead us to expect that this threshold will be exceeded in advanced ion acceleration regimes. In comparison, the acceleration of charged particles through a conventional microwave or radio-frequency accelerator is limited to around 100 MeV/m. Higher electric field strengths lead to electrical breakdown within the cavities [27].

It is envisioned that the multiple GV/m electric fields achievable in plasmas will lead to the development of ultra-compact charged particle accelerators with higher brightness and particle energies [28]. There is significant interest in laser-based accelerators across a wide range of sub-disciplines including inertial fusion energy [29, 30], medicine [31–35], and fundamental physics research [3, 36–43].

Advances in particle physics are also strongly linked to the availability of particle beams of increasing energy. The energy of collisions in particle colliders has increased exponentially in the last several decades and is described by the so-called Livingston plot [44]. To achieve the charged particle energies required for further progress in high energy physics, new accelerator designs will need to leverage the higher acceleration gradients achievable with plasma technologies such as those presented in this thesis.

In addition to the maximum particle energy, many proposed applications require bright, pulsed (>10 Hz) sources that approach a constant dose rate. The development of laser-accelerated particle sources has, until recently, been primarily limited by laser-driver technology operating at low shot rates (∼1 shot/hour). Nevertheless, laser-accelerated proton beams have been widely used in single-shot high-energy-density science experiments for the proton-radiographic imaging of laser-produced plasmas [36, 37], for the production of isochorically heated warm dense matter [3, 38–40], and for stopping power measurements in warm and hot dense matter [41–43]. There are ongoing efforts to adapt these scientific platforms to operate at high repetition rates so that larger data sets can be acquired, which will ultimately allow higher fidelity data to be collected over a significantly larger parameter space.

This chapter first provides a description of the characteristic energy deposition of ballistic protons in matter, which is relevant for most applications. This is followed by a discussion of application areas to which this thesis has contributed enabling technologies.

2.1 Trajectory of ballistic MeV-energy ions through matter

The trajectory of a ballistic ion through matter has a characteristic energy deposition curve commonly referred to as the *Bragg Curve* [45]. An example is shown in Fig. 2.1 (a). When a projectile ion travels through cold material, the velocity v decreases after successive inelastic collisions with bound electrons. Due to the large difference in mass between the ion and electrons, the initial ion trajectory is largely unaffected until the ion energy is comparable to that of bound electrons in the material. As the ion slows, the average energy loss per unit path length in the medium, referred to as the *stopping power*, increases proportionally to $1/v^2$ [46].

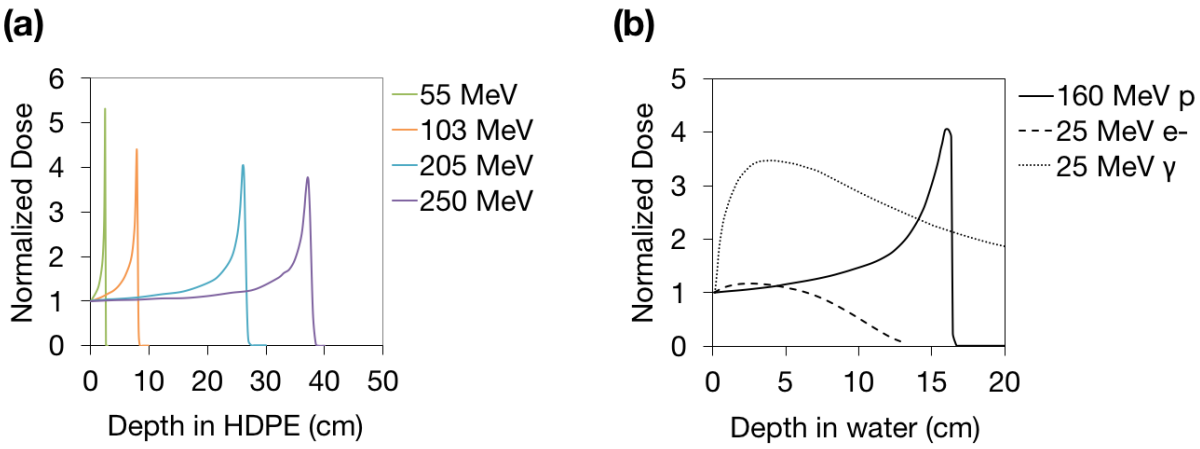

Figure 2.1: (a) Bragg curves for 55 MeV (green), 103 MeV (orange), 205 MeV (blue), and 250 MeV (purple) protons are shown for high-density polyethylene (HDPE) [47]. (b) Depth dose distribution for 160 MeV protons (solid), 25 MeV electrons (dashed), and 25 MeV gamma photons (dotted) in water. Data extracted from [48]. The density of HDPE and water are 0.90 g/cc and 0.97 g/cc, respectively.

Consequently, an ion deposits most of its energy in a small volume of material immediately prior to coming to rest. By tuning the energy of an ion beam, the depth at which the majority of the energy is deposited in a given material can be selected. For example, as shown in 2.1, increasing the proton energy from 55 to 250 MeV increases the Bragg peak depth from 3 to 40 cm in high density polyethylene (HDPE).

The dose deposition by photons and fast electrons is markedly different as shown in 2.1 (b) [48, 49]. The dose deposited by X-rays is directly proportional to the number of photons, and

it decreases with depth because photons are scattered or absorbed by the medium. As with ions, when a projectile electron travels through cold material, it deposits energy continuously along its path. Due to its low mass, however, an electron is significantly scattered by the nuclei of the medium. As a result, electron energy deposition spreads transversely as an electron develops a perpendicular velocity component as a result of successive scattering events. The average energy deposition per unit length therefore decreases rapidly away from the surface of the material [48, 49].

The advantageous dose-depth profile of MeV-energy ions is the central motivation for the applications of laser-accelerated ion beams discussed in the following sections.

2.2 Proton radiography or deflectometry

Not long after their first observation, laser-accelerated proton beams were used to probe high-energy-density conditions via a technique called *proton radiography or deflectometry* [50, 51]. A schematic of a typical setup is shown in Fig. 2.2.

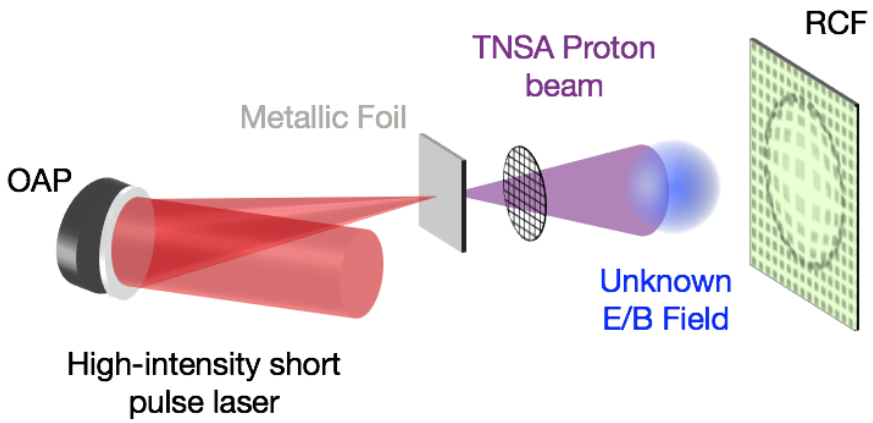

Figure 2.2: Illustration of proton radiography using a laser-accelerated TNSA proton beam. Deviations from a direct projection of a fine metallic grid onto radiochromic film (RCF) or scintillating screen are used to infer the topology of an electric or magnetic field. The distance between the metallic proton-beam-generating foil and the grid is on the order of 100s of microns. The grid-to-field structure is typically 1 to 30 mm and the distance from the metallic foil to the detector is on the order of 30 to 100 mm. These distances are selected based on the proton beam flux and energy, the desired magnification, the required spatial and temporal resolutions, and the expected field strengths.

To date, proton radiography has been the most successful application of laser-driven proton beams. Laminarity, apparent divergence from a point (termed the "virtual source

point"), and broad energy bandwidth make TNSA proton beams ideal for probing electric and magnetic fields that are tens of microns in length and that evolve on the picosecond timescale. Typically, a fine periodic pattern is imprinted on the proton beam using a metallic grid. The deflection of the protons from the target E/B-field then appears as a magnified, perturbed grid on an imaging detector [51, 52]. If the proton beam propagates for tens of millimeters before probing the E/B field, the difference in the transit times of the fastest and slowest protons in the beam can exceed 100 ps. By using a spatially and energetically resolved detector such as a radiochromic film (RCF) stack, one can deduce the temporal evolution of the E/B-fields.

The high-repetition-rate laser-driven ion-beam-generating platform developed in this thesis will directly enable the use of high-repetition-rate radiography measurements of electric and magnetic fields in high-energy-density (HED) plasmas.

2.3 Inertial confinement fusion

Fusion is a nuclear reaction in which two low-Z elements fuse to form a heavier nucleus. The mass of the newly formed nucleus is less than the mass of the two original nuclei. The residual mass is released as energy according to $E = \Delta mc^2$. The process begins naturally in stars when gravitational contraction of the core of a protostar leads to sufficiently high pressures and temperatures to reach the Lawson criterion [53].

To achieve nuclear fusion and net energy gain in the laboratory, the plasma must be sufficiently hot and dense and be effectively confined. The Lawson triple product, which compares the energy produced by fusion reactions to the rate of energy lost to the environment, has a minimum value for net energy gain which is given by,

$$nT\tau_E > 10^{21} \text{ keV s/m}^3 \tag{2.1}$$

where n, T, and τ_E are the plasma density in ions per cubic meter, temperature in kiloelectron volts, and plasma confinement time in seconds, respectively [53].

To date, the deuterium-tritium (D-T) fusion reaction has been discussed as a promising alternative energy source with the potential to fulfill the global energy demand with less harmful byproducts. As a result, many fusion energy research programs and recent start-up companies have emerged worldwide.

The D-T fusion reaction is described by

$$^{2}_{1}\text{D} + ^{3}_{1}\text{T} \rightarrow ^{4}_{2}\text{He (3.5 MeV)} + ^{1}_{0}\text{n (14.1 MeV)}. \tag{2.2}$$

Currently, the approaches to laboratory fusion energy research can be broadly classified as either: (1) Magnetic confinement fusion, in which a D-T plasma is confined using magnetic fields, typically in a toroidal device referred to as a *tokamak* or (2) Inertial confinement fusion (ICF), which uses high-power lasers to compress a comparatively smaller volume of D-T to a very high density for a much shorter length of time. ICF relies on the inertia of the imploded fuel to provide the confinement. Alpha particles produced by the D-T fusion reaction deposit energy in the remaining fuel resulting in a positive feedback effect on the fusion reaction rate. Alpha heating is the primary mechanism for ignition and the propagation of a nuclear burn wave [54, 55].

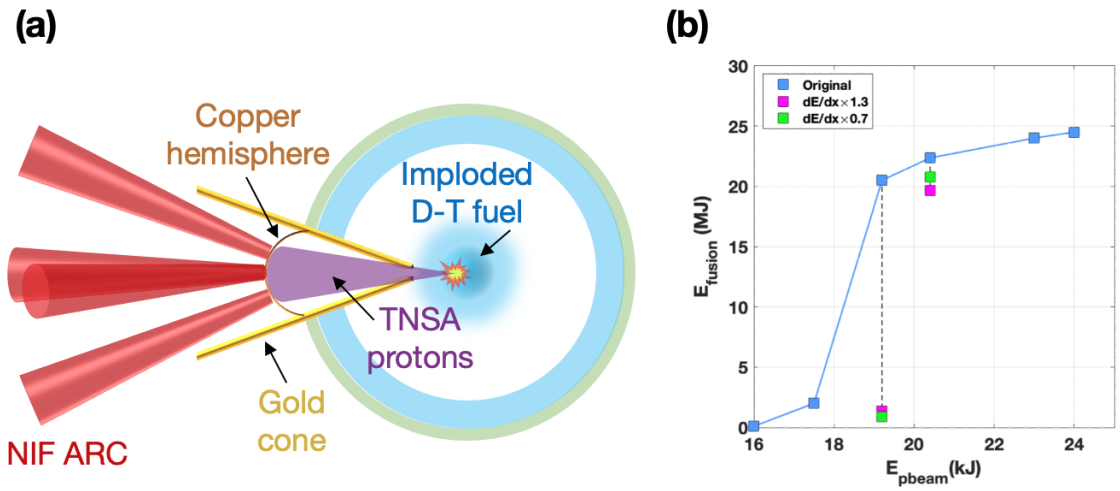

Figure 2.3: (a) Illustration of inertial confinement fusion D-T fuel capsule with Au cone and Cu hemisphere for the fast-ignition approach to inertial confinement fusion. A high-intensity short-pulse laser such as a combination of the four NIF ARC beams is incident on the Cu hemisphere, which produces a converging TNSA proton beam that deposits energy in a small volume, thus igniting a pre-compressed fuel core. Figure adapted from [30]. (b) Calculated fusion energy yield as a function of proton beam energy (blue squares). Additional simulations with stopping power multipliers show how the ignition cliff can be severely affected by changes in the stopping power (magenta and green squares). The plot is courtesy of S. Atzeni.

There are two main approaches to inertial confinement fusion (ICF), namely direct drive and indirect drive. For the direct drive approach, as the name suggests, nanosecond lasers are focused directly onto the fuel capsule. The indirect drive approach instead involves using the lasers to heat the inner walls of a high-Z hohlraum, thereby generating x-rays that drive the capsule implosion. The fuel capsule typically consists of deuterium and tritium ice layers surrounded by a plastic or carbon ablator. Under both approaches, the ablator is ionized and

the blow-off launches a spherical shock wave traveling inward. The spherical compression from the shock increases the density and temperature at the center to create the conditions necessary for fusion [54].

2.3.1 Fast ignition approach to inertial confinement fusion

One of the first proposed applications of energetic laser-accelerated proton beams was in ICF research [29]. A schematic of a sample direct drive fast-ignition (FI) inertial confinement fusion setup is shown in Fig. 2.3.

In this particular design, the D-T fuel is pre-compressed using nanosecond lasers to a dense state of ∼300 g/cc and to a temperature of only hundreds of eV. An intense laser-generated proton beam is then focused into the fuel in order to heat it to ignition temperatures of 5 to 10 keV. This design is one of the leading concepts for improving the energy gain of an igniting implosion.

To initiate a nuclear burn wave with FI, current estimates suggest that ∼20 kJ of energy must be deposited by the protons within the 20 ps inertial confinement time. This sets an upper limit on the source-to-hot-spot distance of less than 1 mm to take full advantage of the useful spread of proton energies [56]. To generate an intense proton beam, the laser pulse needs to be focused onto a metallic hemisphere [38] that is protected by a gold guiding cone [29, 30, 57]. Assuming a proton-generation efficiency of 15% as reported in C. M. Brenner et al. [58], the pulse energy of the high-intensity laser must exceed 100 kJ [59].

2.3.2 Ion stopping power

There is significant uncertainty in the total proton energy, and therefore laser energy, required for ignition and high energy gain in the FI approach. The calculation depends critically on the stopping power of the protons in the imploding D-T fuel, which passes through a wide range of plasma conditions as it is heated from hundreds of eV to 5 keV temperatures. The theoretical descriptions of the ion stopping power in the so-called warm dense and hot dense matter regimes are challenging due to strong electron coupling and high degeneracy as well as partial ionization. Such systems are described either with *ab initio* calculations [60, 61] that include a self-consistent treatment of ionization but are very computationally demanding or using ad-hoc, semi-empirical models [62–64] that are computationally faster but include simplifying approximations.

While ion stopping power in cold matter and classical plasmas has been extensively studied experimentally, there are very few experimental measurements at ICF-relevant plasma conditions [42, 43, 65]. As a result, there are large discrepancies between stopping power models, in some cases ≥30%. Outside the ignition cliff, the fusion energy yield is nearly

unaffected by changes in the stopping power whereas changes near the cliff lead to substantially different energies (Fig. 2.3 (b)). This uncertainty can cause a significant error in the estimated proton beam energy required to ignite the fuel.

In addition, alpha particle transport and stopping power are equally important for both direct and indirect ICF schemes since alpha particle heating plays a key role in triggering ignition. For example, in typical ICF implosions, the dense D-T fuel reaches conditions corresponding to Coulomb coupling parameter $\Gamma = 0.8$ under which alpha particles approach the Bragg peak regime, which means that the alpha particle velocity is approximately equal to thermal electron velocity [66, 67]. Disagreement between theoretical models, particularly near the Bragg peak, can lead to large uncertainties in the predicted performance of ICF implosions near the ignition cliff. It is therefore critically important to develop experimental methods to measure ion stopping power in plasma conditions relevant to ICF. The experimental validation of the models is extremely difficult, mainly due to the measurement precision required to characterize the plasma conditions.

Some of the prominent measurements of the atomic and structural properties of warm dense matter and high-pressure material states have been performed using the Matter in Extreme Conditions (MEC) instrument at SLAC National Accelerator Laboratory. The plasma states are generated with either the long pulse or short pulse laser prior to diagnosis with the Linac Coherent Light Source (LCLS), the world's first hard x-ray free electron laser (XFEL).

In 2021, the U.S. Department of Energy (DOE) Office of Science (SC) gave preliminary approval for the design and construction of a new high-power laser facility currently referred to as the MEC Upgrade (MEC-U) project. The proposed facility has significantly upgraded laser and experimental capabilities compared to the present-day MEC. It combines three optical laser drivers: a high-power short pulse (150 J, 150 fs 10 Hz), a 100 J-class long pulse (10 Hz), and a kJ long pulse with the LCLS XFEL [68]. The unique combination of laser drivers at MEC-U will directly enable measurements of proton and ion stopping in ICF-relevant plasma conditions. The kJ long pulse laser could be used to produce the ICF-relevant plasma conditions precisely characterized with LCLS. Then, the high-energy short pulse laser could simultaneously be used to produce a bright proton or ion beam utilizing the experimental platform developed during this thesis to perform stopping power measurements.

With additional development, the cryogenic jet system could also be used to generate alpha particles at high repetition rate for the study of alpha particle transport in HED plasmas. Such measurements would provide benchmarks for existing models and contribute to the development of the global alpha particle stopping power model needed for high gain

designs and the successful prediction of ICF implosions. The proton stopping power measurements will help accurately estimate the proton beam parameters required for the fast ignition approach to ICF.

2.3.3 Inertial fusion energy

Progress in inertial confinement fusion has been substantial in the last decade. Especially noteworthy are implosion symmetry improvements, instability reductions, and increases in our understanding of the thermal and electrical properties associated with high-energy-density conditions in compressed fuel [69]. With the recent demonstration of ICF implosions reaching the burning plasma regime [70, 71] followed by ignition and net target energy gain at the National Ignition Facility in Dec. 2022, there has been a resurgence of interest in developing the ICF scheme into a commercially viable source of energy commonly referred to as Inertial Fusion Energy (IFE). IFE will require the development of high-gain approaches to ICF such as FI or other advanced schemes in addition to the enabling technologies needed for ignition at high repetition rate.

An economically viable IFE power plant with 1 GW electrical power output will likely require a gain of approximately 100 and operate at a 10 to 20 Hz repetition rate [72]. Areas that require significant research and development for the realization of IFE include high-repetition-rate laser drivers, laser-accelerated ion beams for testing the FI approach to high-gain, rapid target fabrication and injection, target chamber designs, and fusion materials [69, 72, 73].

Progress in several of these areas was made during this thesis. Cryogenic hydrogen and deuterium targets were developed and qualified at a high repetition rate (See Chapter 5 and 7). The targets were injected at very high speeds then reliably irradiated by a 10 µm laser focus (See Chapter 8). Chapter 8 demonstrates the production of bright proton and deuteron beams using a high repetition rate compatible experimental platform that could also be used to study materials in radiation environments such as those found in a fusion reactor. High repetition rate particle sources from cryogenic liquid jets (protons, deuterons, or neutrons) will allow in only a few hours to days the systematic and controlled study of radiation damage accumulated in fusion materials over years. Radiation damage is a cumulative, long-term effect due to atomic displacement within a solid material.

2.4 Warm Dense Matter

Warm dense matter (WDM) refers to matter near solid density with temperatures ranging from 0.1 to 100 eV ($\sim 10^3 - 10^6$ K). These states occur naturally in planetary and astrophysical systems but are also produced during ICF and high-energy-density physics experiments. In

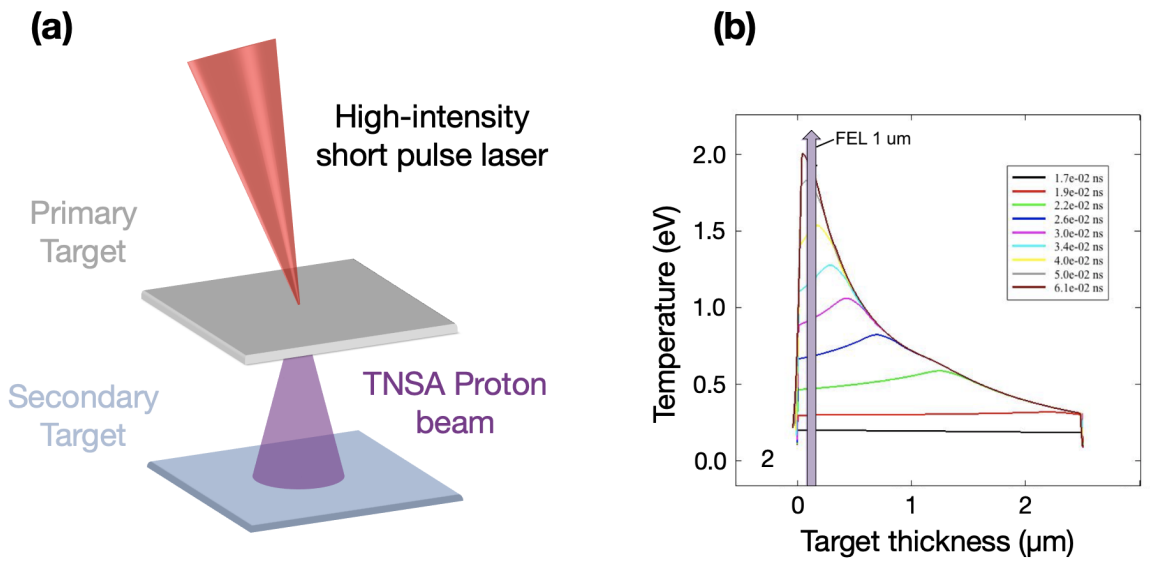

Figure 2.4: (a) Schematic of an experimental setup for proton heated warm dense matter study using a high-intensity short-pulse laser. (b) Temperature of a proton beam heated sample as a function of depth at different times computed with the 1-D hydrodynamic code HELIOS [74] using the measured proton spectrum from the Draco laser (1 J, 30 fs) courtesy of M. Gauthier. The light purple arrow on the plot represents a free-electron laser (FEL) such as LCLS which can be used to probe the temporal evolution of the warm dense state.

this regime, the predictions of condensed matter physics or plasma physics are insufficient to describe the complicated interplay between Coulomb fields and temperature-driven processes.

To date, it remains challenging to produce and characterize single-state WDM, which exhibits no density or temperature gradients, in the laboratory. As a result, there are few high-quality studies to guide the development of theoretical models. Several techniques can produce such states including strong shock compression using nanosecond lasers up to multi-megabar pressures [75, 76], isochoric heating using femtosecond lasers and ultra-thin samples [77–79], and heating by laser-accelerated proton beams [38, 41, 80]. Proton heating has produced some of the highest quality measurements since the heating is isochoric and hydrodynamic expansion is negligible on the timescale of the proton beam duration. An example of an experimental setup that uses proton beams as drivers is shown in Fig. 2.4 (a). A short-pulse laser is incident on a proton-generating primary target, which produces a broadband TNSA proton beam normally incident on a secondary target. The protons deposit their energy at their Bragg peak depths, resulting in layers of homogeneous heating in the sample. The temperature in the sample at different times can be predicted using the 1-D hydrodyamic code HELIOS [74] as shown in Fig. 2.4 (b). The WDM state can then be

characterized using optical and X-rays diagnostic probing techniques.

A wide range of proton-heated temperatures surpassing the current state-of-the-art will be accessible by utilizing the MEC-U high-energy PW laser with the high repetition rate proton-generating experimental platform developed in this thesis. This will allow the validation of theoretical models and simulations of WDM conditions that have broad implications in laser-plasma interaction physics.

2.5 Proton radiotherapy treatment of cancer

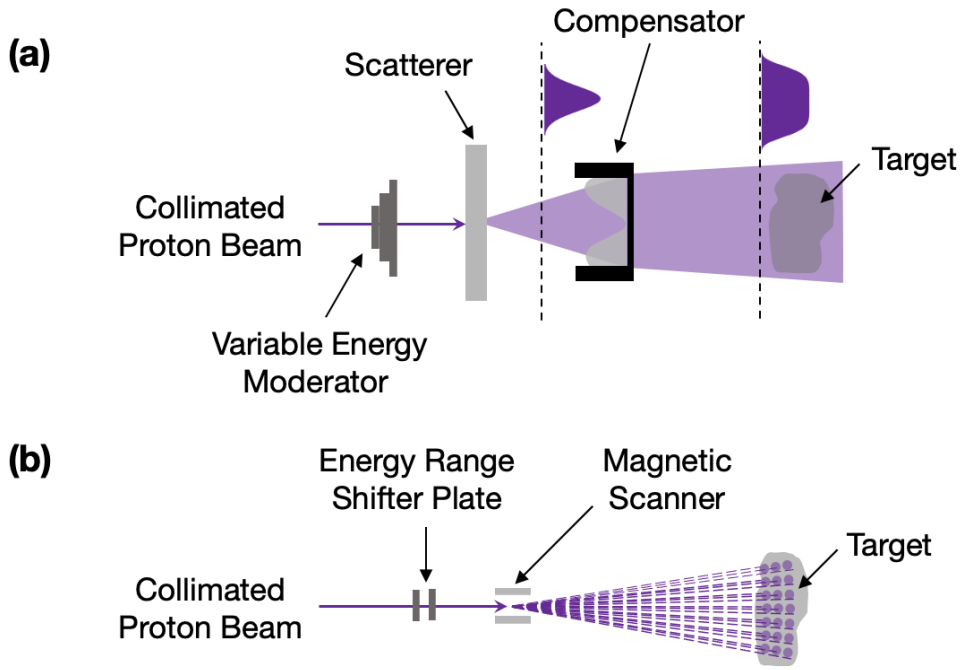

Figure 2.5: Illustration of (a) Passive Scattering and (b) Active Scanning approaches to proton radiotherapy. Both methods start with a collimated, quasi-monoenergetic proton beam (purple). The energy of the proton beam is tuned so that the protons deposit energy at different depths in the target object. Their names indicate whether the directionality of the proton beam is controlled passively with scatterers/compensators or actively using electromagnets. Here, the target corresponds to a cancerous tumor in a patient. Adapted from [81].

The last application we will discuss is proton radiotherapy. It was also one of the first and probably one of the most compelling societal applications of laser-accelerated proton beams. Radiotherapy broadly refers to the use of high doses of ionizing radiation to damage cancerous cells. Cancer care continues to rely on x-ray radiotherapy despite the substantial radiation-induced toxicity to healthy surrounding tissues. An illustration of the passive

scattering and active scanning approaches to proton radiotherapy is shown in Fig. 2.5 (a) and (b), respectively. Based on current technology, the input proton beam is a narrow-energy-bandwidth, pencil-like proton beam oftentimes from a cyclotron.

Treatment with protons or low-Z ions is superior to x-rays since their energy deposition is highly localized to the Bragg peak depth and this significantly reduces the instantaneous and long-term effects [31–35]. A higher dose of radiation can then be delivered with a significantly lower risk of the patient developing secondary cancer due to exposure to radiation or to other known side effects [82]. As of 2023, proton therapy is available at 41 facilities across the United States. These cyclotron-based facilities have a large footprint and are very expensive to build.

Laser-plasma accelerators could dramatically decrease the size and cost of medical particle accelerator facilities, thereby making them more widely available for medical research and potential future therapies. However, several challenges have yet to be addressed. The repetition rate of the lasers and the availability of rapidly refreshing target delivery systems have restricted their prospective use to ultra-high dose-rate (>40 Gy/s) deposition from one laser pulse, which is known as FLASH radiotherapy [83]. These dose rates are more than two orders of magnitude higher than typical clinical dose rates (∼5 Gy/min), but early studies have shown promise for further reduction in radiation-induced toxicity via a not-yet-understood process termed the "FLASH effect" [82, 84, 85]. Laser-accelerated proton sources have already been used in a number of irradiation studies [86–89].

The typical proton beam accelerated by Target Normal Sheath Acceleration (TNSA) has a characteristic broadband energy spectrum and, to date, maximum cut-off energy of ∼94 MeV [90], which makes it unsuitable for direct use in proton therapy. Recently, Kroll et al. developed a pulsed, two-solenoid beamline with an energy selection aperture for the transport and selection of a narrow interval of the energy spectrum of a TNSA proton beam. The beamline was used to perform the first in vivo treatment of mouse-model human tumors with a laser-accelerated proton beam [91]. In this design, the maximum proton energy was restricted to the initial laser-accelerated proton beam energy spectrum. For utility in cancer treatment, an ideal proton therapy device should have continuously tunable energy from 20 to 250 MeV and a quasi-monoenergic bandwidth to 'trace' the margins of tumors from those on the skin to those deeply embedded in healthy tissue. Since the density of high-density polyethyelene (HDPE) and water are comparable to human tissue, Fig. 2.1 (a) can provide the approximate proton energy required to target a tumor at various depths.

Designs for an alternative approach capable of proton energy outputs across the full energy range needed for proton therapy have recently emerged. A bright, low emittance charged particle beam initially accelerated during a laser-plasma interaction is subsequently injected

into a conventional RF linear accelerator (linac) to further increase its energy. These multi-stage ion accelerators, more often termed 'hybrid ion accelerators,' are leading contenders for the production of a high-stability, tunable-energy proton beam for applications [92].

Coupling the bright, laser-accelerated proton beam from cryogenic hydrogen jets either directly or after ion beam shaping and the transport of components into an RF linac is currently being investigated. This thesis qualified laser-driven proton beams from cryogenic hydrogen jets as a viable candidate for the first stage of a hybrid ion accelerator. This may allow a reduction in the size and cost of medical accelerator facilities and a subsequent increase in the availability of proton radiotherapy.

Chapter 3
Theoretical Background

This chapter provides the theoretical background and physical principles in high-intensity ($>10^{18}$ W/cm^2) laser-matter interactions. It focuses primarily on experiments in which laser-accelerated ion beams are generated by irradiating a so-called "target" with a high-intensity short pulse ($<$1 ps) laser. The laser and initial target parameters determine the dominant ionization, electron heating, and laser-driven ion acceleration mechanisms.

3.1 Electromagnetic waves in vacuum

We begin with *Maxwell's equations*, a set of coupled partial differential equations that form the foundation of classical electromagnetism. They describe the generation of electric and magnetic fields from charges and currents and changes in those fields.

$$\boldsymbol{\nabla} \cdot \boldsymbol{E} = \frac{\rho}{\epsilon_0} \tag{3.1}$$

$$\boldsymbol{\nabla} \times \boldsymbol{E} = -\frac{\partial \boldsymbol{B}}{\partial t} \tag{3.2}$$

$$\boldsymbol{\nabla} \cdot \boldsymbol{B} = 0 \tag{3.3}$$

$$\boldsymbol{\nabla} \times \boldsymbol{B} = \mu_0 \boldsymbol{J} + \mu_0 \epsilon_0 \frac{\partial \boldsymbol{E}}{\partial t} \tag{3.4}$$

In addition, the principle of charge conservation leads to the *continuity equation*

$$\boldsymbol{\nabla} \cdot \boldsymbol{J} = -\frac{\partial \rho}{\partial t}. \tag{3.5}$$

In vacuum, the source terms are zero, so $\boldsymbol{\nabla} \cdot \boldsymbol{E} = 0$, $\boldsymbol{\nabla} \cdot \boldsymbol{B} = 0$, and $\boldsymbol{J} = 0$. Taking the curl in Eqns. 3.2 and 3.4 and applying the identity $\boldsymbol{\nabla} \times \boldsymbol{\nabla} \times \boldsymbol{A} = \boldsymbol{\nabla}(\boldsymbol{\nabla} \cdot \boldsymbol{A}) - \boldsymbol{\nabla}^2 \boldsymbol{A}$ leads to the system

$$\mu_0 \epsilon_0 \frac{\partial^2 \boldsymbol{E}}{\partial t^2} - \boldsymbol{\nabla}^2 \boldsymbol{E} = 0 \tag{3.6}$$

$$\mu_0 \epsilon_0 \frac{\partial^2 \boldsymbol{B}}{\partial t^2} - \boldsymbol{\nabla}^2 \boldsymbol{B} = 0. \tag{3.7}$$

These equations describe waves propagating at the speed of light $c = 1/\sqrt{\mu_0 \epsilon_0} = 2.99792 \times 10^8$ m/s. One solution to Eqns. 3.6 and 3.7 describes an infinite monochromatic plane wave

and is given by

$$\boldsymbol{E}(\boldsymbol{r},t) = E_0\hat{\boldsymbol{\varepsilon}}_{\mathbf{1}}e^{i\boldsymbol{k}\cdot\boldsymbol{r}-i\omega t}, \qquad \boldsymbol{B}(\boldsymbol{r},t) = B_0\hat{\boldsymbol{\varepsilon}}_{\mathbf{2}}e^{i\boldsymbol{k}\cdot\boldsymbol{r}-i\omega t} \tag{3.8}$$

where $\omega = 2\pi f$ is the angular frequency, $\boldsymbol{k} = (2\pi/\lambda)\hat{\varepsilon}_3$, and λ is the wavelength.

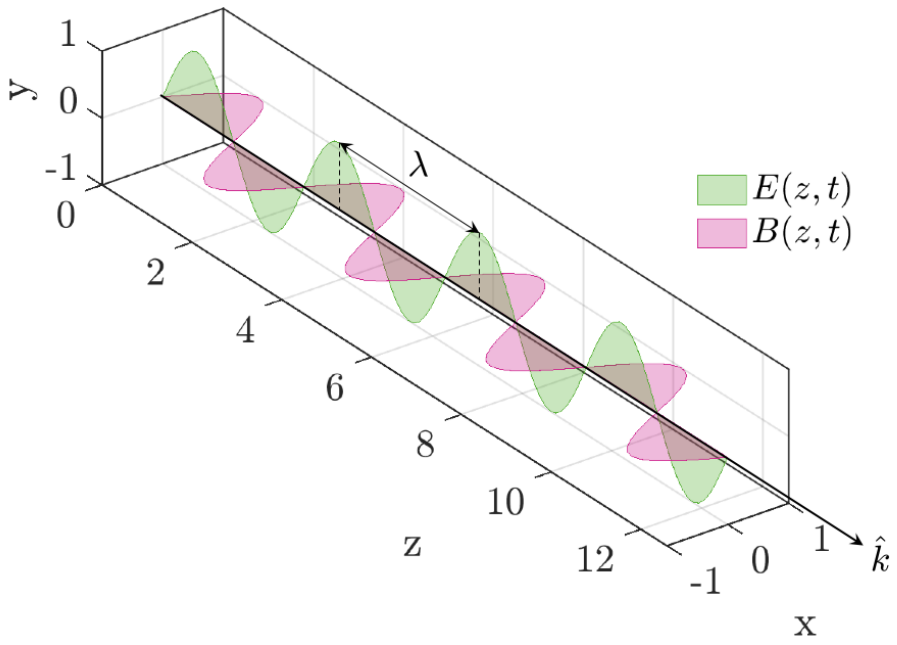

Figure 3.1: Linearly polarized electromagnetic wave with a vacuum wavelength λ traveling in the positive z direction. The electric (green) and magnetic (pink) fields are indicated.

It is then possible to show that in vacuum $\hat{\varepsilon}_1 \perp \hat{\varepsilon}_2$, $\hat{\varepsilon}_1 \perp \hat{\varepsilon}_3$, and $\hat{\varepsilon}_2 \perp \hat{\varepsilon}_3$ where $\hat{\varepsilon}_3 \coloneqq \hat{k}$. The real components of the electric and magnetic fields are orthogonal and oscillate sinusoidally as shown in Fig. 3.1. Inserting the plane wave solutions into Eqn. 3.2 and 3.4 gives rise to the Helmholtz equations

$$(\boldsymbol{\nabla}^2 + k^2)\boldsymbol{E} = 0, \qquad (\boldsymbol{\nabla}^2 + k^2)\boldsymbol{B} = 0. \tag{3.9}$$

Due the linearity of Maxwell's equations in vacuum, any superposition of plane waves will also be a solution to the generalized Helmholtz equation.

The directional energy flux carried by an electromagnetic wave is expressed by the *Poynting vector* and is given by

$$\boldsymbol{S} = \frac{\boldsymbol{E}\times\boldsymbol{B}}{\mu_0}. \tag{3.10}$$

The instantaneous Poynting vector in vacuum is always in the same direction as the wave propagation direction and oscillates in magnitude according to

$$|\boldsymbol{S}| = \frac{|\boldsymbol{E} \times \boldsymbol{B}|}{\mu_0} = \frac{E_0 B_0}{\mu_0} \cos^2(\boldsymbol{k} \cdot \boldsymbol{r} - \omega t). \tag{3.11}$$

The time-averaged magnitude is then

$$\langle S \rangle = \frac{E_0 B_0}{2\mu_0} = \frac{1}{2} c \epsilon_0 E_0^2, \tag{3.12}$$

where the relation $B_0 = E_0/c$ follows from the plane wave solution to Maxwell's equations in vacuum. The momentum flux is given by $\langle S \rangle / c$, which by conservation of momentum gives rise to *radiation pressure* p_{rad} on a perfectly absorbing surface. This is given by

$$p_{rad} = \frac{\langle S \rangle}{c} = \frac{1}{2} \epsilon_0 E_0^2 = 0.334 I_{18} \text{ Gbar} \tag{3.13}$$

where I_{18} is the laser intensity with unit 10^{18} W/cm^2.

If we now consider a plane wave with a reasonably well-defined direction propagating along the positive z direction, we look for solutions that take the form $\boldsymbol{E}(\boldsymbol{r}) = f(\boldsymbol{r}) e^{ikz}$. If the transverse profile of the wave $f(\boldsymbol{r})$ varies slowly relative to the oscillation of an electromagnetic wave described by e^{ikz} due to diffraction and propagation effects, we can say that it is *paraxial*. The Helmholtz equation in the *paraxial approximation* can then be given in cylindrical coordinates by

$$\frac{1}{r} \frac{\partial}{\partial r} \left(r \frac{\partial f}{\partial r} \right) + \frac{1}{r^2} \frac{\partial^2 f}{\partial \theta^2} + 2ik \frac{\partial f}{\partial z} = 0 \tag{3.14}$$

where $r = \sqrt{x^2 + y^2}$ is the distance from the z-axis, and $\theta = \arctan(y/x)$ is the azimuthal coordinate. For a cylindrically symmetric beam, it has the general solution given by

$$f(r, z) = f_0 \exp \left(ip(z) + i \frac{kr^2}{2q(z)} \right) \tag{3.15}$$

where $q(z)$ is the *complex radius of curvature*. Thanks to a change of variables and non-trivial algebra that is left to the reader, a possible solution to the paraxial wave equation is a Gaussian given by

$$f(r, z)_{gauss} = f_0 \frac{w_0}{w(z)} \exp \left(-\frac{r^2}{w^2(z)} \right) \exp \left(i \frac{kr^2}{2R(z)} - i\varphi(z) \right) \tag{3.16}$$

where the real and imaginary components of the complex radius of curvature ($q = w + iR$), the *Guoy phase* (φ), and the *Rayleigh range* (z_R), are given by

$$w(z) = w_0\sqrt{(1 + z^2/z_R^2)} \tag{3.17}$$

$$R(z) = z(1 + z_R^2/z^2) \tag{3.18}$$

$$\varphi(z) = \arctan(z/z_R) \tag{3.19}$$

$$z_R = \pi w_0^2/\lambda. \tag{3.20}$$

The Gaussian solution to the paraxial Helmholtz equation gives an excellent approximation for laser propagation. We find that the laser spatial profile is fully described by parameters ω_0 and λ. The intensity $I(r, z) \propto |E(r, z)|^2$ can then be written as

$$I(r, z) = I_0 \left(\frac{w_0}{w(z)}\right)^2 \exp\left(-\frac{2r^2}{w^2(z)}\right) \tag{3.21}$$

where I_0 is the peak laser intensity at the *laser focus*, which is defined to be the point with $z = 0$. Integrating the laser intensity over the beam cross-sectional area must give the total laser power P_L, and this leads to the expression

$$P_L = \frac{\pi w_0^2 I_0}{2}. \tag{3.22}$$

The radius of the beam $w(z)$ is defined to be the distance from the laser axis at which the laser's intensity has decreased by a factor of $1/e^2$. At the focus, the beam radius is w_0. This laser parameter is important for determining the laser-plasma dynamics described in subsequent sections and chapters.

In the paraxial approximation, a Gaussian beam has curved wavefronts, and their radii of curvature change as with distance along the propagation axis. The wavefront is flat at $z = 0$ and in the limit as $z \to \pm\infty$. At distances $z \gg z_0$, the Gaussian wave is well approximated by a spherical wave.

When a focusing element such as a lens is inserted in a Gaussian beam, it alters the curvature of the wavefronts. This can be expressed by the *lens-maker equation*

$$\frac{1}{R'} = \frac{1}{R} - \frac{1}{f} \tag{3.23}$$

where f is the *effective focal length*.

This can then be expanded using Eqn. 3.20 and 3.18 to

$$\left(-z'\left[1+\left(\frac{\pi w_0'^2}{\lambda^2}\right)^2\frac{1}{z'^2}\right]\right)^{-1}=\left(-z\left[1+\left(\frac{\pi w_0^2}{\lambda^2}\right)^2\frac{1}{z^2}\right]\right)^{-1}-\frac{1}{f}. \tag{3.24}$$

Requiring constant width across the focusing element and applying Eqn. 3.17 gives us

$$w'(z)=w(z) \tag{3.25}$$

$$w_0'\sqrt{1+z^2\left(\frac{\lambda}{\pi w_0'^2}\right)^2}=w_0\sqrt{1+z^2\left(\frac{\lambda}{\pi w_0^2}\right)^2}. \tag{3.26}$$

This system of two equations in two unknowns w_0' and z' can be solved to find

$$w_0'=Mw_0 \tag{3.27}$$

$$z'=M^2z+f(1-M^2) \tag{3.28}$$

where $M=|f|/\sqrt{(z-f)^2+z_0^2}$ is the magnification.

To understand far field diffraction, we consider each point on the wavefront as a source of secondary spherical wavelets according to the Huygens-Fresnel Principle. The diffraction through an aperture is then the field produced at a distant plane by an array of in-phase point sources. In the Fraunhofer approximation, a coordinate system with $r=\sqrt{X^2+(Y-y)^2+(Z-z)^2}$ is used, and the total contribution to the total wave at an observation point $P(X,Y,Z)$ in the continuous limit can be expressed as

$$dE=\frac{\varepsilon_A}{r}e^{i(kr-\omega t)}dS. \tag{3.29}$$

Now, if y^2/R and z^2/R are much smaller than the wavelength, a binomial expansion in y/R and z/R can be applied and we can approximate r as

$$r\approx R\left(1-\frac{yY+zZ}{R^2}\right). \tag{3.30}$$

The total disturbance that arrives at point $P(X,Y,Z)$ is then given by

$$E(X,Y,Z)=\frac{\varepsilon_A e^{i(kR-\omega t)}}{R}\int\int e^{-ik(yY_zZ)/R}dS. \tag{3.31}$$

In the case of a circular aperture, we change to cylindrical coordinates

$$z = \rho\cos\phi \qquad y = \rho\sin\phi \tag{3.32}$$

$$Z = Q\cos\Phi \qquad Y = Q\sin\Phi, \tag{3.33}$$

which gives

$$E = \frac{\varepsilon_A e^{i(kR-\omega t)}}{R}\int_{\rho=0}^{a}\int_{\phi=1}^{2\pi} e^{ik(\rho Q/R)\cos\phi}\rho d\rho d\phi E = \frac{\varepsilon_A e^{i(kR-\omega t)}}{R}\int_{\rho=0}^{a} J_0\left(\frac{k\rho Q}{R}\right)\rho d\rho \tag{3.34}$$

with a the radius of the circular aperture and the integral over ϕ given by the zeroth order Bessel function J_0. Integrating again we obtain

$$E = \frac{\varepsilon_A e^{i(kR-\omega t)}}{R} 2\pi a^2\left(\frac{R}{kaQ}\right) J_1\left(\frac{kaQ}{R}\right) \tag{3.35}$$

where J_1 is the first order Bessel function. Recalling that the intensity is given by $I = |E|^2$, we arrive at

$$I = \frac{\varepsilon_A A^2}{2R^2}\left[\frac{2J_1(kaQ/R)}{(kaQ/R)}\right]^2, \tag{3.36}$$

which is known as the *Airy function*. This function is useful for describing the far field of both an imaging system with circular lenses, and also for a laser that has a flat-top circular aperture near field. Realistic lasers often have a super-Gaussian near field which can be well approximated by a flat-top beam. The first minimum occurs when $kaQ_1/R = 3.83$, and this defines the *Airy disk*. The general solution for a circular aperture is given by

$$Q_1 = 1.22\frac{R\lambda}{2a}, \tag{3.37}$$

for a focusing element with effective focal length f and diameter D, this becomes

$$Q_1 = 1.22\frac{f\lambda}{D}, \tag{3.38}$$

also known as the *diffraction limit*. This expression also describes the resolution limit of an optical imaging system. The minimum distance that two point sources need to be separated by in order to be resolved by an imaging system is given by the same expression, that is,

$$\Delta l_{min} = Q_1. \tag{3.39}$$

This principle has been illustrated in (Fig. 3.2) where we show the image of two point sources separated by l_{min} imaged to a line in the image plane.

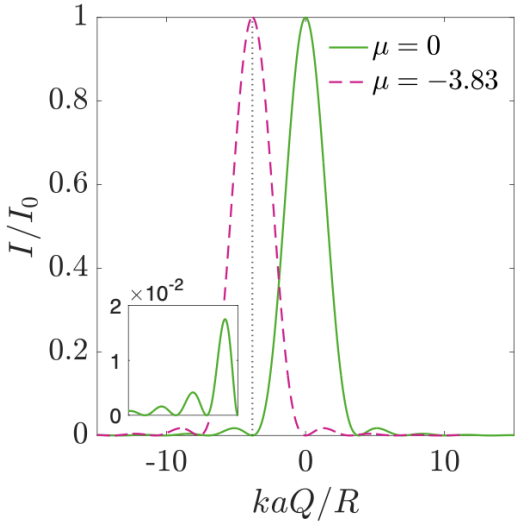

Figure 3.2: Graphical depiction of the minimum resolution of an optical imaging system. One is centered at $\mu_1 = 0$ (green) and the other is centered on the first minimum at $\mu_2 = -3.83$ (pink dashed) where $\mu_1 - \mu_2 = \Delta\ell_{min}$. Inset: First through forth minima of the Airy function centered on $\mu = 0$.

It is also instructive to consider the diffraction of a laser beam with a Gaussian near field profile. We omit the derivation here for brevity, but note that the Gaussian function is its own Fourier transform such that the far field image of a Gaussian near field, is itself a Gaussian. Assuming the radius of the near field Gaussian can be written by R_0, we can relate it to the far field Gaussian beam waist through the relation

$$w_0 = \frac{\lambda f}{\pi R_0} \approx \lambda f_{\#}. \tag{3.40}$$

Here we have introduced the f-number, $f_{\#}$, of the focusing optic given by $f_{\#} = f/D \approx f/\pi R_0$. There is some discussion surrounding the validity of the paraxial approximation for various f-numbers. In vacuum, it has been shown that f-numbers as small as $f/2$ can be well approximated by the paraxial regime [93].

Given that the intensity of the focused laser spot is proportional to the inverse square of w_0, we often want to minimize this quantity. To decrease w_0, one should either (i) decrease the f-number of the focusing element, or (ii) decrease the wavelength. The beam waist and Rayleigh range for a 1053 nm laser for $f_{\#} \in \{1,\ 3,\ 10\}$ are shown in Fig. 3.3. Here we can clearly observe the dependence of divergence angle on the f-number. To be considered paraxial, the spatial envelope must change slowly along z when compared to r which is clear

in the case of the $f/10$ and even $f/3$ focusing, but not for $f/1$.

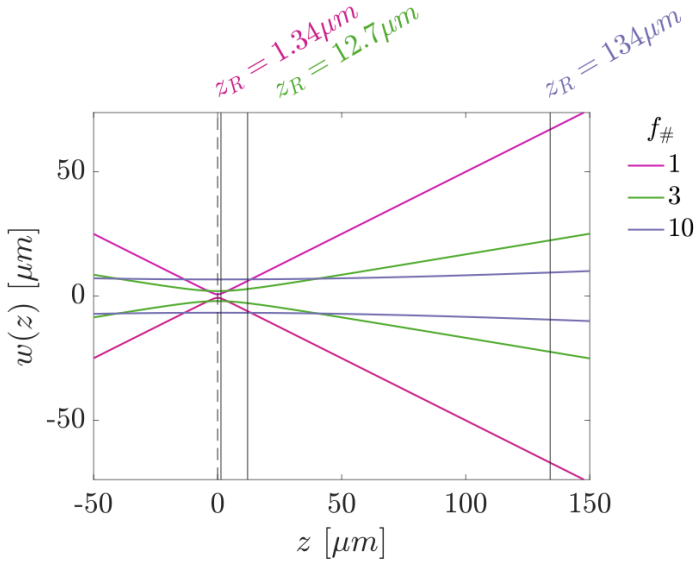

Figure 3.3: Beam waist $w(z)$ of a Gaussian beam focused with f/1 (pink), f/3 (green), and f/10 (purple). The minimum beam waist w_0 occurs at $z = 0$ and is indicated by a black dashed line. The Rayleigh range z_R for each $f_\#$ is indicated by a solid black line that is labeled above the plot with the same colors.

The relationship between beam waist w_0 and the typically-measured-experimentally full-width-half-maximum (FWHM) for a Gaussian beam $\sim e^{-2r^2/w_0^2}$ (Eqn. 3.16) is given by

$$1/2 = \exp\left(-\frac{\text{FWHM}^2}{2w_0^2}\right), \tag{3.41}$$

or approximately equal to,

$$w_0 \approx 0.85 \times \text{FWHM}. \tag{3.42}$$

3.2 Properties of plasmas

A plasma is an ensemble of free electrons and ions that is typically charge neutral. The condition of local charge quasi-neutrality in a mono-atomic plasma is given by

$$-en_e + Z^* en_i = 0 \tag{3.43}$$

where e, n_e, Z^*, and n_i are respectively the elementary charge, the electron density, the average ionization. Charge separation between the ions and electrons leads to electric fields, and the collective motion of charged particles results in currents and magnetic fields. Naturally occurring plasmas and those produced in the laboratory exhibit a very large range of

particle densities (10^{-1} to 10^{25} /cm^3) and electron temperatures (10^{-2} to 10^4 eV with 1 eV = 11604 K) for space plasmas to the conditions achieved in ICF experiments.

The electron population is often well described by an ensemble of non-relativistic classical particles in thermodynamic equilibrium according to the 3-D Maxwell-Boltzmann distribution:

$$g(\boldsymbol{v}) = \frac{n_e}{\pi^{3/2} v_{th}^3} \exp\left(-\frac{|\boldsymbol{v} - \boldsymbol{v}_0|^2}{v_{th}^2}\right). \tag{3.44}$$

where n, $\boldsymbol{v}$, $\boldsymbol{v_0}$ are the density, velocity, initial velocity, and and v_{th} is the thermal velocity of the particle has been defined as

$$v_{th} = \sqrt{\frac{2k_B T}{m}}. \tag{3.45}$$

Here, k_B is the Boltzmann constant and T is the temperature. The electron density is obtained by integrating the distribution function over all available microstates according to

$$n_e = \int_{-\infty}^{\infty} g(\boldsymbol{v}) d\boldsymbol{v}. \tag{3.46}$$

Another important plasma property is that the electrons are very mobile and tend to shield electric perturbations. In the electrostatic approximation, it is possible to derive an expression for the length scale at which this shielding is effective. We consider the insertion of a positive test charge at the origin leading to an electrostatic potential ϕ_0. Assuming an electron distribution in a uniform background of positive immobile ions, the electron energy distribution is then

$$g(x, u) = n_0 \sqrt{\frac{m}{2\pi k_B T}} \exp\left(-\frac{1/2mu^2 - e\phi(x)}{k_B T}\right), \tag{3.47}$$

which leads to a Boltzmann density distribution given by

$$n(x) = n_0 \exp\left(\frac{-e\phi}{k_B T}\right). \tag{3.48}$$

Since $E = -\nabla\phi$, Gauss's Law (Eqn. 3.1) leads to Poisson's equation for electrostatics:

$$\frac{d^2\phi}{dx^2} = \frac{-e(n_i - n_e)}{\epsilon_0} \tag{3.49}$$

$$= \frac{n_0 e}{\epsilon_0}(e^{e\phi/k_B T} - 1). \tag{3.50}$$

For $\phi \ll k_B T$, the exponential function can be approximated by a Taylor series expansion

which gives

$$\frac{d^2\phi}{dx^2} = \frac{n_0 e}{\epsilon_0}\left[1 + \frac{e\phi}{k_B T} + ... - 1\right] \tag{3.51}$$

$$\approx \frac{n_0 e^2 \phi}{\epsilon_0 k_B T} \equiv \frac{\phi}{\lambda_D^2} \tag{3.52}$$

where λ_D is referred to as the *Debye length*. The solution to this equation is given by

$$\phi(x) = \phi_0 e^{-|x|/\lambda_D} \tag{3.53}$$

where λ_D is the exponential shielding length within the plasma. In physical units, this is equivalent to

$$\lambda_D = 743\sqrt{\frac{T_e[eV]}{n_e[cm^{-3}]}}\ cm. \tag{3.54}$$

A few important observations can be made from this result. Effective shielding requires that the characteristic length scales of the system are significantly larger than the Debye length ($\lambda_D \ll L$) and that $\lambda_D \propto \sqrt{T_e/n_e}$.

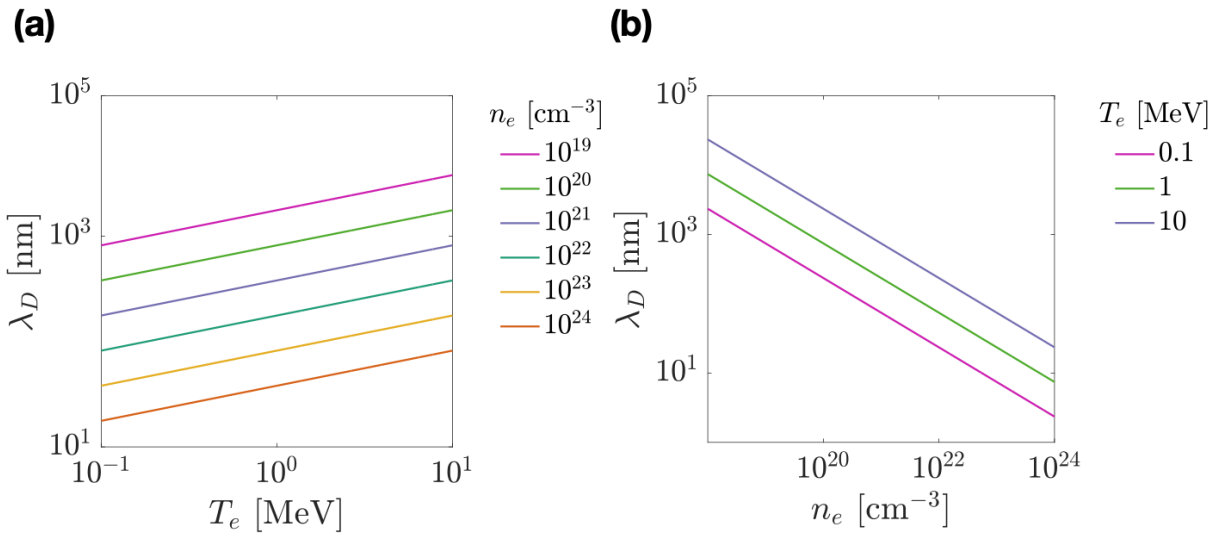

Figure 3.4: Debye length λ_D as a function of (a) electron temperature T_e and (b) electron density n_e.

The functional dependence of Debye length on electron temperature and electron plasma density are shown in Fig. 3.4. There are three main methods used to model plasma behaviour: 1) Single Particle Motion, 2) Kinetic Theory, and 3) Fluid Model. In this thesis, the single particle motion treatment is used throughout. Specifically, we rely on Particle-

in-Cell (PIC) simulations which use Maxwell's equations to calculate the motions and fields of macroparticles. Each macroparticle typically represents between 10^3 and 10^6 particles. While often cost-prohibitive, PIC simulations should capture the microphysics when the spatial-temporal grid is set to resolve the Debye length as well as the characteristic timescale which, in the case of high-intensity laser-plasma interactions, is typically the laser cycle. For reference, the Debye length of a hydrogen plasma with an electron density of $4.69 \times 10^2 2/\mathrm{cm}^3$ and electron temperature of 100 keV is 10.85 nm.

3.3 Electromagnetic waves interacting with plasmas

In the previous section, we introduced the concept that free electrons in plasmas locally suppress electric perturbations. We now consider the optical properties of plasmas due to the motion of free electrons. In this section, the complex dielectric function and conductivity of a collisionless plasma will be derived using the simple harmonic oscillator model, otherwise known as the Drude-Lorentz model closely following the derivation by Fox [94].

The force on a charged particle due to an electric or magnetic field is known as the *Lorentz force* and given by

$$\frac{d\boldsymbol{p}}{dt} = q(\boldsymbol{E} + \boldsymbol{v} \times \boldsymbol{B}) \tag{3.55}$$

where $\boldsymbol{p} = m\boldsymbol{v}$, $\boldsymbol{v}$, m, q, are respectively the momentum, velocity, mass, and the charge of the particle. In the non-relativistic limit, the $\boldsymbol{v} \times \boldsymbol{B}$ term is negligible, leading to

$$\frac{d\boldsymbol{p}}{dt} = -e\boldsymbol{E} \tag{3.56}$$

for free electrons. The general equation of motion of a free electron is then

$$m_e \frac{dx^2}{dt} + m_e \gamma \frac{dx}{dt} = -eE(t) = -eE_0 e^{-i\omega t} \tag{3.57}$$

where ω is the frequency of the electromagnetic wave, $E(t)$ is the time-dependent electric field, and E_0 is the amplitude. The terms on the left hand side of this equation represent the acceleration and possible frictional damping of the electron. This equation of motion can be recognized as a simple harmonic oscillator without a restoring force since free electrons do not experience a restoring force when an external force is applied. Since the position of the electron should also vary in time according to $x = x_0 e^{-i\omega t}$, we obtain

$$x(t) = \frac{eE(t)}{m_e(\omega^2 + i\gamma\omega)}. \tag{3.58}$$

The electron displacement D is defined by

$$D = \epsilon_0 E + P. \tag{3.59}$$

where P is the polarization. In a linear, homogeneous, isotropic medium, P depends linearly on the electric field according to $P = \epsilon_0 \chi E$ where $\chi = \epsilon_r - 1$ is a constant of proportionality called the *electric susceptibility* and ϵ_r is the *relative dielectric constant*. This allows us to write

$$D = \epsilon_r \epsilon_0 E \tag{3.60}$$

Then equating Eqn. 3.59 with Eqn. 3.60 together with $P = -n_e e x$ for a free electron gas gives

$$\epsilon_r \epsilon_0 E = \epsilon_0 E + P \tag{3.61}$$

$$\epsilon_r \epsilon_0 = \epsilon_0 - \frac{n_e e^2}{m_e(\omega^2 + i\gamma\omega)}. \tag{3.62}$$

This expression can then be rearranged to obtain

$$\epsilon_r(\omega) = 1 - \frac{n_e e^2}{\epsilon_0 m_e} \frac{1}{(\omega^2 + i\gamma\omega)} \tag{3.63}$$

$$= 1 - \frac{\omega_{pe}^2}{(\omega^2 + i\gamma\omega)} \tag{3.64}$$

where the *electron plasma frequency* is defined as

$$w_{pe}^2 \equiv \frac{n_e e^2}{\epsilon_0 m_e}. \tag{3.65}$$

In physical units, it can be calculated using the relation

$$\omega_{pe} = \sqrt{\frac{n_e e^2}{\varepsilon_0 m_e}} \cong 5.64 \times 10^4 \sqrt{n_e[cm^{-3}]}\ rad/s. \tag{3.66}$$

Eqn. 3.64 simplifies in the case of a collisionless plasma to

$$\epsilon_r(\omega) = 1 - \frac{\omega_{pe}^2}{\omega^2}. \tag{3.67}$$

The *complex refractive index* is related to the complex dielectric constant by the relation

$$\tilde{n} = \sqrt{\epsilon_r} = \frac{kc}{w} = \sqrt{1 - \frac{\omega_{pe}^2}{\omega^2}}. \tag{3.68}$$

When $\omega > \omega_{pe}$, $\tilde{n}$ is real and positive, and the wave will propagate through the plasma according to the dispersion relation:

$$\omega^2 = \omega_{pe}^2 + c^2 k^2. \tag{3.69}$$

If $\omega < \omega_{pe}$, $\tilde{n}$ is imaginary therefore the wave cannot propagate and becomes evanescent. The electric field decays exponentially. The *collisionless skin depth* is the distance where the amplitude of an electromagnetic wave has been attenuated by a factor of $1/e$. It is approximately equal to [95]

$$\delta \approx \frac{c}{\omega_{pe}} \cong \sqrt{\frac{2.8 \times 10^{19}}{n_e \ [cm^{-3}]}} \ \mu m. \tag{3.70}$$

The plasma reflectivity R can be calculated according to

$$R = \left| \frac{\tilde{n} - 1}{\tilde{n} + 1} \right|^2 \tag{3.71}$$

For $\omega \leq \omega_{pe}$, the plasma is purely reflective ($R = 1$). The reflectivity decreases as a function of ω for $\omega > \omega_{pe}$. In the limit $\omega \to \infty$, $R \to 0$. It is convenient to discuss the condition $\omega_{pe} = \omega$ in terms of electron density for a fixed laser frequency. This threshold density is known as the *critical electron density* and is given by

$$n_c = \frac{m_e \varepsilon_0 \omega^2}{e^2} \tag{3.72}$$

$$\cong \frac{1.11 \times 10^{21}}{\lambda_{0,\mu m}^2} \ cm^{-3}. \tag{3.73}$$

When $n_e < n_c$ the plasma is said to be *underdense*. Similarly, when $n_e > n_c$ it is said to be *overdense*. Returning now to Eqn. 3.57, the general equation of motion for the electron in terms of velocity $\boldsymbol{v}$ is

$$m_e \frac{d\boldsymbol{v}}{dt} + m_e \gamma \boldsymbol{v} = -e\boldsymbol{E}. \tag{3.74}$$

It is then convenient to replace the damping coefficient γ with the damping time $\tau = 1/\gamma$ resulting in

$$m_e \frac{d\boldsymbol{v}}{dt} + \frac{m_e \boldsymbol{v}}{\tau} = -e\boldsymbol{E}. \tag{3.75}$$

Since all quantities vary in time $\propto e^{-i\omega t}$, we obtain

$$\boldsymbol{v}(t) = \frac{-e\tau}{m_e} \frac{1}{1 - i\omega\tau} \boldsymbol{E}(t). \tag{3.76}$$

The *plasma current density* is then

$$\boldsymbol{J} = -n_e e \boldsymbol{v} = \sigma(\omega)\boldsymbol{E}. \tag{3.77}$$

which gives the following expression for the *plasma conductivity*

$$\sigma(\omega) = \frac{\sigma_0}{1 - i\omega\tau} \tag{3.78}$$

where the *DC conductivity* is defined as

$$\sigma_0 \equiv \frac{n_e e^2 \tau}{m_e}. \tag{3.79}$$

If we consider the case where damping is negligible as in collisionless plasmas, the conductivity simplifies to

$$\sigma(\omega) \equiv \frac{i n_e e^2}{m_e \omega} \tag{3.80}$$

which is purely imaginary. This indicates that the current is $\pi/2$ out of phase with respect to the electric field of the electromagnetic wave. In laser-plasma experiments, a planar solid or liquid target typically has an initial 1-D density profile described by a Heaviside function. When it is ionized during the rising edge of the laser pulse and begins to expand hydrodynamically, the 1-D *plasma electron density profile* is often well approximated by a smooth, exponentially decreasing function such as

$$n_e(z) = n_{e_0} \exp\left(-\frac{z}{\ell_s}\right) \tag{3.81}$$

where n_{e_0} is the initial electron density of the material, z is the position along the laser axis with the origin at the initial front surface, and ℓ_s is defined as the *plasma density scale length*, which corresponds to the distance from the target surface at which the density has decreased by a factor of $1/e$.

As a result, when overdense targets are irradiated by ultra-intense lasers, underdense plasma processes may be important if the target has been pre-expanded by the rising edge of the laser pulse. The plasma parameters for a liquid density hydrogen plasma are summarized in Table 3.1.

Parameter	Value
ρ_0	0.07085 g/cm^3
$n_e = n_i$	4.69×10^{22} /cm^3
$n_e/n_c, \lambda_L = 800\ nm$	27.0
$n_e/n_c, \lambda_L = 1053\ nm$	46.8
ω_{pe}	1.22×10^{16} rad/s
δ	24.43 nm

Table 3.1: Plasma parameters for fully ionized hydrogen plasma produced from liquid hydrogen.

3.4 Single electron motion due to an electromagnetic plane wave

3.4.1 Non-relativistic regime

In an *ideal plasma*, the electron collision time is much longer than a wave period and electrons are freely accelerated by the electric field of an electromagnetic wave. In the laboratory frame, a population of free electrons that is initially at rest begins to oscillate in the electromagnetic field of the laser according to the Lorentz force (Eqn. 3.55). To obtain an analytical expression for electron velocity, we again consider the electric field of a plane wave traveling in the positive z direction and varying in time according to $\boldsymbol{E}(t) = E(z)\hat{\boldsymbol{\varepsilon}}e^{-i\omega t}$.

To first order, we neglect the $\boldsymbol{v} \times \boldsymbol{B}$ term since $|v| \ll c$ for weak fields, and we restrict ourselves to solutions describing oscillation at the frequency of the electromagnetic wave. Together with $\boldsymbol{v} = d\boldsymbol{r}/dt$, the linear solution to the Lorentz equation is

$$\boldsymbol{v} = -i\frac{e\boldsymbol{E}}{m_e\omega} \tag{3.82}$$

$$\boldsymbol{r} = \frac{e\boldsymbol{E}}{m_e\omega^2}. \tag{3.83}$$

3.4.2 Relativistic regime

When $|\boldsymbol{v}| \to c$, the contribution of the $\boldsymbol{v} \times \boldsymbol{B}$ term becomes relevant to electron motion. It is often useful to refer to a dimensionless parameter called the *normalized vector potential*

that is defined by

$$a_0 = \frac{eE_0}{m_e c\omega} \approx 0.85\sqrt{I_{18}\lambda_{0,\mu m}^2} \tag{3.84}$$

where I_{18} is the laser intensity in 10^{18} W/cm^2 and $\lambda_{0,\mu m}$ is the laser wavelength in microns. This quantity indicates the importance of relativistic effects when describing electron motion due to an electromagnetic wave. If $a_0 \ll 1$, we say the interaction is non-relativistic, and when $a_0 \geq 1$, we refer to it as the relativistic regime. For example, a laser with wavelength 1-micron focused to an intensity of $\sim 10^{18}$ W/cm^2 accelerates electrons to relativistic velocities corresponding to $a_0 \simeq 1$. Present-day petawatt (PW) lasers routinely achieve $a_0 \geq 10$, and next-generation 10-100 PW lasers are currently in development that are designed to achieve $a_0 = 300$.

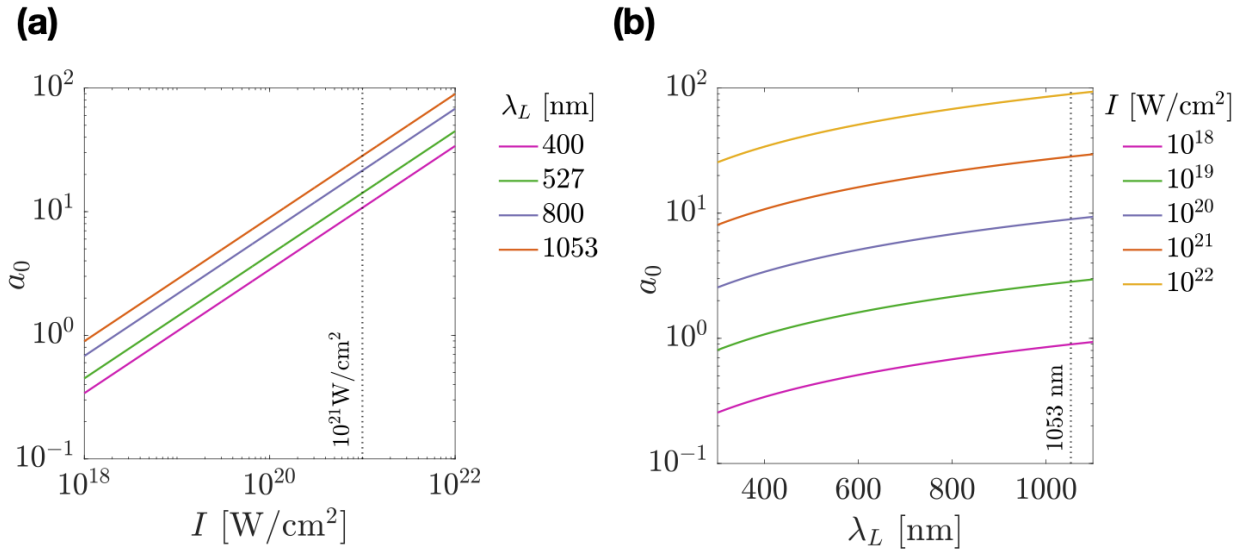

Figure 3.5: Normalized vector potential a_0 as a function of (a) laser intensity I and (b) laser wavelength λ_L.

In addition to the Lorentz force (Eqn. 3.55), we also have the energy equation

$$\frac{d}{dt}\left(\gamma m_e c^2\right) = -e(\boldsymbol{E}\cdot\boldsymbol{v}) \tag{3.85}$$

where $\boldsymbol{p} = \gamma m_e \boldsymbol{v}$ and $\boldsymbol{v}$, m_e, e, and γ are respectively the momentum, velocity, rest mass, absolute charge, and Lorentz factor of the electron. The Lorentz factor, also referred to as the *relativistic gamma factor*, is defined as

$$\gamma = \frac{1}{\sqrt{1-\frac{v^2}{c^2}}} = \sqrt{1+\frac{p^2}{m_e^2 c^2}}. \tag{3.86}$$

It describes the relativistic correction to measurements of time, length, and other physical quantities associated with an object in motion. As the velocity of an object approaches the speed of light, γ becomes large. According to special relativity, the effective mass of a relativistic electron is given by γm_e where m_e is the rest mass of the electron. Consequently, the plasma frequency (Eqn. 3.65) and critical density (Eqn. 3.72) become $\omega_{pe}/\sqrt{\gamma}$ and γn_c, respectively. Relativistic effects allow an electromagnetic wave to propagate to a higher density than the non-relativistic case. This phenomenon is referred to as relativistically induced transparency.

We now consider the equations of motion for an electron in the relativistic regime. Since $\boldsymbol{\nabla} \cdot \boldsymbol{B} = 0$, we can define a magnetic vector potential $\boldsymbol{A}$ where $\boldsymbol{B} = \boldsymbol{\nabla} \times \boldsymbol{A}$.
Substituting this into Ampere's equation (Eqn. 3.4), we find that

$$\boldsymbol{\nabla} \times \boldsymbol{E} = -\frac{\partial \boldsymbol{B}}{\partial t} = -\frac{\partial}{\partial t}\boldsymbol{\nabla} \times \boldsymbol{A}, \tag{3.87}$$

and by rearranging we obtain that

$$\boldsymbol{\nabla}\left(\boldsymbol{E} - \frac{\partial \boldsymbol{A}}{\partial t}\right) = 0. \tag{3.88}$$

We therefore have $\boldsymbol{E} = -\partial \boldsymbol{A}/\partial t$, and we can rewrite the Lorentz equation in terms of the magnetic vector potential A for a linearly polarized wave as

$$\frac{d\boldsymbol{p}_\perp}{dt} = e\frac{\partial \boldsymbol{A}}{\partial t} - ev_z\frac{\partial \boldsymbol{A}}{\partial z}. \tag{3.89}$$

Recognizing the material derivative as

$$\frac{d}{dt} = \frac{\partial}{\partial t} + \boldsymbol{v} \cdot \boldsymbol{\nabla} \tag{3.90}$$

allows us to simplify further to

$$\frac{d}{dt}(\boldsymbol{p}_\perp + e\boldsymbol{A}) = 0, \tag{3.91}$$

and this is then straightforwardly integrated to

$$\boldsymbol{p}_\perp + e\boldsymbol{A} = \boldsymbol{p}_{\perp 0} \tag{3.92}$$

where $\boldsymbol{p}_{\perp 0}$ is the initial perpendicular electron momentum.

Now we consider the longitudinal component of the electron momentum. Eqn. 3.55 and 3.85 yield a pair of equations that we can subtract from each other to write

$$\frac{dp_z}{dt} - \frac{d\gamma}{dt} = -v_y \left(\frac{\partial A_y}{\partial t} + \frac{\partial A_y}{\partial z} \right) - v_x \left(\frac{\partial A_x}{\partial t} + \frac{\partial A_x}{\partial z} \right). \tag{3.93}$$

Since A is a function of (z, t) only, the terms on the RHS of this equation vanish, and we can integrate to obtain

$$\gamma - p_z = \alpha \tag{3.94}$$

where α is a constant of the motion. Using the relativistic kinematics identity $\gamma^2 - p_z^2 - p_\perp^2 = 1$ and choosing $\boldsymbol{p}_{\perp 0} = 0$, we can solve to get the expression

$$p_z = \frac{1 - \alpha^2 + p_\perp^2}{2\alpha}. \tag{3.95}$$

For an electron initially at rest, conservation of momentum requires that $\alpha = 1$. In the laboratory frame, the electron equations of motion in polar coordinates can be expressed as

$$p_x = 0 \tag{3.96}$$

$$p_y = a_0 \cos\varphi \tag{3.97}$$

$$p_z = \frac{a_0^2}{4}[1 + \cos 2\varphi], \tag{3.98}$$

where φ is the angular coordinate, so an electron begins to drift in the presence of an electromagnetic wave with *average drift momentum*

$$p_D \equiv \bar{p_z} = \frac{a_0^2}{4}. \tag{3.99}$$

Integrating again, the electron position in the laboratory frame is then [95]

$$x = 0 \tag{3.100}$$

$$y = a_0 \sin\varphi \tag{3.101}$$

$$z = \frac{a_0^2}{4}\left[1 + \frac{1}{2}\sin 2\varphi\right]. \tag{3.102}$$

Electron trajectories for different values of a_0 are shown in Fig. 3.6 (a). Since the electron is drifting in the positive z direction, we can also look for the electron motion in the average rest frame.

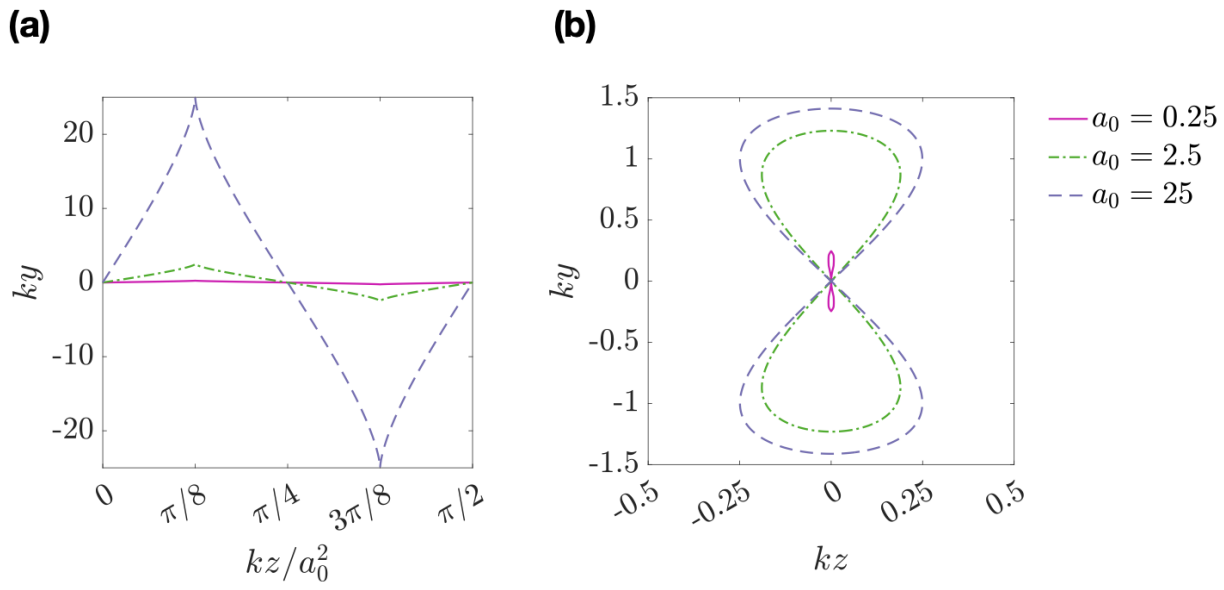

Figure 3.6: Single electron orbits in a large-amplitude, linearly polarized electromagnetic wave traveling in the $\hat{z}$ direction in the (a) laboratory frame and (b) average rest frame for $a_0 = 0.25$ (pink), $a_0 = 2.5$ (green dot-dashed), and $a_0 = 25$ (purple dashed).

This requires a different choice of α in Eqn. 3.94 given by

$$\alpha = \sqrt{1 + \frac{a_0^2}{2}} \equiv \gamma_0, \tag{3.103}$$

and the electron trajectories in the average rest frame are then [95]

$$x = 0 \tag{3.104}$$

$$y = 2q \sin\varphi \tag{3.105}$$

$$z = \frac{1}{2} q^2 \sin 2\varphi \tag{3.106}$$

where $q = a_0/(2\gamma_0)$. These equations correspond to the figure eight orbit shape described by $16z^2 = y^2(4q^2 - y^2)$ which is shown in Fig. 3.6 (b) for different values of a_0.

The analytical solutions of plane wave equations are important for gaining physical intuition about single electron motion due to an electromagnetic wave, but they do not fully capture the actual motion caused by a real laser pulse. A better approximation can be obtained by imposing a temporal envelope function $f(t)$ on the wave vector such as

$$\boldsymbol{A}(x,t) = a_0 f(t) \cos\varphi, \tag{3.107}$$

which ensures that transverse momentum is conserved, that is $p_y(t) = A_y(t)$, and that once the laser pulse ends, the electron returns to rest.

3.5 Ponderomotive force

The solutions derived thus far are valid only for infinite plane waves and radiation that is uniform in space and slowly varying in time. Short-pulse lasers violate both of these conditions. A tight focus means strong radial intensity gradients at wavelength scale, and ultra-short, few-cycle pulses are highly dispersive. As a result, a fully non-adiabatic treatment is required to obtain analytic expressions for the electron equations of motion, and the equations are nonlinear.

For this derivation, we return to the non-relativistic regime with $a_0 \ll 1$ to gain physical intuition of the ponderomotive force. We consider the linear equation for electron motion caused by a linearly polarized wave propagating in the positive z direction:

$$\frac{\partial v_y}{\partial t} = -\frac{e}{m_e} E_y(y). \tag{3.108}$$

By taking the real components of the fields and performing a Taylor expansion, we obtain that

$$E_y(r) \simeq E_0(y) \cos\varphi + y \frac{\partial E_0(y)}{\partial y} \cos\varphi + \ldots, \tag{3.109}$$

which to lowest order has the solutions

$$v_y^{(1)} = -v_{os} \sin\varphi \tag{3.110}$$

$$y^{(1)} = \frac{v_{os}}{\omega} \cos\varphi \tag{3.111}$$

where

$$v_{os} \equiv \frac{eE_0}{m_e \omega} \tag{3.112}$$

is the *electron quiver velocity*. Recalling Eqn. 3.84, we see that v_{os} is related to a_0 by $v_{os} = a_0 c$. The second order terms from Eqn. 3.108 give

$$\frac{\partial v_y^{(2)}}{\partial t} = -\frac{e^2}{m_e^2 \omega^2} E_0 \frac{\partial E_0(y)}{\partial y} \cos^2\varphi, \tag{3.113}$$

and to obtain the cycle-averaged force on the electron, we can multiply both sides by m_e

and average over the electromagnetic wave cycle. We obtain

$$f_p \equiv \left\langle m_e \frac{\partial v_y^{(2)}}{\partial t} \right\rangle = -\frac{e^2}{2m_e\omega^2}\frac{\partial E_0^2}{\partial y} = -m_e c^2 \nabla \left| \frac{\boldsymbol{a}(r)}{2} \right|^2 \tag{3.114}$$

where $\boldsymbol{a}(\boldsymbol{r})$ can be given by Eqn. 3.84. This force can be intuitively understood as a force that pushes electrons away from regions of higher local intensity. In general, electron trajectories due to the Lorentz force at relativistic intensities can only be found numerically, but we can get important physical insight by considering the motion of electrons in plane waves and the *ejection angle* relative to the laser focus. For an electron initially at rest, the total increase in energy due to multiphoton energy transfer from the electromagnetic field can be given by

$$\Delta U = (\gamma - 1)mc^2. \tag{3.115}$$

Because of the conservation of parallel momentum, we also have

$$\mathrm{p}_{||} = n\hbar k = \frac{n\hbar\omega}{c} = \frac{\delta U}{c} = (\gamma - 1)mc, \tag{3.116}$$

and using the relationship between longitudinal and perpendicular momentum derived in the previous section (Eqn. 3.95) with $\alpha = 1$, we conclude that

$$\mathrm{p}_{||} = \frac{\mathrm{p}_\perp^2}{2mc}. \tag{3.117}$$

Trigonometry then requires that the emission angle is

$$\tan\theta = \frac{\mathrm{p}_\perp}{\mathrm{p}_{||}} = \sqrt{\frac{2}{\gamma - 1}} \tag{3.118}$$

as shown graphically in Fig. 3.7. We see that relative to the laser propagation axis, higher energy electrons are emitted at smaller angles.

3.6 Relativistic ponderomotive force

The derivations in the previous section assumed that the laser was non-relativistic, that is, $a_0 < 1$. The inclusion of relativistic effects is non-trivial and has been studied thoroughly in the literature. Given the extensive derivations required, we omit them and state the main result [96], namely that

$$\frac{d\tilde{\boldsymbol{p}}}{dt} = -\frac{m_e c^2}{2\tilde{\gamma}} \nabla \left| \tilde{\boldsymbol{a}} \right|^2 \tag{3.119}$$

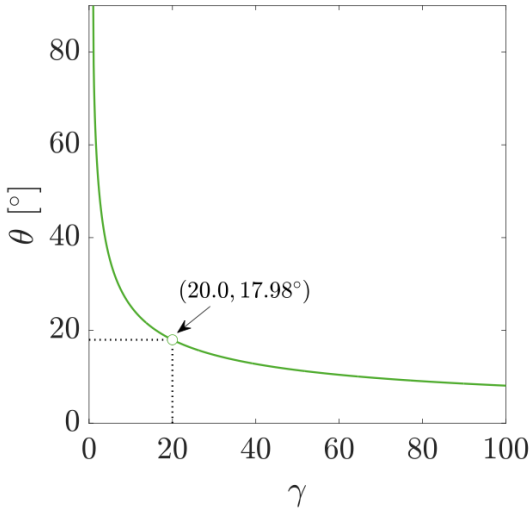

Figure 3.7: Electron emission angle θ from an extended laser focus as a function of the relativistic gamma factor γ.

where

$$\tilde{\gamma} = \sqrt{1 + \left|\frac{\tilde{\boldsymbol{p}}_\perp}{m_e c}\right|^2 + \left|\frac{\tilde{p_z}}{m_e c}\right|^2 + |\tilde{\boldsymbol{a}}|^2} \tag{3.120}$$

and

$$\tilde{\boldsymbol{a}} = \frac{1}{\sqrt{2}} |a(r,t)| \, \hat{x}. \tag{3.121}$$

Here, $\tilde{b}$ denotes the time-averaged quantity. As we see, the result is almost identical to the non-relativistic case except for a factor of $\tilde{\gamma}$. This factor can be attributed to the effective electron mass increasing with the increase in $\tilde{\gamma}$. As we will see later in this thesis, this effect plays an important role in the interaction between a high-intensity laser and a near-critical density plasma.

3.7 High-intensity laser interactions with overdense plasmas

We have so far only considered the motion of a single electron driven by an electromagnetic wave in a uniform plasma slab of fixed density and temperature. In reality, high-intensity laser-plasma interactions give rise to large density and temperature gradients and oftentimes the collective motion of electrons and ions. The initial ionization of a solid or liquid to plasma and heating by a tightly focused, high-intensity laser strongly influences the subsequent interaction dynamics. We therefore briefly introduce the dominant ionization, laser absorption, and electron heating mechanisms for laser irradiances $I_0\lambda_0^2$ exceeding 10^{18} Wcm$^{-2}\mu$m^2 in cases in which the electron oscillation amplitude in the laser field (v_{os}/ω) can exceed the

skin depth δ (Eqn. 3.70).

3.7.1 Ionization dynamics

For ultra-fast lasers (<1 ps), the laser pulse interacts with a near solid density plasma. The initial ionization of the target due to the laser field occurs primarily through collisionless processes such as tunneling ionization, multi-photon ionization, or barrier suppression ionization. Heating of the electrons occurs on the sub-ps timescale and can be estimated from the electron-electron collision frequencies. The heating of the ions typically occurs well beyond the laser pulse duration with a timescale can be estimated from the electron-ion collision frequency. Subsequently, the heated electrons and ions will expand outward leading to an expanding plasma with a density gradient. The electron-ion collision frequency in this case is given by

$$\nu_{ei} \simeq 2.53 \times 10^{-6} \frac{n_e[cm^{-3}] \ln \Lambda}{T_e[eV]^{3/2}} \ s^{-1} \tag{3.122}$$

where $\ln \Lambda$ is the Coulomb logarithm. This quantity can be calculated using the following formula, which includes the quantum correction for the electron wavepacket [97]:

$$\ln \Lambda = 24.0 - 0.5 \ln(n_e[cm^{-3}]) + 1.0 \ln(T_e[eV]). \tag{3.123}$$

For $n_e = 4.69 \times 10^{22}/\text{cm}^{-3}$ and $T_e = 100$ keV, $\ln \Lambda = 9.41$ leads to $\nu_{ei} = 3.53 \times 10^{10}/\text{s}$. This implies approximately one electron-ion collision every 28.3 ps. The functional dependence of the Coulomb logarithm and electron-ion collision frequency on density and temperature are shown in Fig. 3.8 and Fig. 3.9, respectively.

Ionization of the target up to the critical surface thus occurs primarily through a collisionless process such as tunneling ionization, multi-photon ionization, or field ionization. To determine which of these processes is dominant, we calculate the Keldysh parameter according to

$$\gamma_K = \omega \sqrt{\frac{2U_{ion}}{I(\boldsymbol{r}, t)}} \sim \sqrt{\frac{U_{ion}}{\mathcal{E}_p}} \tag{3.124}$$

where U_{ion} is the energy required to remove the electron and $\mathcal{E}_p$ is the *ponderomotive potential energy* given by

$$\mathcal{E}_p = \frac{e^2 |\boldsymbol{E}(\boldsymbol{r}, t)|^2}{4 m_e \omega^2} = \left[\sqrt{1 + a_0^2} - 1 \right] m_e c^2. \tag{3.125}$$

The functional relationship between the Keldysh parameter and a_0 is shown in Fig. 3.10. The condition $\gamma_K < 1$ occurs in the context of strong fields and long wavelengths, and tunneling ionization is dominant in this case.

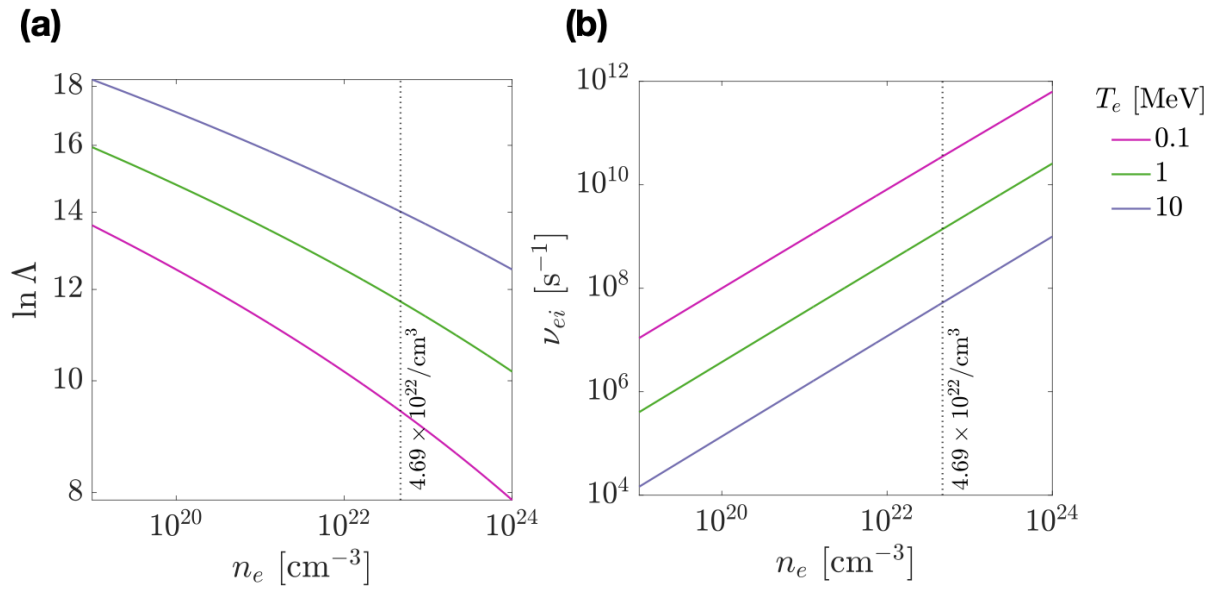

Figure 3.8: (a) Coulomb logarithm $\ln\Lambda$ and (b) electron-ion collision frequency ν_{ei} as a function of electron density n_e.

The Coulomb potential is modified by an electric field according to

$$V(x) = \frac{Ze^2}{x} - e\varepsilon x. \tag{3.126}$$

Equating the Coulomb potential and the energy U_{ion} required to remove an electron from the atom, we calculate the threshold field strength at which barrier suppression ionization can occur to be

$$\varepsilon_c = \frac{U_{ion}^2}{4Ze^3}. \tag{3.127}$$

For hydrogen with $U_{ion} = 13.61$ eV, $\varepsilon = 0.8506$, the effective *appearance intensity* is given by

$$I_{app} = \frac{c}{8\pi}\varepsilon_c^2 = \frac{cU_{ion}^4}{128\pi Z^2 e^6} \simeq 4 \times 10^9 \left(\frac{U_{ion}}{eV}\right)^4 Z^{-2} \text{ W/cm}^2. \tag{3.128}$$

Tunneling ionization occurs for hydrogen when the laser intensity exceeds $I_{app} \simeq 1.4 \times 10^{14}$ W/cm^2.

When $\gamma_K > 1$, atoms are most likely to be ionized by multi-photon ionization, a process in which an electron is liberated after multiple photons are absorbed by the atom. The ionization potential of simple, single-electron atoms such as hydrogen and deuterium studied in this thesis can be calculated using the Schrodinger equation. The ionization potentials for

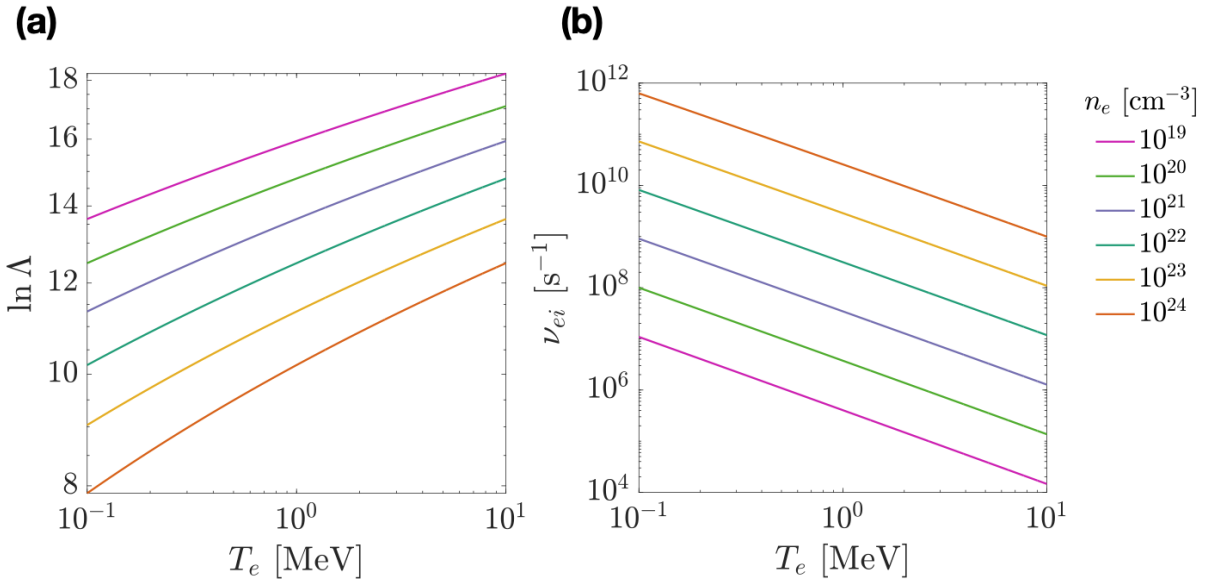

Figure 3.9: (a) Coulomb logarithm $\ln\Lambda$ and (b) electron-ion collision frequency ν_{ei} as a function of electron temperature T_e.

hydrogen and deuterium are 13.61 eV, and the energy of a photon can be calculated from

$$E = \frac{hc}{\lambda_0} \tag{3.129}$$

where h is *Planck's constant*. For a 1053 nm laser, the average photon energy is 1.886×10^{-19} J $= 1.177$ eV.

To ionize hydrogen or deuterium, at least 12 photons need to be absorbed by the atom. While the peak laser intensities used in this work correspond to $\gamma_K \ll 1$, low-Z solids are often ionized by the laser pre-pulse, which has intensity orders of magnitude lower than the peak laser intensity and that occurs from a few picoseconds to nanoseconds before the peak laser intensity. In this case, multi-photon ionization can occur.

Lastly, we consider *field ionization*, which is ionization attributed solely to the strength of the electric field. The electric field strength of a bound hydrogen atom can be expressed as

$$E_a = \frac{1}{4\pi\epsilon_0}\frac{e}{a_B^2} \simeq 5.1\times10^9 \text{ V/m} \tag{3.130}$$

where $a_B = \hbar^2/me^2$ is the *Bohr radius*. The *atomic intensity*, or intensity at which hydrogen will be fully ionized, is then given by

$$I_a = \frac{\epsilon_0 c E_a^2}{2} \simeq 3.51\times10^{16} \text{ W/cm}^2. \tag{3.131}$$

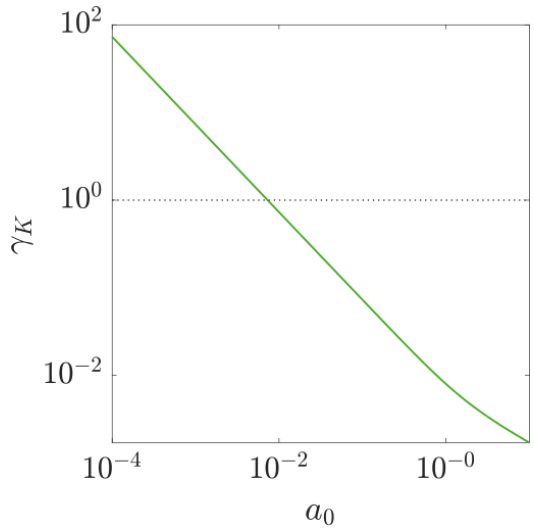

Figure 3.10: Keldysh parameter γ_K as a function of the laser normalized vector potential a_0.

Barrier suppression ionization becomes dominant over tunneling ionization if the laser field strength E exceeds the atomic critical field, E_{cr}, which is a parameter proportional to E_a. For short intense laser pulses, multiphoton ionization is typically small and both the tunneling ionization and barrier suppression ionization can be important. Even for strong laser fields with peak field, $E_{pk} \gg E_{cr}$, tunneling ionization can still occur during the rising edge of the laser pulse until the laser field increases to E_{cr}. Thus, both the laser field strength and rise time are important parameters that determine the dominant ionization process.

Following ionization, the transfer of laser energy into a target through absorption depends on laser intensity and density. In the following section, we will focus specifically on absorption mechanisms that are dominant when a high-intensity laser is incident on near- to over-critical targets. Relativistically induced transparency, as first introduced in Sec. 3.4.2, is an important phenomenon for near-critical density targets with $a_0 \gg 1$. In this case, the laser penetrates to higher electron densities ($n_c \rightarrow \gamma n_c$), which leads to absorption deeper within the target.

3.7.2 Absorption mechanisms

Many absorption mechanisms couple laser energy to plasma electrons. Their relative importance depends on the laser pulse duration τ_L, the laser intensity I, and the plasma density profile $n_e(z)$ (Eqn. 3.81) [95]. For low laser intensities ($<10^{14}$ W/cm^2) and longer pulse (>ps), collisional processes such as the normal skin effect and inverse Bremsstrahlung are dominant for ionized materials. The physical picture for inverse Bremsstrahlung is the absorption of a photon during the collision of an electron and an ion. As such, the rate is

proportional to the electron-ion collision frequency (Eqn. 3.122). At higher laser intensities, the laser rapidly heats the plasma electrons to 100s of eV in picoseconds. Collisional processes quickly become inefficient, and the relativistic electrons are able to penetrate more deeply into the plasma than the laser. Several collisionless processes have been identified including resonance absorption near the critical surface, vacuum heating, and $\boldsymbol{J} \times \boldsymbol{B}$ heating [95].

In resonance absorption, a non-normal incidence p-polarized laser penetrates a plasma with an extended density gradient ($\ell_s \gg \lambda_L$) up to the critical surface where it drives a plasma wave that grows with each laser cycle. In the high-intensity regime, the plasma wave is damped by particle trapping and wave breaking. This absorption mechanism does not occur in the case of steep density profiles where the electron oscillation amplitude often exceeds the plasma density scale length. In this case, electrons near the surface can be dragged out into vacuum well beyond the Debye sheath $\lambda_D = v_{te}/\omega_p$. When the field reverses, the electron reverses direction and is accelerated back into the plasma in what is known as vacuum heating or the Brunel mechanism. The Brunel mechanism, however, neglects the force on the electron due to the magnetic field of the laser pulse, which becomes non-negligible at high laser intensities.

Relativistic $\boldsymbol{J} \times \boldsymbol{B}$ heating

Electrons can also be directly accelerated by a laser field with steep density profiles by the high-frequency $\boldsymbol{v} \times \boldsymbol{B}$ component of the Lorentz force (Eqn. 3.55). $\boldsymbol{J} \times \boldsymbol{B}$ heating becomes the dominant absorption mechanism at high laser irradiances, that is when $I_0\lambda_0^2 \geq 10^{18}$ W cm^{-2}µm^2.

To understand this heating mechanism, we again consider a linearly polarized wave traveling in the positive z direction with $E = E_0(z)\hat{y}\sin\omega t$. This setup produces a longitudinal force term

$$f_z = -\frac{m_e}{4}\frac{\partial v_{os}^2(z)}{\partial z}(1 - \cos 2\omega t). \tag{3.132}$$

The first term represents the ponderomotive force (Eqn. 3.114) while the second, high-frequency term oscillates at twice the laser frequency. This oscillation causes electrons at the steep vacuum interface to oscillate along the laser propagation axis. This oscillation in turn generates hot electron bunches with energies up to several MeV that inject into the target every half laser cycle in a phenomenon known as 2ω *bunching* [98]. It is most efficient at normal incidence and becomes significant at relativistic quiver velocities.

The upshot is that when a high-intensity laser is incident on a micron-thick solid-density target, electrons are pushed away from local regions of high-intensity both radially and inside the target. The collective electron motion establishes an electric field by charge separation, and this field leads to ion acceleration on the picosecond timescale (see Section 3.8).

3.7.3 Hot electron heating models

The production of energetic electrons is an inevitable consequence of irradiating solids with a short-pulse laser. The collisionless absorption mechanisms just described result in the superheating of some fraction of the electrons to a few MeV, a much higher energy than the bulk plasma electron temperature. Typically this "suprathermal" or "hot" electron population has a semi-Maxwellian distribution with a characteristic hot electron temperature $T_{e,hot} \gg T_e$. These electrons penetrate into the overdense plasma beyond the critical surface from which the laser is primarily reflected. The hot electrons have a characteristic angular divergence due to the transverse component of the ponderomotive force, and the highest energy electrons are emitted closest to the laser axis. For a given a_0, the electron energies can be estimated to first order by the ponderomotive energy (Eqn. 3.125) since the collisionless $\boldsymbol{J} \times \boldsymbol{B}$ process dominates and the ponderomotive force is the main source of energy. The physical reasoning for this is that when the laser reflects from the critical surface, it produces a standing wave with $\boldsymbol{a} \simeq \boldsymbol{a}(x) \cos \omega t$. The standing wave generates a *ponderomotive potential*

$$\Phi_p \simeq m_e c^2 \sqrt{1 + \boldsymbol{a}^2(x)/2}. \tag{3.133}$$

The hot electron temperature, which is strictly due to the ponderomotive potential, was estimated by Wilks *et* al. as [99]

$$T_{e,hot}^{\text{Wilks}} = m_e c^2 \left(\sqrt{1 + a_0^2} - 1 \right) \cong 511 \left(\sqrt{1 + \frac{I_{18} \lambda_{0,\mu m}^2}{1.37}} - 1 \right) \text{ keV}. \tag{3.134}$$

Beg *et al.* found experimentally that electron spectra differed significantly from the ponderomotive scaling. They instead found the empirical fit [100]

$$T_{e,hot}^{\text{Beg}} = 215 \ (I_{18} \lambda_{0,\mu m}^2)^{1/3} \text{ keV}. \tag{3.135}$$

More recently, Haines *et al.* developed a theoretical model in which the electrons are accelerated during part of the laser cycle before escaping beyond the light penetration depth. This results in [101]

$$T_{e,hot}^{\text{Haines}} = m_e c^2 \left(\sqrt{1 + a_0 \sqrt{2}} - 1 \right) \cong 511 \left(\sqrt{1 + 1.2 \sqrt{I_{18} \lambda_{0,\mu m}^2}} - 1 \right) \text{ keV}. \tag{3.136}$$

If we now consider a 1053 nm laser focused to 10^{20} (10^{21}) W/cm^2, the hot electron temperature predicted by the Haines scaling law is 1.88 MeV (3.27 MeV). The three models

are compared in Fig. 3.11. The Haines scaling agrees well with the empirical scaling found by Beg et al. in the intensity range of 10^{18} – 10^{21} W/cm^2.

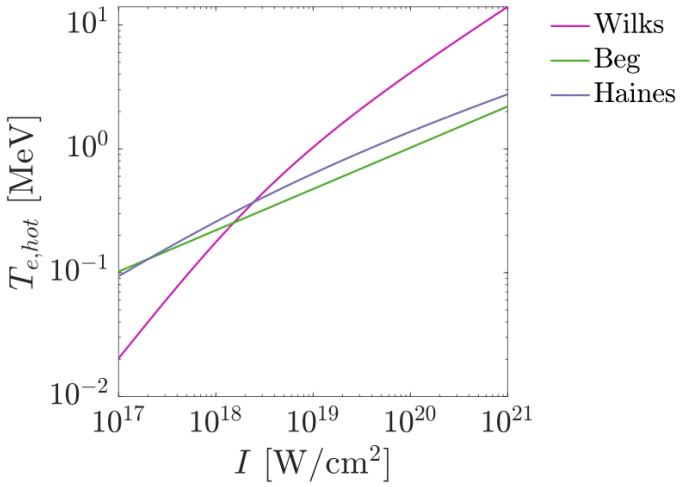

Figure 3.11: Models of the hot electron temperature produced from a high-intensity laser ranging from 10^{17} to 10^{21} W/cm^2. The Wilks pondermotive scaling (pink), Beg scaling (green), and Haines scaling (purple) are shown [99–101].

3.8 Laser-driven ion acceleration mechanisms

As discussed in the previous section, the heating and excitation of electrons occurs on the sub-ps timescale whereas the heating of the ions typically takes longer than pulse duration of short-pulse laser. Thus, in the absence of electric and magnetic fields, the ions have negligible thermal motion during the laser pulse duration.

For a laser to directly accelerate protons, we consider the quiver velocity of a proton in an electromagnetic field. Following the derivation already demonstrated for electrons (Eqn. 3.112), we find

$$\frac{v_{os,i}}{c} = \frac{ZeE_0}{M\omega c} = \frac{Zm_e}{M}a_0, \tag{3.137}$$

which yields the requirement that $a_0 \sim 1836$. This exceeds the current state-of-the-art by more than an order of magnitude, so contrary to what the term "laser-driven ion acceleration" implies, the laser interacts with and transfers energy to the electron population to produce hot electrons. Generally, collective displacement of the hot electrons gives rise to electric fields through which the ions are accelerated. The resulting energy spread of the laser-accelerated ion beam depends on the hot electron energy distribution.

3.8.1 Target Normal Sheath Acceleration (TNSA)

For a large range of target densities ($10^{21}-10^{24}/\text{cm}^3$) and laser intensities ($10^{16}-10^{22}$ W/cm^2), the dominant acceleration mechanism is the Target Normal Sheath Acceleration (TNSA) mechanism. The name arises from the fact that hot electrons establish an electrostatic "sheath" field at the rear plasma-vacuum interface that accelerates ions in the direction normal to the target surface. The hot electrons responsible for the sheath field are accelerated into the target from the front surface with MeV energies predominantly by the $\boldsymbol{J} \times \boldsymbol{B}$ mechanism (Sect. 3.7.3) as depicted in Fig. 3.12. Due to their high energy, these electrons travel through the target without significantly slowing down or scattering.

When the most energetic electrons reach the rear surface, they escape from the target into vacuum, thereby establishing a strong electrostatic sheath field that is often on the order of TV/m. The subsequent hot electrons are reflected and return back into the target, and this creates a region of non-neutralized negative charge. The resulting sheath field is bell-shaped, and the smoothness of the isopotential leads to the high laminarity of TNSA ion beams [102]. The initial sheath field formed by the "electron cloud" exceeds the threshold for field ionization by approximately three orders of magnitude, and thus guarantees the ionization of all atoms near the rear surface of the target (Eqn. 3.130). The ion population within a thin layer is then accelerated through the electrostatic field. Protons, carbon ions, and oxygen ions are also accelerated from metallic targets that do not naturally contain them due to a thin ($10-100$ nm) hydrocarbon layer that forms naturally when such materials are exposed to air [103].

During the laser pulse, the hot electron temperature is maintained by successive bunches of electrons twice per laser cycle via the ponderomotive force. At the end of the laser pulse, the process transitions from isothermal to adiabatic. The electrostatic field strength decreases on the picosecond timescale as plasma expands and cools, thus ending the acceleration phase. Here, the plasma is contained by a non-rigid wall with no heat exchange with the surroundings ($Q = 0$) however the total work $W \neq 0$. The plasma does work in the form of pressure–volume work ($W > 0$) which causes the temperature of the system to drop in what is known as *adiabatic cooling*.

The TNSA mechanism results in a spatially dense, temporally short MeV-energy ion beam that is locally charge neutral due to co-moving electrons [3, 104, 105]. The temporal evolution of the sheath field leads to an energy-dependent proton emission angle. Higher-energy protons are emitted with divergence angles down to a 5° half angle at the highest proton energy. The highest ion energy is referred to as the *cut-off energy*.

Experimentally observed proton energy spectra are in good agreement with the derivation

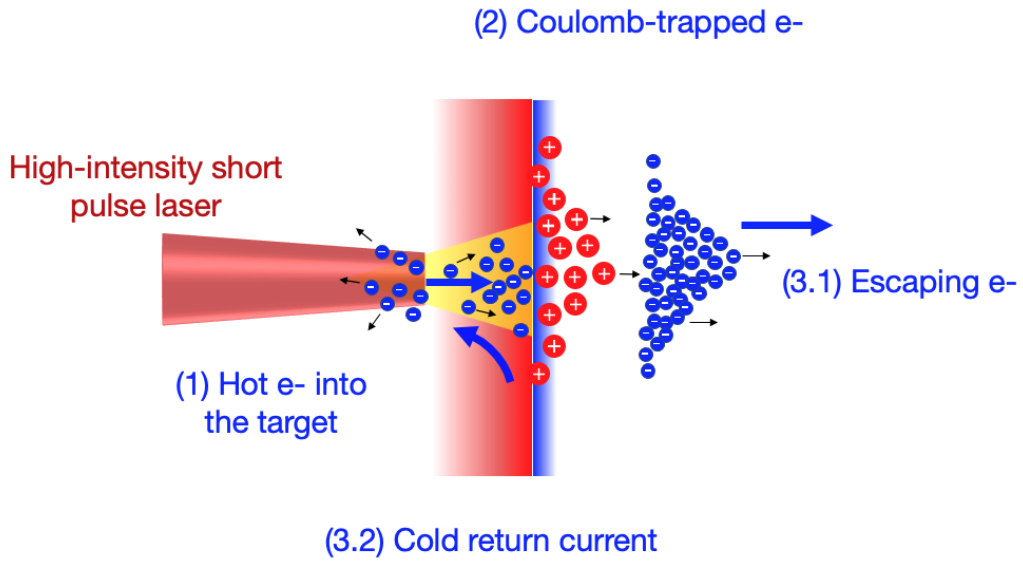

Figure 3.12: Illustration of the Target Normal Sheath Acceleration mechanism. Hot electrons are generated from the interaction of a high-intensity short-pulse laser with a thick, overdense target and the formation of the electrostatic sheath field accelerates protons to MeV energies. Adapted from [106].

of Mora et al. [104] that considers the 1-D adiabatic expansion of plasma into vacuum to find the semi-Maxwellian expression

$$\frac{dN}{dE} = \frac{n_{i_0} c_s \tau}{\sqrt{2EZk_BT_{e,hot}}} \exp\left(-\sqrt{\frac{2E}{Zk_BT_{e,hot}}}\right) \tag{3.138}$$

where c_s is the ion acoustic speed given by

$$c_s = \sqrt{\frac{Zk_BT_e}{M}} \simeq 3.1 \times 10^4 \sqrt{(Z/A)T_e[\text{keV}]}\ \text{cm/s}. \tag{3.139}$$

The equation relates the ion number N to the ion energy E, and with it the hot electron temperature of the laser-plasma interaction can be inferred from the slope of the spectra.

While several empirical models have been developed to explain the cut-off energies observed in laser-plasma experiments, most expressions are proportional to the ponderomotive potential $I\lambda_0^2$ or the laser energy E_L. More recently, Zeil et al. [107] developed an empirical scaling that extends predictions for TNSA proton acceleration to include ultra-short pulse lasers with a pulse duration of less than 100 fs. They find that the maximum proton cut-off energy E_{max} is proportional to the laser-to-hot electron conversion efficiency η and the laser

power P_L. In the ultra-short pulse duration limit where $\tau_L \ll 100$ fs,

$$E_{max} \propto \eta P_L, \tag{3.140}$$

whereas in the other limit that $\tau_L \gg 100$ fs,

$$E_{max} \propto \sqrt{\eta P_L}. \tag{3.141}$$

The scaling robustly reproduces the cut-off energies observed in a large number of experiments with different class laser systems.

To date, the maximum proton cut-off energy and laser-to-ion conversion efficiency reported for single-shot experimental platforms are 94 MeV [90] and 15% [58], respectively. The conversion efficiency is more typically ∼10%. It has been postulated that there is an upper bound on the conversion efficiency for metallic targets due to contaminant layer depletion. If we assume protons are accelerated from a 200 µm region that is 100 nm thick, there are approximately $N_p \approx 8.4 \times 10^{12}$ protons in this volume. For an initial laser energy of 100 J and an average proton energy of 10 MeV, the maximum conversion efficiency would be ∼7.4% [108]. Pure hydrogen targets may allow higher conversion efficiencies.

3.8.2 Advanced laser-driven ion acceleration regimes

With higher laser intensities ($>10^{20}$ W/cm^2) and specific electron density profiles, several alternative acceleration mechanisms are expected to surpass TNSA in maximum ion energy, energy spread, beam divergence, and laser-to-ion conversion efficiency. The transitions between the mechanisms are not well defined, and the acceleration processes often occur simultaneously. The approximate parameter space against which several advanced ion acceleration mechanisms might occur has been predicted using simulation and is shown in Fig. 3.13. The mechanisms include Enhanced Sheath Field (ESF) acceleration (purple), Collisionless Shockwave Acceleration (CSWA) and Magnetic Vortex Acceleration (MVA) (yellow), Coulomb Explosion (CE) regime (orange), and Radiation Pressure Acceleration (RPA) (red). The dashed line is a reference for the relativistic transition from opaque ($n_e/\gamma n_c > 1$) to transparent plasma ($n_e/\gamma n_c < 1$). Regions below but near this line are referred to as near-critical-density regions. Many of these advanced acceleration regimes rely on enhanced laser absorption and, therefore, electron heating. A number of microphysical processes such as strong self-focusing, laser hole boring, relativistic transparency, and plasma channel formation occur when ultra-high-intensity lasers irradiate near-critical-density plasmas, which complicates the interaction dynamics [109–114].

The planar liquid-cryogenic hydrogen jet target used for this thesis (Chapter 5) had an

initial electron density of $4.69 \times 10^{22}/\mathrm{cm}^3$ and can be used to explore several of the advanced acceleration regimes described in the following sections by varying the laser pulse shape, duration, and intensity. It is indicated in Fig. 3.13 as a vertical dotted line.

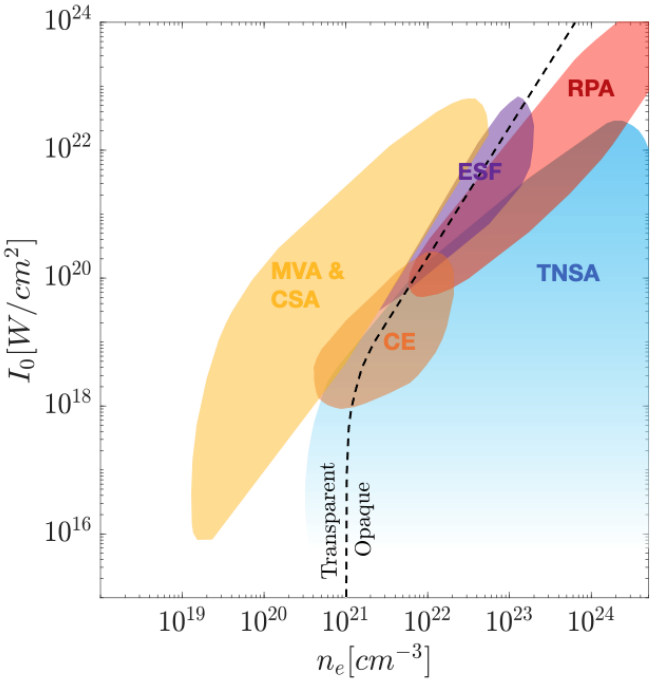

Figure 3.13: Dominant ion acceleration mechanism as a function of laser intensity and target density. The dashed line indicates the transition from over-critical density to relativistically transparent for a laser wavelength of 1053 nm. Approximate parameters for Magnetic Vortex Acceleration and Collisionless Shockwave Acceleration (MVA & CSA, yellow), Coulomb Explosion (CE, orange), Enhanced Sheath Field Acceleration (ESF, purple), Radiation Pressure Acceleration (RPA, red), and Target Normal Sheath Acceleration (TNSA, blue) are indicated. Adapted from [115].

Enhanced Sheath Field Acceleration

When a high-intensity, high-contrast, short-pulse laser interacts with a near-critical-density target, an Enhanced Sheath Field (ESF) can arise, which is alternatively referred to as *breakout afterburner* (BOA) in the literature [8–10]. ESF acceleration was studied in detail by R. Mishra et al. using 2-D and 3-D PIC simulations [5]. Ion beams accelerated by ESF are TNSA-like and exhibit boosted cut-off energies due to increased hot electron temperature. At early times, hot electrons are accelerated into the target by the ponderomotive force, thus establishing a strong electrostatic field at the rear surface of the target as in the case of TNSA. The target begins to expand rapidly due to the high electron temperature, and this causes the electron density to rapidly drop. If the plasma transitions from opaque to relativistically transparent near the peak of the laser pulse, the laser passes through the

plasma and can efficiently reheat the hot electron population in the sheath region. This transition occurs when $n_e \simeq \gamma n_c$ where $\gamma = (1 + a_0^2/2)^{1/2} \approx a_0/\sqrt{2}$ for $a_0 \gg 1$. The range of validity of this approximation is shown graphically in Fig. 3.14.

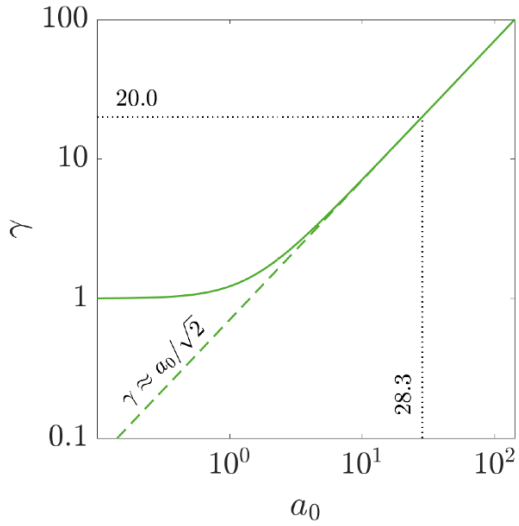

Figure 3.14: Graphical verification of the range of validity for the approximate form of the relativistic gamma factor $\gamma \approx a_0/\sqrt{2}$ when $a_0 \gg 1$.

To determine the optimal initial target density profile, we consider the 1-D expansion of an isothermal plasma slab. First, conservation of mass gives the condition that

$$n_{e0} L_0 = n_e L \tag{3.142}$$

where n_e and L are respectively the peak electron density and the target thickness measured at a later time t. The expansion of the target can be approximated by the ion acoustic velocity $c_{s,hot}$ given by

$$c_{s,hot} = \sqrt{\frac{Z k_B T_{e,hot}}{m_i}} \tag{3.143}$$

where the hot electron temperature is estimated using the ponderomotive scaling (Eqn. 3.134). This causes n_e to drop and the thickness of the target to increase as a function of time. The latter can then be expressed as $L \simeq L_0 + 2c_s t$. The optimal areal density is found to exist when the target transitions from opaque to transparent at the peak of the laser pulse.

As a function of the initial target and laser parameters, this condition is

$$\frac{n_{e0}}{n_c}L_0 \approx c\tau_L\sqrt{\frac{a_0^3}{2^{3/2}}\frac{Zm_e}{m_i}} \approx 0.59c\tau_L\sqrt{a_0^3\frac{Zm_e}{m_p}} \propto \tau_L I^{3/4}. \tag{3.144}$$

The ion beam produced through ESF acceleration exhibits a more than doubling of cut-off energy and a ∼20% increase in hot electron temperature as shown in Fig. 3.15.

If the target is too thick, the onset of transparency is delayed so that minimal to no light reaches the rear surface of the target to re-heat the electron population. This is the limit at which ESF acceleration becomes TNSA. In contrast, a target that is too thin will become transparent prematurely and allow the laser to pass through the target, thereby forming a plasma channel. This is the limit at which ESF is expected to become magnetic vortex acceleration.

In the absence of a prepulse, another condition is that the laser pulse duration τ_L must be longer than the time required for the plasma density to decrease to the relativistic transparency threshold density. This leads to an expression for the optimal pulse duration given by

$$\tau_L > \frac{L_0}{2c_{s,hot}}\left(\frac{\sqrt{2}n_{e0}}{a_0 n_c} - 1\right). \tag{3.145}$$

ESF is expected to be the dominant laser-driven ion acceleration mechanism in the experiments presented in Chapter 8.

Radiation Pressure Acceleration

Radiation pressure acceleration (RPA) occurs at higher laser intensities than TNSA and with thinner targets. It has attracted significant interest due to its potential to produce quasi-monoenergetic ion beams.

At highly relativistic laser intensities, radiation pressure on a steep overdense plasma-vacuum interface can produce ion motion on the timescale of the pulse duration due to radiation pressure. Allowing possible transmission and attenuation through the target, the effective radiation pressure is given by

$$p_{\text{rad, eff}} = (1 + R - T)I/c = (2R + A)I/c \tag{3.146}$$

where R, T, and A are respectively the reflection, transmission, and absorption coefficients of the target as obtained from the Fresnel equations. These quantities are related by the condition that $R + T + A = 1$. Radiation pressure is directly proportional to intensity and is highest for targets that remain opaque to the laser. Consequently, RPA is dominant for

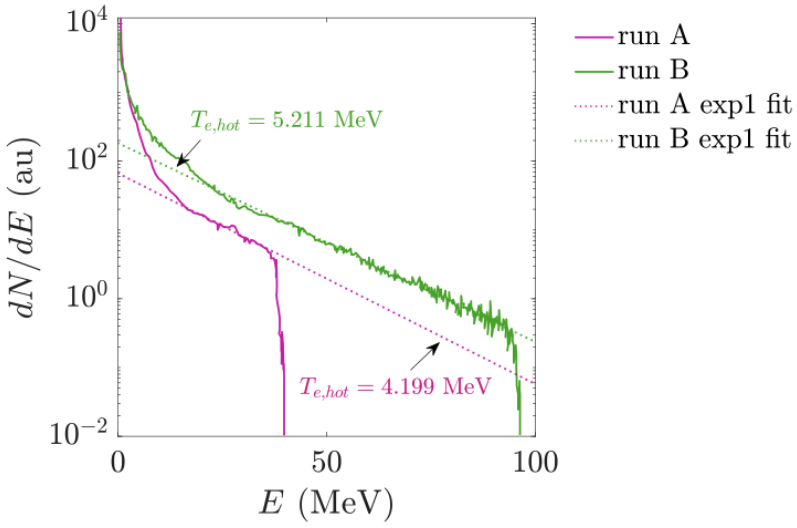

Figure 3.15: Laser-accelerated proton spectra from a 1 µm laser focused to a 5 µm spot size on a 2.5 µm thick hydrogen target with sharp boundaries and an initial density of $15n_c$ in the ESF acceleration regime (run A, green) compared to TNSA acceleration from target with an initial density of $23n_c$ that remains overcritical throughout the laser-plasma interaction (run B, pink). Adapted from [5].

the highest intensities when the target remains overcritical as shown in Fig. 3.13. There are two distinct regimes of RPA, namely the light sail regime and the hole boring regime.

In the light sail regime [6, 116], the laser accelerates nearly all electrons from the bulk of a very thin overdense target (<100 nm), and this results in a strong electrostatic field. This field accelerates all the ions lagging behind to form a quasi-monoenergetic ion layer that acts as a moving mirror and co-propagates with the laser pulse. Recently, Chou et al. showed that in this regime, the development of the Rayleigh Taylor-like instability (RTI) at the front surface is the dominant electron heating mechanism and that it contributes to the energy spectral bandwidth. They found that the RTI growth rate sets upper bounds on the laser pulse duration and the intensity at which quasi-monoenergetic ion beams will still be produced [117].

The other regime results primarily from a pressure imbalance between the radiation pressure p_{rad} from the laser and the plasma electron pressure p_e. When this imbalance occurs, a laser with finite spot size and high irradiance can bore a hole several wavelengths deep through an overdense plasma on the sub-ps timescale. The relevant pressure ratio is

$$\frac{p_{rad}}{p_e} = \frac{(2R + A)I_0/c}{n_e k_B T_e} \simeq \frac{660 I_{18}}{160 n_{23} T_{keV}}. \tag{3.147}$$

When the radiation pressure ratio p_{rad}/p_e is less than 1, the plasma expands towards the incoming laser pulse in what is known as the *plasma blowoff regime*. If instead $p_{rad}/p_e > 1$, the plasma is pushed preferentially inward toward the center of the laser focus.

We can derive the hole boring velocity from the 1-D continuity and momentum equations

$$\frac{\partial \rho}{\partial t} + \frac{\partial}{\partial z}(\rho u) = 0 \tag{3.148}$$

$$\frac{\partial \rho u}{\partial t} + \frac{\partial}{\partial z}(\rho u^2) + \frac{\partial}{\partial z}(Z p_e + p_{rad}) = 0 \tag{3.149}$$

where ρ is the plasma electron fluid density and u is the 1-D plasma electron fluid velocity. In the frame of the hole boring front with $\mathcal{E} = z - u_{\mathrm{HB}} t$, the fluid quantities are stationary in time so that the time derivatives are zero. Restricting the laser absorption to η_a and assuming $p_{rad} \gg Z p_e$, integration of the equations across the steep vacuum-target interface leads to

$$\rho u = \mathscr{C} \tag{3.150}$$

$$\rho u^2 = p_{rad} = \frac{I_0}{c}(2 - \eta_a)\cos\theta \tag{3.151}$$

where $\mathscr{C}$ is a constant.

We can then rearrange and solve for u_{HB} to get

$$\frac{u_{\mathrm{HB}}}{c} = \left[\frac{(2-\eta_a) I_0 \cos\theta}{2\rho c}\right]^{1/2} \tag{3.152}$$

$$= \left[\left(\frac{Z m_e}{M}\right)\left(\frac{n_c}{n_e}\right)\left(\frac{(2-\eta_a)\cos\theta}{4}\right)\left(\frac{I_{18}\lambda_{\mu m}^2}{1.37}\right)\right]^{1/2} \tag{3.153}$$

where θ is the angle of incidence of the laser. Computing for a fully ionized hydrogen plasma with an initial electron density of $\sim 46.8 n_c$ and laser intensity from 10^{20} (10^{21}) W/cm^2 at normal incidence leads to a hole boring velocity of $0.02c$ ($0.07c$). During a 150 fs laser pulse, the shock front propagates 0.83 (2.64) µm. This effect is therefore very important at early times for interactions with planar cryogenic hydrogen and deuterium jets with thicknesses below 1 µm.

Collisionless Shock Acceleration

Collisionless shockwave acceleration (CSWA) [118, 119] can occur in comparatively thicker near-critical to transparent targets driven at relativistic intensities with large focal spots and longer (>100 fs) laser pulses.

At the front surface of the target, the laser acts through radiation pressure like a piston

to push the plasma inward (Eqn. 3.13) via the hole boring effect [120]. The piston velocity u_p is estimated using conservation of momentum as

$$u_p = \left(\frac{I}{m_i n_i c}\right)^{1/2} = \left(\frac{Z}{A}\frac{m_e}{m_p}\frac{n_e}{n_c}\right)^{1/2} a_0 c. \tag{3.154}$$

In this regime, Weibel-type instabilities arising from the filamentation between the laser-produced hot electrons and the cold return current become dominant. The combination of magnetic turbulence and electrostatic fields associated with $T_e \gg T_i$ can slow down plasma flow to produce a collisionless shock with $\nu_{sh} \simeq u_p$ in the rear plasma density gradient. If the thermal velocity of the background ions is smaller than the shock velocity, upstream ions are reflected at the shock front and accelerate the ions to the velocity $\nu_{ions} \approx 2u_p$. The energy of the reflected ions is then given by

$$m_i(2u_p)^2/2 = 2m_i\nu_{ions}^2 = 2ZM^2T_{e,hot}. \tag{3.155}$$

A nearly constant shock speed can be maintained by tuning the plasma density profile to produce a quasi-monoenergetic ion beam [10], which is highly desirable for many applications.

Magnetic Vortex Acceleration

Magnetic Vortex Acceleration (MVA) occurs when a high-intensity laser penetrates a near-critical density target to form a low electron density channel as electrons are ejected from the laser propagation axis by the ponderomotive force. It is a promising scheme for laser-driven ion acceleration since the proton beam is highly collimated and does not exhibit energy-dependent divergence like TNSA. The conversion efficiency from laser energy to protons depends on the coupling of the laser energy to the self-generated channel in the target.

For petawatt-class lasers, this acceleration regime provides a favorable scaling of the maximum ion energy with the laser power. The megatesla-level magnetic fields generated by the laser-driven channel through the target may lead to proton acceleration up to several hundred MeV.

Following the derivation by Park et al. [11], the waveguide model can be used to describe the laser fields within the channel. In a waveguide with cylindrical geometry, the magnetic field is described by the Transverse Electric (TE) mode with $E_z = 0$, $H_z = Aj_1(\kappa r)\cos(\omega t - kz)$ where $\kappa = 1.84/R_{ch}$ is the radius of the channel given by

$$R_{ch} = \frac{\lambda}{2}\sqrt{\frac{a_{ch}n_e}{n_c}} = \frac{\lambda}{\pi}\left(\frac{n_c}{n_e}\right)^{1/3}\left(\frac{2P}{KP_c}\right)^{1/6}. \tag{3.156}$$

The normalized vector potential in the channel a_{ch} is then given by

$$a_{ch} = \left(\frac{2Pn_e}{KP_c n_c} \right)^{1/3} \tag{3.157}$$

where K = 1/13.5 is a geometrical factor, P is the laser power, and $P_c = 2m_e^2 c^5/e^2 = 17$ GW is the characteristic power for self-focusing.

The maximum ion energy in the MVA scheme is determined by several parameters such as the target density, target thickness, laser power, and laser focal spot size. The optimum condition is obtained by equating the laser energy inside the channel W_p to the total electron energy W_e after interaction with the laser pulse according to

$$W_p = W_e \tag{3.158}$$

$$\pi R_{ch}^2 \tau a_{ch}^2 m_e c n_c K = \pi R^2 L_{ch} n_e \varepsilon_e \tag{3.159}$$

$$R_{ch}^2 \tau a_{ch}^2 m_e c c n_c K = R^2 L_{ch} n_e (m_e c^2 a_{ch}) \tag{3.160}$$

where the average energy an electron acquires in the channel is given by $m_e c^2 a_{ch}$. We can then rearrange to find optimal electron density in units of critical density as

$$\frac{n_e}{n_c} = \sqrt{2} K \sqrt{\frac{P}{P_c}} \left(\frac{L_p}{L_{ch}} \right)^{3/2} \tag{3.161}$$

where $L_p = c\tau$ is the laser pulse length and τ is the laser pulse duration. If we consider a laser similar to the Texas Petawatt Laser (135 J, 135 fs, $P = 1$ PW) with $L_p = 43.5$ µm together with $L_{ch} = 20$ µm, then the optimal target density is $7.92 n_c$. This regime is straightforwardly accessed by pre-expanding the planar cryogenic hydrogen jet ($n_{e,i} = 46.8 n_c$) with a prepulse heater beam.

Coulomb Explosions

Lastly, Coulomb Explosions (CE) occur when the target dimensions of an overcritical target are of the same order as the laser wavelength. These are typically referred to as *mass-limited targets*. In this case, the laser can expel all of the electrons within the target. The ions are then accelerated by the space-charge field. The maximum electrostatic field that can be generated for a target depends only on the target diameter and the initial electron density. This regime is accessed with small clusters formed in low-temperature gas jets [121].

According to Gauss's theorem, $E(r)$ increases as a function of r with r measured from

the center of the cluster according to the equation of motion

$$m_i \frac{d^2 r_i(t)}{dt^2} = \frac{ZeQ_i}{r_i^2(t)} = \frac{(Ze)^2 N}{r_i^2(t)} \left(\frac{r_i(0)}{R} \right)^3 . \tag{3.162}$$

This suggests that the acceleration of ions located in the outer layers will be higher than those located in the inner layers. Thus, ions in the layer with the initial radius $r_i(0)$ gain the energy $\mathcal{E} = (Ze)^2 N r_i^2(0)/R^3$, which has a maximum value of $\mathcal{E}_{max} = (Ze)^2 N/R$. The energy spectrum is distinct from other mechanisms and is given analytically by

$$\frac{dN}{d\mathcal{E}} = \frac{dN/dr_i(0)}{d\mathcal{E}/dr_i(0)} = \frac{3N}{2} \frac{\mathcal{E}^{1/2}}{\mathcal{E}_{max}^{3/2}} \tag{3.163}$$

where $\mathcal{E} < \mathcal{E}_{max}$, $dN = 4\pi n_0 r_i^2(0) dr_i(0)$, and $n_0 = N/(4\pi R^3/3)$. If we consider a liquid hydrogen cluster that is 10 nm in diameter, the total number of protons that can be accelerated is 2.46×10^5. The CE mechanism accelerates 5 or more orders of magnitude fewer protons per shot compared to TNSA. Additionally, the protons are emitted isotropically in 4π. Consequently, it is the least desirable acceleration mechanism for applications.

3.9 Exemplary laser and plasma parameters

Parameter	Value
ω_0	1.79×10^{15} rad/s
I	$\sim 10^{21}$ W/cm^2
λ_0	1053 nm
τ_L	135 fs
a_0	28.3
γ	20.0
$n_e/\gamma n_c$	2.34
ω_{pe}	1.22×10^{16} rad/s
$\gamma\omega_{pe}$	2.44×10^{17} rad/s
ω_{pi}	6.64×10^{12} rad/s
Φ_p	13.96 MeV
T_e	$\sim$100 keV
$T_{e,hot}^{\text{Haines}}$	3.27 MeV
θ	31.33°
$\ln \Omega$	9.41
$\lambda_D(T_e)$	10.95 nm
$N_D(T_e)$	2.58×10^5
v_{ei}	3.53×10^{10}/s
$1/v_{ei}$	28.3 ps
$c_s(T_e)$	3.1×10^6 m/s
$c_s(T_e)\tau_L$	419 nm
$c_s(T_{e,hot})$	1.63×10^7 m/s
$c_s(T_{e,hot})\tau_L$	2.20 μm
u_{HB}	0.0651c
$u_{HB}\tau_L$	2.635 μm

Table 3.2: Laser and plasma parameters for a 1053 nm, 135 fs laser focused to an intensity of 10^{21} W/cm^2 on a liquid density hydrogen slab.

Chapter 4
High-power Short Pulse Lasers

In recent years, petawatt-class (10^{15} W) laser systems have become increasingly common [122–124], and the commissioning of the first 10 PW beamlines has already begun at the Extreme Light Infrastructure Nuclear Physics (ELI-NP) in Romania [125]. When focused to the diffraction limit with a small $f_{\#}$ optic (e.g. 1 – 4 µm FWHM), peak laser intensities exceeding 10^{23} W/cm^2 have now been demonstrated for the first time [126].

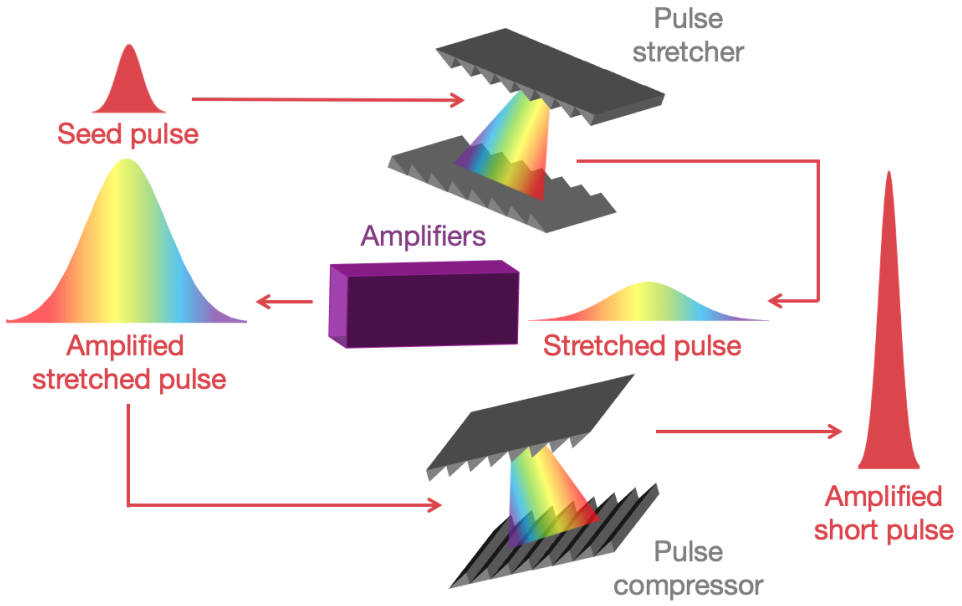

Figure 4.1: Illustration of the Chirped Pulse Amplification (CPA) technique.

4.1 Chirped Pulse Amplification (CPA)

Petawatt laser systems rely on the chirped pulse amplification (CPA) technique that is shown in Figure 4.1 and that was first demonstrated by Strickland and Mourou [1]. In CPA, a low-energy short pulse with spectral bandwidth $\Delta\lambda$ is stretched in time by a prism or a diffraction grating pair before passing through a series of high-gain amplifiers. Compared to the initial short seed pulse, significantly higher amplification of the stretched, nanosecond pulse is possible. Since the diffraction gratings typically have the lowest damage threshold within the laser chain, the beam diameter is sequentially increased using re-collimating telescopes, often to >30 cm for petawatt lasers. The beam is then passed through a second grating pair

to recompress the pulse [127]. A typical pulse generated from a CPA laser is depicted in Fig. 4.2 (a). It often consists of an Amplified Spontaneous Emission (ASE) pedestal with the same duration as the pump pulse, discrete prepulses, and a pedestal around the main laser pulse due to imperfect compression. In this thesis, typical values for the nanosecond contrast and the contrast 10 ps before the main pulse before implementing a pulse contrast enhancement technique are 10^{-11} and 10^{-5} respectively.

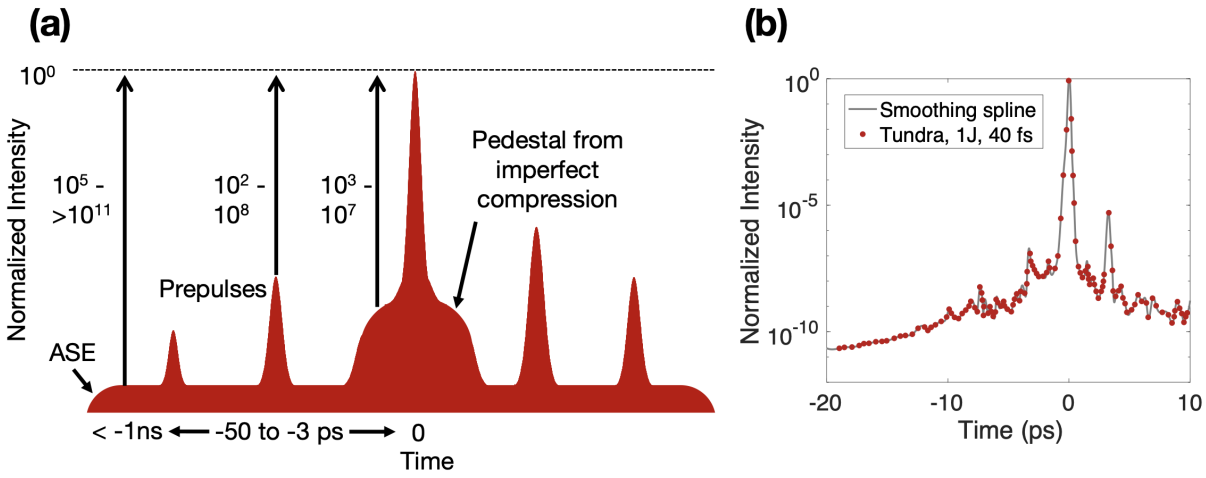

Figure 4.2: (a) Schematic of a typical CPA laser pulse. The Amplified Spontaneous Emission (ASE) pedestal and discrete prepulses typically observed picoseconds to nanoseconds prior to the main pulse are indicated. (b) Pulse contrast curve of the MEC short-pulse laser measured at full laser power (1 J, 40 fs) using a Tundra 3$^{\text{rd}}$ order autocorrelator measurement is courtesy of E. C. Galtier. The contrast is better than 10^{-10} at -30 ps and 10^{-8} at -5 ps.

4.2 Optical Parametric Chirped Pulse Amplification (OPCPA)

Not long after its first demonstration, the CPA technique was combined with optical parametric amplification (OPA) in optical parametric CPA (OPCPA) [128, 129]. In OPCPA, a high-energy nanosecond duration pump pulse with initial frequency ω_p is phase-matched with a stretched seed pulse with frequency ω_s in a non-linear crystal such as Barium Borate (BBO) or Potassium Dihydrogen Phosphate (KDP). Parametric amplification, in which the pump photons are converted to photons with the same frequency as the seed pulse, can only occur when there is temporal overlap between the stretched seed pulse and pump pulse which eliminates the amplified spontaneous emission (ASE) otherwise present in CPA [124]. Residual energy is carried away in a beam referred to as the *idler beam* with frequency ω_i satisfying $\omega_p = \omega_s + \omega_i$. An illustration of the OPCPA technique is shown in Fig. 4.3. The main advantage of OPCPA is that noise on the phase and amplitude of the pump pulse is

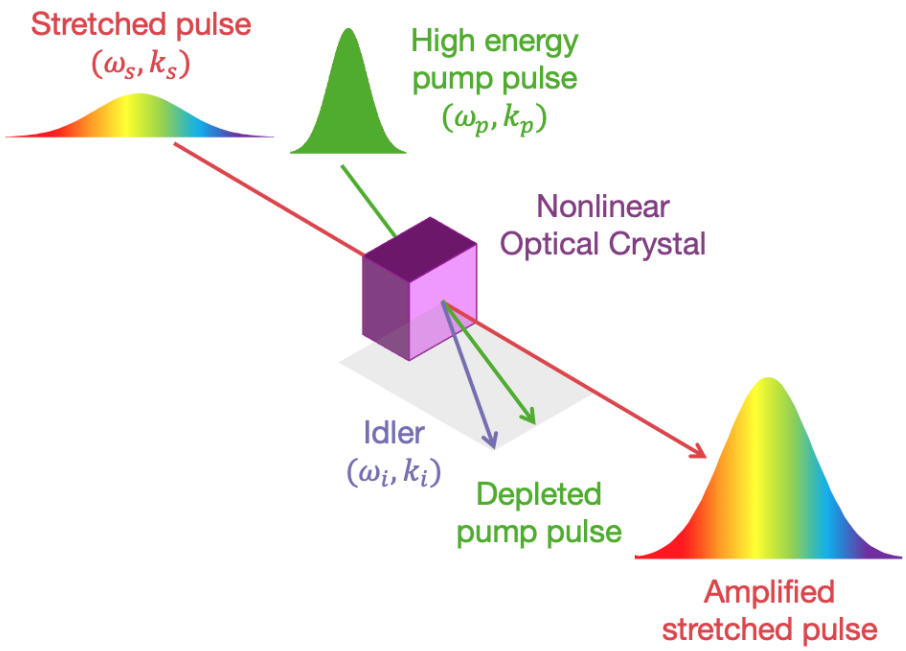

Figure 4.3: Illustration of the Optical Parametric Chirped Pulse Amplification (OPCPA) technique.

transferred onto the idler pulse. In addition, the nonlinear process between the pump and beam in the nonlinear optical crystal results in improved laser pulse contrast. The gain bandwidth in non-linear crystals can be very large, which allows ultra-short high energy pulses to be produced with fewer amplification stages than are required with conventional CPA [122–124].

The three high-power laser systems utilized in this thesis were (1) the DRACO Ti:Sapphire laser [130, 131], (2) the Nd:Glass Titan laser [132], and (3) the Mixed Nd:Glass Texas Petawatt laser [133, 134].

4.3 Measuring laser pulse duration and contrast

Typically, the pulse duration of a short pulse laser system is measured using a 2^{nd} order autocorrelation. While many variations have been developed, the basic operating principle is that the laser pulse is split into two beams. One beam is delayed in time with respect to the other, and then they are spatially overlapped in a nonlinear optical medium such as a second-harmonic-generation (SHG) crystal. In this case, measurement of the second-harmonic emission vs. delay provides the intensity autocorrelation [135]. For a laser pulse with time-dependent intensity $I(t) = |E(t)|^2$, the second order intensity autocorrelation is

given by

$$A_2(\tau) = \int_{-\infty}^{\infty} I(t) \cdot I(t+\tau) dt, \tag{4.1}$$

where τ is the time delay. The autocorrelation does not have a unique laser pulse inversion. By assuming a pulse intensity shape (e.g. Gaussian or sech^2(t)), the pulse width can be determined. Additionally, the function $A_2(\tau)$ is symmetric about $\tau = 0$ and, as such, pre- and post-pulse shapes are indistinguishable.

In contrast, third-order autocorrelation results in an asymmetric autocorrelation function, $A_3(\tau)$ defined as

$$A_3(\tau) = \int_{-\infty}^{\infty} I^2(t) \cdot I(t+\tau) dt. \tag{4.2}$$

The asymmetry allows pulse characteristics before the main pulse to be distinguished from those after the main pulse.

Unlike the dynamic range of a second order autocorrelation which is often limited by scattered light, the dynamic range of third order autocorrelation depends on the damage thresholds and the sensitivity of the detection system [136]. With sophisticated designs, dynamic ranges exceeding 10^{10} are possible as shown in Fig. 4.2 (b). The pulse contrast is then defined as the ratio between the intensity at time t and the peak intensity I_0 according to [137–139]

$$K(t) = I(t)/I_0. \tag{4.3}$$

The onset of plasma formation occurs at approximately 10^{11} W/cm^2 for solid-density materials [95]. Therefore, for peak intensities in excess of 10^{21} W/cm^2 on target, a pulse contrast of better than 10^{-10} is necessary to remain below the ionization threshold. We note however that intensity and fluence of the laser prepulse should be considered since the thresholds for preplasma generation depend on both. When a high-power short pulse laser is tightly focused on a micron-thick low-Z target, it is ionized and begins to hydrodynamically expand on the picosecond timescale. To interact with a planar plasma slab at its initial density, the laser-pulse intensity should remain below the ionization threshold until as close to the rising edge of the main pulse as possible.

It is difficult to achieve a picosecond laser-pulse contrast greater than 10^{-7} directly from the laser amplifier using CPA due to on-axis Amplified Spontaneous Emission (ASE) which lasts for the duration of the pump pulse, a picosecond pedestal around the main pulse due to imperfect compression [127, 137–139], and pre-pulses which originate from leakage from

a Pockels cell, for example. A Pockels cell is an electro-optic device that contains an optical crystal with birefringence that varies linearly with applied voltage. It can be thought of as a high-speed voltage-controlled wave plate. In high-power short-pulse laser systems, Pockels cells are often used as pulse-pickers between the seed laser and the amplification stages to reduce the repetition rate from MHz to Hz. Leakage through a Pockels cell is observed as discrete pre-pulses with a similar pulse duration as the main pulse arriving at integer multiples of the cavity round trip time.

Both the nanosecond and picosecond contrast can significantly influence the laser-matter interaction processes by altering the density and temperate from the initial target conditions before the arrival of the main laser pulse [140, 141].

4.3.1 Plasma mirrors for laser pulse contrast enhancement

Several techniques have been developed to further increase the pulse contrast of CPA laser systems including fast-switching Pockels cells or polarizers [140], pulse conversion in non-linear media (e.g. frequency doubling or cross-polarized wave generation) [142–144], ps-OPCPA [145], and self-induced plasma shuttering using plasma mirrors (PM) [137–139, 146]. In this thesis, plasma mirrors are the primary tool used to improve the laser pulse contrast, especially on the picosecond time scale.

A plasma mirror is typically a dielectric substrate such as borosilicate glass or fused silica that is anti-reflection (AR) coated. When the incident laser fluence is low, the laser pulse will be mostly transmitted. When the intensity of the pulse approaches 10^{16} W/cm^2, the surface is rapidly ionized, which causes the reflectivity to increase from negligible (e.g. $< 0.5\%$) to over 70%. The onset of the change in reflectivity of the substrate is referred to as the *trigger point*.

A schematic of a double PM is shown in Fig. 4.4. With proper placement of the PM, the ASE pedestal and pre-pulses will have a sufficiently low intensity to allow their transmission through the substrate. The leading edge of the main pulse triggers the PM. The main pulse must be sufficiently short so that it is spectrally reflected before the plasma mirror expands and is no longer optically flat.

The upper limit on wavefront aberration due to plasma expansion can be approximated by computing the plasma scale length. First, we calculate the hot electron temperature (Eqn. 3.136) and ion acoustic velocity (Eqn. 3.143) for a laser intensity of $I_0 = 10^{16}$ W/cm^2 to be 180 keV and 2.94×10^5 cm/s, respectively. Assuming isothermal expansion, the scale

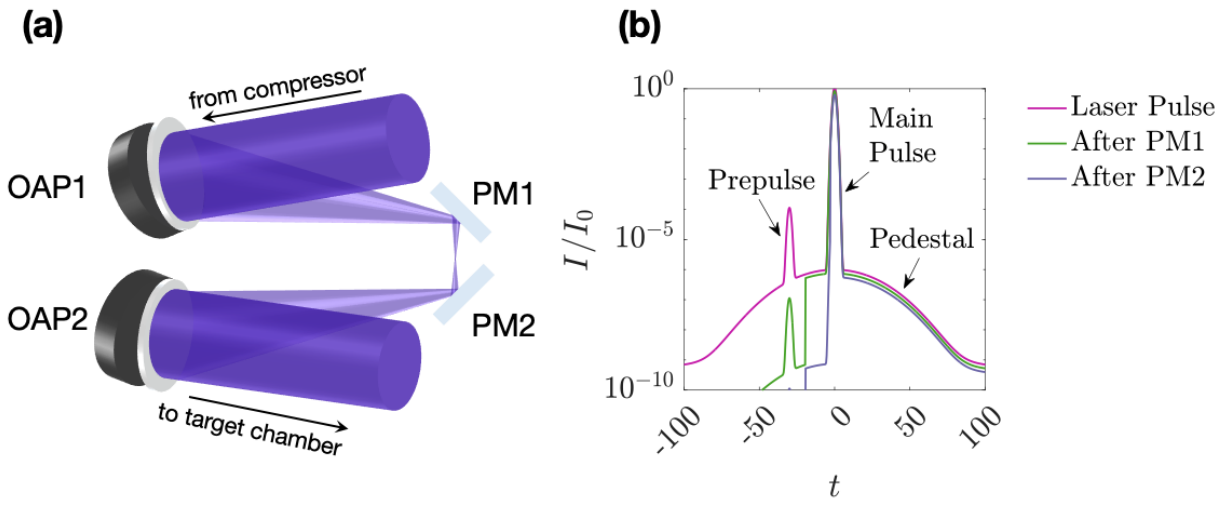

Figure 4.4: (a) Illustration of a double Plasma Mirror (PM1/PM2) including the focusing and recollimating off-axis parabolic mirrors (OAP1 and OAP2, respectively). (b) A laser pulse with an ASE pedestal and prepulse (pink); after PM1, the low fluence ASE and prepulses are transmitted, and the rising edge of the main pulse rapidly ionizes the surface, thus reflecting the remainder of the laser pulse (green); PM2 further increases the contrast (purple).

length after a time $t = 3$ ps is therefore

$$l_s = c_s \times t \tag{4.4}$$

$$= (2.94 \times 10^5 \text{ cm/s}) \times (3 \text{ ps}) \tag{4.5}$$

$$\approx 8.83 \text{ nm} \ll \lambda/20. \tag{4.6}$$

As the wavefront error increases, the focussability of the beam decreases. If the plasma mirror is triggered by a prepulse arriving tens of picoseconds before the arrival of the main pulse, the wavefront error can be substantial and result in large aberrations in the spatial profile of the focused beam. To achieve the maximum intensity on a target when using a plasma mirror, it is therefore important for the initial contrast of the pulse to be sufficiently high and for the spatial intensity profile of the beam to be relatively smooth.

The change in the pulse contrast is limited by the ratio between the reflectivity of the plasma and the reflectivity of the AR coating written as

$$\Delta K = \frac{R_{plasma}}{R_{AR}} \tag{4.7}$$

where R_{plasma} is the maximum reflectivity of the ionized plasma, typically $50\% - 80\%$, and R_{AR} is the cold reflectivity of the AR coating. By minimizing the reflectivity of the AR coating at the laser wavelength, bandwidth, and polarization, the pulse contrast enhancement

is maximized. In the specific case of a PM in a converging high-power laser beam, the AR coating should also be optimized over the range of angles of incidence in the converging beam.

An AR coating utilizes the principle of complete destructive interference by introducing a phase shift of $\lambda/4$ between the front and back surface reflections of the thin film. The condition for complete destructive interference therefore becomes

$$n_{AR} = \sqrt{n_{substrate}} \tag{4.8}$$

where n_{AR} and $n_{substrate}$ are respectively the indexes of refraction of the AR coating and substrate.

4.3.2 Beam splitting plasma mirror for 2-beam experiments

A beam-splitting plasma mirror (BSPM) was developed using the Titan short pulse laser (1053 nm, 700 fs, 130 J) in the Jupiter Laser Facility at Lawrence Livermore National Laboratory. A schematic of the BSPM is shown in Figure 4.6 (a). During standard single-beam laser operation, the main apodizer is installed before the first beam-expanding telescope and doubles as a spatial filter (SP1) to smooth the outer edge of the beam. At this location in the laser chain, the major and minor beam axes measure 9.1 mm and 7.8 mm, respectively. The beam was expanded to 18.1 mm by 15.5 mm after SP1. To deliver a split beam to the target chamber for the BSPM, a 1.4 mm FWHM split-beam apodizer was installed at a relay plane before SP2. With both apodizers installed, the on-target laser energy was measured using a full aperture calibrated in-vacuum calorimeter. The alignment of the split on the beam was adjusted to deliver the same energy in each beam with a 50/50 splitting ratio, but the platform is continuously tunable up to approximately a 90/10 splitting ratio by translating the split-beam apodizer.

The final relay plane occurs after compression, 200 mm beyond the last transport mirror in the vacuum compressor or 6520 mm ahead of the off-axis parabola (OAP), which results in a smooth, bar-like, vertical shadow that is ∼20 mm wide. The near field profile of the beam before and after compression, imaged through leaky mirrors at full laser energy, are shown in Fig. 4.5 (b) and (c), respectively. The near field profile was measured at full energy by imaging the diffuse scatter from a 30×30 cm^2 Teflon screen installed 62.1 cm after focus in the diverging beam after the BSPM using a long working distance zoom lens and a CCD camera is shown in Fig. 4.5 (d). A square nickel mesh was fixed to the Teflon screen to calculate the spatial calibration, determine the projection viewing angle, and estimate the resolution and blurring due to the diffuse scatter.

In the target chamber, the apodized beam was focused using a single f/3 off-axis parabola

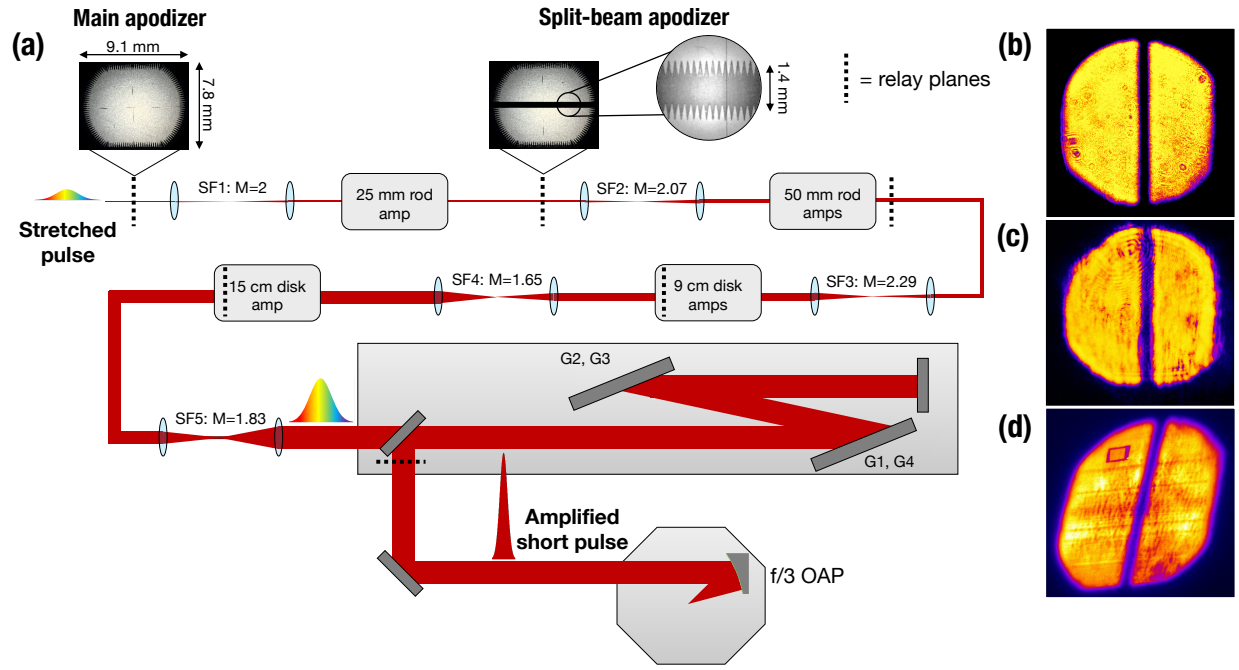

Figure 4.5: (a) Schematic of Titan short pulse laser architecture with the main and split-beam apodizers shown as inset photos installed before SF1 and SF2, respectively, and the split-beam near field profile at full energy, (b) before compression and after SF5, (c) after compression, and (d) through the focus in the target chamber off a Teflon screen. The distortion is due to the viewing angle of the imaging system. The square on the upper left quadrant of the beam is a nickel mesh used for resolution and projection calculations.

(OAP) such that the apodizer shadow decreased from 20 mm to 1.7 mm where the two halves of the beam were incident on two anti-reflective (AR) coated optics serving as plasma mirrors. An illustration of the laser beam paths in the target chamber with the BSPM is shown in Fig. 4.6. The BSPM was designed for the purpose of delivering two quasi-collinear high-intensity, high-contrast laser beams with variable separation distance on a target. To align the BSPM for this purpose, the high-power alignment continuous wave (CW) laser, which co-propagates with the main laser, was used to set the lateral position of the optics using infrared viewers. The separation between the two optics and tip-tilt was then corrected to reconstruct the inverted near-field profile on the Teflon screen. In the first part of the alignment, the two halves of the beams were overlapped spatially, and the focal position of one of the optics was independently scanned to put both beams in the best focus at the same position.

The two laser foci of the unamplified laser were relay imaged onto a 12-bit CCD camera with a single long working distance f/1.4 objective with a magnification of 26.8 (0.2402 $\pm$0.001 µm/pixel). The objective was normalized and aligned to the mid-point between the two laser focal spots. We do not expect any significant imaging distortions to the foci from

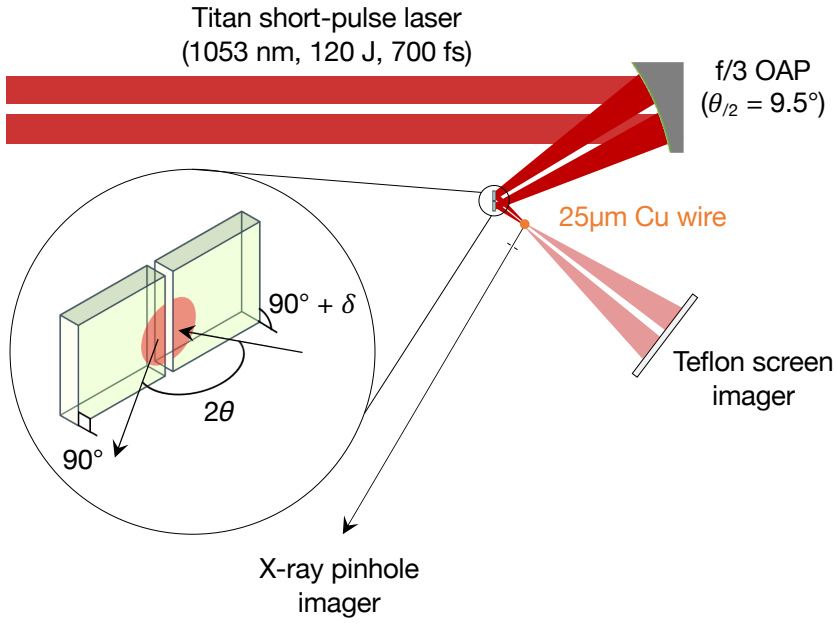

Figure 4.6: Illustration of a Beam Splitting Plasma Mirror (BSPM). Circular inset: the apodized beam is reflected from two independent AR-coated optics which have a small relative angle δ, thereby providing a controllable vertical separation at focus.

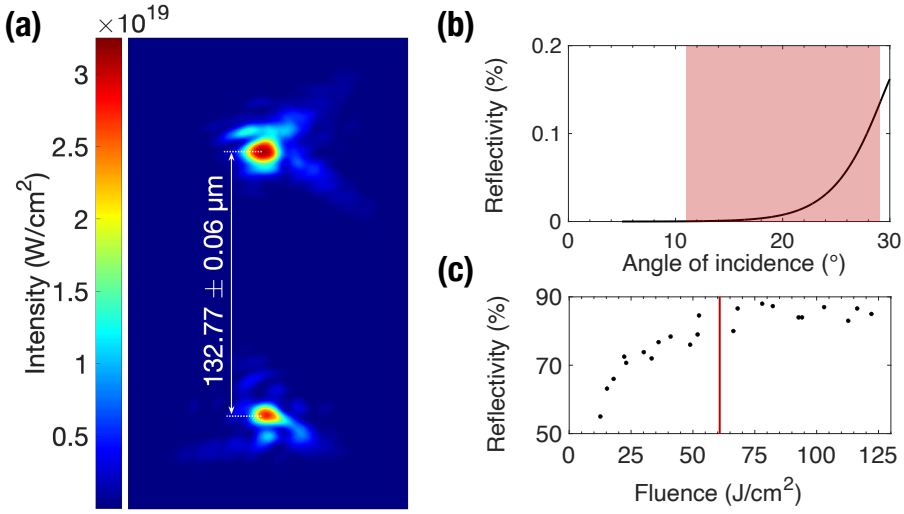

Figure 4.7: (a) High-magnification relay image of the laser foci at vacuum measured using the unamplified OPCPA front-end when reflected from the aligned Beam Splitting Plasma Mirror (BSPM). (b) Reflectivity curve of the AR coating on the BSPM optics as a function of incidence angle. The shaded red region corresponds to the range of incidence angles due to the f/3 convergence angle of the laser about the central angle of 19.5°. (c) Measurement of the PM reflectivity as a function of incident laser fluence to determine the optimal operational fluence of 55 J/cm^2 (red line).

the small angle δ relative to the single beam. After background subtraction, the predicted on-shot intensity is indicated by the color axis in Fig. 4.7. The precision in the temporal overlap is estimated to be better than twice the Rayleigh range, $2z_R = 25.4\,\mu\text{m}$ (Eqn. 3.20), when focused with an f/3 OAP , which corresponds to ∼85 fs. By adjusting the gain on the camera, we observe interference between the two low-energy halos of the foci when they are overlapped in time, which occurs for the full pulse duration (τ_L = ∼700 fs). However, we confirmed that the fringe visibility of the two-beam interference was maximized when both beams were at best focus. Independent astigmatism correction of the focal spots was not possible with the current BSPM design, so the two focal spot diameters were larger than the focal spot diameter associated with the fully optimized single-beam configuration of the Titan laser. Finally, once temporal and spatial overlap were obtained, a small angular offset δ was applied to one of the beams in order to set the separation distance between the two beams on target.

At the time of these measurements, the BSPM consisted of manual translation, tip-tilt, and rotation stages. Successful alignment of the system at air required compensation for the beam distortion introduced by a wedged vacuum window located immediately before the target chamber since the wedged window is only removed for full energy shots when the target chamber is at vacuum.

The AR coating on the BSPM optics was optimized to provide low, relatively uniform reflectivity (less than 0.3%) across the laser bandwidth and converging laser cone angle (Fig. 4.7 (b)). From the ratio of the plasma reflectivity to that of the cold non-ionized AR coating, the change in the pulse contrast is estimated to be greater than 1600. We note that there is a threefold difference in the cold reflectivity of the outermost rays compared to the central ray. The BSPM was designed to operate at an angle of incidence of 19.5°, which aligned the transmitted laser light with a diagnostic port on the vacuum chamber. A fluence versus reflectivity scan was performed by varying the distance of the BSPM from focus while keeping the laser energy constant. The results are shown in Fig. 4.7 (c) and summarized in Table 4.1.

We observe a steep decrease in reflectivity at fluences less than approximately 40 J/cm^2. The reflectivity plateaus to 85% at fluences greater than 70 J/cm^2. An operational fluence of 55 J/cm^2 was selected, which corresponds to a maximum intensity of 7.9×10^{13} W/cm^2. Images of the beam profile after the BSPM at full energy showed no significant degradation from the BSPM.

An optimal operational fluence, maximizes the laser-pulse contrast enhancement, minimizes spherical aberrations, and is robust to shot-to-shot variations in laser energy. If the PM is operated at too high of laser intensity, there will be decreased focusability of the

Shot No.	Energy (J)	Fluence (J/cm^2)	Reflectivity
T1029181210	100.5	112.7	0.83
T1029181500	131.0	122.1	0.85
T1029181546	113.4	103.0	0.87
T1029181641	109.1	92.7	0.84
T1029181705	110.1	94.1	0.84
T1029181759	121.4	78.0	0.88
T1030181021	115.5	66.3	0.80
T1030181208	102.4	33.3	0.72
T1030181330	117.3	48.9	0.76
T1030181530	107.6	51.9	0.79
T1030181634	83.8	18.0	0.66
T1121181513	86.4	12.6	0.55

Table 4.1: Summary of full-energy shots used to determine the optimal operational fluence of a single plasma mirror installed on the Titan short pulse laser.

reflected beam due to spherical aberrations. This typically occurs for intensities in excess of 10^{16} W/cm^2 on the plasma mirror.

To confirm the separation distance between the two beams on a target during a full-energy shot, a pinhole x-ray imager was used. It consisted of a 20 µm-diameter platinum-iridium pinhole at a distance of 30 ± 2 mm from the target followed by a 1 mm-thick tapered ∼50 µm-diameter tungsten pinhole to reduce X-ray background. An imaging plate (Fuji BAS-TR) wrapped in 13 µm aluminum foil was then mounted at a distance of 60.5 mm from the pinhole, which produced a geometric magnification of 20.1 ± 0.2.

A 25 µm-diameter copper wire was used as the laser target for the proof-of-principle demonstration of the BSPM. The dominant X-ray source expected from the interaction is 8.048 keV corresponding to the K-α emission line. We confirmed this by installing a 10 µm tungsten foil filter on selected shots to attenuate the K-alpha X-ray signal by 24x. The signal recorded on the IP was extracted with an image plate scanner and converted to photostimulated luminescence (PSL). It is shown to the left of the plot in Fig. 4.8. Based on the geometric magnification, the separation between the two high-intensity focal spots was 132 ± 3µm, and the dominant source of error was the uncertainty in the distance from the target to the pinhole. When compared to the separation measured in the unamplified beam case, we see no change in separation distance or pointing stability. The X-ray emission spectrum was later verified using a 1-D imaging X-ray spectrometer that spanned 280 eV and had a resolving power better than 1500 at 8.048 keV when taking into account the line-width of the Cu K-alpha but neglecting source broadening.

It is straightforward to adapt this system to deliver three or four beamlets by replacing

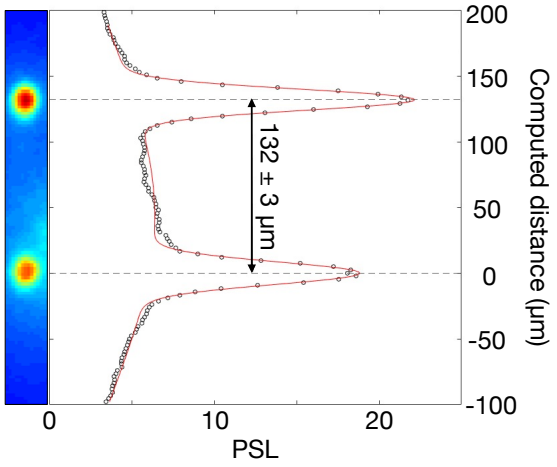

Figure 4.8: Copper K-α emission from a 25 µm Cu wire imaged with an X-ray pinhole camera to verify vertical separation of two high-intensity high-contrast laser beams produced by a BSPM at full energy.

the upstream apodizer and adjusting the number and dimensions of the PM optics. This would allow the conditions achieved using the four beamlets of the Advanced Radiographic Capability (ARC) at the National Ignition Facility to be accessed at mid-scale single-beam facilities. By simply adjusting the position of the PM optics in space, one can achieve unequal splitting or spatial offsets between the focal spots to provide different intensities on the same target or the same intensity on two spatially separated targets. With the present design, variable temporal delays can also be added independently to the beamlets upstream using an optical delay line.

Beam-splitting plasma mirrors will ultimately provide access to a long-sought-after regime of high-contrast, multi-beam interactions without the need for new, high-cost multi-beam facilities.

Chapter 5
Cryogenic Low-Z Liquid Jets

5.1 Preface

Micron-sized cryogenic jets are formed by cryogenically cooling an ultra-high purity (99.9999%) gas until it condenses to a liquid which is then injected into a vacuum through a micron-sized aperture [147]. In the case of hydrogen and deuterium, the liquid continues to cool by evaporative cooling and begins to solidify within $\sim 100\,\mu m$ before spontaneous breakup due to the Plateau-Rayleigh instability can occur. The laminarity, high flow velocity, and rapid solidification process result in a fast-replenishing, near-critical-density target that maintains the geometry of the output aperture. As a result, circular and rectangular apertures can be used to generate cylindrical and planar cryogenic jets. More recently, spherical cryogenic hydrogen droplet jets have been developed. By mechanically fixing a piezoelectric actuator to the jet aperture, a multi-MHz oscillating force can be applied directly to the source near the aperture, thus driving the controlled breakup of the cylindrical liquid hydrogen stream into a mono-dispersed droplet train.

Cryogenic low-Z jets were initially developed to address several longstanding technical challenges associated with high-repetition rate laser-driven ion acceleration: (i) rapid replacement and alignment of an ion-generating target to within ± 10 µm within 100 ms for 10 Hz pulsed laser operation, (ii) debris mitigation from plasma-based material deposition of residual target material, and (iii) producing a pure, single-species target without a hydrocarbon contaminant layer to simplify ion beam transport and manipulation.

With a typical flow velocity on the order of $100\,m/s$, cryogenic hydrogen jets are the leading contender for high (>1 Hz) to ultra-high (>1 kHz) repetition rate laser-driven ion sources. Cryogenic liquid targets are inherently debris free since any residual liquid will vaporize on contact with ambient temperature optics or hardware and then can be evacuated by the vacuum pumping system. Lastly, due to the sample gas purity and in-situ formation, laser-ion acceleration from the cryogenic liquid jets produces a single species (>99%) ion beam. Pure proton and deuteron beams have been produced from cryogenic liquid hydrogen and deuterium jets as confirmed by Thomson Parabola measurements shown in this thesis.

Not only do planar cryogenic low-Z jets satisfy these technical requirements, but 2-D/3-D particle-in-cell simulations have also identified that due to their tunable thickness and near-critical density, they are ideal targets for the systematic optimization of laser-driven ion acceleration in relativistically-enhanced acceleration regimes.

The remainder of Chapter 5 is published as: C. B. Curry, C. Schoenwaelder, S. Goede, J. B. Kim, M. Rehwald, F. Treffert, K. Zeil, S. H. Glenzer, and M. Gauthier, *Cryogenic Liquid Jets for High Repetition Rate Discovery Science*, J. Vis. Exp., **159**, e61130, (2020). The operation procedure presented in this manuscript will allow other research institutions to replicate the system for fundamental studies in laboratory astrophysics and materials science and for applications such as next-generation hybrid particle accelerators. Development and optimization of the procedure to operate the cryogenic jet system was a multi-year effort first led by S. Goede and then by J. B. Kim at SLAC National Accelerator Laboratory. M. Gauthier, J. B. Kim, and I began performing high-intensity laser-plasma experiments with the cryogenic jet at the Jupiter Laser Facility in 2015. Due to the complex and often dynamic experimental environment, we adopted a robust, empirical procedure with conservative baseline requirements for stable jet operation.

I was heavily involved in the collaborative research and development of the experimental platform. The P&ID diagram of the cryogenic jet delivery platform shown in Fig. 5.1 was systematically improved during a series of experiments at the Texas Petawatt Laser Facility in 2016, 2017, and 2019. Representative results shown in Fig. 5.4 and Fig. 5.6 were obtained during the experiment that I led as co-principal investigator and that is presented in Chapter 8. C. Schoenwaelder was responsible for jet operation during this experiment. M. Rehwald performed the jet position stability measurement for similar conditions at the DRACO laser facility at the Helmholtz-Zentrum Dresden-Rosendorf. These results are presented in Fig. 5.5. I wrote the manuscript with input from all co-authors and share first authorship with C. Schoenwaelder, a PhD student at Friedrich-Alexander Universität Erlangen-Nürnberg. Results on laser-driven ion acceleration utilizing the cryogenic jet system are presented in Chapters 7 and 8.

5.2 Abstract

This protocol presents a detailed procedure for the operation of continuous, micron-sized cryogenic cylindrical and planar liquid jets. When operated as described here, the jet exhibits high laminarity and stability for centimeters. Successful operation of a cryogenic liquid jet in the Rayleigh regime requires a basic understanding of fluid dynamics and thermodynamics at cryogenic temperatures. Theoretical calculations and typical empirical values are provided as a guide to design a comparable system. This report identifies the importance of both cleanliness during cryogenic source assembly and stability of the cryogenic source temperature once liquefied. The system can be used for high repetition rate laser-driven proton acceleration, with an envisioned application in proton therapy. Other applications include laboratory astrophysics, materials science, and next-generation particle accelerators.

5.3 Introduction

The goal of this method is to produce a high-speed, cryogenic liquid flow consisting of pure elements or chemical compounds. Since cryogenic liquids evaporate at ambient temperature and pressure, residual samples from operation at high repetition rates (e.g., 1 kHz) can be entirely evacuated from the vacuum chamber [14]. Based on the initial work by Grisenti et al. [148], this system was first developed using cryogenic hydrogen for high intensity laser driven proton acceleration [147]. It has subsequently been extended to other gases and used in a number of experiments, including: ion acceleration [149, 150], answering of questions in plasma physics such as plasma instabilities [151], rapid crystallization and phase transitions in hydrogen [152] and deuterium, and meV inelastic X-ray scattering [153] to resolve acoustic waves in argon in the Matter in Extreme Conditions (MEC) instrument at the Linac Coherent Light Source (LCLS) [154].

Until now, other alternative methods have been developed to generate high repetition rate solid cryogenic hydrogen and deuterium samples. Garcia et al. developed a method in which hydrogen is liquefied and solidified in a reservoir and extruded through an aperture [155]. Due to the high pressure required for extrusion, the minimum sample thickness demonstrated (to date) is 62 µm [156]. This system also exhibits large spatial jitter [157]. More recently, Polz et al. produced a cryogenic hydrogen jet through a glass capillary nozzle using a sample gas backing pressure of 435 psig (pounds per square inch, gauge). The resulting 10 µm cylindrical jet is continuous but appears highly rippled [158].

Presented here is a method that produces cylindrical (diameter = 5–10 µm) and planar jets with various aspect ratios (1–7 µm x 10–40 µm). The pointing jitter increases linearly as a function of distance from the aperture [150]. Fluid properties and the equation of state dictate the elements and chemical compounds that can be operated in this system. For example, methane cannot form a continuous jet due to Rayleigh breakup, but it can be used as droplets [159]. Moreover, the optimal pressure and temperature conditions vary significantly among aperture dimensions. The following paragraphs provide the theory needed to produce laminar, turbulent-free cryogenic hydrogen jets. This can be extended to other gases.

The cryogenic jet system consists of three main subsystems: (1) sample gas delivery, (2) vacuum, and (3) cryostat and cryogenic source. The system depicted in Figure 5.1 has been designed to be highly adaptable for installation in different vacuum chambers.

The gas delivery system is comprised of an ultra-high purity compressed gas cylinder, gas regulator, and mass flow controller. The backing pressure of the sample gas is set by the gas regulator, while the mass flow controller is used to measure and restrict the gas flow delivered to the system. The sample gas is first filtered in a liquid nitrogen cold trap to

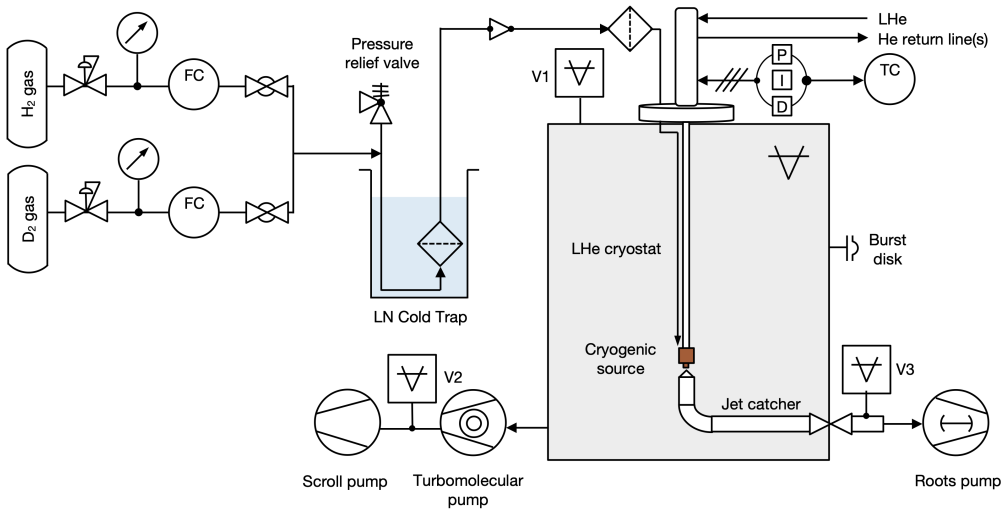

Figure 5.1: P&ID diagram of a typical cryogenic liquid jet delivery platform. The sample gas, vacuum, and cryogenic subsystems are depicted. The vacuum chamber, turbomolecular pump foreline, and jet catcher foreline pressures are monitored with vacuum gauges V1, V2, and V3, respectively. The cryostat temperature is actively regulated using a P-I-D temperature controller.

freeze out contaminant gases and water vapor. A second in-line particulate filter prevents debris from entering the final segment of the gas line.

Turbomolecular pumps backed with high pumping speed scroll pumps maintain high vacuum conditions in the sample chamber. The chamber and foreline vacuum pressures are monitored using vacuum gauges V1 and V2, respectively. It should be noted that operating the cryogenic jet introduces a substantial gas load (proportional to the total sample flow) to the vacuum system when the liquid vaporizes.

A proven method to reduce the gas load is to capture the residual liquid before bulk vaporization can occur. The jet catcher system consists of an independent vacuum line terminated by an ø800 µm differential pumping aperture located up to 20 mm from the cryogenic source cap. The line is evacuated with a pump that exhibits optimal efficiency in the 1 x 10^{-2} mBar range (i.e., a roots blower vacuum pump or hybrid turbomolecular pump) and is monitored by a vacuum gauge V3. More recently, this has allowed cryogenic hydrogen jets of up to 7 µm x 13 µm to be operated with two orders of magnitude improvement to the vacuum chamber pressure.

The sample gas enters the vacuum chamber through a custom feedthrough on the cryostat flange. A fixed length, continuous flow liquid helium cryostat is used to cool the source to cryogenic temperatures. Liquid helium is drawn from a supply dewar using a transfer line. The return flow is connected to an adjustable flowmeter panel to regulate the cooling power.

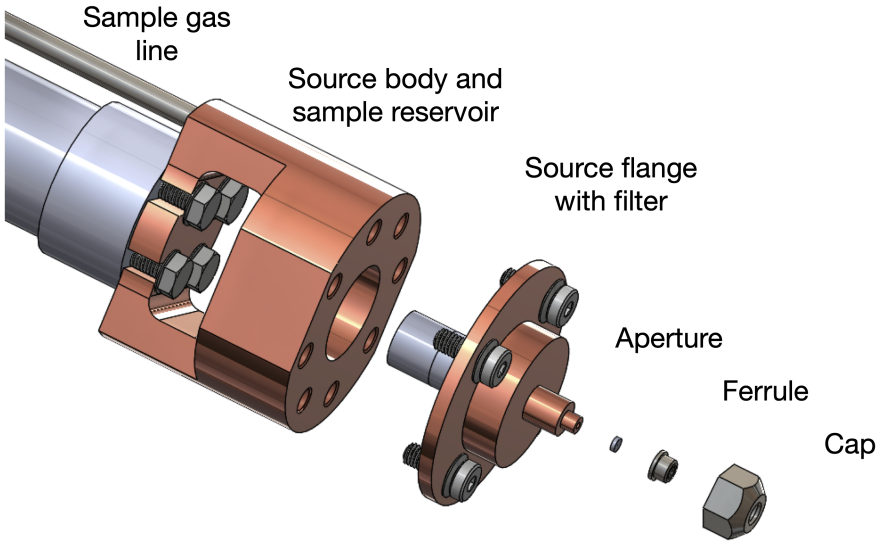

Figure 5.2: Three-dimensional exploded-view drawing of the cryogenic source assembly. Indium seals are installed between the cold finger and source body, source body and flange, and source flange and aperture.

The temperature of the cold finger and cryogenic source is measured with four lead silicon diode temperature sensors. A proportional-integral-derivative (P-I-D) temperature controller delivers variable voltage to a heater installed near the cold finger to adjust and stabilize the temperature. The sample gas enters the vacuum chamber through a custom feedthrough on the cryostat flange. Inside the chamber, the gas line wraps around the cryostat to precool the gas before connecting to a fixed gas line on the cryogenic source assembly. Stainless steel screws and a 51 µm thick layer of indium thermally seal the cryogenic source to the cold finger.

The cryogenic source (Figure 5.2) consists of six main components: a (1) sample gas line, (2) source body, (3) source flange with in-line particulate filter, (4) aperture, (5) ferrule, and (6) cap. The source body contains a void, which acts as the sample reservoir. A threaded Swagelok sintered 0.5 µm stainless steel filter prevents any debris or solidified contaminants from entering the liquid channel and obstructing the aperture. A thicker, 76 µm thick indium ring is placed between the aperture and liquid channel to increase the deformation length and reliably seal the aperture. When the cap is threaded onto the source flange, the indium is compressed to form a liquid and thermal seal. The ferrule and source cap center the aperture during installation.

There are a number of overall considerations in the initial design of a system for cryogenic liquid jets operated in the continuous, laminar regime. Users must estimate the total

cooling power of the cryostat, thermal properties of the cryogenic source design, vacuum system performance, and liquid temperature and pressure. Provided below is the theoretical framework required.

5.3.1 Cooling power considerations

1) Liquefying hydrogen [160]: the specific energy required to to liquify hydrogen from 300 K can be roughly estimated by starting with the following equation:

$$e_{liq} = L_h(T_l(p)) + \int_{T_c}^{300K} C_p(T,p)\,dT \tag{5.1}$$

Where: T_c is the temperature of the cryogenic source, C_p is the specific heat at constant pressure p, and L_h the latent heat of vaporization of H_2 at the pressure-dependent liquefaction temperature (T_l). For instance, a cryogenic hydrogen jet operated at 60 psig gas pressure and cooled down to 17 K requires a minimum of 4013 kJ/kg. With a hydrogen gas flow of 150 sccm (standard cubic centimeters per second), this corresponds to a power of 0.9 W.

It should be noted that the liquefaction process contributes only one-tenth of the total cooling power required. To reduce the heat load on the cryostat, the gas can be precooled to an intermediate temperature before entering the source body.

2) Radiative heat: to maintain the cryogenic source at a temperature T_c, the cryostat needs to compensate for radiative heating. Radiation between the cryogenic source and the vacuum chamber that are diffuse-gray enclosures, can be approximated by two enclosed cylinders or spheres using the following equation [161]:

$$P_{rad} = \frac{\sigma A_c (T_{vc}^4 - T_c^4)}{\frac{1}{\varepsilon_c} + \frac{A_c}{A_{vc}}\left(\frac{1}{\varepsilon_{vc}} - 1\right)}, \tag{5.2}$$

Where: A_c and A_{vc} are the surface area of the cryogenic source and interior vacuum chamber wall, ε_c and ε_{vc} are the material-dependent emissivities, σ is the Stefan-Boltzmann constant, and T_{vc} is the temperature of the vacuum chamber wall. For a black body, $\varepsilon = 1$ whereas a real object is a non-ideal emitter with $\varepsilon < 1$, referred to as a grey body. Radiative heating can be locally decreased by adding an actively cooled radiation shield covering a substantial part of the cryogenic source. Without radiation shielding, radiative heating contributes ~0.1 mW to the total cooling power required.

3) Residual gas conduction: although thermal radiation is dominant in ultra-high vacuum conditions, the contribution due to conduction in the residual gas becomes non-negligible

during jet operation. The liquid jet introduces substantial gas load in the chamber, resulting in an increase in vacuum pressure. The net heat loss from thermal conduction of the gas at a pressure p is calculated using the following equation:

$$P_{gas} = Aa\Omega p(T_{vc} - T_c) \tag{5.3}$$

Where: Ω is a coefficient depending on the gas species (3.85 x 10^{-2} W/cm2/K/mBar for H_2), and α is the accommodation coefficient that depends on the gas species, geometry of the source, and temperature of the source and the gas [162, 163]. When operating a cryogenic hydrogen jet at 17 K, assuming a cylindrical geometry of the source and that hydrogen is the main gas present in the vacuum chamber, gas conduction generates heat that can be estimated using the following equation:

$$P_{gas}/A \approx 10.9 \times p_{mBar} W/cm^2 \tag{5.4}$$

For example, gas conduction at a vacuum pressure of 4.2 x 10^{-3} mBar generates as much heat as thermal radiation. Therefore, the vacuum pressure is generally kept below 1 x 10^{-3} mBar during jet operation, adding a 0.55 W heat load to the system (A = 50 cm^2).

The gas load introduced in the chamber during operation is obtained by the flow of the cryogenic jet. The resulting vacuum pressure is then determined by the effective pumping speed of the vacuum system and volume of the vacuum chamber.

To operate the cryogenic jet, the cryostat has to generate sufficient cooling power to compensate for the different heat sources above (e.g. 1.55 W), not including the heat losses of the cryostat system itself. Note that the cryostat efficiency also strongly depends on the desired cold finger temperature.

5.3.2 Estimating cryogenic jet fluid parameters

To establish continuous laminar flow, several conditions must be satisfied. For brevity, the case of a cylindrical liquid flow is shown here. The formation of planar jets involves additional forces, resulting in a more complex derivation that is beyond the scope of this paper [164].

1) Pressure-speed relationship: for incompressible liquid flows, conservation of energy yields the Bernoulli equation, as follows:

$$\frac{1}{2}\rho v^2 + \rho g z + p = const. \tag{5.5}$$

Where: ρ is the fluid atomic density, v is the fluid velocity, gz is gravitational potential energy, and p is the pressure. Applying the Bernoulli equation across the aperture, the functional relationship between the jet velocity and sample backing pressure can be estimated using the following equation:

$$v \simeq \sqrt{2p/\rho} \tag{5.6}$$

2) Jet operation regime: the regime of a cylindrical liquid jet can be inferred using the Reynolds and the Ohnesorge numbers. The Reynolds number, defined as the ratio between the inertial and viscous forces within the fluid, is calculated using the following equation:

$$R_e = \frac{\rho v d_0}{\eta} \tag{5.7}$$

Where: ρ, v, d_0, and η are the density, speed, diameter, and dynamic viscosity of the fluid, respectively. Laminar flow occurs when the Reynolds number is less than 2,000. Similarly, the Weber number compares the relative magnitude of the inertia to the surface tension and is calculated using the following equation:

$$W_e = \frac{\rho v^2 d_0}{\sigma} \tag{5.8}$$

Where: σ is the surface tension of the liquid. The Ohnesorge number is then calculated as follows:

$$Oh = \frac{\sqrt{W_e}}{R_e} \tag{5.9}$$

This velocity-independent quantity is used in combination with the Reynolds number to identify the four liquid jet regimes: (1) Rayleigh, (2) first wind-induced, (3) second wind-induced, and (4) atomization.

For laminar turbulent-free cryogenic liquid flow, parameters should be selected to operate within the Rayleigh regime [165] (i.e., $Oh \ll 1$). In this regime, the fluid column will remain continuous with a smooth surface until the so-called intact length is estimated as follows [166]:

$$l \approx 12v \left(\sqrt{\frac{\rho d_0^3}{\sigma}} + \frac{3\eta d_0}{\sigma} \right) \tag{5.10}$$

Density	ρ	74.42 kg/m^3
Velocity	ν	105 m/s
Viscosity	η	18.583E-6 Pa s
Surface Tension	σ	2.4958E-3 N/m
Reynolds number	R_σ	2102
Weber number	W_e	1644
Ohnesorge number	Oh	1.928E-2
Intact length	l	2.43 mm

Table 5.1: Summary of fluid dynamics parameters. Parameters are provided, assuming a ø5 µm cylindrical cryogenic hydrogen jet operated at 60 psig and 17 K. Values for density, viscosity, and surface tension are from NIST [160].

The different fluid parameters for a 5 µm diameter cylindrical cryogenic hydrogen jet operated at 60 psig and 17 K are summarized in Table 5.1. To maintain a continuous jet for longer distances, the liquid must be cooled sufficiently close to the liquid-solid phase transition (Figure 5.3) so that evaporative cooling, occurring once the jet propagates in vacuum, solidifies the jet before the onset of Rayleigh breakup [147, 167].

5.4 Cryogenic liquid jet operation procedures

The following protocols detail the assembly and operation of a 5 µm diameter cylindrical cryogenic hydrogen jet operated at 17 K, 60 psig as an example case. An extension of this platform to other aperture types and gases requires operation at different pressures and temperatures. As a reference, working parameters for other jets are listed in Table 5.2. Protocols 1, 2, 3 and 7 are performed at ambient temperature and pressure, while Protocols 4, 5, and 6 are performed at high vacuum.

1. Installation of the cryostat in the vacuum chamber

Caution: A vacuum vessel can be hazardous to personnel and equipment from collapse, rupture due to back-fill pressurization, or implosion due to vacuum window failure. Pressure relief valves and burst disks must be installed on vacuum vessels within a cryogenic system to prevent over-pressurization.

1.1 Carefully insert the cryostat into the vacuum chamber. Vibrationally isolate the cryostat from the vacuum chamber using a stabilization platform.

1.2 Perform a vacuum test to determine the baseline vacuum pressure which, we have found, must be better than 5 x 10^{-5} mBar. A residual gas analyzer (RGA) is often helpful to identify moisture and contaminant gases present in the system.

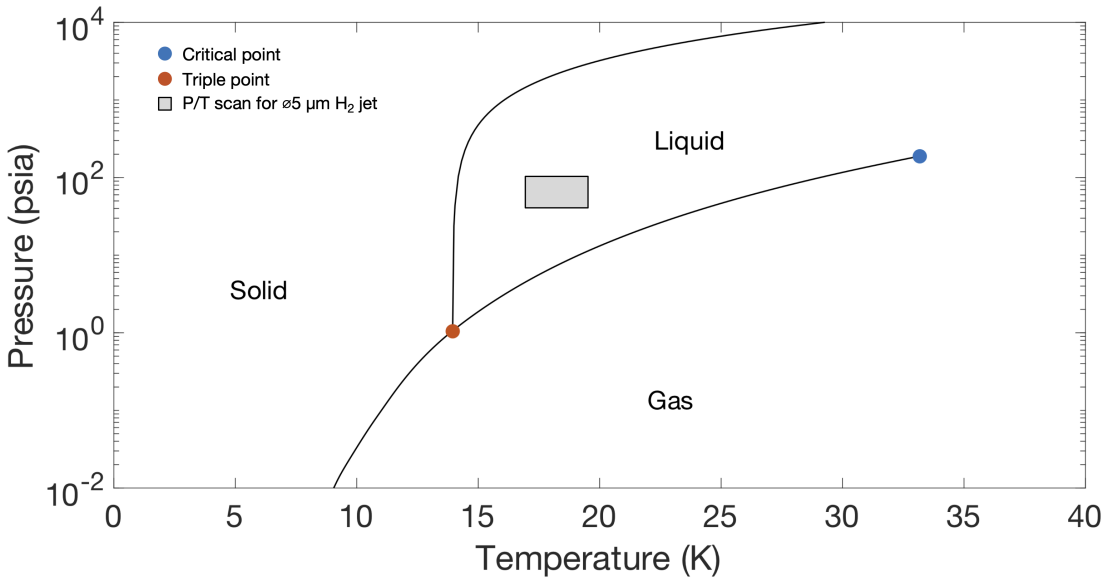

Figure 5.3: Hydrogen equation of state at cryogenic temperatures [160]. The critical and triple points are indicated by blue and orange filled circles, respectively. Jet operation follows an isobar through the gas-liquid phase transition. The jet solidifies via evaporative cooling in the vacuum chamber. The grey box indicates the range of backing pressures (40–90 psia) and temperatures (17–20 K) which are scanned over to optimize the stability of a ø5 µm cylindrical cryogenic hydrogen jet.

1.3 Connect the temperature controller and heater to the cryostat and confirm an accurate reading at ambient temperature.

1.3.1 If an unexpected value is measured, verify continuity from the temperature sensor to the correct terminals on the temperature controller. Otherwise, replace the temperature sensor.

1.4 Connect the helium return line(s) to an adjustable flow meter panel.

1.5 Evacuate the insulating vacuum shroud on the transfer line to better than 1 x 10^{-2} mBar using a turbomolecular pump backed by a dry scroll pump.

1.6 Apply a thin layer of cryogenic vacuum grease to the O-ring inside the head of the cryostat.

1.7 Slowly insert the transfer line refrigerator bayonet into the cryostat until the adjustment screw contacts the cryostat head. There should be minimal resistance. Tighten the adjustment screw to set the needle valve on the refrigerator bayonet to the desired position.

1.8 Conduct a cryostat performance test to verify the temperature sensor reliability by cooling down to the lowest attainable temperature. If unexpected temperatures are

measured during the cool-down, visually inspect the temperature sensors for good contact with the cryostat. If necessary, reposition and apply cryogenic vacuum grease to improve contact.

Caution: Hydrogen, deuterium, and methane are extremely flammable gases. Use piping and equipment designed to withstand the pressures and physical hazards. Local exhaust or ventilation are required to keep the concentration below the explosion limit. Before applying this procedure with any other gases, consult the associated safety data sheet (SDS).

1.9 Assemble the sample gas line according to the P&ID diagram in Figure 5.1. Use a high sensitivity leak detector to identify any leaks.

1.10 Purge the gas line according to the continuous flow purging technique to dilute contaminant gases and water vapor to the purity of the sample gas. The total time depends on the volume of the gas line and gas flow at a given backing pressure.

1.11 After the initial purge is complete, maintain constant positive pressure (e.g., 30 sccm at 50 psig) on the line to mitigate the risk of contaminant gases entering the line when the vacuum chamber is at ambient pressure.

Caution: While purging the line, ensure the vacuum chamber is adequately ventilated or maintained under vacuum to prevent accumulation of flammable gases.

2. Installation of the cryogenic source components

Note: All preparation and assembly of the cryogenic source components should be performed in a clean environment with the appropriate cleanroom clothing (i.e., gloves, hairnets, lab coats, etc.).

2.1 Use indirect ultrasonic cleaning to remove contaminants (e.g., residual indium) from the cryogenic source components.

2.1.1 Fill a sonicator with distilled water and add a surfactant to reduce the surface tension of the water.

2.1.2 Place cryogenic source parts in individual glass beakers, fully submerge them in electronics-grade isopropanol, and loosely cover the beakers with aluminum foil to reduce evaporation and to prevent particle contamination.

2.1.3 Place the beakers in the cleaning basket or a beaker stand in the sonicator to maximize cavitation. Beakers should not touch the bottom of the sonicator.

2.1.4 Activate the sonicator for 60 min.

2.1.5 Inspect the isopropanol using a bright white light for suspended particles or residue.

2.1.6 If particles are visible, rinse the parts with clean isopropanol, and replace the isopropanol bath. Sonicate in cycles of 60 min until no particles or residue are visible.

2.1.7 Place the parts on a covered, clean surface to desiccate for a minimum of 30 min before assembly.

2.2 Repeat Step 2.1 for the stainless-steel filter, source cap, ferrule, and assembly screws.

2.3 Cut a piece of indium to maximally cover the junction between the cryogenic source body and cold finger of the cryostat.

2.4 Place the indium on the cryogenic source and hold it flush with the cold finger of the cryostat. Tighten the retaining screws, ensuring the indium remains flat, to establish a thermal seal between the components. Do not to overtighten, as the copper threads are easily damaged.

2.5 Screw the threaded stainless-steel filter onto the cryogenic source flange.

2.6 Place an indium gasket on the source flange. Attach the source flange to the cryogenic source body using the flange screws. Tighten the screws diagonally instead of sequentially around the circumference.

2.7 Connect the sample gas line on the cryostat to the cryogenic source. Check for leaks using a high sensitivity leak detector.

3. Installation of aperture

3.1 Select an aperture according to experimental needs.

3.1.1 Inspect the aperture using brightfield and darkfield microscopy techniques to identify imperfections in the aperture, physical obstructions, or residual photoresist.

3.1.2 Some physical obstructions can be removed easily when rinsed with isopropanol. Otherwise, discard the aperture.

3.1.3 If there is residual photoresist from the nanofabrication of the aperture, use an acetone bath or piranha solution to remove it.

Caution: Piranha solution, consisting of 3:1 sulfuric acid (H_2SO_4) and hydrogen peroxide (H_2O_2), is extremely corrosive to organic material, including the skin and respiratory tract. The reaction of Piranha with organic material releases gas, which may become explosive. Never seal containers containing Piranha.

A full-face shield, chemical resistant apron, lab coat, and neoprene gloves are required.

3.2 Rinse the aperture with electronics-grade isopropanol to remove any debris or surface contamination. Allow the aperture to dry on a clean and covered surface for 10 min before installation.

3.3 Place the ferrule inside the cap.

3.4 Use clean, soft-tipped tweezers to place the aperture inside the ferrule. Tap the cap to center the aperture in the ferrule.

3.5 Drop an indium ring on top of the aperture. Again, tap the edge of the cap to center the indium ring on the aperture.

3.6 Hand-tighten the cap onto the source flange until minimal resistance is detected.

3.7 Derestrict the flow rate on the mass flow controller by increasing the setpoint to 500 sccm and set the gas pressure to ∼50 psig on the pressure regulator.

3.8 Tighten the aperture delicately by a few degrees at a time using a wrench until the flow rate begins to decrease.

3.9 Finish tightening the cap by checking the leak rate at the top of the cap with the high-sensitivity leak detector instead of the mass flow controller. Stop when tightening no longer decreases the measured leak rate.

3.10 If the flow rate does not drop below approximately 50 sccm, proceed with the following steps.

3.10.1 Use the leak detector to check for leaks around the source flange and cap. Retighten the screws on the source flange and remeasure the leak rate.

3.10.2 Remove the cap and inspect the aperture and tip of the source flange.

3.10.2.1 If the aperture is damaged, clean the cap according to step 2.2 and repeat Protocol 3.

3.10.2.2 If the indium ring is fixed to the aperture, discard the aperture and repeat Protocol 3.

3.10.2.3 If the complete indium ring is fixed to the flange, use a clean plastic razor blade to scrape off residual indium, then repeat Steps 3.2–3.10.

3.10.3 Over time, indium may accumulate on the tip of the source flange preventing subsequent apertures from sealing. In this case, remove the source flange and repeat Steps 2.1–2.2 followed by Steps 2.5–2.7.

3.11 As a safety precaution, change the setpoint on the mass flow controller to 10 sccm higher than the final flow determined by the dimensions of the aperture.

4. Cool-down procedure

4.1 Verify vacuum chamber pressure has reached the expected baseline for a given sample gas flow. To ensure the absence of contaminant gases, which will deposit on the cryogenic source during cool-down, the vacuum chamber is typically pumped for at least 1 h after reaching baseline pressure. This duration varies with local humidity levels and the vacuum system.

4.2 Turn on the cryostat exhaust heater to prevent frosting of the cryostat head from the return flow of helium gas.

4.3 Derestrict the gas flow on the mass flow controller by increasing the setpoint to 500 sccm.

Caution: Contact with cryogenic liquids, such as liquid nitrogen or liquid helium, will burn the skin, face, and eyes. When handling large volumes of cryogenic liquids (multi-liter), wear a face shield, safety glasses, thermally insulated cryogenic gloves, cryogenic apron, long pants without cuffs, and close-toed shoes. Such liquids may displace oxygen and cause rapid suffocation.

4.4 Fill the open-cycle cold trap with liquid nitrogen. Ensure that the level of liquid nitrogen is above the in-line filter at all times. Monitor and refill as required during cool-down and jet operation.

4.5 Set the adjustable flow meter(s) on the helium return line(s) to fully open.

4.6 Depressurize the liquid helium dewar using the vent valve.

4.7 Close the ball valve to the low pressure relief valve on the liquid helium dewar. The recommended dewar pressure during cool-down is 10 psig. An angle valve on the dewar adapter allows the operator to reduce the dewar pressure if there is surplus cooling power after sample liquefaction.

4.8 Insert the supply dewar bayonet into the liquid helium dewar in one smooth motion. The dewar should pressurize to 10 psig when the bayonet contacts the liquid.

Caution: Keep all exposed skin away from the neck of the dewar at all times.

4.9 Check for helium gas leaks between the dewar and dewar adapter once the connection has been tightened using a leak detector.

4.10 Activate the heater on the temperature controller and set the temperature setpoint to 295 K.

4.11 Once the transfer line fills and cools, the cryostat temperature will drop from ambient temperature to 295 K, at which point the heater will activate to prevent a further drop in temperature. Note that the time required for the initial drop in temperature depends on the dewar pressure and total transfer line and cryostat length.

4.12 Set the ramp rate on the temperature controller to 0.1 K/s and the setpoint to 200 K. Regulate the helium flow to follow the ramp so the heater does not turn on. Hold at 200 K for a brief dwell segment (e.g., 5 min) to allow the cryostat to thermalize. Repeat for two additional ramp-dwell segments to 120 K then 40 K. A conservative cool-down procedure is used to avoid strong temperature gradients along the system and allows the system parameters to be closely monitored. The dwell temperatures are selected away from sublimation temperatures for contaminant gases.

4.12.1 If the gas flow increases unexpectedly, the indium seal on the source flange or aperture may have failed. Abort the cool-down procedure by proceeding to step 6.4. Once the vacuum chamber has been vented, inspect the seals and refer to Step 3.10 to retighten and check for leaks.

4.13 At 40 K, manually tune the temperature controller P-I-D parameters following the Ziegler-Nichols method [168] until the temperature stability is better than ±0.02 K.

5. Liquefication and jet operation

5.1 Confirm that the liquid nitrogen level is above the in-line filter.

5.2 Disable the temperature ramp and change the setpoint temperature to well below the theoretical vapor-liquid phase transition temperature (e.g., 20 K for hydrogen).

5.3 At the onset of liquefaction, the gas flow will increase up to the maximum and a mixture of gas and liquid will spray from the aperture. Increase the helium flow(s) to provide additional cooling power to quickly pass through the phase transition.

5.4 Use high magnification shadowgraphy with pulsed, sub-nanosecond illumination to visualize the jet stability and laminarity [169].

5.5 Optional: If an application or experiment has a pre-determined location for the sample (e.g., detectors aligned to the same position in space), translate the cryogenic source using a multi-axis manipulator on the cryostat flange or motorized push-pin actuators in the vacuum chamber.

5.6 Translate the catcher to maximize the pressure in the catcher foreline.

5.7 Optimize the P-I-D parameters and helium flow to improve the temperature stability to better than ±0.02 K. Note that the overall stability of the jet strongly depends on

the vacuum chamber pressure, gas backing pressure, and temperature. For example, a change in as little as 1 x 10-5 mBar may require reoptimization.

5.8 Scan in temperature and pressure to optimize the jet stability and laminarity. Sample jet parameters are listed in Table 5.2.

5.8.1 If the jet breaks up into a spray, the pressure and temperature in phase space may be too close to the boiling curve. Optimal jet performance is away from the vaporization curve.

5.8.2 Large amplitude temperature or helium flow oscillations will result in periodic spatial perturbations, which (in the extreme case) result in driven breakup of the jet. Reduce the helium flow and reoptimize P-I-D parameters to damp the oscillations.

5.8.3 If the jet exhibits transverse (i.e., first-wind regime) or longitudinal waves (i.e., Plateau-Rayleigh instability), decrease the temperature to increase the viscosity, thereby reducing the Reynolds number.

5.8.4 If laminarity cannot be achieved and the jet characteristics are independent of changes in temperature and pressure, there may be a physical obstruction (e.g., physical debris or ice) in the aperture. Before aborting the test, follow Steps 6.1–6.5 and closely monitor the vacuum pressure and cryostat temperature. If a contaminant gas or water has sublimated on the aperture causing a partial or full blockage, it can be identified by the boil-off temperature. Repeat Steps 4.11–4.12 and 5.1–5.6 to determine if the jet stability improves.

6. Warm-up procedure

Note: If the aperture is damaged during operation, immediately limit the sample gas flow to 10 sccm and reduce the sample gas pressure to 30 psig. Then, proceed directly to step 6.5.

6.1 Change the setpoint to 20 K and decrease the gas pressure from operating pressure to approximately 30 psig.

6.2 Increase the temperature setpoint in steps of 1 K while monitoring the pressure on the gas regulator. As the liquid in the cryogenic source vaporizes, the pressure in the gas line will rapidly increase and the flow across the mass flow controller will read 0 sccm.

Note: Do not allow the gas pressure to exceed the maximum operating pressure of the components on the sample gas line. If this occurs, wait until the line depressurizes to

a safe value through the aperture or pressure relief valve before increasing the setpoint further.

6.3 Repeat step 6.2 until increasing the temperature setpoint by 1 K does not result in an increase in gas line pressure.

6.4 Enable the temperature ramp, change the temperature setpoint to 300 K, and regulate the helium flow as required to maintain a temperature increase of 0.1 K/s.

6.5 Once the source temperature is above 100 K, close the adjustable flowmeter(s) on the helium return line(s). Depressurize the dewar and open the ball valve to the lowest pressure relief valve.

6.6 Wait until the cryostat thermalizes at 300 K before venting the vacuum chamber. This will prevent water vapor from condensing on the cryostat and cryogenic source components.

6.7 Depressurize the dewar, then remove the supply dewar bayonet.

6.8 Remove the liquid nitrogen cold trap.

6.9 Limit the gas flow on the mass flow controller to 30 sccm.

6.10 Turn off the exhaust gas heater.

6.11 Deactivate the heater on the temperature controller.

6.12 If the aperture is damaged or an obstruction is suspected from a change in flow, proceed to Protocol 7. Otherwise, the aperture does not need to be replaced.

7. Replacement of aperture

7.1 Remove the cap and inspect the aperture and tip of the source flange.

7.1.1 If the indium ring sticks to the flange, use a clean plastic razor blade to scrape it off using moderate pressure.

7.1.2 If the aperture remains sealed to the source flange when the cap is removed, limit the gas flow to 10 sccm and confirm the gas backing pressure has dropped to 30 psig. Remove the aperture carefully with a plastic razor blade. If removed prematurely, over-pressurization in the line may damage or eject the aperture.

7.2 Repeat Protocol 3 to install a new aperture.

5.5 Characterization of cryogenic jets

Following Step 5.4, high magnification shadowgraphs are used to assess laminarity, positioning jitter, and long-term stability during jet operation. It is critical to use pulsed, subnanosecond illumination to record an instantaneous image of the jet so that the jet motion

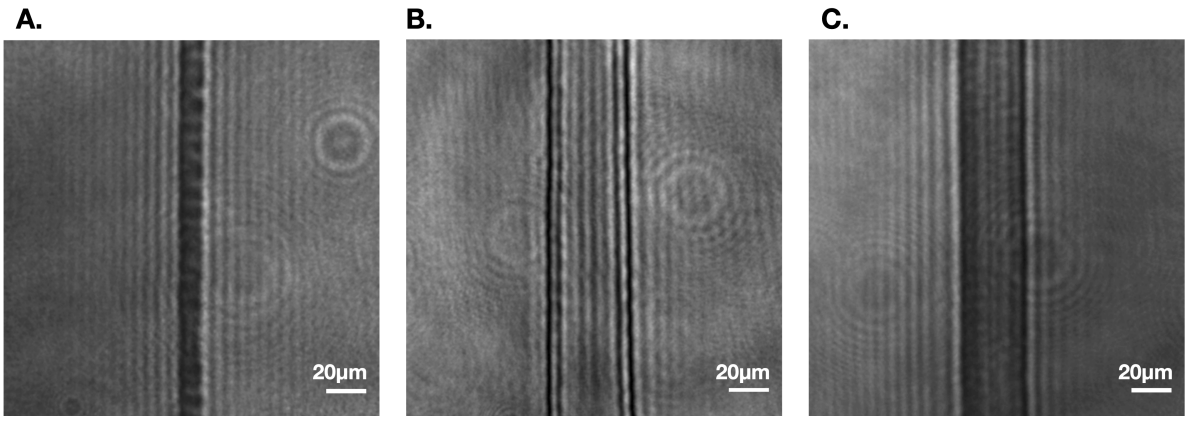

Figure 5.4: Representative 20x magnification shadowgraphs of turbulent-free, laminar cryogenic liquid jets using a 10 ps/1057 nm wavelength laser. (A) Aperture = 2 x 20 µm^2, gas = H_2, T = 15.8 K, P = 188 psig. (B) Aperture = 4 x 12 µm^2, gas = H_2, T = 17.2 K, P = 80 psig. (C) Aperture = 4 x 20 µm^2, gas: D_2, T = 20 K, P = 141 psig.

(∼0.1 µm/ns for H_2) does not blur surface irregularities or turbulence. Sample images of 2 x 20 µm^2 H_2, 4 x 12 µm^2 H_2, and 4 x 20 µm^2 D_2 jets are shown in Figure 5.4.

An additional high magnification imaging system is used to precisely position the cryogenic liquid jet in space. For simplicity, the imaging systems are designed to provide front and side views of the jet. It is particularly important to assess the jet stability and determine the orientation of the planar jets. A study of the spatial jitter of a 2 x 20 µm^2 H_2 as a function of distance from the aperture, performed during a single test over several hours, is shown in Figure 5.5. The 1σ positioning jitter for each datapoint in Figure 5.5 (A) was calculated from 49 images recorded at 10 Hz. Here, the jet position was determined relative to a fixed reference position. Figure 5.5 (B) shows the normalized histograms of the jet position at 23 mm as an example. A more detailed study can be found in Obst et al.5. On average, the spatial jitter increases linearly away from the nozzle.

Typical system observables during liquefying and jet operation (according to Protocol 5) of a 4 x 20 µm^2 cryogenic deuterium jet are shown in Figure 5.6. Careful monitoring of the temperature, flow, sample backing pressure, and vacuum pressures allow the operator to quickly identify any irregularities and react accordingly. For example, if the jet leaves the catcher, indicated by a dashed box, the vacuum chamber and foreline pressure increase significantly. Additional cooling power is then needed to maintain the setpoint temperature.

Once stabilized, all observables should be constant with minimal oscillations. Any long-term drift is indicative of a problem (e.g., leaks, gas contamination, decrease in vacuum system performance, positioning drift in catcher). The choice of aperture strongly dictates the operational parameters of the jet in the Rayleigh regime. Once the optimal parameters

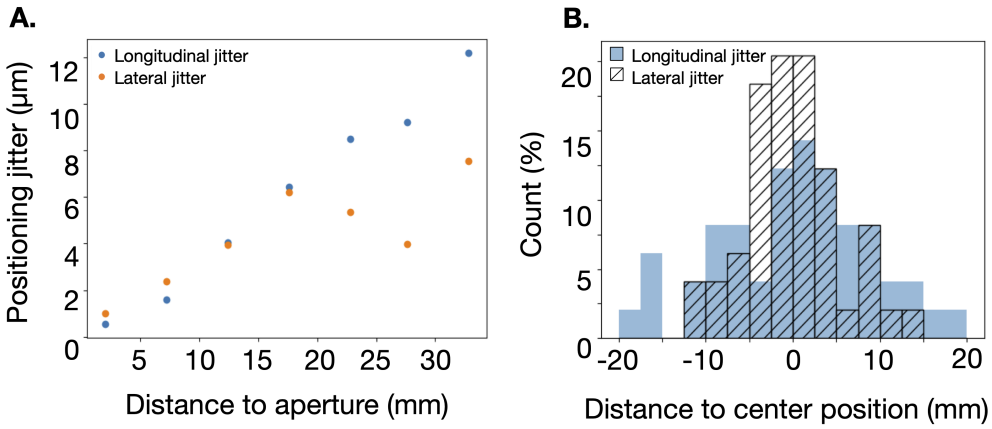

Figure 5.5: Jet position stability for 2 x 20 µm^2 cryogenic hydrogen jet. Parameters are 18 K, 60 psig, and Re ≈ 1887. (A) Positioning jitter as a function of distance from the aperture. The longitudinal (lateral) jitter corresponds to motion parallel to the short (long) axis of the rectangular sheet. (B) Normalized histogram of jet position to determine the lateral jitter (σ = 5.5 µm) and longitudinal jitter (σ = 8.5 µm) at a distance of 23 mm from the nozzle.

are identified for a given gas and aperture type, the resulting jet is highly reproducible; however, any minor deviations in the aperture require reoptimization starting from the previously identified values. Typical operation parameters are summarized in Table 5.2.

5.6 Discussion

Successful operation of the cryogenic liquid jet requires meticulous cleanliness and careful monitoring of temperature stability. One of the most frequent and avoidable failures is a partial or full blockage of the micron-sized aperture. Copper, stainless steel, or indium from the source or airborne particles can be introduced at any step of the source assembly. All components must undergo a robust cleaning process using indirect sonication. Assembly and storage in a Class-10,000 cleanroom or further improves the success rate.

Another critical step of the procedure is to stabilize the cryogenic source temperature. Users must ensure that the temperature of the liquid exiting the source is measured independently from the variable heat released by continuous liquefaction in the reservoir. This is accomplished by placing the temperature sensor near the aperture (e.g., on the source flange) or far from the heat source. Furthermore, P-I-D parameters must be manually optimized using the Ziegler-Nichols method for each combination of temperature and backing pressure. If the temperature fluctuations become too large, periodic oscillations can be observed on the jet sometimes leading to periodic breakup. It should be noted that built-in autotuning functions or low-pass filters have not been successful in stabilizing the temperature during

Sample gas	Aperture	Temperature (K)	Pressure (psig)	Flow (sccm)
H_2	5µm cylindrical	17	60	150
50% H_2, 50% D_2	5µm cylindrical	20	30, 30	130
D_2	5µm cylindrical	22	75	80
H_2	1 µm x 20 µm planar	18	182	150
H_2	2 µm x 20 µm planar	18	218	236
H_2	4 µm x 20 µm planar	17.5	140	414
D_2	4 µm x 20 µm planar	20.5	117	267
Ar	5 µm cylindrical	90	50	18.5
CH_4	5 µm cylindrical	100	75	46

Table 5.2: Sample cryogenic jet operation conditions.

jet operation.

The cryogenic liquid jet system, while highly adaptable, is challenging to implement at large-scale facilities with established vacuum protocols. For instance, differential pumping stages are required when upstream equipment is sensitive to the residual gas (e.g., FLASH free-electron laser at DESY or MeV-UED instrument at SLAC). In addition, large diameter vacuum chambers, such as those for multi-PW lasers, likely require in-vacuum flexible cryostats. Compared to conventional fixed length cryostats, they can be readily decoupled from chamber vibrations and have a shorter lever arm. A flexible in-vacuum cryostat has already been implemented with the Draco Petawatt laser at Helmholtz-Zentrum Dresden-Rossendorf (HZDR). Another observation is that the aperture can be damaged when the jet is irradiated by an ultra-high intensity laser too close to the source. Recently, a mechanical chopper blade (operating at 150 Hz and synchronized with the laser pulse) has been implemented to protect and isolate the aperture from the laser-plasma interaction.

This system produces micron-scale, highly tunable, turbulent-free, laminar cylindrical and planar cryogenic liquid jets. Ongoing development of the cryogenic liquid jet system is focused on advanced aperture materials and design, vacuum system and catcher improvements, and advanced hydrogen isotope mixing. This system will enable a transition to high repetition rate high energy density science and pave the way to the development of next-generation particle accelerators.

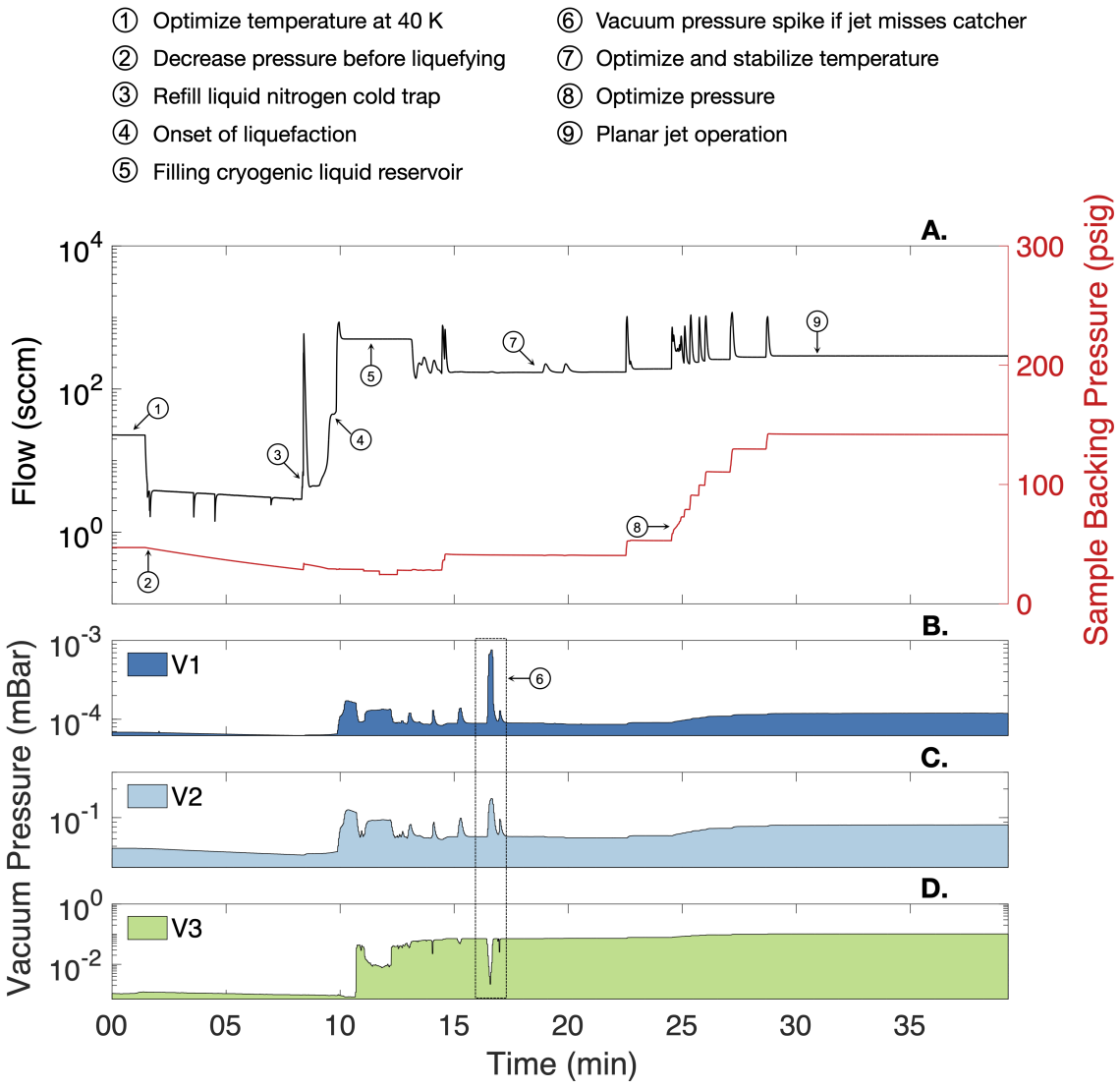

Figure 5.6: Representative flow and pressures during cryogenic jet operation. (A) Left: sample gas flow, right: sample gas backing pressure as a function of time. Semi-log plot of the vacuum chamber pressure (V1; B), turbomolecular pump foreline pressure (V2; C), and jet catcher pressure (V3; D) as functions of time. Circled numbers identify changes in the system observed during Protocol 5.

Chapter 6
Diagnosing Laser-Accelerated Proton and Deuteron Beams

6.1 Introduction

Most uses of laser-driven ion beams require thorough characterization of the ion beam energy, spatial distribution, and total particle number. Over the years, a variety of charged particle diagnostics have been developed including time-of-flight detectors [170–173], magnetic and/or electric spectrometers [174–179], radiochromic film stacks [180, 181], and solid-state nuclear track detectors employing allyl diglycol carbonate (CR-39) [182–184]. In recent years, as high-repetition rate high-intensity laser systems have become increasingly available, many film and imaging plate-based diagnostics have been retrofit with high repetition rate detectors. Examples include scintillator-based rate ion imagers [185–188] and spectrometers equipped with microchannel plates [14, 183, 184, 189, 190] or LANEX fluorescence screens. Additional research and development have gone into the modernization of data acquisition systems and data management tools capable of high >GB/s data production rates. The paradigm shift from single-shot or shot-on-demand to >10 Hz experiments that began with this thesis will require more sophisticated data handling and filtering algorithms due to the anticipated 100 GB/s to TB/s data rates.

In the following sections, additional details on the two primary ion diagnostics used in this thesis are presented.

6.2 Thomson parabola ion spectrometers

Thomson Parabola (TP) ion spectrometers are a specific combination of parallel or anti-parallel electric (E) and magnetic (B) fields that deflect energetic ions along parabolic trajectories according to their energy and charge-to-mass ratio [191]. X-rays, gammas, and neutral particles also generated by the high-intensity laser-plasma interaction pass through the TP without being deflected and are recorded as the "zero order" on the detector.

An illustration of a Thomson Parabola is shown in Fig. 6.1. The main components of a TP are: (i) a pinhole ($50-500\,\mu m$) that samples a small solid angle of the ion beam, (ii) a permanent magnet pair with field strengths on the order of 1 T, (iii) two high voltage electrodes typically charged to $\pm 3-5$ kV with the distance between the electrodes determining the E-field, and (iv) a large-area radiation sensitive detector to record the parabolic trajectories of the detected ions.

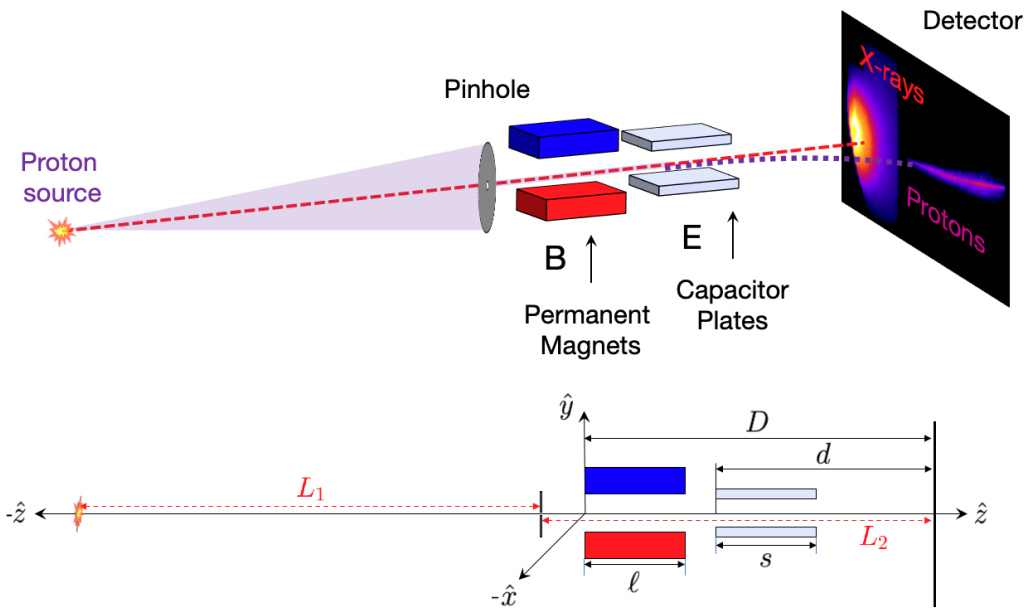

Figure 6.1: Illustration and schematic of a Thomson Parabola Ion Spectrometer

Several design parameters are varied to obtain the optimal ion energy spectra during an experiment. First, the size and location of the pinhole are varied to optimize the signal level on the detector. It should be noted that the pinhole diameter is convolved with the magnetic dispersion which sets the minimum energy resolution. The electric field strength is selected so that neighboring parabolic traces for different charge-to-mass ratios do not overlap on the detector.

To extract the energy spectra from the traces recorded on the detector, we compute the ion trajectories either numerically or analytically, assuming uniform fields. Numeric calculations use a conventional particle pusher program that calculates the ion trajectories on a 3-D grid according to the Lorentz force using a measured or generated field map. The Radia software package for magegnetostatics [192, 193] is a useful tool to produce realistic magnetic field maps based on the material, dimensions, and geometry of the magnets.

Analytical ion trajectories

To obtain the analytical expression for the ion trajectories, let us consider an ion with mass M, charge q, and initial non-relativistic velocity $\mathbf{v} = v_0\hat{z}$. We arbitrarily set the origin $(0, 0, 0)$ as the input of the magnetic yoke, which has a total length along the $\hat{z}$ direction of $\Delta z = \ell$. Starting from the Lorentz equation for a positively charged ion in a static magnetic

field with $\mathbf{B} = B_0\hat{y}$, we have that

$$M\frac{d\mathbf{v}}{dt} = q(\mathbf{v} \times \mathbf{B}). \tag{6.1}$$

Separating into the $\hat{x}$, $\hat{y}$, and $\hat{z}$ components, we get

$$\frac{d^2x}{dt^2} = -\omega_c\frac{dz}{dt} \tag{6.2}$$
$$\frac{d^2y}{dt^2} = 0 \tag{6.3}$$
$$\frac{d^2z}{dt^2} = \omega_c\frac{dx}{dt} \tag{6.4}$$

where ω_c is the *cyclotron frequency* given by

$$\omega_c = \frac{qB_0}{M}. \tag{6.5}$$

We then obtain

$$\frac{dx}{dt} = -\omega_c z \tag{6.6}$$
$$\frac{dy}{dt} = \mathscr{C}_1 \tag{6.7}$$
$$y(t) = \mathscr{C}_1 t + \mathscr{C}_2, \tag{6.8}$$
$$\tag{6.9}$$

but at $t = 0$, $y(0) = 0$, and $dy(0)/dt = 0$, so $\mathscr{C}_1 = 0$ and $\mathscr{C}_2 = 0$ and therefore

$$y(t) = 0. \tag{6.10}$$

Inserting Eqn. 6.6 into Eqn. 6.4 yields

$$\frac{d^2z}{dt^2} = -\omega_c^2 z \tag{6.11}$$
$$z(t) = \mathscr{C}_4 \sin(\omega_c t) + \mathscr{C}_3 \cos(\omega_c t), \tag{6.12}$$

but at $t = 0$, $z(0) = 0$, and $dz(0)/dt = v_0$, so $\mathscr{C}_3 = 0$ and $\mathscr{C}_4 = v_0/\omega_c$ and therefore

$$z(t) = R_c \sin(\omega_c t) \tag{6.13}$$
$$x(t) = -R_c(1 - \cos(\omega_c t)) \tag{6.14}$$

where we have defined $R_c = v_0/\omega_c$ to correspond with the radius of the curvature of the trajectory. At the end of the magnets where $z = \ell$ and the ion has

$$\mathbf{r}(t) = \left(\sqrt{R_c^2 - \ell^2} - R_c\right)\hat{x} + \ell\hat{z} \tag{6.15}$$

$$\mathbf{v}(t) = \omega_c \ell \hat{x} + \left(\omega_c \sqrt{R_c^2 - \ell^2}\right)\hat{z}. \tag{6.16}$$

After the ion exits the magnets, it freely propagates until it reaches the capacitor plates. Let us define $x_\ell = \sqrt{R_c^2 - \ell^2} - R_c$, $v_x = \omega_c \ell$, and $v_z = \omega_c \sqrt{R_c^2 - \ell^2}$. The time it takes for the ion to travel from the end of the magnets to the detector is $t_1 = (D - \ell)/v_z$. By design, the deflection from the electric field is orthogonal to the magnetic deflection so that the motion is independent. The x coordinate on the detector plane $z = D$ is then given by

$$x = x_\ell + v_x t_1 \tag{6.17}$$

$$= x_\ell + \frac{v_x(D - l)}{v_z} \tag{6.18}$$

$$= \left(\sqrt{R_c^2 - \ell^2} - R_c\right) - \frac{\ell(D - \ell)}{\sqrt{R_c^2 - \ell^2}}. \tag{6.19}$$

Again assuming a static, spatially uniform electric field between the capacitor plates with $\mathbf{E} = E_0\hat{y}$, we have that

$$\frac{d^2y}{dt2} = a_E \tag{6.20}$$

$$\frac{dy}{dt} = a_E t + \mathscr{C}_5 \tag{6.21}$$

$$y(t) = \frac{1}{2}a_E t^2 + \mathscr{C}_5 t + \mathscr{C}_6 \tag{6.22}$$

where $a_E = qE_0/m$ and the initial conditions $y(0) = 0$ and $v_y(0) = 0$ lead to $\mathscr{C}_5 = 0$ and $\mathscr{C}_6 = 0$. Then the final expression for y(t) is

$$y(t) = \frac{1}{2}a_E t^2. \tag{6.23}$$

Since the $\hat{z}$ component of the ion velocity remains constant, the time it takes for the ion to pass through capacitor plates with length s is given by $t_2 = s/v_z$. The $\hat{y}$ component of the ion position and the velocity at the output of the capacitor plates are then given by

$$y(t_2) = y(s/v_z) = \frac{1}{2}a_E \left(\frac{s}{v_z}\right)^2 \tag{6.24}$$

$$v_y(t_2) = v_y(s/v_z) = a_E \left(\frac{s}{v_z}\right). \tag{6.25}$$

The y coordinate on the detector plane $z = D$ after time $t_3 = (D - s)/v_z$ is then

$$\begin{aligned} y &= y_s + v_y t_3 && (6.26)\\ &= \frac{1}{2} a_E \left(\frac{s}{v_z}\right)^2 + v_y \left(\frac{D-s}{v_z}\right) && (6.27)\\ &= \frac{a_E s}{v_z^2}\left(D - \frac{s}{2}\right) && (6.28)\\ &= \frac{a_E s}{\omega_c^2 (R_c^2 - \ell^2)}\left(D - \frac{s}{2}\right) && (6.29) \end{aligned}$$

where d is the distance from the capacitor plate input to the detector at $z = D$. We've thus determined the coordinates of an ion on the 2-D detector after it has passed through the parallel magnetic and electric fields and freely propagated to a detector. Expressed as a function of the ion mass, charge, initial velocity, and Thomson Parabola design parameters, the expression is

$$\mathbf{r} = \left(\sqrt{R_c^2 - \ell^2} - R_c - \frac{\ell(D-\ell)}{\sqrt{R_c^2 - \ell^2}}\right)\hat{x} + \left(\frac{s a_E}{\omega_c^2 (R_c^2 - \ell^2)}\left(D - \frac{s}{2}\right)\right)\hat{y}. \tag{6.30}$$

Magnetic dispersion calibration

The analytical expressions derived in the previous section assume that the magnetic and electric fields are spatially uniform. They can be used to accurately predict trajectories of weakly deflected ions. If the ions are deflected significantly from the propagation axis ($+\hat{z}$), their trajectories can differ significantly from the analytical expressions due to the realistic spatially non-uniform fields. Typically, a Thomson parabola is designed with analytical estimates for a desired energy range, expected ions, and charge states. It is then straightforward to calibrate the energy dispersion on the detector using metallic filters with different thicknesses. Based on the filter material and thickness, protons or ions with energies higher than the "break-through energy" are detected. This threshold energy is computed using the software SRIM (the stopping and range of ions in matter) [194]. The positions of at least three break-through energies are required for a robust energy calibration. A sample energy calibration for a TP is shown in Fig. 6.2, and the associated details for the measurements are summarized in Table 6.1.

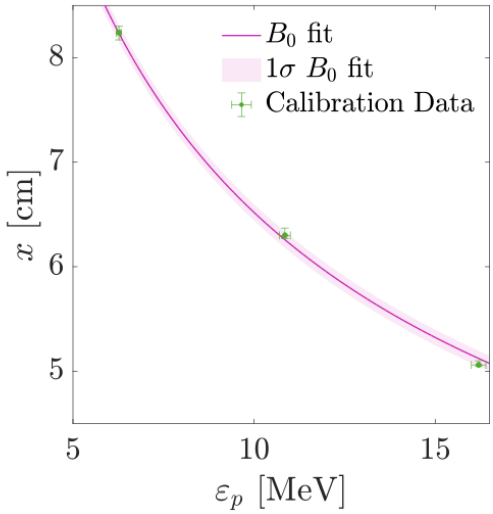

Figure 6.2: Thomson Parabola ion spectrometer with magnetic field calibration. The filters used are summarized in Table 6.1. The calibration was performed on one of the Thomson Parabolas used during experiment at the Texas Petawatt Laser Facility described in Chapter 8.

Shot No.	**Filter 1**	**Filter 2**	$\varepsilon_\mathbf{p}$ **[MeV]**	**x [cm]**
12241	254 ± 5 µm Al	13 µm Al	6.27 ± 0.07	8.24 [8.30, 8.17]
12243	530 ± 10 µm Cu	13 µm Al	16.2 ± 0.2	5.06 [5.10, 5.05]
12245	250 ± 5 µm Cu	13 µm Al	10.9 ± 0.2	6.30 [6.37, 6.27]

Table 6.1: Filters used for the magnetic dispersion calibration of a Thomson Parabola ion spectrometer. Column 3 gives the proton break-through energy ε_p calculated for Filter 1 and Filter 20 using SRIM [194]. Column 4 is the deflection distance x from the zero-order position on the detector.

Imaging plates

Imaging plates (IP) are the standard detector used for charged particles in low repetition rate ($\lesssim$1 shot/hr) experiments. They consist of an active phosphor layer on top of a magnetic base. Ionizing radiation excites the molecules in the phosphor layer to a metastable state that persists for hours. The excited state decays either via spontaneous emission at a known rate or by stimulated emission. Obtaining a quantitative measurement of the ion signal requires stimulating emission by irradiating the imaging plate with light at an appropriate wavelength. Image plate scanners such as the Fujifilm FLA-5000 use 635 nm, 45 mW laser radiation to stimulate the emission of 400 nm photons, which are detected and recorded by the scanner as a pixel value. The pixel value must be converted into a photostimulated luminescence (PSL) value before analysis using a file-type specific formula given by Fujifilm.

Layer	Parameter	BAS-SR	BAS-MS	BAS-TR
Protective	Composition	C_2H_2O	C_2H_2O	none
	Density ($g\,cm^{-3}$)	1.273	1.66	0
	Thickness (µm)	6	9	0
Phosphor	Composition	BaFBr	$BaFBr_{0.85}I_{0.15}:Eu^{2+}$	
	Density ($g\,cm^{-3}$)	3.1	3.31	2.85
	Thickness (µm)	120	115	50
Support	Composition	C_2H_2O		
	Density ($g\,cm^{-3}$)	1.273	1.66	1.66
	Thickness (µm)	188	190	250
Magnetic	Composition	$ZnMn_2Fe_5NO_{40}H_{15}C_{10}$		
	Density ($g\,cm^{-3}$)	3.1	2.77	2.77
	Thickness (µm)	160	160	160

Table 6.2: Composition of Fujifilm BAS-SR, BAS-MS, and BAS-TR Imaging Plates.

For .img file formats, the pixel value is referred to as the quantum level QL and the formula is

$$PSL = \left(\frac{R_{\mu m}}{100}\right)^2 \times \frac{4000}{S} \times 10^{L\left(\frac{QL}{2^{16}-1}-\frac{1}{2}\right)} \tag{6.31}$$

where R is the scanning resolution in microns, S is the scanner sensitivity ranging from 1000 to 10000, $L = 5$ is the latitude. Alternatively, for .gel file formats, where G is the pixel value out of 65535 for 16 bit, the formula is

$$PSL = \left(\frac{G}{2^{16}-1}\right)^2 \left(\frac{R_{\mu m}}{100}\right)^2 S_{cal}(V) 10^{L/2} \tag{6.32}$$

where $S_{cal}(V)$ is an empirically determined scanner sensitivity function that depends on the photomultiplier tube (PMT) voltage V. This sensitivity is obtained using a radioactive source with known activity such as a ^{14}C source [195]. The $S_{cal}(V)$ measured for the imaging plate scanner at the Texas Petawatt Laser facility is shown in Fig. 6.3.

The characteristics of the most common IPs used in laser-plasma experiments are summarized in Table 6.2. BAS-TR are typically used to detect protons and ions in TPs since the active phosphor layer is exposed without a protective layer. This allows detection of lower energy ions which would otherwise be stopped in the protective layer. The active layer of the BAS-TR is a 50 µm thick, europium-doped barium fluoride phosphor with the chemical formula $BaFBr_{0.85}I_{0.15}:Eu^{2+}$ and a density of 2.85 g/cm^3.

Conversion from PSL to particle number is then done with an ion- and energy-dependent calibration [80, 196] or is done in-situ with Polyallyl diglycol carbonate (CR-39) or absolutely calibrated radiochromic film stacks.

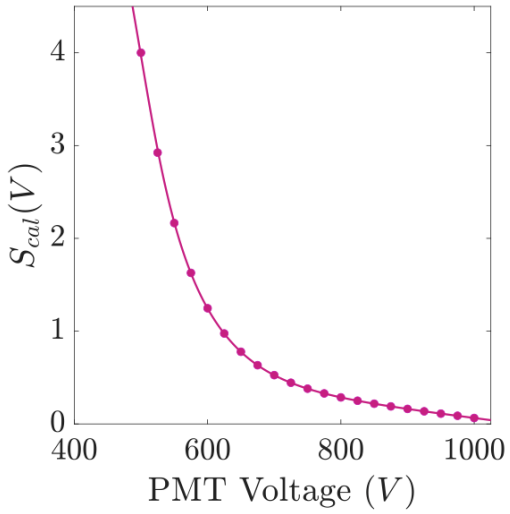

Figure 6.3: Imaging plate scanner sensitivity function $S_{cal}(V)$. The calibration was performed after the experiment at the Texas Petawatt Laser Facility described in Chapter 8.

Absolute ion number calibration using CR-39

The most common method of obtaining a signal to absolute particle calibration relies on calibration with a single-particle-counting Polyallyl diglycol carbonate (CR-39) detector [182–184]. Each ion creates microscopic damage to the bonds of the plastic polymer structure when the deposited energy of the ion exceeds the damage threshold of the material [197, 198]. To extract the particle numbers from an exposed CR-39, the plate is immersed in a high-concentration (*e.g.* 6 mol/L) NaOH solution held at 60 – 80°C. The damaged plastic polymer etches at a faster rate than the undamaged regions, resulting in visible pits [199]. The pits are imaged using a microscope and counted using an image processing software such as Fiji [200]. This yields an absolute calibration that is applied to the signal level on the detector.

An advanced CR-39 diagnostic was designed for the experiments in Chapter 8 to obtain calibration data at multiple energies across the TP energy range. It consisted of metallic filters installed on a slotted CR-39 plate placed in front of a BAS-TR imaging plate. The metallic filters are used to bring the Bragg peak depth for all energies to 175±50 µm so the same etch time could be used. A schematic of the CR-39 diagnostic is shown in Fig. 6.4 with the associated design calculations summarized in Table 6.3. CR-39 was used to obtain an absolute calibration the TPs for protons and deuterons for the experiment described in Chapter 8.

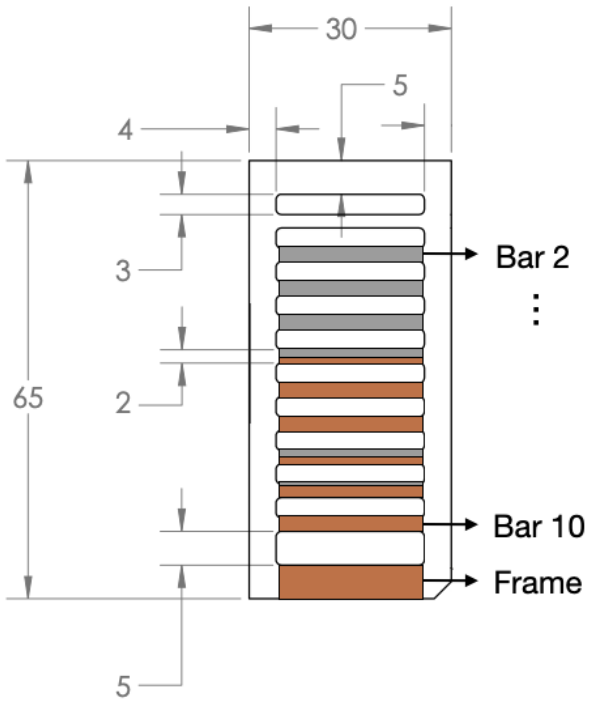

Figure 6.4: Slotted CR-39 plate with aluminum and copper filters to verify the PSL-to-particle number calibration of imaging plates used in a large energy range Thomson Parabola ion spectrometer. Refer to Table 6.3 for filter type and thickness on Bars 2-7.

Bar Number	**ε_p Limits (MeV)**	**ε_p Center (MeV)**	**Filter 1**	**Filter 2**	**ε_p Center Bragg Peak in CR-39 (µm)**
2	[5.9, 6.2]	6.05	150 µm Al	-	164
3	[6.6, 6.9]	6.76	150 µm Al	-	247
4	[7.5, 7.7]	7.61	250 µm Al	-	203
5	[8.5, 8.8]	8.64	150 µm Cu	-	138
6	[9.7, 10.1]	9.89	150 µm Cu	150 µm Al	96
7	[11.2, 11.7]	11.47	250 µm Cu	-	200

Table 6.3: Slotted CR-39 plate to verify the PSL-to-particle number calibration of imaging plates used in a large energy range Thomson Parabola ion spectrometer. Filters were used to moderate the proton energy before the CR-39 so that the Bragg peak depths were comparable depths for all energies.

6.3 Radiochromic film stacks

6.3.1 Preface

Radiochromic film (RCF) is a radiation dose-sensitive film that is routinely used in laser-driven ion-acceleration experiments to measure the spatial and energy distribution of proton beams [201]. The film consists of plastic support layers and a thin (10−28 µm) active layer. Several film types with different dose sensitivity ranges exist, and their characteristics are summarized in Table 6.4.

Layer	Parameter	HD-v2	MD-v3	EBT3
Protective	Composition	none	Polyester Substrate	
	Thickness (µm)	0	125	
Active	Composition	H (56.8%), C (27.6%), O (13.3%), Al (1.6%), and Li (0.6%)		
	Density ($g\,cm^{-3}$)	1.2		
	Thickness (µm)	12	10	28
	Dose Range (Gy)	$10-10^4$	$1-10^3$	0.1−200
Support	Composition	Polyester Substrate		
	Thickness (µm)	97	125	

Table 6.4: Composition of Gafchromic HD-v2, MD-v3, and EBT3 dosimetry films. The optimal doses to transition from HD-v2 to MD-v3 and from MD-v3 to EBT3 so as to maximize visibility are 580.7 Gy and 71.45 Gy, respectively [202].

As described in Chapter 3, a proton with a given energy will deposit most of its energy at the Bragg peak depth. Therefore, film with an active layer of finite thickness provides a 'snapshot' of the ion beam for a small energy interval. To determine which proton energies coincide with the active film layers, the ion stopping ranges are computed using the code SRIM (the Stopping and Range of Ions in Matter) [194]. Often metallic filters are added between film layers to increase the energy separation. A sample RCF stack developed and fielded as part of this thesis to measure proton energies up to 130 MeV is shown in Fig. 6.5.

The remainder of this chapter has been published as: C. B. Curry, C. A. S. Dunning, M. Gauthier, H.-G. J. Chou, F. Fiuza, G. D. Glenn, Y. Y. Tsui, M. Bazalova-Carter, and S. H. Glenzer, *Optimization of radiochromic film stacks to diagnose high-flux laser-accelerated proton beams*, Rev. Sci. Instrum., **91**, 093303 (2020). C. A. S. Dunning and I took the calibration measurements at BC Cancer–Victoria to extend the calibrations of typical film types. R. Fedosejevs assisted with the complementary cyclotron measurements at the Medical Isotope and Cyclotron Facility (MICF) at the University of Alberta. I analyzed the

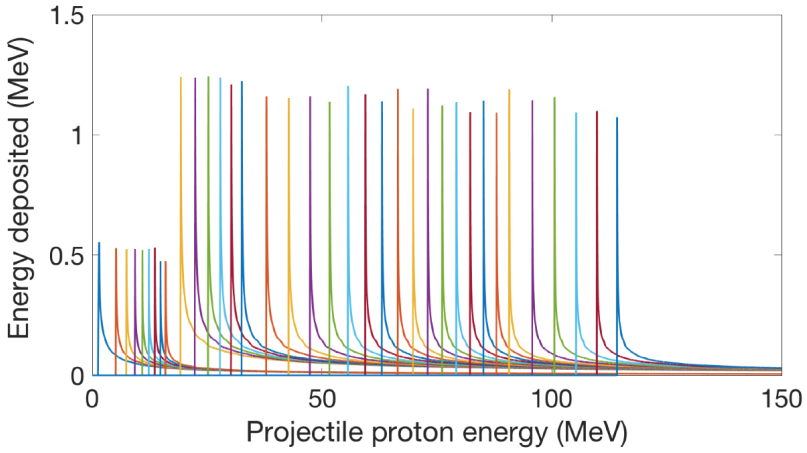

Figure 6.5: Radiochromic film stack to resolve proton energies from 1.5 to 130 MeV. The stack consists of 10 μm Mylar + 13 μm Al + 1x HD-v2, + 8x (100 μm Al + HD-v2) + 6x (150 μm Cu + EBT3) + 16x (500 μm Cu + EBT3) + 5x (1 mm Cu + EBT3). Each curve represents the energy deposited by an incident proton of a given energy in the layer.

results, performed the optimization study, and wrote the manuscript with input from all co-authors. H.-G. J. Chou performed the OSIRIS 2-D simulation under the supervision of F. Fiuza.

6.3.2 Abstract

Here we extend flatbed scanner calibrations of GafChromic EBT3, MD-v3, and HD-v2 radiochromic films using high-precision X-ray irradiation and monoenergetic proton bombardment. By computing a visibility parameter based on fractional errors, optimal dose ranges and transitions between film types are identified. The visibility analysis is used to design an ideal radiochromic film stack for the proton energy spectrum expected from the interaction of a petawatt laser with a cryogenic hydrogen jet target.

6.3.3 Introduction

Ion acceleration from high-intensity laser-plasma interactions has attracted great interest due to potential applications ranging from fast ignition inertial confinement fusion [29, 30] to precision tumor treatment with proton therapy [31–33]. Recently, research in ultra-high dose rate (FLASH) proton radiotherapy ($\geq$40 Gy/s), such as those readily obtained with laser-accelerated proton beams, has been rekindled after a significant reduction in toxicity to healthy surrounding tissues was observed post-treatment [83, 203]. While these applications have yet to be fully realized, laser-accelerated proton beams have been widely used in high-energy-density science experiments for proton radiographic imaging of laser-produced

plasmas [36, 37], stopping power measurements [42, 204], and to produce isochorically heated warm dense matter [3, 38, 205].

Proton radiography has arguably been the most successful application of laser-driven proton beams to date. The laminarity, apparent divergence from a micron-sized virtual source point, and broad energy bandwidth (1−85 MeV) make proton beams accelerated by the Target Normal Sheath Acceleration (TNSA) mechanism well suited for probing electric and magnetic fields that are tens of microns in size and evolving on the picosecond timescale [51]. If the proton beam diverges for tens of millimeters before probing an electric or magnetic field, a geometric magnification of the interaction is obtained; however, the temporal dispersion of the ion beam can exceed ∼100 ps. A spatially and energy resolving detector, such as a radiochromic film stack [206–211], is then required for picosecond resolution snapshots of fast-evolving fields occurring in high-intensity laser-plasma interactions.

Several radiochromic film (RCF) types exist with different dose sensitivities. A 'stack' of RCF consisting of multiple film types is routinely used to collect energy-resolved measurements. Ion energy measurements made with RCF exploit the characteristic energy deposition curve of a ballistic ion through matter, commonly referred to as the Bragg curve. When a projectile ion travels through a cold material, the velocity, v, decreases after successive inelastic collisions with bound electrons. Due to the large difference in mass between the ion and electrons, the initial ion trajectory is unaffected until the ion energy is comparable to that of bound electrons in the cold material. As the ion slows, the interaction cross section, also referred to as the stopping power, increases proportionally to $1/v^2$. A detector consisting of successive layers of radiation-sensitive film can be used to measure the energy profile of an ion beam determined only by the stack thickness. To increase the energy separation between successive layers, metallic filters can be added. This becomes particularly important to design a large-energy-range stack that provides high dynamic range.

In this work, we present the calibrations of GafChromic (Ashland, Covington, KY) EBT3, MD-v3, and HD-v2 films with a primary focus on calibration uncertainty to optimize the RCF stack for use as a quantitative diagnostic in petawatt laser-driven proton acceleration experiments.

6.3.4 Dose deposition in radiochromic film

Radiochromic films are designed for 2-D dosimetry measurements of X-ray, electron, ion, and neutron beams. Upon exposure to ionizing radiation, the dye in the active layer of the film darkens as a function of the deposited dose. GafChromic EBT3, MD-v3, HD-v2 cover low to high dose ranges, respectively. Unlike other detectors (e.g. ionization chambers), radiochromic film are believed to have a dose-rate independent response. An experiment

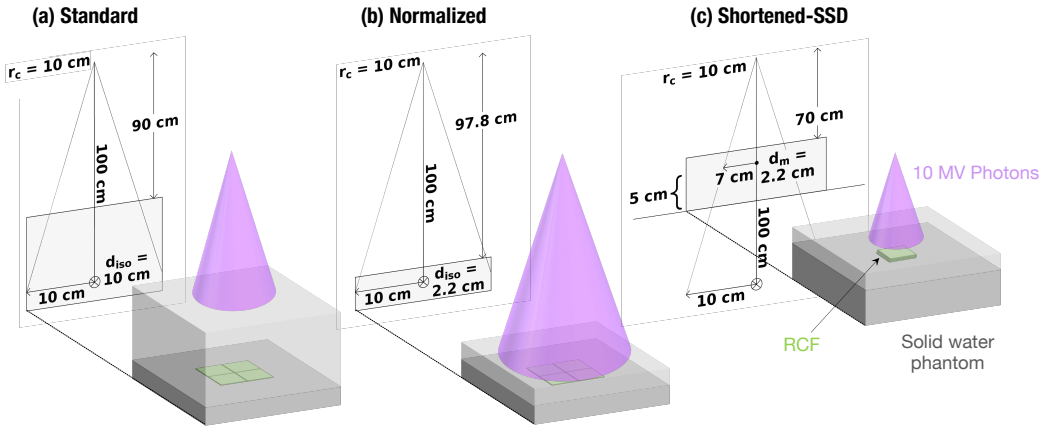

Figure 6.6: (a) Standard treatment setup with 90 cm source-to-surface distance (SSD) and isocenter at a depth (d_{iso}) of 10 cm. The flattening filter was used. (b) Normalized treatment setup with 97.8 cm SSD and isocenter at 2.2 cm depth, which is the depth of maximum dose for 10 MV photons. The flattening filter was used. (c) Shortened-SSD treatment setup with 70 cm SSD with films placed a depth (d_m) of 2.2 cm, which is the depth of maximum dose for 10 MV photons. No flattening filter was used. The grey shaded region represents solid water slabs in all three configurations. RCF was irradiated in a 2×2 grid (standard, normalized) or stack of four (shortened-SSD) as depicted by the green squares.

performed at the Next Linear Collider Test Accelerator (NLCTA) at SLAC National Accelerator Laboratory demonstrated dose-rate independence up to 9×10^{12} Gy/s [212]. Here, we use high-precision X-ray irradiation to accurately resolve the initial increase in optical density then a 2-D Gaussian monoenergetic proton beam to attain higher doses thereby extending the calibrations into the saturation regime. Note that MD-v3 films were not included in the proton measurements.

High-precision X-ray irradiation

Three different setups were used during the the X-ray film irradiations adapted for the total intended dose: standard, normalized, and shortened-source-to-surface distance (shortened-SSD) with 10 MV photon beams from a Truebeam linear accelerator (Varian Medical Systems, Palo Alto, CA) at BC Cancer – Victoria. A schematic of each setup is shown in Fig. 6.6. The films were placed in a rectangular phantom consisting of solid water slabs (CIRS, Norfolk, VA) at a setup-dependent depth described below. In each setup, a 5 cm slab was placed below the films to provide sufficient backscatter. In each of the three different treatment field setups, the collimator jaws were set to produce a 10 cm × 10 cm field at the isocenter of the linear accelerator at 100 cm from the source. The output of the linear accelerator was determined with an N30013 model Farmer ionization chamber (PTW, Freiburg,

Germany) with the chamber placed in the location of the film based on the AAPM TG 51 protocol [213]. The output of the linear accelerator, which differed by shift and configuration, is summarized in Table 6.5.

In the standard setup, the films were placed at 10 cm depth in the phantom at 90 cm SSD. In the normalized setup the films were placed at 2.2 cm depth, the depth of maximum dose for 10 MV photons at SSD of 97.8 cm. For both of these setups, a flattening filter mode with a dose rate of 600 Monitor Units per minute (MU/min) was used that resulted in a flat beam profile to allow for simultaneous irradiation of 4 films arranged in a 2×2 grid. These irradiation setups were suitable for delivering low and medium doses between 0.1 and 255 Gy to the EBT3 and MD-v3 films.

In the shortened-SSD setup the films were placed at a depth of 2.2 cm at an SSD of 70 cm, which is the shortest distance within the geometrical constraints of the linear accelerator. While the reduced-SSD setup doubled the output of the linear accelerator, allowing faster dose delivery, the field size at film location was reduced to 7 cm × 7 cm. The flattening filter was removed in this setup, which quadrupled the dose rate from 600 MU per minute to 2400 MU per minute using the 10 MV flattening filter free (FFF) mode. The combined effect of the reduced SSD and the removed flattening filter increased the irradiation rate eight-fold, which is more suitable for delivering high doses of between 125 and 2000 Gy to the MD-v3 and HD-v2 films. The removal of the flattening filter resulted in a Gaussian beam profile that is flat to within 3% standard deviation in the 2 cm central beam area, which just covered one film. Four films were stacked and irradiated together. Even if the four films were all the thicker MD-v3 film, this stacking would reduce the dose in bottom film by at most 0.4% due to the film thickness of 260 µm.

Monoenergetic proton bombardment

Complementary measurements were performed with monoenergetic protons from the TR24 cyclotron located at the Medical Isotope and Cyclotron Facility (MICF, University of Alberta). The proton beam energy and approximate charge were calculated from the activation

	Standard	**Normalized**	**Shortened-SSD**
Shift 1	5.100	5.940	48.384
Shift 2	N/A	6.090	46.272
Shift 3	N/A	6.090	46.272
Shift 4	N/A	5.982	45.000

Table 6.5: Summary of linear accelerator outputs (Gy/min) on the four different shifts of irradiation for each of the three different treatment setups depicted in Fig. 6.6 (a) – (c).

of natural copper foils placed behind the radiochromic films. The nuclear activity of the copper after proton irradiation was measured using a high purity germanium (HPGe) high resolution gamma spectrometer. Using the ratio of the ^{nat}Cu(p,x)^{62}Zn and ^{nat}Cu(p,x)^{63}Zn reaction probabilities, the incident proton energy can be precisely determined. The proton energy in the active layer of the HD-v2 (18.0 ± 0.3 MeV) and EBT3 (17.2 ± 0.3 MeV) films was inferred using the continuous slow-down approximation (CSDA). The proton stopping powers from the NIST PSTAR data base combined with the proton charge computed from the total copper activity are used to estimate the dose. Major sources of error on the absolute charge arise from the gamma counting statistics, uncertainty in the HPGe detector efficiency, and nuclear activation cross sections. More details about the set-up and methods can be found in Ref. 214.

6.3.5 Extended-range radiochromic film calibrations

After exposure, all radiochromic films were placed in a light-tight box to develop for at least 48 hours. They were then scanned with an Epson Perfection V750 Pro flatbed scanner in transmission mode [215]. Both 16-bit greyscale and 48-bit RGB images were recorded with a resolution of 300 dots per inch (dpi). For each film type and batch, a reference (non-irradiated) film was stored in the same conditions and used to remove background dose accumulation over time, film aging, and batch-to-batch variability. The change in optical density (OD) as a function of dose was then computed directly from the exposed and reference films according to:

$$\Delta OD = OD - OD_0 = -log_{10}\left(\frac{C_{exp}}{C_{ref}}\right) \tag{6.33}$$

where C_{exp} and C_{ref} are the transmitted signal in counts for the exposed and reference film respectively [216]. The OD of the films irradiated by X-rays was measured by averaging across the entire film, excluding a narrow border around the edges and visible irregularities due to dust or scratches on the film.

Monoenergetic protons, on the other hand, were delivered with a Gaussian, radially symmetric dose profile resulting from a 0.5 mm pinhole located 237 mm from the films. A normalized dose profile was obtained from the EBT3 film with the lowest deposited dose which had the full range of OD covered by the X-ray calibration. Benefiting from the overlapping dose ranges provided by the Gaussian distribution, the absolute dose in subsequent films was iteratively determined from low to high dose. The same procedure was performed for HD-v2. In both cases, the more-precise normalized dose profile from EBT3 could be used since the separation between the films was negligible. For clarity, only the maximum dose and the corresponding 1σ variation resulting from the iterative technique are shown in the

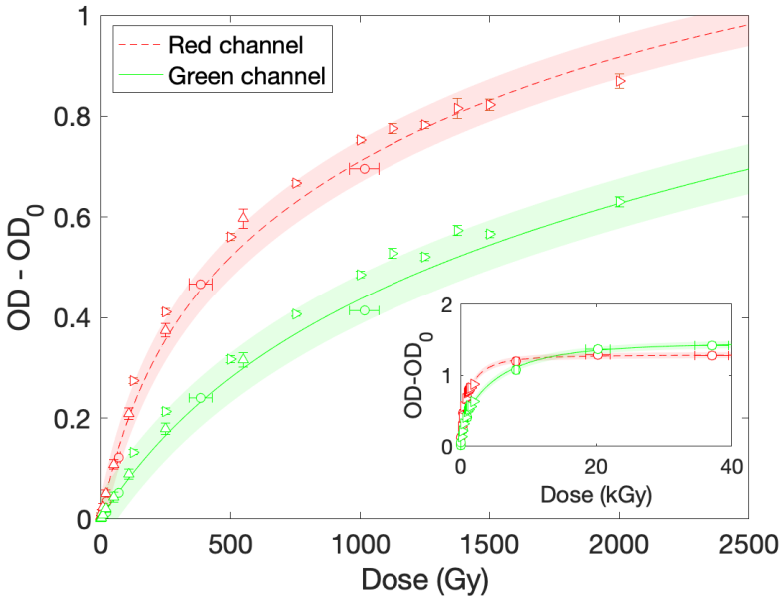

Figure 6.7: Calibration of HD-v2 using an Epson Perfection V750 Pro flatbed scanner in transmission mode. Data consist of X-ray irradiation (right pointing triangles), 18.0 MeV monoenergetic proton bombardment (circles), and measurements by Chen et al. [201] (up pointing triangles) using the same X-ray irradiation methodology as Sec 6.3.4. Inset: Saturation behavior of HD-v2.

calibration figures.

Numerous calibrations of HD-v2 have been conducted in recent years [201, 217, 218]. Bin et al. [218] have shown that calibrations can be extended to very high doses exploiting the high stopping power of low energy protons (i.e. 1.06 MeV); however, the dose must have a linear energy transfer (LET) correction applied to account for a decrease in film response near the Bragg peak due to ionization along the proton trajectory [180]. In addition, the total uncertainty in the calibration and the scanner response function, which were not taken into account in the study, may limit its usable dose range. Alternatively, Feng et al. [214] have developed an advanced scanning technique using a monochromatic (e.g. 468 nm) pixel-by-pixel transmission scanner that can extend the usable range upwards of 25 kGy. Despite this, conventional flatbed scanners remain the most common method to digitize radiochromic film. Here we use use a combination of precision X-ray irradiation and monoenergetic proton bombardment to determine a robust calibration and focus specifically on optimal dose ranges based on total uncertainty.

The resulting calibration for HD-v2 is shown in Fig. 6.7. The inset in Fig. 6.7 shows the very-high dose behavior of the optical density. A saturation plateau is clearly identified above approximately 10 kGy. We tested the manufacturer's suggested model for the functional

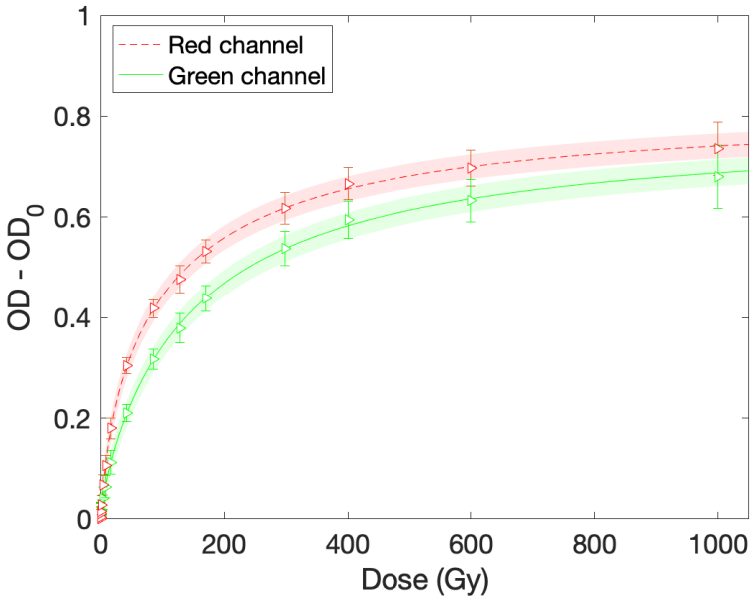

Figure 6.8: Calibration of MD-v3 using an Epson Perfection V750 Pro flatbed scanner in transmission mode. All measurements performed with X-ray irradiation.

dependence between OD and dose but found that the data for all three film types was better fit to second- or third-order rational functions with positive fitting coefficients. The resulting fits for the red and green channel of HD-v2 are given by:

$$\Delta OD_{R,\,HD\text{-}V2}(d) = \frac{1.288d^3 + 5097d^2 + 6.543d \times 10^6}{d^3 + 4018d^2 + (1.049d + 266.6) \times 10^7} \tag{6.34}$$

$$\Delta OD_{G,\,HD\text{-}V2}(d) = \frac{1.475d^3 + 10530d^2 + 6.308d \times 10^7}{d^3 + 7492d^2 + (8.571d + 7775) \times 10^7} \tag{6.35}$$

where ΔOD_R, and ΔOD_G are the change in optical density computed from Eqn. 6.33 for the red and green channels respectively and d is the dose in gray.

In the case of MD-v3 (Fig. 6.8), both the red and green channels provide a high quality calibration curve over the range of 10–1000 Gy. At low doses, the red channel is more responsive but begins to plateau near 180 Gy. Above these doses, the green channel should be used. Both channels reach saturation at approximately 1000 Gy. The calibration curves for MD-v3 are given by:

$$\Delta OD_{R,\,MD\text{-}V3}(d) = \frac{0.8162d^2 + 42.41d}{d^2 + 156.1d + 2394} \tag{6.36}$$

$$\Delta OD_{G,\,MD\text{-}V3}(d) = \frac{0.7846d^2 + 18.33d}{d^2 + 165.6d + 1678} \tag{6.37}$$

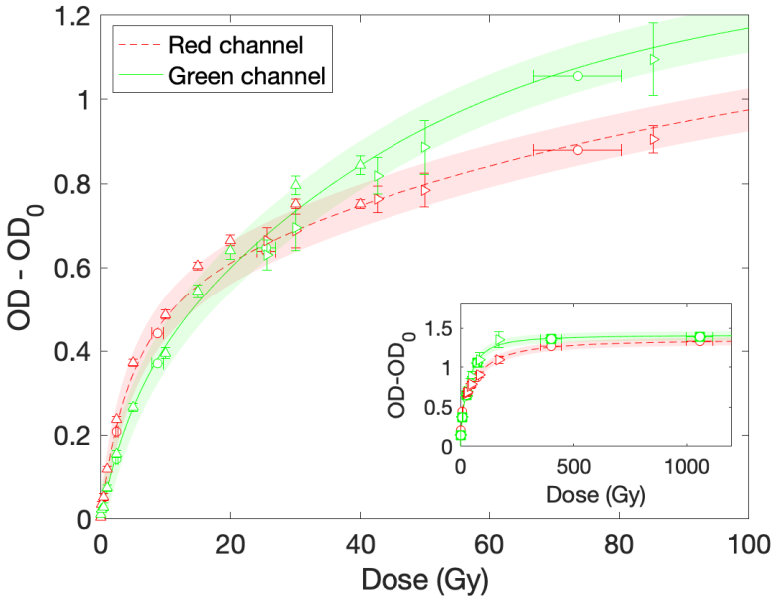

Figure 6.9: Calibration of EBT3 using an Epson Perfection V750 Pro flatbed scanner in transmission mode. Data consist of X-ray irradiation (right pointing triangles), 17.2 MeV monoenergetic proton bombardment (circles), and measurements by Chen et al. [201] (up pointing triangles) using the same X-ray irradiation methodology as Sec 6.3.4. Inset: Saturation behavior of EBT3.

Finally, EBT3 calibrations (Fig. 6.9) were extended from previously published values [201, 219–221] up to approximately 1000 Gy. The red channel is more sensitive at low doses. A saturation plateau is identified at approximately 200 Gy. The fits for the red and green channels of EBT3 are given by:

$$\Delta OD_{R,\,EBT3}(d) = \frac{1.362d^3 + 75.26d^2 + 7247d}{d^3 + 82.22d^2 + 10310d + 57680} \tag{6.38}$$

$$\Delta OD_{G,\,EBT3}(d) = \frac{1.416d^3 + 7.699d^2 + 1969d}{d^3 + 17.48d^2 + 2432d + 26180} \tag{6.39}$$

6.3.6 Diagnosis of high-flux ion beams from petawatt-class lasers

Recently, higher conversion efficiency ion acceleration mechanisms have been demonstrated using high-energy lasers with pulse durations ranging from 1 ps to 10 ps [222]. In particular, recent experiments utilizing the 1.5 kJ Advanced Radiographic Capability (ARC) laser at the National Ignition Facility have demonstrated proton fluxes on the order of 10^{13} protons/MeV/sr [223]. With improvements to beam focusability using hemispherical targets [38], multi-beam synchronization, and laser pulse contrast, it is ultimately expected that

proton beams with fluxes exceeding 10^{14} protons/MeV/sr will be produced.

Since RCF remains the preferred detector for high dynamic range, large-angle measurements of laser-accelerated proton beams, it is important to quantify the dose-dependent error due to the film calibrations and the read-out method. Using this, the stack design can be optimized to yield high visibility measurements at experimentally-relevant energies. Although calibrations have been extended well above the manufacturer's recommended dose range, the uncertainty in dose and computed incident particle flux increases exponentially as the films saturate. To assess this effect quantitatively, we can define a dose-dependent visibility for each film type according to:

$$V(d) = 1 - \max\left(\frac{s\varepsilon_{OD}}{df'(d)}, \frac{\varepsilon_d(d, \varepsilon_{OD})}{d}\right) \tag{6.40}$$

where s, ε_{OD}, d, $f'(d)$ are the minimum signal-to-noise ratio, the average 1σ variation in optical density from the scanner used, the dose in gray, and the first derivative of optical density with respect to dose from the calibration. ε_d is the error in dose computed numerically by convolving the 1σ error in the calibration with the 1σ uncertainty in optical density from the scanner. For our case, we set the minimum signal-to-noise ratio to 2 and found that ε_{OD} was 0.01. The first term in the maximum only considers the error resulting from background noise on the scanner, important at low doses when the films have small changes in OD. Once the OD is several times the scanner noise, the uncertainty in the calibration curve, included with the second term, becomes dominant. Note that a visibility less than or equal to zero represents a >100% uncertainty in the absolute computed dose even if a change in OD is detected.

The computed visibility curves based on the calibration for the green channel of HD-v2, MD-v3 and EBT3 are shown in Fig. 6.10. This metric makes it clear that it is necessary to include a film sensitive to intermediate dose levels, such as MD-v3, in order to resolve a broadband source such as a semi-Maxwellian TNSA proton energy distribution. Also, it is clearly evident that the visibility drops rapidly and far below the maximum calibrated values of HD-v2 to date. In order to maximize the visibility across the RCF stack, the transition from EBT3 to MD-v3 and MD-v3 to HD-v2 should occur at 71.45 Gy and 580.7 Gy respectively.

Using this formalism, we can design an RCF stack that is optimized for laser-driven ion acceleration with a petawatt laser. Here we use a proton energy spectrum from a 2-dimensional (2-D) particle-in-cell simulation performed using OSIRIS [224] for a 1 µm thick planar cryogenic hydrogen jet [149, 150] irradiated at normal incidence by the Texas Petawatt laser (135 J, 135 fs, $\sim 10^{21}$ W/cm^2). The resulting proton energy spectrum, measured in the

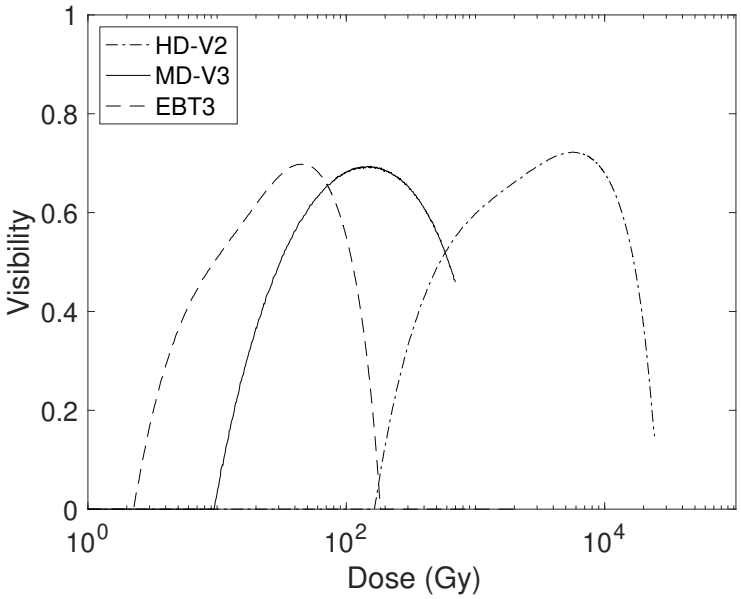

Figure 6.10: Visibility as a function of dose computed from Eqn. 6.40 for the green channel calibration of EBT3 (dashed), MD-v3 (solid), and HD-v2 (dot-dashed).

2-D simulation normal to the target surface, was corrected for 3-D effects by scaling down the proton energy by a factor of 3. In previous studies comparing the results of 2-D and 3-D simulations of laser-jet interactions with experimental data, we have found that this scaling factor typically allows for a reasonable extrapolation of the 2-D proton spectrum to 3-D [15]. Similar scaling factors were observed by other groups [225]. The proton spectrum was then normalized to ensure a number of protons of 2.3×10^{13} protons/MeV/sr consistent with the typical conversion efficiency and half-angle divergence for TNSA (10%, 20° at 1 MeV) and is shown in the top plot in Fig. 6.11. A simulated proton spectrum can be used for the initial stack design followed by iterative improvements with experimental data.

The resulting RCF stack for detection up to 85 MeV which maximizes the visibility consists of 1×(13 µm Al + HD-v2) + 7×(100 µm Al + HD-v2) + 1×(100 µm Al + MD-v3) + 6×(150 µm Cu + MD-v3) + 1×(500 µm Cu + MD-v3) + 12×(500 µm Cu + EBT3). The energy deposition profiles for each RCF layer are shown in the middle row of Fig. 6.11. Stopping power tables from SRIM are used to determine the energy deposited in each layer and an LET correction is applied [180]. The resulting dose is computed for a typical distance of 55 mm to the front of the RCF stack. Since the thickness of large-energy-range RCF stacks is non-negligible, the distance is updated for each successive layer.

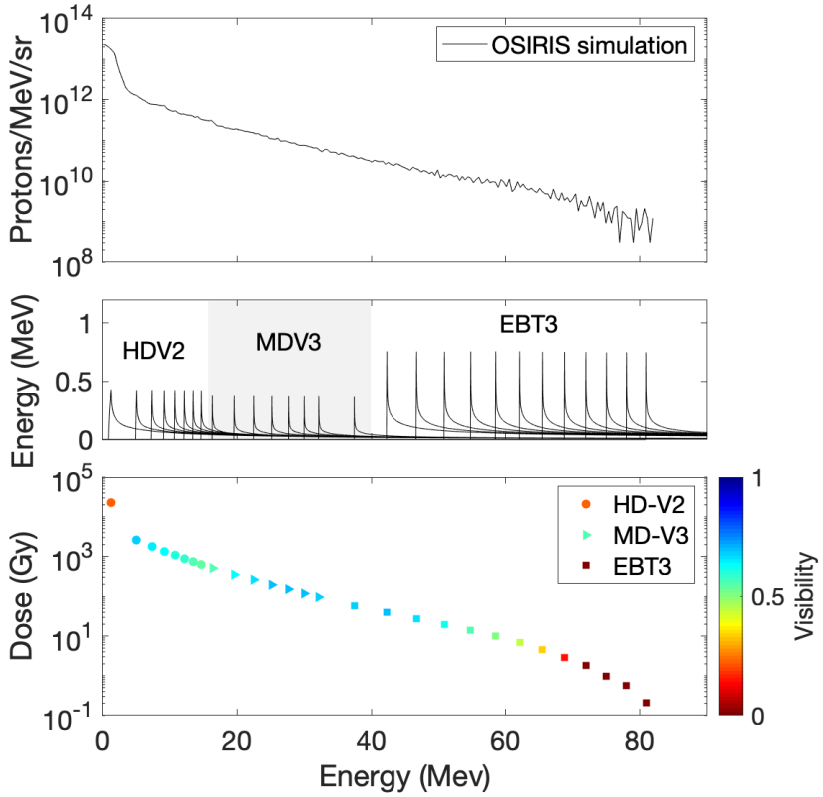

Figure 6.11: Top: Proton energy spectrum obtained from a 2-D PIC simulation of a solid-density 1 µm thick planar hydrogen target irradiated by a high-energy petawatt laser. The proton energy was scaled down by a factor of 3 to correct for the impact of 3-D effects on reducing the maximum energy. Middle: Radiochromic film stack design to detect high-flux proton beams. Each curve represents the average energy deposited per proton in a single RCF layer using SRIM stopping power tables with an LET correction [180] applied. Bottom: Corresponding dose deposited in RCF stack. Visibility of dose variations in HD-v2 (circles), MD-v3 (triangles), and EBT3 (squares) are indicated by the variation in color.

6.3.7 Conclusion

In this work, we have presented extended-dose calibrations of GafChromic EBT3, MD-v3, and HD-v2 radiochromic films and have defined optimal dose ranges for each film type based on visibility. Robust film calibrations are needed when using radiochromic film stacks to record quantitative proton spectra produced by petawatt-class short-pulse lasers. Until now, research in laser-produced ion beams has predominantly focused on smooth, laminar beams. Laser and target technology [226, 227] or the use of pulsed high-field solenoid lenses [228] has recently led to tightly-focused or structured ion beams. The deflections and perturbations observed on the ion beam can contain information about the ultra-fast plasma processes occurring in the interaction. It is therefore necessary to fully resolve these features, as a

function of energy, to gain insight into the temporal and spatial scales of instabilities such as Weibel-type instabilities [15, 229]. These calibration curves, used in conjunction with our visibility analysis, will allow the design of film-based large-angle sampling of high-flux ion beams or laser-driven ion beams with high flux zones (i.e. caustics [230]) formed by >100 MG magnetic fields produced in petawatt laser-plasma interactions [231].

6.3.8 Supplemental material

Epson Perfection V750 Pro response function

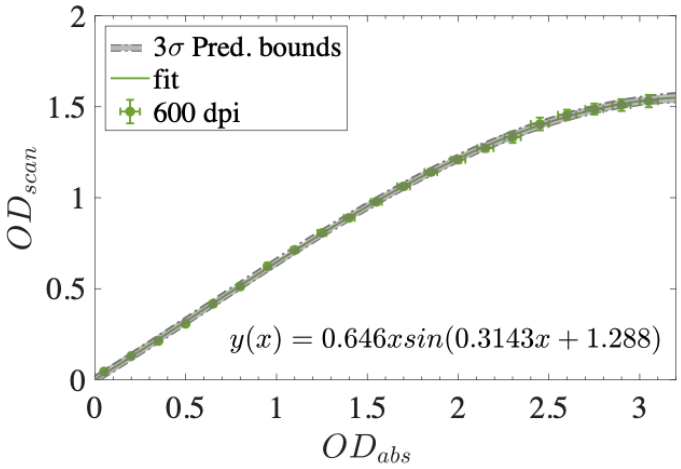

Figure 6.12: Calibrated transmission curve of Epson Perfection V750 Pro conventional flatbed transmission scanner using Stouffer 21-step transmission wedge for the green channel of a 48-bit color image scanned with 600 dpi. The fit (solid black line) and 3σ prediction bounds (dashed grey lines) are shown.

Chapter 7
High Repetition Rate, Multi-MeV Proton Source from Cryogenic Hydrogen Jets

7.1 Preface

Most envisioned commercial applications of laser-plasma ion acceleration rely on continuous or pulsed operation at frequencies above 1 Hz. As described in Chapter 5, cryogenic jets are a promising target for laser-driven ion acceleration using high repetition rate short pulse lasers. An overview of current and future high repetition rate short pulse laser systems can be found in Appendix B. They are inherently debris free since all residual target material will vaporize when it makes contact with an ambient temperature component. The gas is then evacuated from the target chamber through the vacuum system. As a result, they are highly preferred over standard solid targets, which can damage laser transport optics or diagnostics near the interaction when they are coated by plasma deposition or impacted by target shrapnel, for sustained high repetition rate operation. Cryogenic liquid jets can be produced from a range of elements beyond hydrogen and deuterium presented in this thesis. To date, cylindrical liquid neon, argon, methane, and krypton have also been demonstrated with the same system and used in experiments.

In this work, we demonstrate for the first time a stable, 1 Hz pure proton source delivering $\sim 10^{13}$ protons/MeV/sr/min and proton energies up to 6.5 MeV using the Draco 100 TW laser at Helmholtz-Zentrum Dresden-Rosendorf (HZDR) [14]. This study utilized a 5 µm diameter cylindrical cryogenic hydrogen jet (see Chapter 5), Thomson Parabola ion spectrometers, and radiochromic film stacks (see Chapter 6). Subsequently, several studies have been performed to investigate the laser contrast and resulting pre-plasma scale length [232] required to optimize laser-driven ion acceleration to reach higher proton cut-off energies [233]. Additionally, planar hydrogen jets were developed and shown to produce directional ion beams with fluxes comparable to TNSA from metallic foils [150].

The remainder of Chapter 7 is published as: M. Gauthier, C. B. Curry, S. Goede, F.-E. Brack, J. B. Kim, M. J. MacDonald, J. Metzkes, L. Obst, M. Rehwald, C. Roedel, H.-P. Schlenvoigt, W. Schumaker, U. Schramm, K. Zeil, and S. H. Glenzer, *High-repetition rate, multi-MeV proton source from cryogenic hydrogen jets*. Appl. Phys. Lett. **111**, 114102 (2017). The experiment was designed and led by K. Zeil and S. Goede. K. Zeil, S. Goede, M. Gauthier, F.-E. Brack, J. B. Kim, M. J. MacDonald, J. Metzkes, L. Obst, M. Rehwald, C. Roedel, H.-P. Schlenvoigt, and W. Schumaker performed the experiment. U. Schramm

and S. H. Glenzer supervised the project. M. Gauthier was the lead postdoctoral researcher on the high-repetition rate dataset presented in the following manuscript. M. Gauthier and I worked jointly on the data analysis and presentation. I wrote the manuscript with input from all co-authors.

7.2 Abstract

We report on a high repetition rate proton source produced by high-intensity laser irradiation of a continuously flowing, cryogenic hydrogen jet. The proton energy spectra are recorded at 1 Hz for Draco laser powers of 6, 20, 40, 100 TW. The source delivers $\sim 10^{13}$ protons/MeV/sr/min. We find that the average proton number over one minute, at energies sufficiently far from the cut-off energy, is robust to laser-target overlap and nearly constant. This work is therefore a first step towards pulsed laser-driven proton sources for time-resolved radiation damage studies and applications which require quasi-continuous doses at MeV energies.

7.3 Introduction

Laser-driven ion acceleration has attracted great interest due to the potential applications in the fast ignition approach to inertial confinement fusion [29, 30], proton radiographic imaging of laser-produced plasmas [36, 37], and stopping power measurements [41, 42]. Various other applications in medicine [31–35] and industry [234] have also been explored. In the last two decades, several acceleration mechanisms have been proposed and partially demonstrated [12]. The most robust and studied acceleration mechanism is Target Normal Sheath Acceleration (TNSA). When a high power laser is focused to relativistic intensities on a solid-density foil, relativistic electrons are generated at the front surface and propagate through the target. For micron-thick foils, these electrons escape from the rear surface generating a quasi-static electric field, on the order of TV/m, which accelerates protons and ions from the contaminant layer to MeV energies normal to the target surface [3, 104].

Cryogenic hydrogen jets offer an alternative to conventional metallic foils, generating a pure proton beam without producing debris. The latter becomes increasingly important for high-repetition rate pulsed proton sources. Additionally, the low density and tunable target thickness makes the cryogenic hydrogen jet highly suitable for studying alternative proton acceleration regimes [8, 9] predicted to generate higher energy proton beams. Recently, several studies have been conducted on laser-driven proton acceleration from cryogenic hydrogen targets with different laser conditions [149, 151, 156, 235].

In this work, we report on the first experimental demonstration of a 1 Hz pulsed proton

source generated from cryogenic hydrogen jets irradiated by the Draco laser at Helmholtz-Zentrum Dresden-Rossendorf (HDZR). The absolute proton energy spectrum recorded at 1 Hz exhibits a semi-Maxwellian energy distribution characteristic of TNSA. The stability of the proton source was investigated by measuring the statistical fluctuations of the proton flux integrated over one minute at a given energy. Measurements were also collected at several reduced laser powers to study the maximum proton energy scaling for these targets. Furthermore, the advantages of cryogenic jets in high repetition rate experiments are discussed.

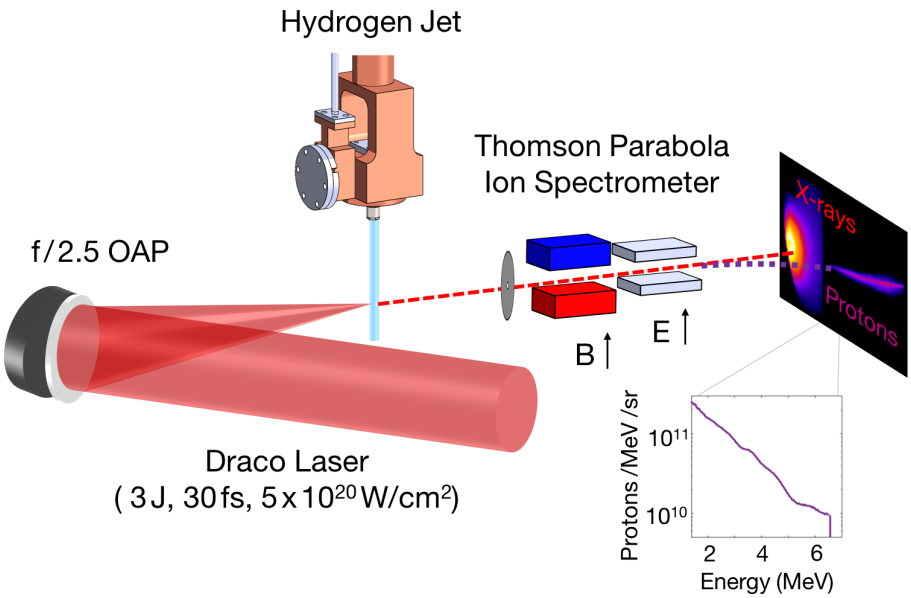

Figure 7.1: Schematic of the experimental set-up for 1 Hz proton acceleration from a hydrogen jet. Fast detection Thomson Parabola (TP) Ion Spectrometers were positioned in the laser forward direction and ±45°. Experimental data of a pure proton spectrum up to 6.5 MeV on the 0° TP is shown. The ±45° TPs and imaging systems are not shown for clarity.

7.4 Experimental setup

The experiment was performed with the Draco short pulse Ti:Sapphire laser system (0.5–3 J, 30 fs, 1 Hz) focused using an f/2.5 off-axis parabola (OAP) to a 3 µm (FWHM) focal spot diameter onto the cryogenic hydrogen jet. This experiment reaches laser intensities of $0.3–5\times10^{20}$ W/cm^2 corresponding to a normalized vector potential, $a_0 \simeq 5–21$. The laser contrast was measured with a third-order autocorrelator to be 10^{-7} at -7 ps. A schematic of the experimental set-up is shown in Fig. 7.1.

The hydrogen jet was generated by a copper assembly cooled by a liquid-helium continuous-

flow cryostat. Hydrogen gas is liquefied in the source assembly, cooled to a temperature of 18 K, then injected through a ⌀10 µm Pt/Ir aperture. In vacuum, the liquid hydrogen continues to cool by evaporative cooling and solidifies before onset of the Plateau-Rayleigh instability [147]. Therefore, the laser interaction region can be up to several centimeters from the source assembly which prevents damage to the aperture from electron heating. At an injection pressure of 2 bar, a jet speed of approximately 70 m/s is expected. We can estimate compatibility of such a target with laser repetition rates up to 1 kHz which greatly exceeds other continuous targets. This estimate assumes a volume element initially in the interaction region has traveled 7 cm away before the arrival of the next laser pulse. It is worth noting that the high repetition rate capabilities of cryogenic hydrogen jets make them ideal targets for experiments combining laser and x-ray free-electron laser (FEL) sources [154].

In this study, two f/2 imaging systems operated at 400 nm and 800 nm were used to align the target position relative to the laser focus with micron precision. The spatial jitter of the jet is dominated by angular motion about the aperture output. Consequently, the spatial jitter of the jet in the laser plane increases linearly with distance away from the source aperture. During this experiment, the interaction region was 15 mm below the nozzle where the spatial jitter of the jet position was measured to be approximately ±7 µm.

7.5 Results

The proton energy spectrum and flux from the interaction were measured using three energy-calibrated Thomson Parabola (TP) ion spectrometers positioned at 0° and ± 45° relative to the laser propagation direction. The 0° TP consisted of a 500 µm pinhole located 0.5 m from the source with a 0.6 T magnetic field to spatially separate the protons by energy. A 40 mm diameter micro-channel plate (MCP) coupled to a phosphor screen and imaged onto a CCD camera allowed fast detection of the proton beam at rates exceeding the laser repetition rate of 1 Hz. The size of the MCP limited the minimum detectable proton energy to ∼1.4 MeV.

The signal-to-proton number calibration of the 0° TP was obtained using Radiochromic film (RCF) stacks, consisting of one layer of HD-810 and several of EBT-2 [236], shielded by a13 µm thick aluminum foil. Each stack was inserted on a single-shot basis in the laser-forward direction (0°) at 55 mm from the proton source covering approximately a ± 20° angle. A 3 mm diameter central clearance hole in the RCF allowed simultaneous proton detection by the TP. The calibration compared the RCF dose in each layer to the TP energy spectrum [80]. This method assumes that the MCP efficiency as a function of proton energy is constant [237]. The uncertainty in the calibration is dominated by the spatial non-uniformity of the proton beam [151] giving a systematic uncertainty of ±20% on the absolute proton number.

The proton beams have a semi-Maxwellian energy distribution with a well defined energy

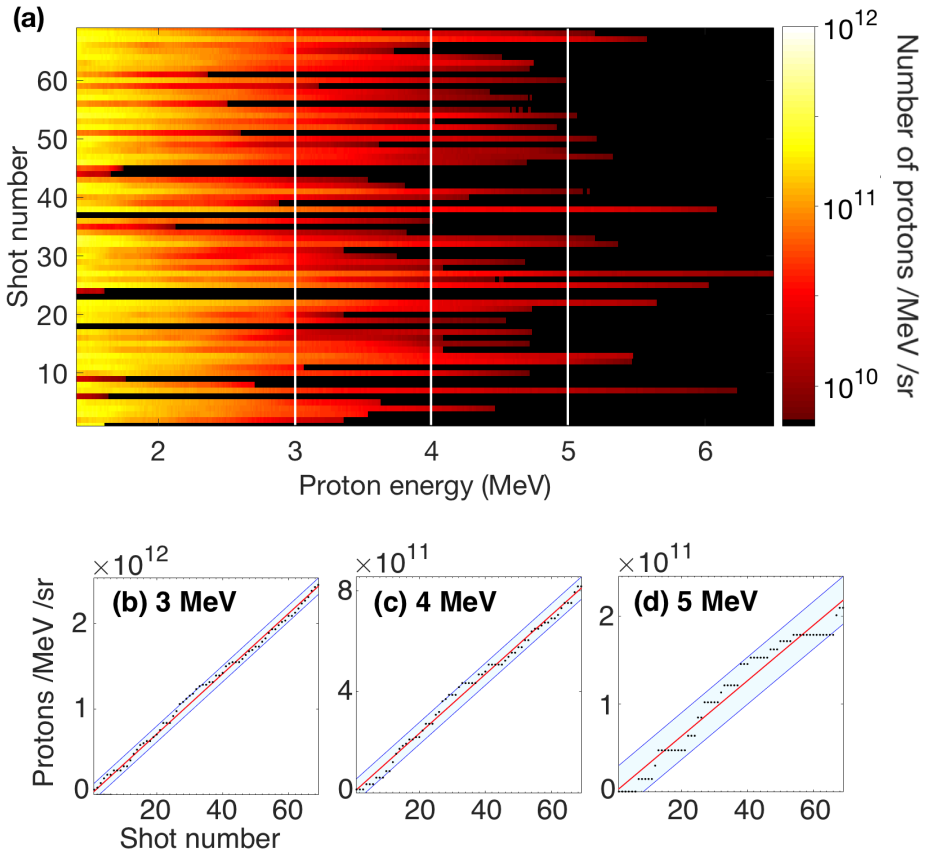

Figure 7.2: (a) Proton energy spectrum in the laser forward direction for 68 shots at a laser power of 100 TW recorded at 1 Hz. Cumulative sum of protons at (b) 3 MeV, (c) 4 MeV, and (d) 5 MeV for the same shots. The solid-red line is a linear fit and the 95% confident limits are indicated by the shaded region.

cut-off (E_{CO}) typical of TNSA [104] as shown in Fig. 7.1. Here, the hot electron temperature inferred from the slope of the spectra is ∼1 MeV for a measured maximum cut-off energy of 6.5 MeV. Measurements of the proton energy spectra at ±45° indicate TNSA-like emission from cylindrical targets [151, 238]. The proton spectra in the laser forward direction, measured at the highest laser intensity (5×10^{20} W/cm^2), for a one-minute series of shots are presented in Fig. 7.2 (a). The stability of the pulsed proton source has been investigated for single-shot and continuous operation.

The proton flux at 3 MeV varies by ∼50% from shot-to-shot and the average cut-off energy is 4.0 ± 1.2 MeV following a normal distribution (see Supplemental material). The spread in proton flux and cut-off energy can be explained by: variation in laser energy (<1% RMS); sampling a spatially nonuniform and fluctuating proton beam[151]; or laser-target overlap. In this experiment, the spatial jitter of the jet (7 µm) is comparable to the target radius (5 µm), and expected to be the dominant source of energy fluctuations. In addition,

the laser energy coupling is further reduced by any offset from the nominal position due to the projection of the laser on the cylindrical target. To improve the stability of the source, the lateral extent of the target could be increased to several times the spatial jitter of the target; however, such cylindrical hydrogen jets would become too thick for optimal TNSA conditions. Moreover, as the jet flow rate is proportional to the square of the radius, the load on the vacuum system would also increase by a considerable amount. An alternative would be to use a hydrogen ribbon [156] or planar sheet[150] more recently demonstrated on a single-shot basis.

In order to quantify the stability of the pulsed proton source at 1 Hz, the cumulative proton flux for three energies is shown in Fig. 7.2 (b), (c), and (d). Each data series follows a linear trend, shown in red, with the 95% confidence bounds represented by blue shaded regions. During continuous operation, a small confidence interval indicates that the cumulative proton flux at a particular energy is more predictable and converges towards an ideal pulsed source. After 1 minute (60 shots), the uncertainty in the total proton flux at 3, 4, and 5 MeV becomes ±4.4%, ±6.2%, and ±14% respectively. Although the proton flux shows important shot-to-shot variation, the shot-to-shot levels are stable at energies significantly below the average cut-off energy (<3 MeV) and operation times exceeding one minute.

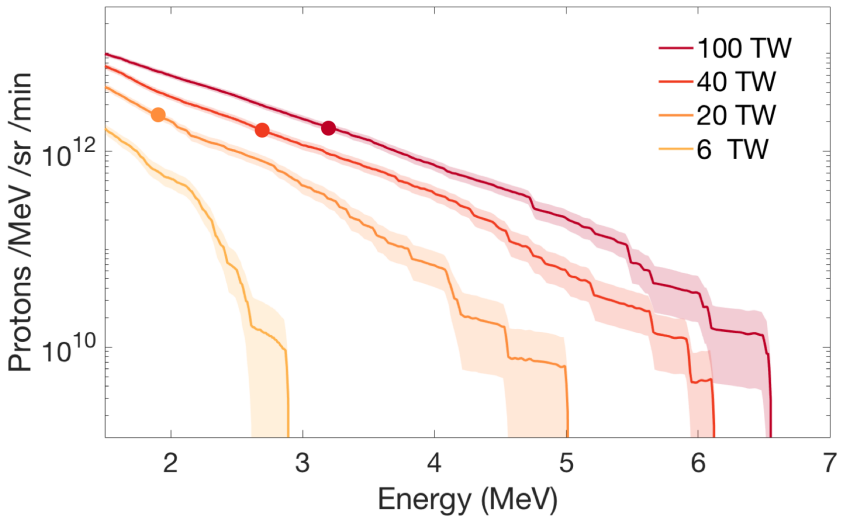

Figure 7.3: Integrated proton flux for 6, 20, 40, 100 TW collected at 1 Hz over one minute. The standard error of the mean is represented by the shaded area. The 0.8 E_{CO} is indicated by filled circles at 1.9 MeV, 2.7 MeV, 3.2 MeV.

The scalability of the maximum proton energy and flux was also studied by measuring the integrated proton energy spectra during 1 Hz operation for laser powers of 6, 20, 40, and

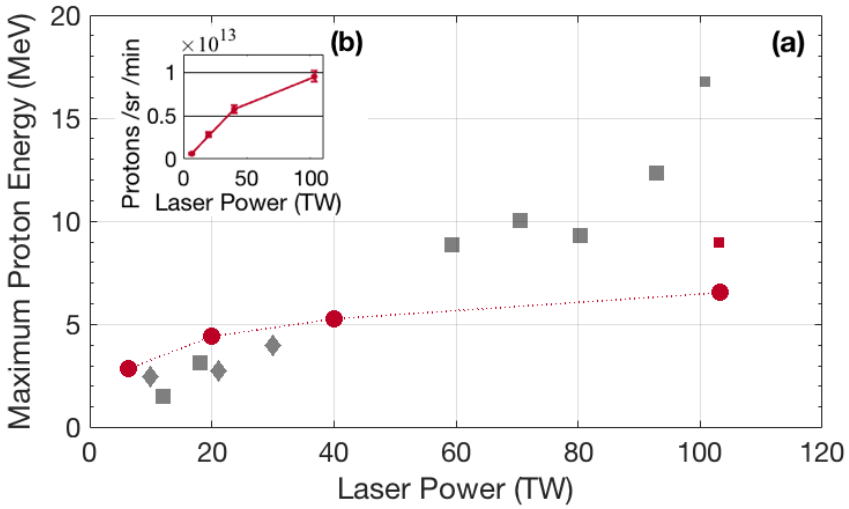

Figure 7.4: (a) The maximum proton cut-off energies from this experiment are shown in red. Red circles correspond to shots on the cylindrical hydrogen jet while the small red square is from a 2 µm Ti foil. The small and large gray squares correspond to 2 µm and 5 µm Ti foil shots from previous experiments with the Draco laser [107]. Black diamonds are maximum proton energies from micron-thick foils with comparable ∼1 J, 25-40 fs laser systems [107, 239]. (b) The number of protons/sr/min are shown as a function of laser power.

100 TW, by varying the laser energy. A representative sample over one minute is shown in Fig. 7.3. Since the hydrogen jet is operable for long periods of time, the sample sets were taken consecutively in order to eliminate other sources of fluctuations. The standard error of the mean (SEM) is represented by the shaded area. For all laser powers, we similarly observe that for energies sufficiently below the average cut-off energy (0.8 E_{CO}), the number of protons at a given energy becomes predictable. For example, the SEM is <10% for 0.8 E_{CO}'s equal to 1.9 MeV, 2.7 MeV, 3.2 MeV for laser powers of 20 TW, 40 TW, 100 TW respectively.

In Fig. 7.4 (a) the maximum cut-off energy from the hydrogen jet for each laser power is plotted. At laser powers <40 TW, we find that our results agree well with, if not exceed, values from micron-thick planar solid-density foils in previous experiments using the Draco laser and other similar laser systems [107, 239]. One explanation for enhanced proton acceleration at low energies is the mass-limited nature of the cylindrical jet [240, 241]. In this case, the hot electrons recirculate more efficiently thereby enhancing the magnitude of the electrostatic sheath field [240]. We note that single-shot experiments with nm-thick foils have demonstrated significantly higher proton energies at low laser powers through alternative acceleration mechanisms [8, 239, 242, 243].

At higher laser powers, however, our spectra are lower than other results from solid-

density foils. The cryogenic hydrogen jet, with a density of only $30n_c$ and its cylindrical geometry, is expected to be more sensitive to the laser pulse contrast compared with standard foils of comparable thickness. At the arrival time of the main 100 TW laser pulse, the scale-length of the pre-plasma was estimated to be $1-2\,\mu m$ at the front and rear sides of the cylindrical jet using interferometry. A more detailed discussion of the target expansion during this experiment can be found in Goede et al., [151]. The lengthening of the density gradient on the target surface, where the TNSA occurs, reduces the electrostatic sheath field, thus decreasing the maximum proton energy [140]. This effect is further confirmed by comparing the maximum proton cut-off energy from a $2\,\mu m$ thick Ti foil measured during this experiment (9 MeV, small red square) to a previous measurement where the laser contrast was optimized for proton acceleration (17 MeV, small gray square, ps-contrast $<5\times10^{-9}$) [107]. As the pre-pulse scales with the laser energy, a smaller expansion is expected at lower laser powers explaining the observed trend.

Similarly, the integrated proton flux within the detection-limit of the TP is plotted with respect to the laser power in Fig. 7.4 (b). The calculated proton number is proportional to the total proton flux, and therefore representative of the conversion efficiency. We find that the proton flux above 1.5 MeV increases linearly with laser power up to 40 TW, in agreement with previous experimental trends [4, 244]. At higher powers, the total number of protons increases more gradually, suggesting that the target has suffered significant pre-expansion which degrades TNSA.

7.6 Conclusion and outlook

Cryogenic hydrogen jets are ideal targets for proton acceleration experiments at high repetition rates facilities as they address two main challenges: target replacement and debris generation. More specifically, the stable proton flux away from the cut-off energy is already suitable for time-resolved radiation damage studies [245]. In addition, the time evolution of microphysical processes occurring in high-intensity laser-plasma interactions can now be investigated at high repetition rate facilities. For example, 100 TW-class laser systems are combined with X-ray free electron lasers (XFELs) such as at the Matter in Extreme Conditions (MEC) end station at SLAC Linac Coherent Light Source (LCLS) [154] or at the future High-Energy-Density (HED) Instrument at European XFEL. To date, several groups have demonstrated continuous tape targets consisting of CH polymers or metals [13, 244, 246] as well as liquid crystal targets [247]. In comparison to these targets, the hydrogen jet produces a pure proton beam and offers additional flexibility in target thickness and geometry.

Interactions with the hydrogen jet are also debris-free and therefore eliminate the need for debris shielding between the target and the large optical components in newly available

high repetition rate petawatt-class laser systems. Not only must these debris shields exhibit exceptional surface flatness to minimize wavefront error and maintain the laser beam focusability; they must also be sufficiently thin such that B-integral effects are negligible. Debris-free targets, such as cryogenic jets, will therefore decrease the operational costs to routinely replace debris shielding, critical for optimal laser performance.

We demonstrate a stable, 1 Hz proton source delivering $\sim 10^{13}$ protons/MeV/sr/min and a maximum proton energy of 6.5 MeV using a 100 TW laser. Subsequent studies will investigate the required laser contrast, and therefore pre-plasma scale length, to reach optimal TNSA conditions and higher proton energies with this target. Additionally, planar hydrogen jets will be fielded to improve laser-jet overlap and potentially increase the shot-to-shot reproducibility of the proton energy spectra. This capability is ready for applications in pump-probe experiments [248] and the study of advanced proton acceleration mechanisms [149] at high repetition rates.

7.7 Supplementary material

Alternate presentation of the proton cut-off energy and flux using the dataset in Fig. 2 (a).

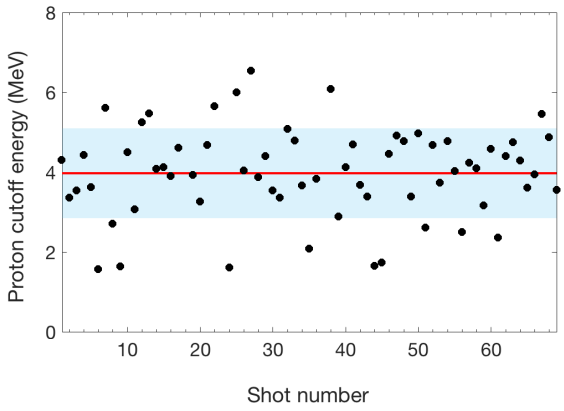

Figure 7.5: Proton cut-off energies as a function of shot number. The shaded blue area represents the standard-of-deviation of the dataset, while the red continuous line corresponds to the average cut-off energy. Note that protons of energy below 1.4 MeV cannot be detected.

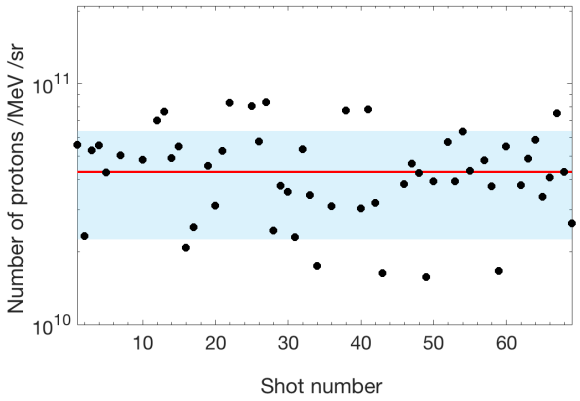

Figure 7.6: Proton flux recorded at 3 MeV as a function of shot number. The shaded blue area represents the standard-of-deviation of the dataset, while the red continuous line corresponds to the average proton flux.

Chapter 8
High-Brightness Proton Beams from Planar Cryogenic Hydrogen Jets

8.1 Preface

In addition to pulsed operation at frequencies above 1 Hz, some applications also demand a high single-shot charge or dose rate. For example, developing experimental techniques to mimic the extreme plasma and radiation environments at the blanket and first wall of tokamaks will aid in testing the radiation hardness and survivability of newly developed fusion-relevant materials and composites. Currently, no materials fully satisfy the requirements of an industrial fusion power plant such as the planned electricity-producing DEMOnstration power plant (DEMO).

In the absence of a laser-driven ion acceleration mechanism that robustly produces a monoenergetic ion beam, applications such as stopping power measurements (Section 2.3), proton therapy and hybrid particle accelerators design (Section 2.5) require the use of a magnetic energy selector to isolate a narrow range from a TNSA-like semi-Maxwellian energy spectrum. To have a sufficient flux after the typical attenuation of 10^{-4} in a magnetic energy selector, a high-charge ion beam is required. High-average-power petawatt-class lasers are expected to enable these applications since the total charge contained in a laser-accelerated ion beam scales approximately linearly with laser energy.

Two manuscripts are in preparation using the materials presented in the following chapter. The first is in preparation by the author of this thesis on the generation and characterization of the laser-accelerated proton and deuteron beams [249]. The second in preparation by F. Treffert will use the proton and deuteron beam characterization to explain neutron generation using a pitcher-catcher setup [250]. It is based on an experiment at the Texas Petawatt Laser facility that was designed and led by C. B. Curry and M. Gauthier. A follow-up experiment on laser-generated neutron sources using the bright, laser-accelerated deuteron beam co-led by F. Treffert, C. B. Curry and M. Gauthier. C. Schoenwaelder operated the cryogenic liquid jet system. E. C. Galtier, G. D. Glenn, H. Quevedo, M. Spinks, and M. Zimmer also assisted with the experiment. S. H. Glenzer supervised the project. R. Mishra, H.-G. J. Chou, and F. Fiuza performed particle-in-cell simulations to design the experiment and interpret the results. T. E. Cowan, T. Ditmire, G. M. Dyer, S. Goede, T. Kluge, M. Rehwald, M. Roth, U. Schramm, and K. Zeil provided valuable input. The work builds on previous experience with the cryogenic liquid jet for experiments conducted in the Jupiter Laser Facility at LLNL

[147, 149] and the Draco laser at HZDR [14, 15, 150, 226, 232, 233].

8.2 Introduction

Planar cryogenic low-Z jets satisfy the technical requirements for high repetition rate targets but are also ideal for systematically optimizing ion acceleration in relativistically-enhanced acceleration regimes due to their tunable thickness and near-critical density. In many cases, experiments can also be modeled one-to-one using fully-explicit particle-in-cell (PIC) simulations. This leads to a better understanding of the microphysics that is difficult to probe experimentally. Here, we investigate one of the most promising regimes which is referred to as Enhanced Sheath Field (ESF) acceleration. In this regime, the target is initially opaque to the incident laser, but deposition of energy into the target causes the density to drop and leads to relativistic transparency. Mishra *et al.* predict significantly higher cutoff energies compared to the Target Normal Sheath Acceleration (TNSA) mechanism when the target transitions from opaque to transparent near the peak of the laser pulse [5]. Recent simulation studies suggest that proton energies beyond the 100 MeV barrier are possible in this regime.

In this experiment, laser-driven ion acceleration was investigated in the ESF regime by irradiating a planar sub-micron-thick cryogenic low-Z liquid jet with the Texas Petawatt laser. The high repetition rate ion diagnostic suite developed in Chapter 7 will be combined with the experimental platform developed during this experiment to enable ultra-intense laser-plasma experiments at 10 Hz in the future Matter in Extreme Conditions Upgrade (MEC-U) project.

8.3 The Texas Petawatt laser

The Texas Petawatt (TPW) laser is a high-energy neodymium mixed-glass (Nd:mixed glass) short-pulse laser system based on OPCPA. The current design consists of two Beta Barium Borate (BBO)-based OPCPA stages pumped by an optically synchronized 8 ps Nd:YLF laser that amplifies the stretched oscillator pulses by six orders of magnitude. After the amplification, there are two LBO-based OPCPA stages that are pumped by 4 ns pulses. The beam is then amplified by two passes in a 25 mm "booster amplifier," four passes in a 64 mm Nd:glass "rod amplifier," and four passes in a 315 mm phosphate Nd:glass slab "main amplifier."

The fully amplified laser pulse is then transported to the compressor, where the pulse is compressed to approximately 135 fs. The laser near-field and far-field are imaged before and after compression using the leakage from one of the transport mirrors. Additionally, the laser pulse duration is measured on shot using a single-shot second-order auto-correlator.

Finally, the laser is delivered to either the Target Chamber 1 (TC1) or 2 (TC2) target area using a rotatable final turning mirror. The experiment presented here used the short-focal length TC1 target area wherein the TPW is focused at the "target chamber center" (TCC) using a dielectric coated f/3 off-axis parabola (OAP).

During the most recent upgrade to the TPW laser, several modifications were made to the system to minimize the laser pre-pulse. All lenses after the OPCPA stages were replaced with OAP mirrors. The laser-pulse contrast on the picosecond timescale was improved by implementing ps-OPCPA. The laser pulse compression and the steepness of the rising edge of the main pulse were optimized using a closed loop between an acoustic-optic programmable dispersive filter (Dazzler from Fastlite) and a self-referring spectral interferometer (Wizzler-1030 from Fastlite).

Nevertheless, a single plasma mirror was placed in the converging beam in the target chamber to further improve the laser pulse contrast (Fig. 8.1 (a)) and to specifically address the ps-contrast that has the potential to dramatically modify the target density profile before the arrival of the main pulse. This is especially true for cryogenic low-Z liquid targets due to their low density and low atomic weight. To enter the ESF regime, the target pre-expansion must be controlled so that the target remains overcritical until close to the peak of the laser pulse.

8.4 Design and commissioning of a single plasma mirror

The plasma mirror used in this experiment was designed for up to 6 shots. A blast shield was installed $\sim$2 mm in front of the plasma mirror, thereby exposing a zone slightly larger than the size of the near field profile on the optic to avoid clipping (Fig. 8.1 (b)). The plasma mirror was fully motorized to translate and align it under vacuum. To maximize the laser pulse contrast enhancement, a custom anti-reflective optical coating was designed with a nearly flat reflectivity $<$0.5% across the laser bandwidth and across the range of incidence angles (Fig. 8.1 (d)) within the focusing laser cone.

To commission the plasma mirror for the experiment, the reflectivity was measured as a function of incident laser fluence by varying the distance of the plasma mirror from the laser focus while keeping the laser energy constant (Fig. 8.1 (c)). An absolutely calibrated calorimeter was placed in the expanding laser beam at a point after it reflected from the plasma mirror and passed through the focus. A sample calorimeter trace for Shot 12207 is shown in Fig. 8.2. The high-amplitude noise at early times is due to the charging of the capacitor banks prior to the fully amplified laser shot. In addition, low-amplitude 60 Hz electrical noise was superimposed on the signal. First, the noise was removed with a low-pass filter. Then, the peak voltage was converted to laser energy using a calibration factor

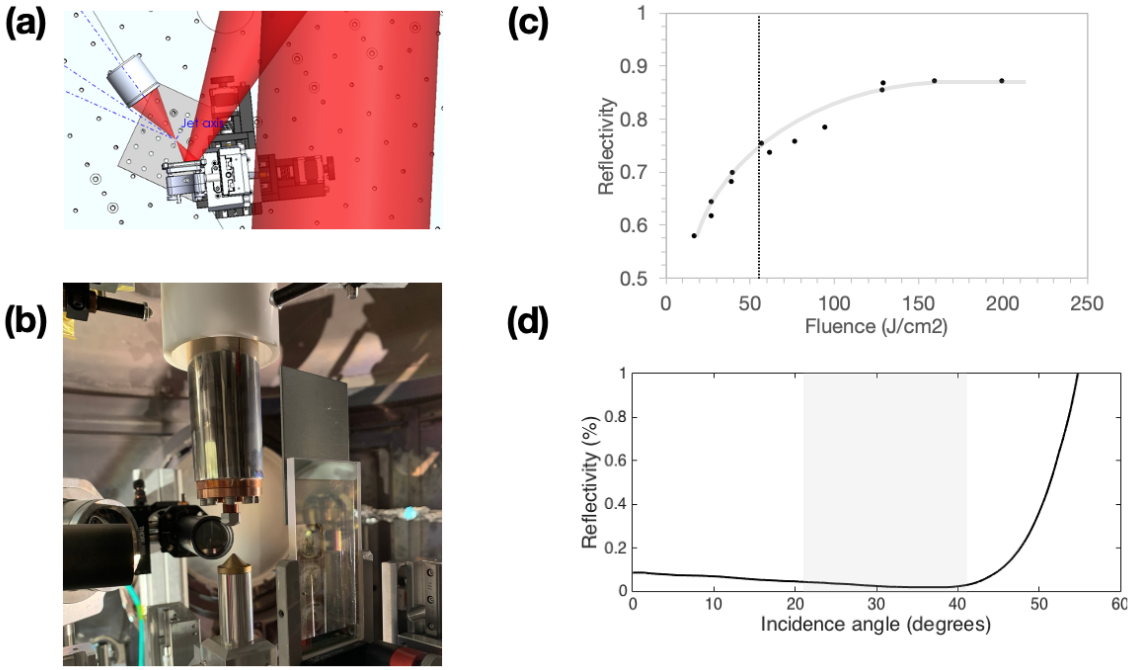

Figure 8.1: (a) Engineering drawing of the converging Texas Petawatt laser reflected from a single PM at a distance of 42 mm from focus. The diverging laser light was collected and relay imaged using an f/1.4 apochromatic objective. (b) Photograph of components inside the vacuum chamber near TCC. The 6-shot PM and blast shield are visible on the right side of the image. (c) Plasma mirror commissioning measurements to determine the reflectivity as a function of fluence incident on the plasma mirror. The operational fluence selected for the experiment is indicated by a vertical black dotted line at 55 J/cm^2. (d) The cold reflectivity of the anti-reflective coated BK7 substrate used for the PM as a function of incidence angle. The grey-shaded region corresponds to the range of incidence angles due to the converging laser about a central angle of 32°.

of 683.9 J/V from a cross-calibration that was performed at the Trident Laser Facility at Los Alamos National Laboratory (LANL). A summary of the plasma mirror commissioning shots is shown in Table 8.1. During the experiment, the plasma mirror was operated at a fluence of 55 J/cm^2, resulting in a typical reflectivity of 75%.

8.5 Experimental setup for laser-driven ion acceleration

A schematic of the experimental set-up is shown in Fig. 8.4. The TPW laser was focused by a dielectric coated 22.26° f/3 OAP and then reflected from a single plasma mirror in the converging beam to improve the intrinsic laser-pulse contrast. The laser focus was relay imaged with an f/1.4 apochromatic objective lens onto a high-dynamic-range 12-bit CCD camera. Images of the laser focal spot were taken with the jet moved to a position fully outside of the field of view of the imaging system. A representative focal spot measured under

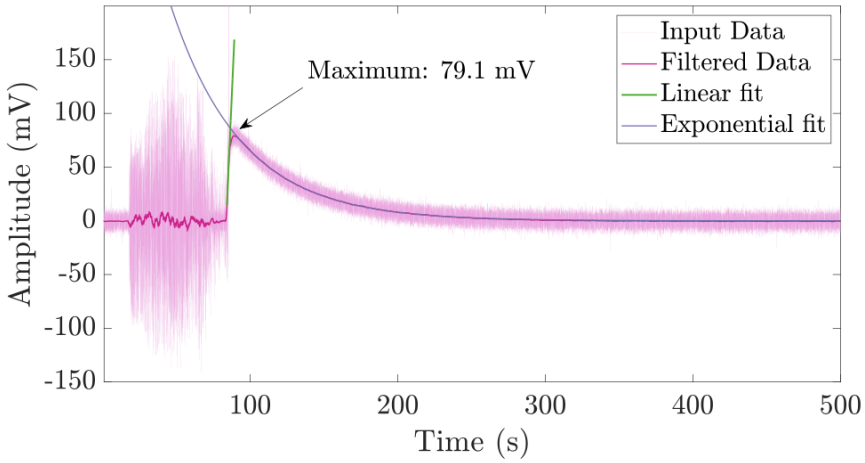

Figure 8.2: Full-aperture calorimeter output voltage as a function of readout time in seconds for Shot 12207. The raw and low-pass filtered signals are indicated in pink. The in-vacuum calorimeter calibration (683.9 J/V) is applied to the maximum voltage (79.1 mV) to obtain an on-target energy of 54.1 J.

vacuum is shown in Fig. 8.3. The focal spot size is $\mathrm{FWHM}_x = 7.51$ µm and $\mathrm{FWHM}_y = 8.14$ µm, leading to an estimated peak laser intensity of 5.8×10^{20} W/cm^2 for this shot. The focus imaging system was motorized in the laser forward direction so that the focal spot could be optimized under vacuum prior to each shot. This was done utilizing the dual deformable mirror system and by adjusting the off-axis parabola alignment to minimize astigmatism. At the time of this experiment, the laser energy was significantly lower than the maximum energy specification of 135 J due to accumulated damage to the transport mirrors in the compressor and to the final focusing off-axis parabola (OAP). The typical laser energy after the OAP during this experiment was (99 ± 3) J. After the single PM, the energy and peak intensity on target were (75 ± 3) J and $(9 \pm 2) \times 10^{20}$ W/cm^2 respectively. A summary of the average laser parameters is presented in Table 8.2.

An illustration of the optical imaging and ion diagnostic paths is shown in Fig. 8.5 (a). A millijoule-level probe beam stretched to 10 ps was timed to arrive 25 ps prior to the main pulse at TCC. The probe beam was injected through the back of the plasma mirror to overlap with the main laser beam path, thereby back-illuminating the cryogenic jet to allow for precision laser-target overlap. Additionally, a flip mirror installed on the focus-imaging beam path redirected the beam into a Michelson interferometer. The apochromatic objective lens was translated by 70 µm such that TCC, and therefore the jet, was in focus at the output of the interferometer. High-magnification transmission interferometry was used to obtain a jet thickness measurement was obtained before each shot. A transmission interferogram of a 4×20 µm^2 cryogenic hydrogen jet before Shot 12331 is shown in Fig. 8.6 (a). The

Shot No.	Energy before OAP (J)	Fluence PM (J/cm^2)	Calorimeter Max. Voltage (mV)	On-Target Energy (J)	Reflectivity (OAP+PM)
12203	102.4	39.6	85.8	58.7	0.68
12205	104.4	40.3	89.8	61.4	0.70
12207	104.4	27.8	79.1	54.1	0.61
12209	103.5	27.6	81.9	56.0	0.64
12211	105.3	128.8	110.6	75.7	0.85
12215	106.1	129.7	113.4	77.6	0.87
12217	98.5	57.6	91.4	62.5	0.75
12219	106.7	62.4	96.7	66.1	0.74
12221	97.6	76.9	91.0	62.2	0.76
12223	98.5	95.2	95.1	65.0	0.78
12225	46.2	17.8	32.9	22.5	0.58

Table 8.1: Summary of the f/3 OAP reflectivity and plasma mirror commissioning measurements with the Texas Petawatt laser. The fluence on the plasma mirror was varied by moving the PM relative to the laser focus while keeping the laser energy constant within shot-to-shot variability. The data is plotted in Fig. 8.1 (c).

computed thickness map obtained from the phase shift is shown in Fig. 8.6 (b). A Michelson interferometer with a rotating retroreflector was used for the measurement (Fig. 8.6 (c)). Shown in Fig. 8.6 (d), the reconstructed cross-section of the jet had a total transverse width of 37 µm and a 0.39×24 µm^2 planar central region with ∼8 µm diameter cylindrical rims. Additional measurements of 4×20 µm^2 cryogenic hydrogen jets with similar temperature and flow produced central thicknesses ranging from 0.39 to 0.53 µm.

An independent tabletop Q-Switched Nd:YAG laser (Quantel Brilliant B), hereafter referred to as the Quantel, was frequency doubled to $2\omega = 527$ nm for back illumination of the jet on the microscopy beam paths. The Quantel was spatially overlapped with the probe beam and then injected into to the TC1 chamber through an uncoated BK7 window. In-

Parameter	Value
Energy after OAP	99 ± 3 J
Energy on Target	75 ± 3 J
Pulse Duration	144 ± 18 fs
Beam Waist (w_0)	5.3 ± 0.3 µm
Strehl	0.68 ± 0.07
Peak Intensity on Target	$(9 \pm 2) \times 10^{20}$ W/cm^2
Pointing Jitter at Target	$\Delta x = \pm 5.99$ µm, $\Delta y = \pm 4.78$ µm

Table 8.2: Average and standard deviation of Texas Petawatt laser parameters during experimental campaign in 2019.

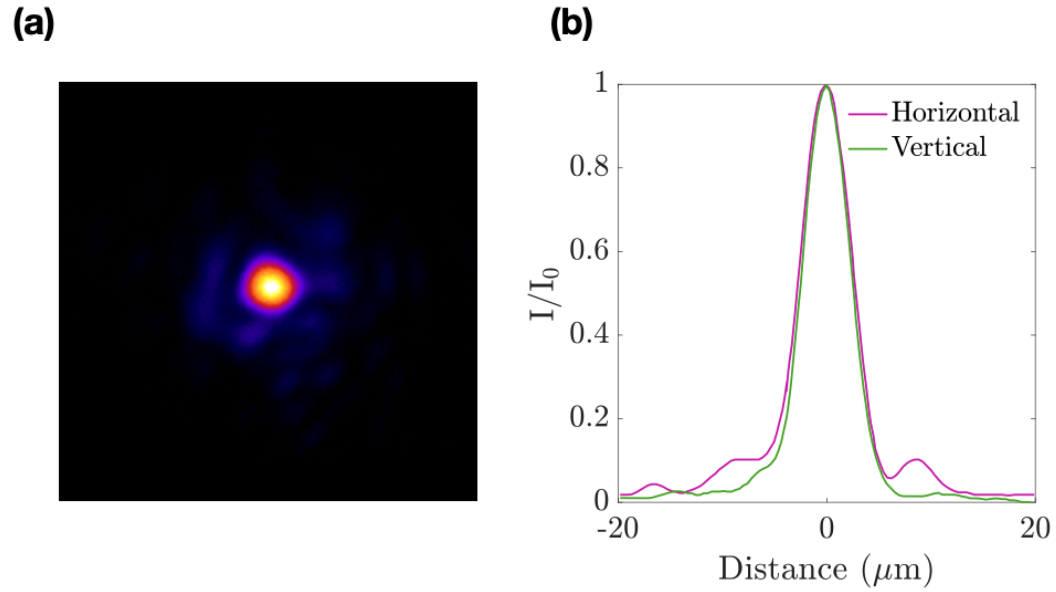

Figure 8.3: High-resolution (0.315 µm/pixel = 20.5× magnification), high-dynamic-range (12-bit) relay image of the TPW laser focus before Shot 12331 taken using a Manta G-145B CCD camera. The measured spot size in the horizontal and vertical direction is FWHM_x = 7.51 µm and FWHM_y = 8.14 µm, respectively. The estimated peak laser intensity is therefore $\sim 5.8 \times 10^{20}$ W/cm^2.

side the target chamber, the Quantel was split from the probe beam using a 1053/527 nm dichroic mirror and then split again onto the two imaging axes using a 50/50 beamsplitter. The imaging lines were at 44.1° and -55.3° with respect to the laser forward direction. Representative images of a 4 × 20 µm^2 cryogenic hydrogen jet are shown in Figs. 8.5 (c). The imaging systems were spatially calibrated using a variable quadrant copper mesh grid (SPI Supplies P/N 2150C-XA). The grid was mounted on a target jig with 6-axis alignment, and its back reflection was used to precisely align it to be normal to the imaging axis.

8.5.1 Planar cryogenic low-Z liquid jets

The planar cryogenic low-Z liquid jet was produced following the methodology described in Chapter 5. The low-Z gas was liquified in an oxygen-free copper source that was mounted in line with a continuous-flow liquid helium cryostat maintained at 17.5–18 K (for hydrogen) using a manually tuned P-I-D feedback loop. The cryostat was inserted into the TPW TC1 chamber through the top central flange along with a rotation stage and a manual XYZ-manipulator for coarse, mm-scale alignment. The combination of the cryostat, manipulator, and copper source extended to the laser beam height in the target chamber. Fine alignment of the jet relative to TCC was accomplished using in-vacuum push-pin actuators that were attached to a stabilization platform.

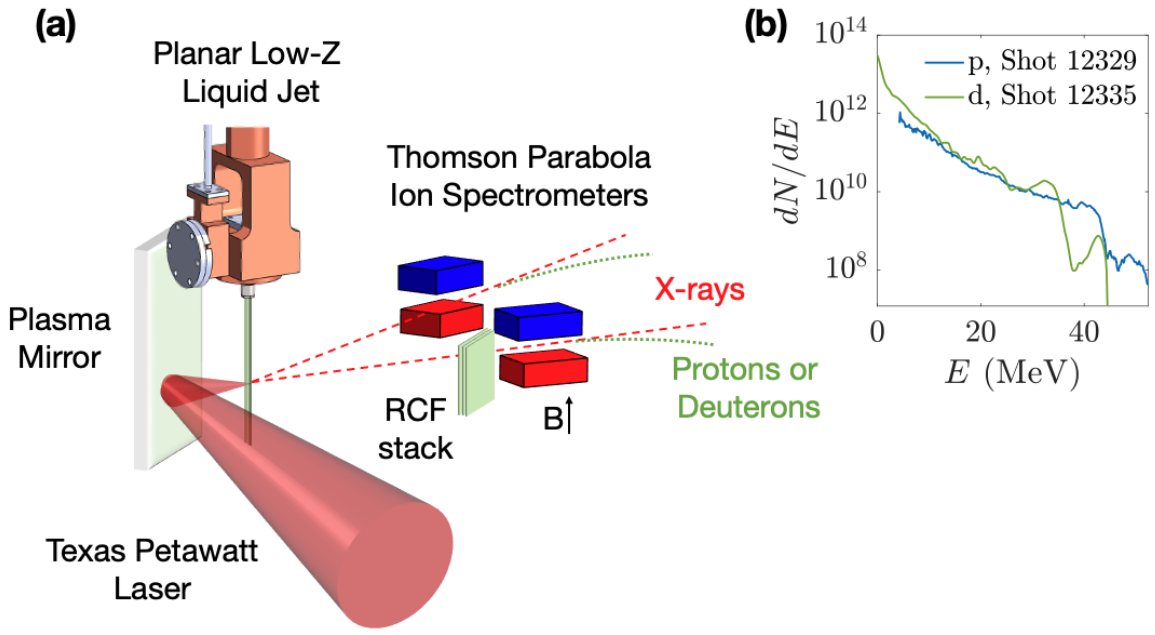

Figure 8.4: (a) Simplified illustration of the experimental set-up for laser-driven ion acceleration from a planar cryogenic low-Z jet using the Texas Petawatt Laser. (b) Sample proton (blue) and deuteron (green) beam energy spectra detected at -30° relative to laser forward direction.

New 4×20 µm^2 apertures were nanofabricated for this experiment from silicon/silicon nitride device wafers and were used to produce turbulent-free, laminar liquid sheets with transverse widths of up to 50 µm and with thicknesses from hundreds of nm to 1.5 µm. On average, the cryogenic liquid deuterium jets were two to three times thicker than the cryogenic liquid hydrogen jets for reasons that are not currently understood.

During jet operation, the cryogenic low-Z liquid vapor is difficult to pump and creates a significant load on the vacuum system. Stable jet operation requires an empirically determined baseline vacuum pressure better than $\sim 2 \times 10^{-5}$ mbar and an operational pressure no greater than $\sim 5 \times 10^{-4}$ mbar. To improve the vacuum conditions during jet operation, an in-vacuum catcher system that collects and evacuates residual liquid passing through TCC and a supplemental turbopump were installed. The in-vacuum catcher significantly improved the jet stability compared to previous cryogenic jet experiments performed at the facility. The jet catcher system consisted of an independent vacuum line terminated by an ⌀800 µm differential pumping aperture located up to 20 mm below the aperture. The line was pumped separately from the TPW vacuum system by a roots-type blower.

The cryogenic liquid sheet was then irradiated by the TPW laser 1.75 mm below the aperture at normal incidence. This is the shortest distance that can be used before the f/3

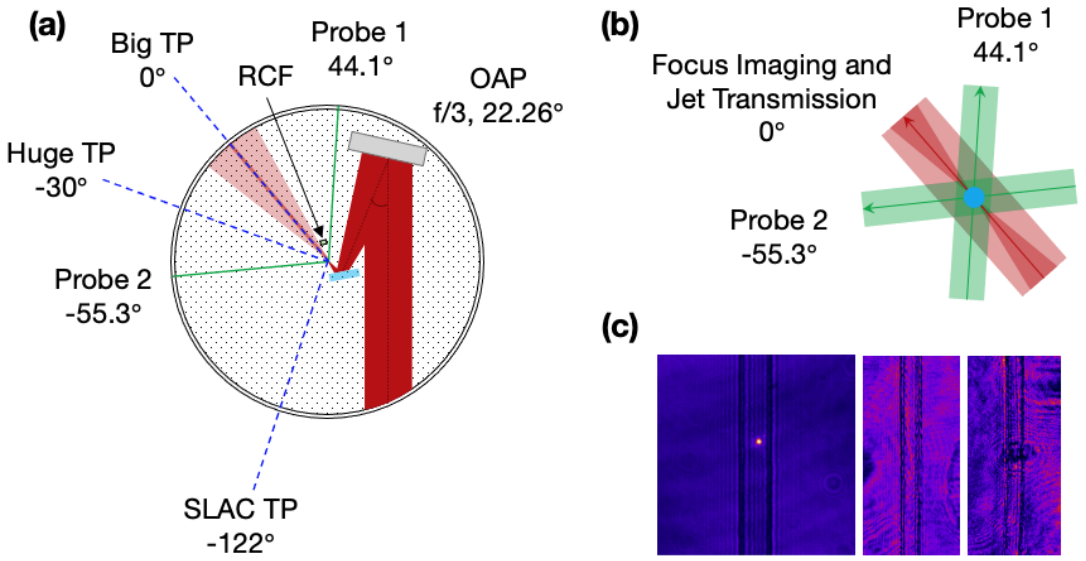

Figure 8.5: (a) Schematic of the diagnostic layout viewed from the top. The Texas Petawatt laser (red) is focused with a 22.26° f/3 OAP. After reflection from a single plasma mirror (cyan rectangle), the beam is focused at TCC. The Thomson Parabola axes (0°, -30°, -122°) are indicated by dashed blue lines. The Probe 1 and 2 axes at 42.3° and -55.3° are shown in green. The RCF stack covered horizontal angles from 1.6° to 24.5° at a distance of 57 mm from TCC. (b) Illustration of the optical beam paths for the main and probe beam (red) and the orthogonal probe imaging lines (green). (c) Representative optical shadowgraphs of a 4×20 µm^2 cryogenic hydrogen jet on the jet transmission, Probe 1, and Probe 2 imaging systems.

converging laser is obstructed by the source cap that holds the aperture in place. At this distance, immediate catastrophic damage to the aperture was observed after each high-intensity laser shot. When this occurred, the few millilitres of cryogenic low-Z liquid contained in the source reservoir instantly vaporized, which resulted in a vacuum spike of multiple orders of magnitude. The aperture before and after such a high-intensity laser-target interaction is shown in Fig. 8.7. Since the aperture needed to be replaced after each shot in a procedure that took six to eight hours, the experiment was limited to at most two shots per day.

8.5.2 Ion diagnostics

The proton energy spectrum and the flux resulting from the interaction were measured using three Thomson parabola ion spectrometers (TP) positioned at angles of 0°, 30°, and 110° from the laser forward direction. The TPs were in independent, differentially pumped vacuum chambers that could be fully disconnected from the target chamber with gate valves. This allowed the imaging plates to be removed and scanned prior to warming up the cryostat

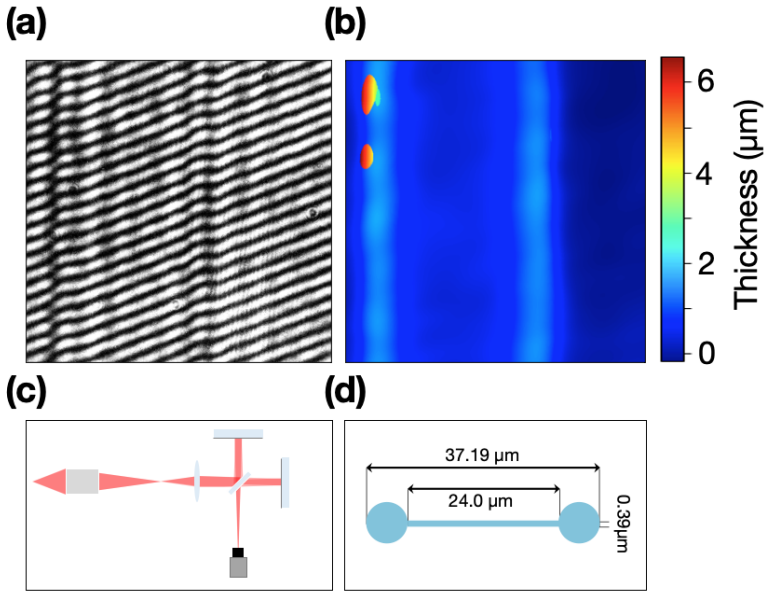

Figure 8.6: (a) Transmission interferogram of a 4×20 μm^2 cryogenic hydrogen jet before Shot 12331. (b) Jet thickness map computed from the phase shift in the interferogram courtesy of C. Schoenwaelder. (c) Illustration of the Michelson interferometer setup. (d) 2-D cross-section of the jet with dimensions obtained using interferometry.

to ambient temperature to vent the target chamber. During the experiment, the TPs were referred to as the Big, Huge, and SLAC TP. The parameters for each TP are outlined in Table 8.3. The magnetic dispersion of each TP was calibrated using metallic filters at multiple breakthrough energies. A slotted CR-39 plate with metallic filters (Fig. 6.4) was installed on selected shots to obtain an absolute calibration of the BAS-TR imaging plates for protons and deuterons. The calibration was also cross-verified using absolutely calibrated radiochromic film stacks. As mentioned above, damage to the aperture on shot resulted in a large spike in vacuum pressure, which could lead to arcing in a TP. During a previous experiment, no contaminant ions were detected from the cryogenic liquid hydrogen jet as expected due to the ultra-high purity gas (99.9999%) used in the system. To avoid the risk of the signal becoming corrupted from electrical arcing in this experiment, voltage was not applied to the electrodes in the TPs for the shots presented. In other words, the TPs were operated as simple B-field spectrometers.

The spatial profile of the proton or deuteron beam generated from the relativistic laser-plasma interaction was simultaneously recorded using absolutely calibrated radiochromic film stacks (RCF). The stack used to detect protons with energies up to 114 MeV consisted of 23.1 mm $\times$ 27.4 mm HD-v2, MD-v3, and EBT3 radiochromic films separated by aluminum and copper filters as summarized in Table 8.4. The stack was assembled and inserted into an aluminum holder which was then mounted at a distance of 57 mm from TCC. The RCF

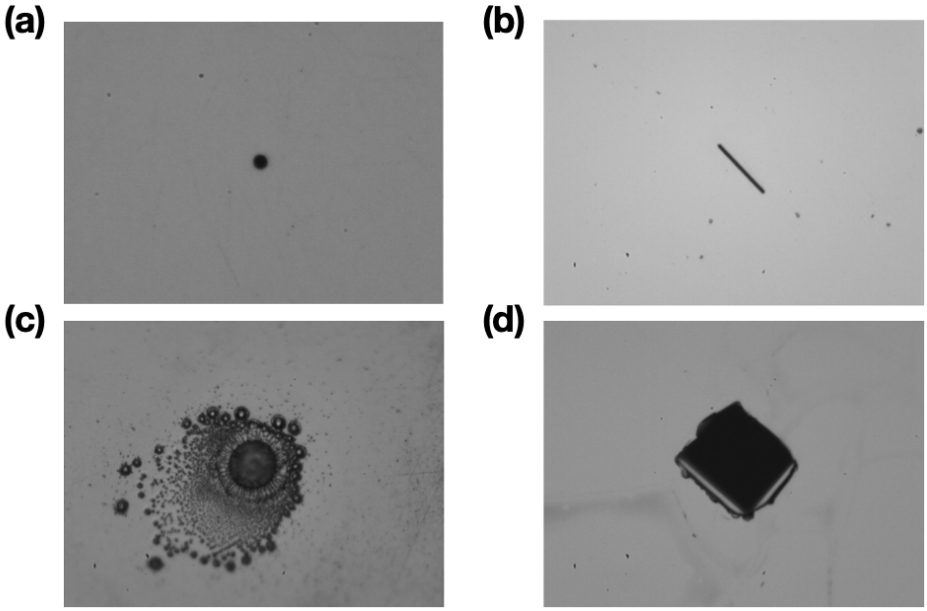

Figure 8.7: Light field microscopy images of (a) a 10 µm Pt/Ir cryogenic jet aperture and (b) a 2×40 µm^2 Si/SiN cryogenic liquid jet aperture before shot. (c)-(d) Damaged cryogenic jet apertures after the jet was irradiated by the Texas Petawatt laser with an intensity of $\sim 9 \times 10^{20}$ W/cm^2 at a distance of 1.75 mm below the aperture.

Name	**Location**	**L_1 (m)**	**L_2 (m)**	**Pinhole ⌀ (µm)**	**Pinhole Ω (µsr)**	**D (mm)**	**ℓ (mm)**	**B_0 (T)**
Big	0°	1.11	0.398	200	2.55×10^{-2}	0.388	0.1	0.55
Huge	-30°	1.11	0.445	200	2.55×10^{-2}	0.435	0.1	0.8
SLAC	-122°	0.851	2.30	200	4.33×10^{-2}	0.288	0.05	1.0

Table 8.3: Thomson Parabola parameters. The definitions of the variables $L1$, $L2$, D, and ℓ can be found in Fig. 6.1.

stack sampled the beam over horizontal angles from 1.6° to 24.5° relative to laser forward direction and vertical angles ±13.5° with respect to the laser plane.

8.5.3 Additional diagnostics to assess shot quality

A plastic X-ray scintillator was installed at a distance of 7.6 m from the target chamber at approximately 120° from the laser-forward direction. The X-ray scintillator provided a sensitive, relative measurement of the laser-generated X-ray radiation that was used to monitor the quality of the laser-plasma interaction. One vertical and one horizontal B-dot probe were also installed in the target chamber to measure the on-shot electromagnetic pulse (EMP). Lastly, a portable ion chamber survey meter (RAM ION, Rotem) measured the integrated dose of beta and gamma radiation emitted.

Name	Film Type	Energy (MeV)
H1	HDv2	1.30
H2	HDv2	5.15
H3	HDv2	7.45
H4	HDv2	9.35
H5	HDv2	11.0
H6	HDv2	12.4
H7	HDv2	13.7
H8	HDv2	14.9
H9	HDv2	16.1
M1	MDv3	19.3
M2	MDv3	22.4
M3	MDv3	25.2
M4	MDv3	27.7
M5	MDv3	30.1
M6	MDv3	32.3
E1	EBT3	37.7
E2	EBT3	42.6
E3	EBT3	47.2

Name	Film Type	Energy (MeV)
E4	EBT3	51.5
E5	EBT3	55.5
E6	EBT3	59.3
E7	EBT3	62.9
E8	EBT3	66.4
E9	EBT3	69.7
E10	EBT3	72.9
E11	EBT3	76.0
E12	EBT3	79.1
E13	EBT3	82.1
E14	EBT3	85.0
E15	EBT3	87.9
E16	EBT3	90.6
E17	EBT3	95.6
E18	EBT3	101
E19	EBT3	105
E20	EBT3	110
E21	EBT3	114

Table 8.4: RCF#4 stack design for protons up to 114 MeV: 13µm Al, 1 HDv2, 8×(100 µm Al + HDv2), 6×(150 µm Cu + MDv3), 16×(500 µm Cu + EBT3), 5×(1 mm Cu + EBT3), 1×100um Al. Aluminum and copper filters were installed between films to optimize the energy spacing and on-film visibility.

8.6 Establishing laser-target overlap

By tracking the position of the central maximum over 502 consecutive shots, the pointing stability of the unamplified OPA was measured to be ±5.99 µm in the lateral direction and ±4.78 µm in the vertical direction. A 3-D histogram of the results is given in Fig. 8.8.

If the fully amplified laser had the same pointing jitter, the minimum target size for consistent (>67% of the shots) partial laser-target overlap would be ∼10 µm. In a series of test shots on a 10 µm diameter wire, however, a high-intensity interaction was not detected despite using the unamplified laser (OPA) to perform a laser-target overlap alignment procedure yielding better than 3-micron precision.

Monitoring the change in position between the last OPA pulse, referred to as the "OPA test shot," and full-energy system shots (SS) revealed a systematic offset as shown by the pink data points and pink shaded region in Fig. 8.9. An empirical pre-shot correction of twenty steps left (SS-20L) was applied to an upstream transport mirror, which improved the centering of the distribution of fully amplified laser positions on the OPA. The green shaded

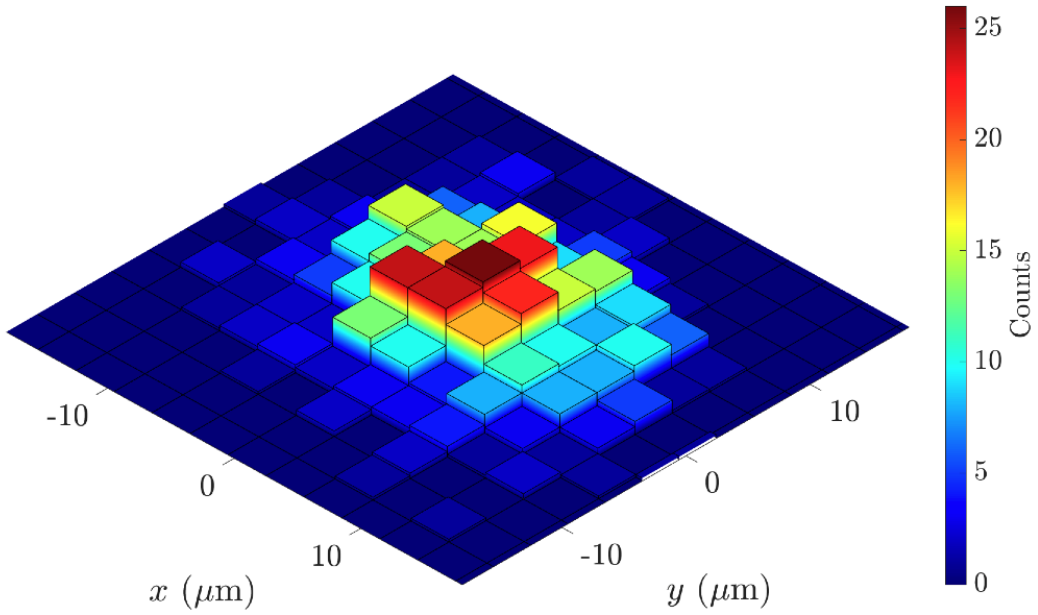

Figure 8.8: Pointing jitter of the unamplified OPA of the Texas Petawatt laser computed from 502 consecutive shots at 2.5 Hz ($\sigma_x = 5.99\,\mu m$, $\sigma_y = 4.78\,\mu m$).

region represents the 1σ standard deviation of the positions when the 20L correction was applied. It is centered at ($x = 3.37$ µm, $y = 1.38$ µm) with $\sigma_x = 8.5$ µm and $\sigma_y = 7.0$ µm. With additional shots, this correction could be fine-tuned. However, it was deemed sufficient for this experiment on the wide planar jets. The pointing jitter of the fully amplified beam was found to be ∼44% larger than that of the unamplified OPA. Future experiments will explore the use of a fast steering mirror to improve the pointing jitter of the fully amplified beam. The dual deformable mirror system was used to correct for changes in the focal plane location that were due to the thermal lensing that occurred in the amplifiers during full-energy system shots. This was done by loading a constant predetermined pre-shot correction. The far field measured post-compression has been designed to function as an equivalent plane monitor to confirm the laser alignment and focus of every shot.

In addition to the on-shot laser pointing jitter, the cryogenic hydrogen jet can sometimes shift by 10 to 50 µm due to vacuum pressure, cryogenic source temperature, or cryogenic liquid flow fluctuation. The combined system jitter was of the same order as the transverse width of the 2×20 µm^2 planar cryogenic liquid jets, which were also investigated during this experiment. As a result, we expect the complete data set to include instances of full, partial, and no laser-target overlap. To maximize the likelihood of full laser-target overlap, the position of the jet was continuously monitored on the orthogonal imaging systems and

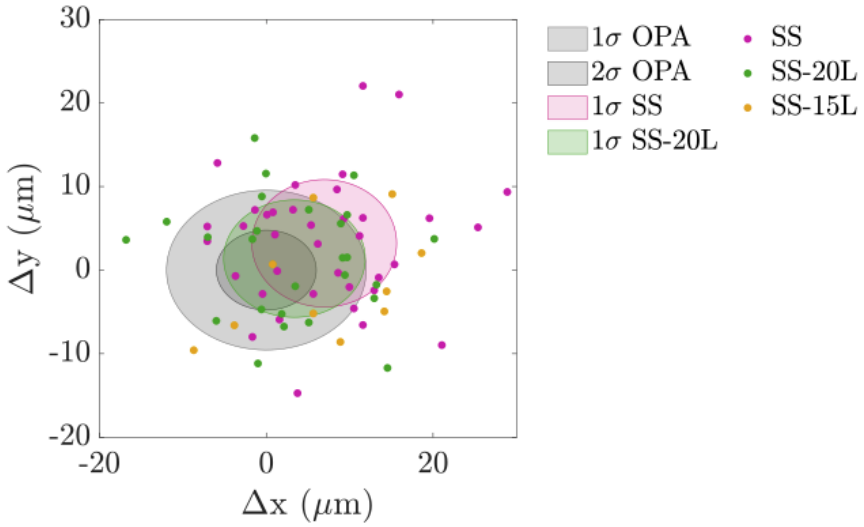

Figure 8.9: The difference in the position of the fully amplified system shot and the OPA test shot of the Texas Petawatt laser. The full system shots (SS, pink) and two pre-shot corrections SS-20L (green) and SS-15L (yellow). The one and two standard deviation pointing jitter of the OPA ($\sigma_x = 5.99\,\mu m$, $\sigma_y = 4.78\,\mu m$) are indicated by dark and light grey shaded regions, respectively. The pointing jitter before (pink) and after applying a -20L correction (green) are shown.

actively corrected until ∼10 seconds before the shot. Optical shutters were manually engaged a few seconds before the shot to protect the CCD cameras from damage due to plasma self-emission.

Shots were grouped into centered, partial-overlap, and missed shots using a combination of the X-ray scintillator voltage, EMP measured with B-dot probes, and spatial characteristics of the laser-accelerated proton or deuteron beam. For the latter, azimuthal symmetry and angular confinement in the vertical direction are good indicators that the highest intensity part of the beam interacted with one of the cylindrical rims of the jet rather than the planar central region.

8.7 Numerical simulations in the Enhanced Shealth Field regime

2-D and 3-D particle-in-cell (PIC) simulations were performed by R. Mishra, H.-G. J. Chou, and F. Fiuza with the fully relativistic kinetic code OSIRIS [224] using realistic laser and target parameters from the experiment. The interaction of a laser polarized along the jet axis with 88 J (110 J before plasma mirror), 137 fs pulse duration focused to a 7.8 µm spot size on the front surface of a cryogenic liquid hydrogen jet located on the plane z = 250 c/ω_p was investigated. In the simulation, the laser was incident from the left boundary, propagated in the positive z direction.

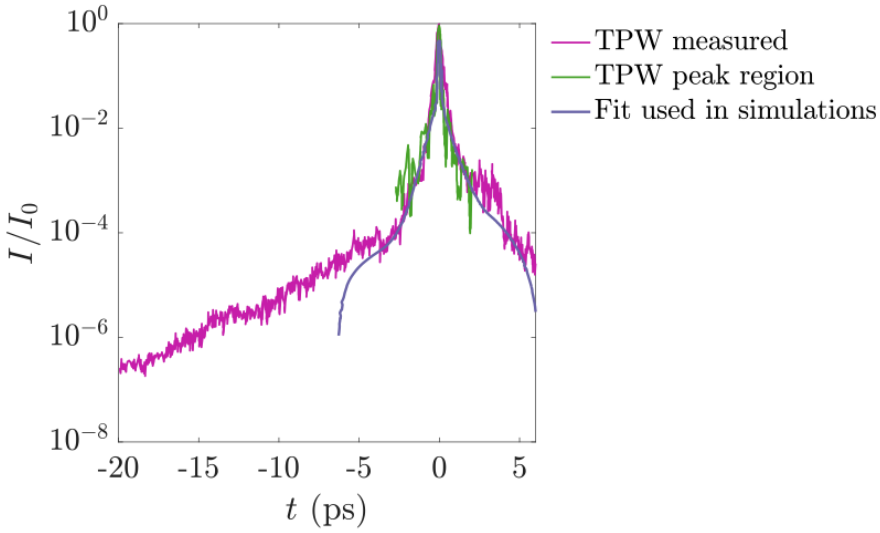

Figure 8.10: Texas Petawatt laser pulse shape without a plasma mirror (a) measured with a 3rd order cross-correlator (RINCON 1.053-4), and (b) measured in the peak region with a self-referring spectral interferometer (Wizzler-1030 from Fastlite). (c) The laser pulse shape used in the 2-D and 3-D PIC simulations. It was obtained by scaling the measured pulse shape by the measured plasma mirror reflectivity. Prior to -6 ps, the single plasma mirror improves the laser-pulse contrast by about three orders, which is below the ionization threshold of hydrogen.

The nanosecond laser prepulse was measured from -120 ns to -0.3 ns using an InGaAs fast photodiode (EOT ET-3000) and calibrated neutral density filters. The nanosecond laser pulse contrast is better than 10^{-11} except for a discrete prepulse at -85 ns which has an estimated pulse contrast of $\sim 10^{-9}$ [134]. Directly before the experiment, a scanning third-order autocorrelator was used to measure the laser pulse shape from -180 ps to +20 ps. The full temporal range accessible with the 3rd order cross-correlator (RINCON 1.053-4) is 990 ps allowing a direct comparison with the photodiode measurement. The main pulse of the laser was measured using a self-referencing spectral interferometer (Wizzler-1030 from Fastlite). Both measurements of the picosecond laser pulse shape are shown in Fig. 8.10. The plasma mirror used in the experiment improved the laser pulse contrast by a factor of approximately 1500 until the anti-reflective coating was ionized and the remainder of the laser pulse was reflected. The laser pulse shape used in the simulation was an analytical fit to the experimentally measured laser prepulse which was then scaled by the measured plasma mirror reflectivity. It started at -6 ps and smoothly connected to a main Gaussian laser pulse with a measured duration of 137 fs FWHM. With the inclusion of the prepulse in the simulations, the laser-driven ion beam parameters were in good agreement with the experimental results discussed in the following section.

We assume that the 2×20 µm^2 hydrogen jet is initially a fully ionized, collisionless hydrogen plasma with a density of $40n_c$ and a horizontal jet cross section consisting of a 3 µm wide $\times$ 1 µm thick planar central region and 3 µm diameter cylindrical rims on both sides (Fig. 8.11 (a)). The two-dimensional 2500×500 simulation box, corresponding to approximately 400 µm $\times$ 80 µm, is resolved in both the longitudinal and transverse directions by 0.21 c/ω_p = 5.5 nm. The time step used in the simulation is 8.4 as. Open boundary conditions are used for the particles and fields in both dimensions. The peak of the laser pulse occurs at $11500/\omega_p$, and this time is defined as $t = 0$. Different resolutions and numbers of particles were tested to ensure convergence of the results.

The proton density map in Fig. 8.11 shows that significant target expansion occurred during the 6 ps prepulse. At this time, a small over-critical planar region is surrounded by an underdense plasma cloud with an average proton density of $0.3n_c$ that extends approximately -20 µm and +50 µm in the z direction from the initial target plane. Two low-density plasma jets are observed in the backward direction at angles of approximately $\pm 10°$. They appear to originate from the cylindrical rims of the jet. A horizontal line out (8.11 (c)) shows the asymmetry between the front and rear surface plasma scale lengths and that the peak proton density is $\sim 7n_c$. In the simulation, we observed that the cylindrical rims expand and collide at the center of the jet, thereby sustaining the critical density planar zone towards the laser. At $t = 0$, the laser crosses the central planar region. The optimal conditions for the ESF regime are confirmed by inspecting the electric field (8.11 (d)) immediately before the peak of the laser pulse at which point the laser begins to break through the target due to relativistically enhanced transparency.

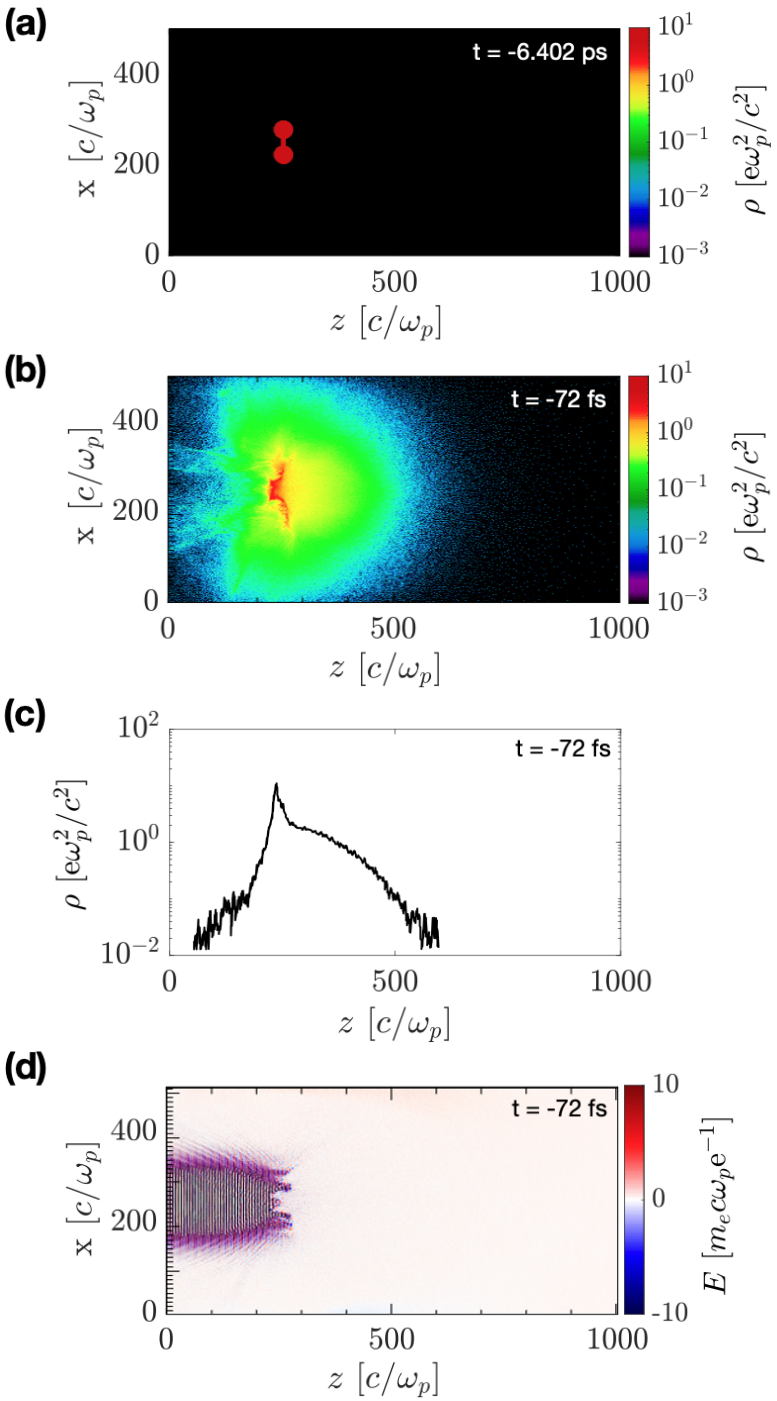

Figure 8.11: 2-D Particle-in-Cell simulation of a high-energy petawatt laser on a 2×20 µm^2 cryogenic hydrogen jet target. The jet is assumed fully ionized with an initial electron density of $40n_c$ and the laser has $a_0 \simeq 30$. The measured pre-pulse of the TPW laser from -6 ps has been included in the simulation. (a) Initial target proton density profile. (b) Proton density 72 fs before the peak of the laser pulse (c) Horizontal line out of the proton density, (d) Electric field of the laser which is polarized in the y-direction. The simulation is courtesy of R. Mirsha.

8.8 Discussion

Directly facilitated by improvements to the vacuum system, the systematic optimization of the cryogenic low-Z liquid jet over a larger P-T parameter space resulted in a significant improvement in jet stability compared to previous work. The new 4×20 µm^2 jet apertures produced wider planar jets, which improved the hit probability and reproducibility of the laser-accelerated proton and deuteron beams for a given set of laser and target parameters.

For example, a 4×20 µm^2 cryogenic hydrogen jet was irradiated with nominal maximum energy and shortest pulse duration in Shots 12297, 12305, and 12329. Laser-target overlap was confirmed for these shots using the shot quality diagnostics as described in Section 8.5.3. The hydrogen jet thickness for Shot 12329 was measured using interferometry to be 0.53 µm. The thickness of the jets used in Shot 12297 and Shot 12305 are expected to be within the range of 0.4 ± 0.1 µm.

Shot No.	$\mathbf{E_L}$ **(J)**	$\tau_\mathbf{L}$ **(fs)**	**Strehl Ratio**	**I (W/cm^2)**	$\varepsilon_\mathbf{p}$ **(MeV)**	$\mathbf{T_{e,hot}}$ **(MeV)**
12297	76.4	143	0.72	8.6×10^{20}	60.2	2.21
12305	77.9	143	0.62	8.6×10^{20}	60.8	1.35
12329	74.0	133	0.78	1.17×10^{21}	64.8	3.69

Table 8.5: Summary of laser parameters, proton cut-off energy, and hot electron temperature for Shots 12297, 12305, and 12329 for the interaction of the Texas Petawatt laser with a 4×20 µm^2 cryogenic hydrogen jet target.

A comparison between the normalized proton energy spectra from Shots 12297, 12305, and 12329 and the proton energy spectrum measured normal to the target surface in the 2-D simulation is shown in Fig. 8.12. The spectrum from the 2-D simulation was corrected for 3-D effects by scaling down the proton energy by a factor of three. Previous comparisons between the results from 2-D and 3-D simulations of laser–jet interactions that were benchmarked with experimental data have found that this scaling factor provides a reasonable extrapolation of the 2-D proton spectrum to 3-D [15]. Similar scaling factors were observed by other groups [225]. The 67.4 MeV proton cut-off energy in the simulation of a 1 µm thick cryogenic hydrogen jet provides an excellent match with the experimental data.

The hot electron temperature for each shot was inferred from an exponential fit to the proton energy spectrum. The laser parameters, proton cut-off energy, and inferred hot electron temperature for Shots 12297, 12305, and 12329 are summarized in Table 8.5. The hot electron temperature is plotted with respect to intensity in Fig. 8.13. Shot 10656 from a previous TPW experiment on a thicker 2×20 µm^2 cryogenic hydrogen jet with similar laser parameters is also included to observe how the hot electron temperature scaled with target thickness. The inferred hot electron temperature for Shots 12297 and 12305 are

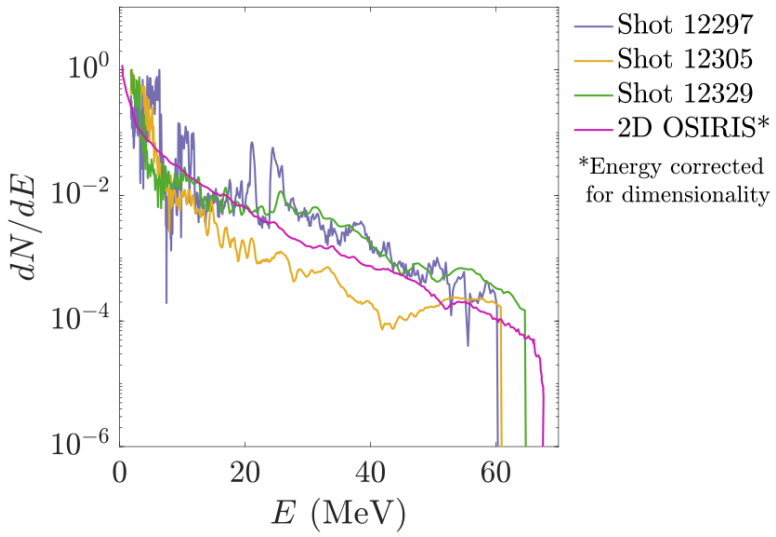

Figure 8.12: Comparison of the measured proton energy spectra from Shots 12297 (purple), 12305 (yellow), and 12329 (green) from a 4×20 µm^2 cryogenic jet with the proton energy spectrum obtained from a 2D PIC simulation (pink) of a uniform-density 1 µm thick planar hydrogen target.

lower than the hot electron temperature predicted by the Haines model (Eqn. 3.136) for a 1053 nm laser pulse (purple). The hot electron temperatures inferred for Shots 12329 and 10656, in contrast, are higher than the hot electron temperature predicted by the Haines model. Shot 10626 is $\sim$2$\times$ higher than the hot electron temperature predicted by Haines model significantly exceeding the 20% increase observed by Mishra et al. [5], which requires further investigation. The hot electron temperatures from Shots 12297 and 120305 suggest that the cryogenic jets were too thin for optimized TNSA or ESF acceleration. In this case, the transition from an opaque to a relativistically transparent plasma occurs too early resulting in less laser energy coupled into the hot electron population. The signals on the radiochromic films installed during Shot 12329 were converted to doses using the absolute calibration presented in Section 6.3 and are presented in Fig. 8.14. The average dose as a function of radius from the center of the proton beam was measured using circular line outs to determine the half-angle divergence of the proton beam as a function of energy (Fig. 8.15 (a)). At 10 MeV (45 MeV), the half-angle divergence is measured to be 18° (7°). At high energies, the half-angle divergence is nearly constant at 10° from 20 to 40 MeV then appears to decrease more slowly as a function of energy relative to TNSA [108], reaching 6.3° at 55 MeV. The half-angle divergence is higher and drops more quickly than TNSA from a planar target for proton energies <20 MeV. There is a visible change in energy dependence at 20 MeV, which may indicate a transition between acceleration processes. With an RCF stack covering a larger angular range, the boundaries of the proton beam were fully resolved

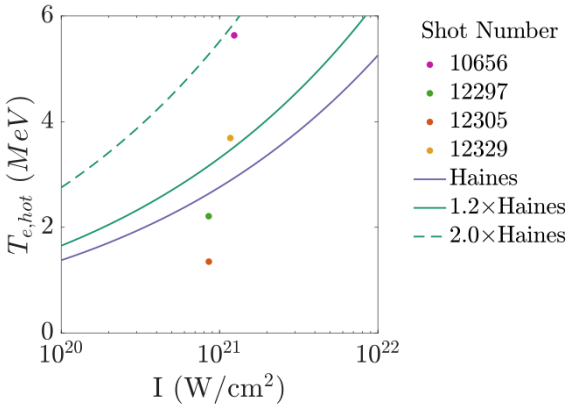

Figure 8.13: Comparison of $T_{e,hot}$ inferred from the slope of the proton energy spectra accelerated from 0.39 to 1 µm thick cryogenic liquid hydrogen jets with the Haines model. The 20% increase in hot electron temperature observed by Mishra et al. [5] is indicated by 1.2× Haines (dashed blue). Shot 10656 had a hot electron temperature of 5.63 MeV, which is 2× higher (blue solid line) than the Haines model.

in a subsequent shot. This confirms the presence of cylindrical spatial features on the proton beam at low energies that fade to TNSA-like conical emissions above ∼18.4 MeV.

The transition between the dominant acceleration processes and spatial features from both cylindrical and planar target geometries could be explained by a target density profile evolving on the picosecond timescale. At early times, low energy protons are accelerated via TNSA normal to the surface of the over-critical dumbell-shaped jet. Hydrodynamic pre-expansion of the jet washes out fine structures leading to oblong shape. Near the peak of the laser pulse, the expanding cylindrical rims coalesce on the laser axis forming a planar overcritical central region of the jet where ESF acceleration responsible for the highest proton energies is predicted to be dominant. Future experiments will deploy thicker jets with larger transverse widths to further investigate the transition from TNSA to ESF from planar low-Z targets.

During the experiment, the jet was irradiated at normal incidence for the majority of the shots. The orientation was set by rotating the jet until its width was maximized on one probe line and minimized on the other. Then, the jet was rotated to normal incidence using the known angle between the probe and the laser forward direction. On selected shots, the jet was rotated from normal incidence by a known amount. This resulted in an equivalent rotation in the ion beam direction and indicates that a fraction of the ions are accelerated in the target normal direction. The optical method used to align the jet orientation resulted in ion beam steering to better than ±5° precision.

Lastly, the peak proton flux through a centered 1.6 mm aperture located 1 mm from the jet is computed using the half-angle divergence and the proton time-of-flight (Fig. 8.15 (b)).

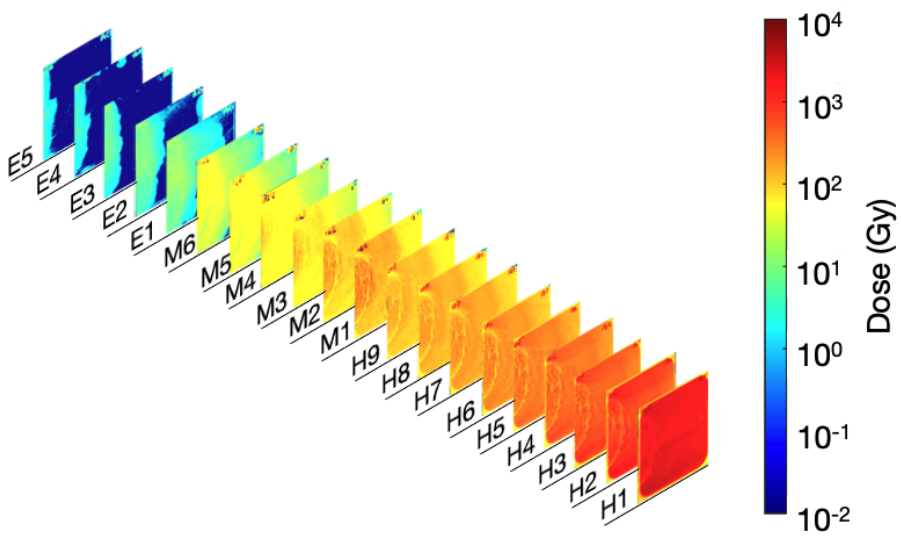

Figure 8.14: Absolutely calibrated radiochromic film stack design RCF#4 (Table 8.4) for Shot 12329. The color map indicates the dose deposited in the active layer of the film.

The diameter of the aperture was set to the half-angle divergence of 1.3 MeV protons. This parameter is a useful metric for comparing front-end injectors for hybrid particle accelerator designs. Then assuming the transverse and longitudinal emittance is on the order of a few µm mrad and 10^{-4} eV [251], we find that the proton and deuteron beams from pure cryogenic low-Z jets produced during this experiment surpass the brightness of current front-end injectors (e.g. GSI-FAIR) for conventional particle accelerators.

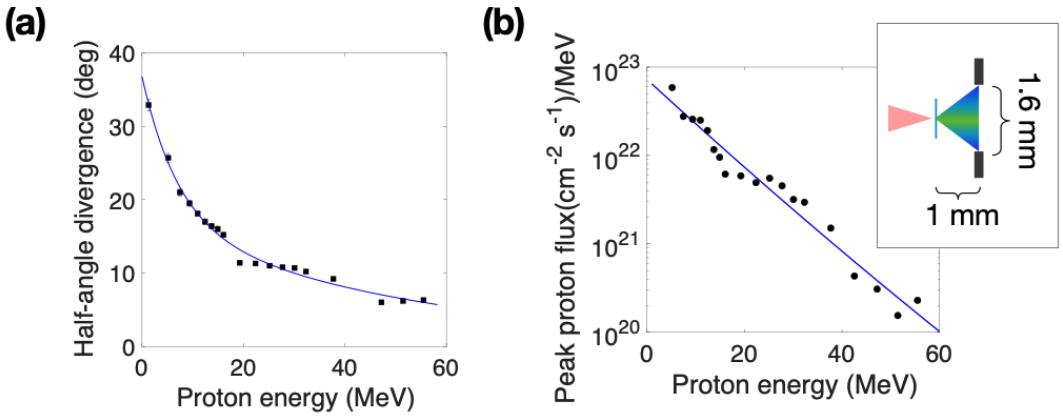

Figure 8.15: (a) Proton beam half-angle divergence as a function of energy computed from the RCF stack for Shot 12329 (Fig. 8.14). (b) Taking the beam divergence and time-of-flight into account, the peak proton flux at 1 mm from the target versus energy was computed. Inset: Illustration of proton beam collection through an aperture at 1 mm from the laser focus.

Chapter 9
Conclusion and Outlook

This thesis has laid the groundwork for the creation of bright, high repetition rate, multi-MeV proton and deuteron sources by the irradiation of a high-speed cryogenic low-Z liquid jet by 100 TW and petawatt-class lasers. The micron-sized cryogenic liquid jet system was developed and characterized [181] before being used to produce the first multi-MeV pure proton source with a 1 Hz repetition rate[14].

The tunable size, near-critical density, and single-element composition of the cryogenic jets enabled laboratory studies of hitherto inaccessible plasma regimes and acceleration processes. Bright, high-energy, directional proton (65 MeV) and deuteron beams (42 MeV) were produced by respectively irradiating a sub-micron-thick planar cryogenic liquid hydrogen or deuterium jet. Significant improvements to the jet stability and to the laser-target alignment procedure allowed for control of the ion beam direction to within less than $\pm 5^\circ$ [249].

The experiments were performed with an experimental platform compatible with high repetition rates. The main platform components are high-resolution transmission interferometry and shadowgraphy, orthogonal optical microscopy, and absolutely-calibrated charged particle diagnostics. Future experiments will study the maximum ion energy as a function of cryogenic jet thickness to identify the optimal target thickness and the transitions between laser-driven ion acceleration regimes. For example, by using a controllable laser prepulse to tailor the target density profile, we can assess the plasma conditions under which magnetic vortex acceleration (MVA) is predicted to occur. Already, the high-flux laser-accelerated deuteron beam was directed onto a stack of lithium and beryllium to generate a high-flux, quasi-directional neutron source via nuclear reactions and deuteron breakup in the materials [250].

To overcome the aperture damage observed in the experiments presented in this thesis that was due to plasma blowoff and hot electrons, an optically synchronized rotating mechanical chopper system has been developed at Helmholtz-Zentrum Dresden-Rossendorf (HZDR). The rotating chopper blade is placed at a typical distance of 10 mm above the interaction point and synchronized so that the direct line of sight between the aperture and the laser-plasma interaction is fully obstructed [233]. The survivability of the chopper blade and the protection of the aperture from a high-energy petawatt-class laser system has recently been demonstrated in an experiment with the PHELIX laser (500 fs, 200 J) at GSI Helmholtz Centre for Heavy Ion Research. With the addition of the mechanical system, the

experimental platform is fully qualified for high repetition rate experiments with high-energy petawatt lasers.

Experiments at high repetition rates will lead to larger, higher-fidelity data sets and will enable scans of the high-dimensional parameter space of ultra-intense laser-plasma processes. Data acquisition systems and control interfaces will be designed to use machine learning algorithms and active laser-target-diagnostic feedback loops to perform intelligent scans. Not only will this take full advantage of the 10 Hz repetition rate petawatt laser planned in the Matter in Extreme Conditions Upgrade (MEC-U) Project, but may also lead to a more holistic description of relativistic plasma and acceleration mechanisms.

As a result, cryogenic liquid jets have been indicated as the preferred primary or secondary target for four out of the five flagship experiments described in the MEC-U Project Conceptual Design Report [68]. The microphysics of collisionless shock waves and hydrogen-helium demixing will use a cryogenic jet as the primary target while the high repetition rate proton and ion source platform developed in this thesis will allow radiography measurements of high-energy-density plasmas, studies of proton, alpha, and ion stopping power in fusion-relevant plasmas, and measurements of the structural changes in fusion-relevant materials that are due to instantaneous and cumulative radiation damage. Together, these research areas address some of the main outstanding scientific questions in inertial fusion energy (IFE). At the same time, high repetition rate experiments with the cryogenic jet, especially cryogenic spherical droplet jets, will drive the development of target injection and tracking methods and critical subsystems for IFE.

The proof-of-concept work contained in this thesis will drive renewed interest in proton and deuteron sources for applications and will enable new technologies such as hybrid particle accelerators. In collaboration with accelerator physicists at SLAC National Accelerator Laboratory, subsequent work will address shot-to-shot stability, transport, and the injection of pulsed laser-accelerated proton sources into a radiofrequency linear accelerator. The ultra-short ($\sim$100 ps) ion beams produced by such future hybrid particle accelerators will enable new studies of the interaction of bright ion beams with matter. These next-generation, ultra-compact particle accelerators are expected to revolutionize radiography in civil and aerospace engineering and national security applications, supplant aging nuclear reactors in the production of medical isotopes, and increase access to proton radiotherapy for the treatment of cancer.

References

[1] D. Strickland and G. Mourou, Optical Communications **56**, 219 (1985).

[2] E. L. Clark et al., Physical Review Letters **84**, 670 (2000).

[3] R. A. Snavely et al., Physical Review Letters **85**, 2945 (2000).

[4] J. Fuchs et al., Nature Physics **2**, 48 (2006).

[5] R. Mishra, F. Fiuza, and S. Glenzer, New Journal of Physics **20**, 043047 (2018).

[6] A. P. L. Robinson, M. Zepf, S. Kar, R. G. Evans, and C. Bellei, New Journal of Physics **10**, 013021 (2008).

[7] L. Yin, B. J. Albright, B. M. Hegelich, and J. C. Fernández, Laser and Particle Beams **24**, 291–298 (2006).

[8] A. Henig et al., Physical Review Letters **103**, 245003 (2009).

[9] D. Haberberger et al., Nature Physics **8**, 95 (2012).

[10] F. Fiuza et al., Physical Review Letters **109**, 215001 (2012).

[11] J. Park et al., Physics of Plasmas **26**, 103108 (2019).

[12] A. Macchi, M. Borghesi, and M. Passoni, Reviews of Modern Physics **85**, 751 (2013).

[13] A. S. Pirozhkov et al., Proceedings of the Society of Photo Optical Instrumentation Engineering **7354** (2009).

[14] M. Gauthier et al., Applied Physics Letters **111**, 114102 (2017).

[15] S. Göde et al., Physical Review Letters **118**, 194801 (2017).

[16] M. Noaman-ul Haq et al., Nuclear Instruments and Methods in Physics Research Section A: Accelerators, Spectrometers, Detectors and Associated Equipment **883**, 191 (2018).

[17] J. T. Morrison et al., New Journal of Physics **20**, 022001 (2018).

[18] Y. Gao, (2020).

[19] J. Hartmann et al., (2021).

[20] T. Chagovets et al., Frontiers in Physics **9** (2022).

[21] P. Puyuelo-Valdes et al., Plasma Physics and Controlled Fusion **64**, 054003 (2022).

[22] F. Treffert et al., Applied Physics Letters **121**, 074104 (2022).

[23] F. Schillaci et al., Quantum Beam Science **6** (2022).

[24] P. W. Hatfield et al., Nature **593**, 351 (2021).

[25] T. Ma et al., Plasma Physics and Controlled Fusion **63**, 104003 (2021).

[26] R. J. Shalloo et al., Nature Communications **11**, 6355 (2020).

[27] E. Gschwendtner et al., Philosophical Transactions of the Royal Society A: Mathematical, Physical and Engineering Sciences **377**, 20180418 (2019).

[28] C. Palmer, New Journal of Physics **20**, 061001 (2018).

[29] M. Roth et al., Physical Review Letters **86**, 436 (2001).

[30] J. C. Fernández et al., Nuclear Fusion **49**, 065004 (2009).

[31] S. V. Bulanov et al., Phys. Lett. A **299**, 240 (2002).

[32] V. Malka et al., Med. Phys. **31**, 1587 (2004).

[33] T. Tajima et al., Reviews of Accelerator Science and Technology **02**, 201 (2009).

[34] S. D. Kraft et al., New Journal of Physics **12**, 085003 (2010).

[35] K. Zeil et al., Applied Physics B **110**, 437 (2013).

[36] M. Borghesi et al., Physics of Plasmas **9**, 2214 (2002).

[37] L. Romagnani et al., Physical Review Letters **95**, 4 (2005).

[38] P. K. Patel et al., Physical Review Letters **91**, 125004 (2003).

[39] A. Mančić et al., Physical Review Letters **104**, 035002 (2010).

[40] G. M. Dyer et al., Physical Review Letters **101**, 015002 (2008).

[41] M. Gauthier et al., Physical Review Letters **110**, 135003 (2013).

[42] A. B. Zylstra et al., Physical Review Letters **114**, 215002 (2015).

[43] S. Malko et al., Nature Communications **13**, 2893 (2022).

[44] M. E. Ferrario and R. Assmann, *in Proceedings of the CERN–Accelerator–School: Introduction to Accelerator Physics* (2021).

[45] W. Bragg and R. Kleeman, The London, Edinburgh, and Dublin Philosophical Magazine and Journal of Science **8**, 726 (1904).

[46] M. J. Berger et al., ICRU, Report 49 (1993).

[47] BNL, Proton Bragg Peak Measurements at NSRL, 2018.

[48] V. S. Khoroshkov and E. I. Minakova, European Journal of Physics **19**, 523 (1998).

[49] M. J. Berger et al., ICRU, Report 37 (1984), Report 37.

[50] M. Borghesi et al., Physical Review Letters **92**, 055003 (2004).

[51] A. J. Mackinnon et al., Review of Scientific Instruments **75**, 3531 (2004).

[52] A. J. Mackinnon et al., Physical Review Letters **97**, 045001 (2006).

[53] J. D. Lawson, Proceedings of the Physical Society. Section B **70**, 6 (1957).

[54] J. Lindl, Physics of Plasmas **2**, 3933 (1995).

[55] A. R. Christopherson et al., Physics of Plasmas **27**, 052708 (2020).

[56] M. H. Key, Physics of Plasmas **14**, 055502 (2007).

[57] R. Drake, *High-Energy-Density Physics: Fundamentals, Inertial Fusion, and Experimental Astrophysics*, Shock Wave and High Pressure Phenomena, Springer Berlin Heidelberg, 2006.

[58] C. M. Brenner et al., Applied Physics Letters **104**, 081123 (2014).

[59] S. Atzeni, M. Temporal, and J. Honrubia, Nuclear Fusion **42**, L1 (2002).

[60] Y. H. Ding, A. J. White, S. X. Hu, O. Certik, and L. A. Collins, Physical Review Letters **121**, 145001 (2018).

[61] A. J. White, O. Certik, Y. H. Ding, S. X. Hu, and L. A. Collins, Physical Review B **98**, 144302 (2018).

[62] L. S. Brown, D. L. Preston, and R. L. Singleton Jr., Physics Reports **410**, 237 (2005).

[63] D. O. Gericke, M. S. Murillo, and M. Schlanges, Physical Review E **65**, 036418 (2002).

[64] A. B. Zylstra, H. G. Rinderknecht, J. A. Frenje, C. K. Li, and R. D. Petrasso, Physics of Plasmas **26**, 122703 (2019).

[65] J. A. Frenje et al., Physical Review Letters **122**, 015002 (2019).

[66] A. B. Zylstra and O. A. Hurricane, Physics of Plasmas **26**, 062701 (2019).

[67] O. A. Hurricane et al., Physics of Plasmas **26**, 052704 (2019).

[68] G. Dyer and A. Fry, Technical Report: Matter in Extreme Conditions Upgrade Conceptual Design Report (2021).

[69] N. R. Council, *An Assessment of the Prospects for Inertial Fusion Energy*, The National Academies Press, Washington, DC, 2013.

[70] A. L. Kritcher et al., Nature Physics **18**, 251 (2022).

[71] A. B. Zylstra et al., Nature **601**, 542 (2022).

[72] E. I. Moses, Nuclear Fusion **49**, 104022 (2009).

[73] P. A. Norreys, C. Ridgers, K. Lancaster, M. Koepke, and G. Tynan, Philosophical Transactions of the Royal Society A: Mathematical, Physical and Engineering Sciences **378**, 20200006 (2020).

[74] J. J. Macfarlane, I. E. Golovkin, and P. R. Woodruff, Journal of Quantitative Spectroscopy and Radiative Transfer **99**, 381 (2006).

[75] L. B. Fletcher et al., Nature Photonics **9**, 274 EP (2015), Article.

[76] M. Millot et al., Science **347**, 418 (2015).

[77] B. I. Cho et al., Physical Review Letters **106**, 167601 (2011).

[78] K. Engelhorn et al., Physical Review B **91**, 214305 (2015).

[79] Y. Ping et al., High Energy Density Physics **4** (2010).

[80] A. Mančicć et al., Review of Scientific Instruments **79**, 073301 (2008).

[81] E. J. Hall, International Journal of Radiation Oncology, Biology, Physics **65**, 1 (2006).

[82] J. D. Wilson, E. M. Hammond, G. S. Higgins, and K. Petersson, Frontiers in Oncology **9** (2020).

[83] N. Esplen, M. S. Mendonca, and M. Bazalova-Carter, Physics in Medicine & Biology **65**, 23TR03 (2020).

[84] J. R. Hughes and J. L. Parsons, International Journal of Molecular Sciences **21** (2020).

[85] B. Lin et al., Frontiers in Oncology **11** (2021).

[86] A. Yogo et al., Applied Physics Letters **94**, 181502 (2009).

[87] K. Zeil et al., Applied Physics B **110**, 437 (2013).

[88] E. Bayart et al., Scientific Reports **9**, 10132 (2019).

[89] J. Bin et al., Scientific Reports **12**, 1484 (2022).

[90] A. Higginson et al., Nature Communications **9**, 724 (2018).

[91] F. Kroll et al., Nature Physics **18**, 316 (2022).

[92] G. Aymar et al., Frontiers in Physics **8** (2020).

[93] J. Peatross, M. Berrondo, D. Smith, and M. Ware, Opt. Express **25**, 13990 (2017).

[94] A. Fox, *Optical Properties of Solids*, Oxford master series in condensed matter physics, Oxford University Press, 2001.

[95] P. Gibbon, *Short Pulse Laser Interactions with Matter: An Introduction*, Imperial College Press, 2005.

[96] B. Quesnel and P. Mora, Physical Review E **58**, 3719 (1998).

[97] R. Fedosejevs, Introduction to Plasma Engineering, ECE 675, University of Alberta, 2016.

[98] W. L. Kruer and K. Estabrook, Physics of Fluids **28**, 430 (1985).

[99] S. C. Wilks, W. L. Kruer, M. Tabak, and A. B. Langdon, Physical Review Letters **69**, 1383 (1992).

[100] F. N. Beg et al., Physics of Plasmas **4**, 447 (1997).

[101] M. G. Haines, M. S. Wei, F. N. Beg, and R. B. Stephens, Physical Review Letters **102**, 045008 (2009).

[102] A. Macchi, M. Borghesi, and M. Passoni, Reviews of Modern Physics **85**, 751 (2013).

[103] J. Schreiber, P. R. Bolton, and K. Parodi, Review of Scientific Instruments **87**, 071101 (2016).

[104] P. Mora, Physical Review Letters **90**, 185002 (2003).

[105] S. C. Wilks et al., Physics of Plasmas **8**, 542 (2001).

[106] H.-P. Schlenvoigt, O. Jäckel, S. M. Pfotenhauer, and M. C. Kaluza, Laser-based particle acceleration, in *Advances in Solid State Lasers*, IntechOpen, 2010.

[107] K. Zeil et al., New Journal of Physics **12**, 045015 (2010).

[108] M. Roth and M. Schollmeier, *in Proceedings of the CAS-CERN Accelerator School: Plasma Wake Acceleration* (2016).

[109] L. Fedeli, A. Formenti, L. Cialfi, A. Pazzaglia, and M. Passoni, Scientific Reports **8**, 3834 (2018).

[110] A. Pukhov and J. Meyer-ter Vehn, Physical Review Letters **76**, 3975 (1996).

[111] C. D. Decker, W. B. Mori, K. Tzeng, and T. Katsouleas, Physics of Plasmas **3**, 2047 (1996).

[112] A. P. L. Robinson, R. M. G. M. Trines, J. Polz, and M. Kaluza, Plasma Physics and Controlled Fusion **53**, 065019 (2011).

[113] M. Lontano and M. Passoni, *Ultraintense Electromagnetic Radiation in Plasmas: Part II. Relativistic Electromagnetic Solitons and Laser-Driven Ion Acceleration*, Springer Berlin Heidelberg, 2007.

[114] A. Pukhov, Z.-M. Sheng, and J. Meyer-ter Vehn, Physics of Plasmas **6**, 2847 (1999).

[115] E. National Academies of Sciences and Medicine, *Plasma Science: Enabling Technology, Sustainability, Security, and Exploration*, The National Academies Press, Washington, DC, 2021.

[116] C. A. J. Palmer et al., Physical Review Letters **106**, 014801 (2011).

[117] H.-G. J. Chou, A. Grassi, S. H. Glenzer, and F. Fiuza, Physical Review Research **4**, L022056 (2022).

[118] A. Stockem Novo, M. C. Kaluza, R. A. Fonseca, and L. O. Silva, Scientific Reports **6**, 29402 (2016).

[119] E. d'Humières et al., Plasma Physics and Controlled Fusion **55**, 124025 (2013).

[120] F. Fiuza, R. A. Fonseca, J. Tonge, W. B. Mori, and L. O. Silva, Physical Review Letters **108**, 235004 (2012).

[121] B. Aurand et al., New Journal of Physics **22**, 033025 (2020).

[122] L. Waxer et al., Optics & Photonics News **16**, 30 (2005).

[123] C. Danson et al., Laser and Particle Beams **23**, 87–93 (2005).

[124] Y. Kitagawa et al., IEEE Journal of Selected Topics in Quantum Electronics **40**, 281 (2004).

[125] S. Gales, The European Physical Journal Special Topics **224**, 2631 (2015).

[126] J. W. Yoon et al., Optica **8**, 630 (2021).

[127] J. Igor, Optik & Photonik **5**, 30 (2010).

[128] A. Dubietis, G. Jonušauskas, and A. Piskarskas, Optical Communications **88**, 437 (1992).

[129] I. Ross, P. Matousek, M. Towrie, A. Langley, and J. Collier, Optical Communications **144**, 125 (1997).

[130] T. Oksenhendler, P. Bizouard, O. Albert, S. Bock, and U. Schramm, Opt. Express **25**, 12588 (2017).

[131] L. Obst et al., Plasma Physics and Controlled Fusion **60**, 054007 (2018).

[132] B. Stuart et al., CLEO, Lasers and Electro-Optics , 1 (2006).

[133] M. Martinez et al., AIP Conference Proceedings **1507**, 874 (2012).

[134] E. Gaul et al., Journal of Physics: Conference Series **717**, 012092 (2016).

[135] J. Collier, C. Hernandez-Gomez, R. Allott, C. Danson, and A. Hall, Laser and Particle Beams **19**, 231–235 (2001).

[136] S. Luan, M. H. R. Hutchinson, R. A. Smith, and F. Zhou, Measurement Science and Technology **4**, 1426 (1993).

[137] G. Doumy et al., Physical Review E **69**, 026402 (2004).

[138] B. Dromey et al., Review of Scientific Instruments **75**, 645 (2004).

[139] C. Rödel et al., Applied Physics B **103**, 295 (2011).

[140] M. Kaluza et al., Physical Review Letters **93**, 045003 (2004).

[141] J. Peebles et al., New Journal of Physics **19**, 023008 (2017).

[142] A. Marcinkevičius et al., Applied Physics B **79**, 547 (2004).

[143] V. Chvykov, P. Rousseau, S. Reed, G. Kalinchenko, and V. Yanovsky, Optical Letters **31**, 1456 (2006).

[144] O. Albert et al., Optical Letters **31**, 2990 (2006).

[145] A. Kessel et al., Optica **5**, 434 (2018).

[146] P. Gibbon, Nature Physics **3**, 369 (2007).

[147] J. B. Kim, S. Göde, and S. H. Glenzer, Review of Scientific Instruments **87**, 1 (2016).

[148] R. E. Grisenti, R. A. C. Fraga, N. Petridis, R. Dörner, and J. Deppe, Europhysics Letters (EPL) **73**, 540 (2006).

[149] M. Gauthier et al., Review of Scientific Instruments **87**, 13 (2016).

[150] L. Obst et al., Scientific Reports **7**, 10248 (2017).

[151] S. Göde et al., Physical Review Letters **118**, 194801 (2017).

[152] M. Kühnel et al., Physical Review Letters **106**, 245301 (2011).

[153] E. E. McBride et al., Review of Scientific Instruments **89**, 10F104 (2018).

[154] S. H. Glenzer et al., Journal of Physics B: Atomic, Molecular and Optical Physics **49**, 092001 (2016).

[155] S. Garcia, D. Chatain, and J. P. Perin, Laser and Particle Beams **32**, 569–575 (2014).

[156] D. Margarone et al., Physical Review X **6**, 041030 (2016).

[157] S. D. Kraft et al., Plasma Physics and Controlled Fusion **60**, 044010 (2018).

[158] J. Polz et al., Scientific Reports **9**, 16534 (2019).

[159] J. B. Kim, C. Schoenwaelder, and S. H. Glenzer, Review of Scientific Instruments **89**, 10K105 (2018).

[160] NIST Standard Reference Database Number **69**.

[161] V. Parma, *in the Proceedings of the CAS-CERN Accelerator School: Superconductivity for Accelerators* (2014).

[162] R. Corruccini, Vacuum **7-8**, 19 (1959).

[163] A. G. Monroe, Technology and Uses of Liquid Hydrogen : Edited by R. B. Scott, W. H. Denton, and C. M. Nicholls: Pergamon Press Oxford, 1964.

[164] B. Ha, D. P. DePonte, and J. G. Santiago, Physical Review Fluids **3**, 114202 (2018).

[165] J. Eggers and E. Villermaux, Reports on Progress in Physics **71**, 036601 (2008).

[166] M. McCarthy and N. Molloy, The Chemical Engineering Journal **7**, 1 (1974), *An International Journal of Research and Development.*

[167] P. Neumayer et al., Physics of Plasmas **19**, 122708 (2012).

[168] J. G. Ziegler and N. B. Nichols, Journal of Dynamic Systems Measurement and Control **115**, 220 (1942), *Transactions of the ASME.*

[169] T. Ziegler et al., Plasma Physics and Controlled Fusion **60**, 074003 (2018).

[170] V. Scuderi et al., Journal of Instrumentation **12**, C03086 (2017).

[171] S. Vallières et al., Review of Scientific Instruments **91**, 103303 (2020).

[172] M. Salvadori et al., Scientific Reports **11**, 3071 (2021).

[173] M. Reimold et al., Scientific Reports **12**, 21488 (2022).

[174] H. Chen et al., Review of Scientific Instruments **79**, 10E533 (2008).

[175] D. Jung et al., Review of Scientific Instruments **82**, 043301 (2011).

[176] J. A. Cobble et al., Review of Scientific Instruments **82**, 113504 (2011).

[177] H. Sakaki et al., Review of Scientific Instruments **84**, 013301 (2013).

[178] F. Treffert et al., Review of Scientific Instruments **89**, 103302 (2018).

[179] G. Glenn et al., Journal of Instrumentation **14**, P03012 (2019).

[180] M. Schollmeier, M. Geissel, A. B. Sefkow, and K. A. Flippo, Review of Scientific Instruments **85**, 043305 (2014).

[181] C. B. Curry et al., Journal of Visualized Experiments **159**, e61130 (2020).

[182] F. H. Séguin et al., Review of Scientific Instruments **74**, 975 (2003).

[183] K. Harres et al., Review of Scientific Instruments **79**, 093306 (2008).

[184] R. Prasad et al., Nuclear Instruments and Methods in Physics Research Section A: Accelerators, Spectrometers, Detectors and Associated Equipment **623**, 712 (2010), *1st International Conference on Frontiers in Diagnostics Technologies*.

[185] B. Aurand et al., Laser and Particle Beams **33**, 59–64 (2015).

[186] J. Metzkes et al., Review of Scientific Instruments **87**, 083310 (2016).

[187] M. Huault et al., High Power Laser Science and Engineering **7**, e60 (2019).

[188] D. A. Mariscal et al., Plasma Physics and Controlled Fusion **63**, 114003 (2021).

[189] A. McIlvenny et al., Journal of Instrumentation **14**, C04002 (2019).

[190] C. Salgado-López et al., Sensors **22** (2022).

[191] S. J. Thomson, The London, Edinburgh, and Dublin Philosophical Magazine and Journal of Science **21**, 225 (1911).

[192] P. Elleaume, O. Chubar, and J. Chavanne, *in Proceedings of the 1997 Particle Accelerator Conference (Cat. No.97CH36167)* **3** (1997).

[193] O. Chubar, P. Elleaume, and J. Chavanne, Journal of Synchrotron Radiation **5**, 481 (1998).

[194] J. F. Ziegler, M. D. Ziegler, and J. P. Biersack, Nuclear Instruments and Methods in Physics Research Section B: Beam Interactions with Materials and Atoms **268**, 1818 (2010).

[195] G. J. Williams, B. R. Maddox, H. Chen, S. Kojima, and M. Millecchia, Review of Scientific Instruments **85**, 11E604 (2014).

[196] P. Martin et al., Review of Scientific Instruments **93**, 053303 (2022).

[197] D. Nikezic and K. Yu, Materials Science and Engineering: R: Reports **46**, 51 (2004).

[198] J. Strehlow et al., Review of Scientific Instruments **90**, 083302 (2019).

[199] E. K. S. B. G. Cartwright and P. B. Price, Nuclear Instruments and Methods **153**, 457 (1978).

[200] J. Schindelin et al., Nature Methods **9**, 676 (2012).

[201] S. N. Chen et al., Review of Scientific Instruments **87**, 073301 (2016).

[202] C. B. Curry et al., Review of Scientific Instruments **91**, 093303 (2020).

[203] E. S. Diffenderfer et al., International Journal of Radiation Oncology, Biology, Physics **106**, 440 (2020).

[204] M. Gauthier et al., Physical Review Letters **110**, 135003 (2013).

[205] A. Pelka et al., Physical Review Letters **105**, 265701 (2010).

[206] M. Borghesi et al., Review of Scientific Instruments **74**, 1688 (2003).

[207] E. Breschi et al., Nuclear Instruments and Methods in Physics Research Section A: Accelerators, Spectrometers, Detectors and Associated Equipment **522**, 190 (2004).

[208] D. S. Hey et al., Review of Scientific Instruments **79**, 053501 (2008).

[209] F. Nürnberg et al., Review of Scientific Instruments **80**, 033301 (2009).

[210] D. Kirby et al., Laser and Particle Beams **29**, 231 (2011).

[211] P. Bolton et al., Physica Medica **30**, 255 (2014).

[212] M. Bazalova-Carter et al., Medical Physics **42**, 1606 (2015).

[213] P. R. Almond et al., Medical Physics **26**, 1847 (1999).

[214] Y. Feng, H. F. Tiedje, K. Gagnon, and R. Fedosejevs, Review of Scientific Instruments **89**, 043511 (2018).

[215] S. Devic et al., Medical Physics **32**, 2245 (2005).

[216] S. Devic, Physica Medica **27**, 122 (2011).

[217] X. H. Xu et al., Review of Scientific Instruments **90**, 033306 (2019).

[218] J. H. Bin et al., Review of Scientific Instruments **90**, 053301 (2019).

[219] M. Vadrucci et al., Medical Physics **42**, 4678 (2015).

[220] M. Najafi, G. Geraily, A. Shirazi, M. Esfahani, and J. Teimouri, Medical Dosimetry **42**, 159 (2017).

[221] S. Aldelaijan and S. Devic, Physica Medica **49**, 112 (2018).

[222] A. Yogo et al., Scientific Reports **7**, 42451 (2017).

[223] D. Mariscal et al., Physics of Plasmas **26**, 43110 (2019).

[224] F. Fiuza et al., Plasma Physics and Controlled Fusion **53**, 074004 (2011).

[225] K. D. Xiao et al., Physics of Plasmas **25**, 023103 (2018).

[226] L. Obst-Huebl et al., Nature Communications **9**, 5292 (2018).

[227] S. Kar et al., Nature Communications **7**, 10792 (2016).

[228] F.-E. Brack et al., Scientific Reports **10**, 9118 (2020).

[229] C. Ruyer et al., Nature Physics (2020).

[230] N. L. Kugland, D. D. Ryutov, C. Plechaty, J. S. Ross, and H.-S. Park, Review of Scientific Instruments **83**, 101301 (2012).

[231] M. Nakatsutsumi et al., Nature Communications **9**, 280 (2018).

[232] C. Bernert et al., Scientific Reports **12**, 7287 (2022).

[233] M. Rehwald et al., *in review* (2023).

[234] M. Rosiński et al., Vacuum **78**, 435 (2005), Proceedings of the Fifth International Conference on Ion Implantation and other Applications of Ions and Electrons (ION 2004).

[235] R. A. Costa-Fraga et al., Review of Scientific Instruments **83**, 025102 (2012).

[236] Ashland, GAFchromic Radiology Films, 2017.

[237] T. W. Jeong et al., Review of Scientific Instruments **87**, 083301 (2016).

[238] M. Roth et al., Physical Review Accelerators and Beams **5**, 061301 (2002).

[239] A. Macchi, A. Sgattoni, S. Sinigardi, M. Borghesi, and M. Passoni, Plasma Phys. Controlled Fusion **55**, 124020 (2013).

[240] K. Zeil et al., Plasma Phys. Controlled Fusion **56**, 084004 (2014).

[241] T. Kluge et al., Physics of Plasmas **17**, 123103 (2010).

[242] D. Neely et al., Applied Physics Letters **89**, 021502 (2006).

[243] B. M. Hegelich et al., New Journal of Physics **15**, 085015 (2013).

[244] J. Schreiber, P. R. Bolton, and K. Parodi, Review of Scientific Instruments **87** (2016).

[245] B. Dromey et al., Nature Communications **7**, 10642 (2016).

[246] M. Noaman-ul Haq et al., Physical Review Accelerators and Beams **20**, 041301 (2017).

[247] P. L. Poole et al., Sci. Rep. **6**, 32041 (2016).

[248] L. B. Fletcher et al., Review of Scientific Instruments **87**, 11E524 (2016).

[249] C. B. Curry, et al., (in preparation) .

[250] F. Treffert, C. B. Curry et al., (in preparation) .

[251] T. E. Cowan et al., Phys. Rev. Lett. **92**, 204801 (2004).

[252] P. McKenna et al., Review of Scientific Instruments **73**, 4176 (2002).

[253] T. Fujii et al., Applied Physics Letters **83**, 1524 (2003).

[254] I. Spencer et al., Physical Review E **67**, 046402 (2003).

[255] B. Hou et al., Applied Physics Letters **95**, 101503 (2009).

[256] M. Noaman-ul Haq et al., Nuclear Instruments and Methods in Physics Research Section A: Accelerators, Spectrometers, Detectors and Associated Equipment **909**, 164 (2018).

[257] Y. Gershuni et al., Nuclear Instruments and Methods in Physics Research Section A: Accelerators, Spectrometers, Detectors and Associated Equipment **934**, 58 (2019).

Appendices

Appendix A: Overview of high repetition rate laser-driven ion acceleration

Extended from the table presented in the supplementary material of Treffert *et al.* [22].

Literature		Laser Parameters			Ion Beam Parameters		
Year	**Reference**	**Rep. Rate (Hz)**	**E_L (J)**	**I_0 (W/cm^2)**	**Ion**	**E_{ion} (MeV)**	**Flux (#/sr/min)**
2002	McKenna *et al.* [252]	< 10	< 0.2	$< 10^{19}$	p	1.5	$\sim 10^{10}$*
2003	Fujii *et al.* [253]	< 10	0.088	6.8×10^{18}	p	1.2	–
2003	Spencer *et al.* [254]	2	0.2	$< 10^{19}$	p	1.5	$\sim 10^{10}$*
2009	Hou *et al.* [255]	500	0.003	2×10^{18}	p	0.5	$\sim 10^{12}$
2009	Pirozkhov *et al.* [13]	1	1	1×10^{20}	p	4	$\sim 10^{11}$*
2017	**Gauthier et al.**† [14]	**1**	**3**	$\mathbf{5 \times 10^{20}}$	**p**	**6.5**	$\mathbf{\sim 10^{12}}$
2017	Noaman-ul-Haq *et al.* [246]	0.2	2	$\sim 6 \times 10^{19}$	p	6	–
2017	Goede *et al.* [15]	~ 1	3	5×10^{20}	p	6.5	$\sim 10^{12}$
2018	Morrison *et al.* [17]	5	0.011	5×10^{18}	p	2	$\sim 10^{11}$
2018	Noaman-ul-Haq *et al.* [256]	0.2	1.5	5×10^{19}	p	6	–
2018	Noaman-ul-Haq *et al.* [16]	~ 1	2	$\sim 10^{20}$	p	4.5	–
2019	Aurand *et al.* [121]	5	0.7	10^{20}	p	0.065	$\sim 10^{12}$
2019	Gershuni *et al.* [257]	0.2	0.5	$\sim 10^{19}$	p	2	$\sim 10^{11}$
2020	Gao [18]	0.5	2.4	3.4×10^{20}	p	8	–
2021	Hartmann *et al.* [19]	0.5	5	$\sim \times 10^{20}$	p	20	–
2021	Jinno *et al.* [19]	0.1	9	1.6×10^{20}	p	12.4	–
2022	Chagovets *et al.* [20]	3.3	1	5×10^{19}	p	1.5	–
2022	Puyuelo-Valdes *et al.* [21]	< 1	4	4×10^{19}	p	3.5	$\sim 10^{11}$
2022	Treffert *et al.* [22]	0.5	5.5	1.2×10^{20}	d	4.4	$\sim 10^{12}$
2022	Schillaci *et al.* [23]	0.5	10.4	$\sim \times 10^{21}$	p	14	–

*estimated from spectrum in published work

†work contained in this thesis

Appendix B: Overview of current and future high repetition rate short pulse laser systems

Laser Name	**Energy (J)**	**Pulse Duration (fs)**	**Rep. Rate (Hz)**	**Laser Technology**
J-KAREN	23	33	10	Ti:Sa
J-KAREN	63	33	0.1	Ti:Sa
SILEX-I	9	30	0.15	Ti:Sa
Astra-Gemini	15	30	5	Ti:Sa
GIST	33	30	0.1	Ti:Sa
ALLS	3.2	22	2.5	Ti:Sa
PULSAR	5	20	5-10	Ti:Sa
VEGA2	6	30	10	Ti:Sa
ELI L3 HAPLS	>30	<30	10	Ti:Sa
DRACO	>30	<30	10	Ti:Sa
BELLA	40	<30	1	Ti:Sa
ALEPH	26	30	3.3	Ti:Sa
VEGA3	30	30	1	Ti:Sa
ELI-ALPS	40	15	5	Ti:Sa
ELI-NP	20	<20	1	Ti:Sa
ELI-NP	220	<20	1/60	Ti:Sa
APOLLON	150	15	1/60	Ti:Sa
ELI L4 ATON	1500	150	1/60	Nd:Glass
MEC-U	150	150	10	Nd:Glass
PENELOPE	150	60	1	Yb-doped glass/CaF_2